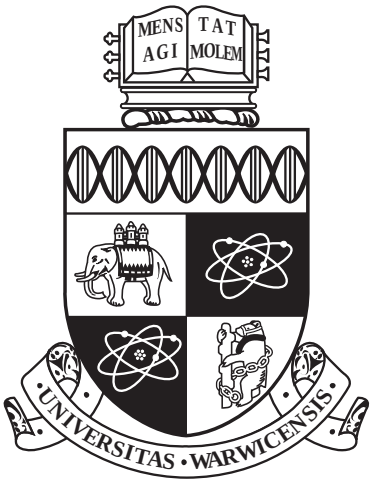

Ground and Space-based Transit Surveys: Exoplanet Detection and Evaporating Atmospheres

by

Wai Fun Lam

Thesis

Submitted to the University of Warwick

for the degree of PhD Physics

Doctor of Philosophy

Department of Physics

.... 2018

THE UNIVERSITY OF
WARWICK

Contents

List of Tables

List of Figures

Acknowledgments

First and foremost, I would like to thank my supervisor and mentor Don Pollacco for his guidance and immense patience throughout my PhD. He has provided great support and ideas during many unscheduled visits, and without him the completion of this PhD would not be possible.

I am grateful for the assistance and advice offered by the post-docs in the Warwick Exoplanet group, David Armstrong, David Brown, Francesca Faedi, and James McCormac. In particular, DA and DB for proofreading several chapters in this thesis and provided constructive feedbacks.

The final stages of a PhD are not easy but I am lucky to have a number of fellow PhD students who shared this stressful time. James Kirk, Chris Manser, Odette Toloza, and Louise Wang - thanks for helping me through this period!

Special mention to members of the University of Warwick Volleyball Club for creating a memorable overall PhD experience. In particular, Zofia Garajova, Marie Grypioti, Maria Chiara Roffin, Sophia Spadoni, Veronika Vohlmuthova for sharing those coffee moments.

I thank Andreas Iskra for his valuable discussion on atomic spectroscopy and his encouragement in the past 3.5 years. You are a star! Last but not least, I would also like to thank my family for their unconditional support in my decision to continue in academia.

Finally, I am grateful to STFC for funding my PhD.

Declarations

I declare that work presented in this thesis is my original research carried out at the University of Warwick during the period from October 2014 to May 2018, under the supervision of Prof. Don Pollacco. Collaborative work done by others and published work are clearly indicated in each chapter, and are summarised below.

The work in chapter 3 has been published in the paper by Lam et al. (2017), and contains some collaborative work. The WASP photometry reduction was performed as part of the well-established pipeline. Follow up photometric and spectroscopic observations were obtained by the D.R. Anderson, G. Hébrard, M. Lendl, L. Mancini, TRAPPIST team, and A. H. M. Triaud. Spectral analysis was performed by B. Smalley. I was involved in the candidate detection, stellar age analysis, joint lightcurve and RV analysis for system characterisation, and lead the publication of the work.

Chapter 4 contains collaborative work in the ESO-K2 consortium. These include follow up RV and direct imaging observations. The *K2* photometry reduction was performed by S. C. C. Barros and D. J. Armstrong. Spectral analysis was performed by collaborators at University of Porto, and T. Lopez derived the stellar rotation period using the stellar activity measurement. Initial MCMC analysis of the planetary system was performed by myself, A. Santerne ran the final and improved MCMC analysis with `PASTIS` and the result was adopted in the chapter. I was also involved in the candidate detection, follow up observations, stellar rotational analysis using the auto-correlation function, stellar ages estimate using gyrochronology and [Y/Mg] ratio, planet composition analysis, and spearheading the publication of this work.

The work in chapters 5 and 6 is entirely work of my own unless or otherwise stated.

The WASP-12 HIRES data used in chapter 5 were obtained from the KECK archive. The candidate selection process in chapter 6 was done by D. J. A. Brown, and the FLAMES-GIRAFFE data were observed with service mode and reduced by the ESO dedicated pipeline.

Abstract

The characteristics and dynamics of exoplanets are broad and diverse. Detailed analysis of the systems can shed light on the history of their formation and evolution. This thesis presents the discovery and analysis of a range of exoplanets. The evaporating planet WASP-12 b was studied to understand the evolution of its atmosphere. Further, the investigation of a new planet detection method through measuring the stellar activity index is presented.

Three gas giant planets were detected by SuperWASP. The inflated Neptune WASP-127 b is one of the least dense planets detected to date. It has a striking atmospheric scale height of 2500 km, which provides an optimal target for atmospheric studies with the James Webb Space Telescope. The hot Jupiter WASP-136 b was found to be in a re-inflation phase as its host star is evolving, and the planet is predicted to have an age of 0.420 Gyr. The detection of WASP-138 b around a slightly metal-poor host weakens the correlation between formation of planets and the metallicity of stars. In addition to ground-based discoveries, the super-Earth EPIC 206011496 b was detected with the *K2* mission. The mass of EPIC 206011496 b was determined with HARPS RV with a precision of 13%. The bulk density of the planet implies an Earth-like composition which has a predominantly rocky interior. EPIC 206011496 b lies at the lower limit of the photoevaporation gap, which suggests its atmosphere may have been eroded away in the past.

The variability of the evaporating hot Jupiter WASP-12 b was investigated using archival KECK/HIRES spectra. Enhanced absorption in the cores of both Ca II H and K and Na I D lines were detected throughout the planetary orbit, supporting the presence of a circumstellar gas disc formed by the evaporated planet material. The mean column density of Ca II was measured as 6×10^{14} cm^{-2}, which indicates an overall circumstellar gas density of 5.83×10^{-14} g cm^{-3}.

Inspired by the anomalously low activity index of a number of planet hosting stars, a survey was conducted to test a new detection technique which measures the activity index of stars in open clusters. An activity-age relation was determined for young mid-A to F type stars. Although no planet hosting candidate was identified, a significant increase in the sample size can ascertain the feasibility of this detection method.

Abbreviations

2MASS ..... Two Micron All–Sky Survey
AO ..... Adaptive optics
APASS ..... AAVSO Photometric All–Sky Survey
BIS ..... Bisector velocity span
BLS ..... Box-least squared algorithm
CCD ..... Charge–coupled device
CCF ..... Cross-correlation function
CHEOPS ..... CHaracterising ExOPlanet Satellite
CoRoT ..... Convection, Rotation and planetary Transits
COS ..... Cosmic Origin Spectrograph
EPIC ..... Ecliptic Plane Input Catalogue
ESO ..... European Southern Observatory
EW ..... Equivalent width
FLAMES ..... Fibre Large Array Multi Element Spectrograph
FoV ..... Field of view
FWHM ..... Full width half maximum
HARPS ..... High Accuracy Radial velocity Planet Searcher
HIRES ..... High Resolution Echelle Spectrometer
HJD ..... Heliocentric Julian Date
HST ..... Hubble Space Telescope
JWST ..... James Webb Space Telescope
MCMC ..... Markov–chain Monte Carlo
NASA ..... National Aeronautics and Space Administration
NUV ..... Near–ultraviolet
PLATO ..... PLAnetary Transits and Oscillations

RV ..... Radial velocity

SNR ..... Signal–to–noise ratio

STIS ..... Space Telescope Imaging Spectrograph

TESS ..... Transiting Exoplanet Survey Satellite

UTC ..... Universal time coordinated

VLT ..... Very Large Telescope

WASP ..... Wide Angle Search for Planets

XUV ..... X–ray and ultra–violet

Chapter 1

Introduction

1.1 Exoplanets: The Story So Far...

Astronomers have wondered for many years whether there are planets beyond our Solar System. Yet, technical challenge of detecting a low-mass, low-luminosity object in very close proximity to a star have been the barrier in the race to hunt for exoplanets. The first breakthrough came about in 1992 when Wolszczan and Frail (1992) confirmed the first detection of exoplanets around the millisecond pulsar PSR1257 + 12 with radio pulsar timing. A few years later, 51 Peg b (Mayor and Queloz, 1995) was discovered with the radial velocity (Doppler) method using high precision fibre-fed spectrograph ELODIE (Baranne et al., 1996). 51 Peg b has a mass of 0.5 M_{Jup} and an orbital period of 4.2 days, and is the first exoplanet known to orbit a main sequence star. What was surprising, of course, was the period and mass of the object - a hot Jupiter. The detection of such an unusual exoplanetary body had sparked great interest in astronomy, and by the end of the decade, a dozen exoplanets were discovered. Most notably, the first transiting hot Jupiter HD 209458 b (Henry et al., 2000; Charbonneau et al., 2000) was found, confirming the capability of the transit technique (Borucki and Summers, 1984; Borucki et al., 1985) in exoplanet searches. HD 209458 b went on to become the first planet to have its atmosphere detected and characterised with modern spectroscopic techniques (Charbonneau et al., 2002).

With the advancement of technologies and detection methods, much progress has been made over the past two decades. Multiple detection techniques are well established for efficient searches of planets: radial velocity measurements (Section 1.2.1), photometry and transit observations (Section 1.2.2), microlensing (Section 1.2.3), astrometry (Section 1.2.4) and direct imaging (Section 1.2.5). At the time of writing, 3706 validated exoplanets were discovered (Figure 1.2). The radial velocity and transit detection methods are responsible for majority of detections. Transit photometry makes use of orbital properties of a planet to

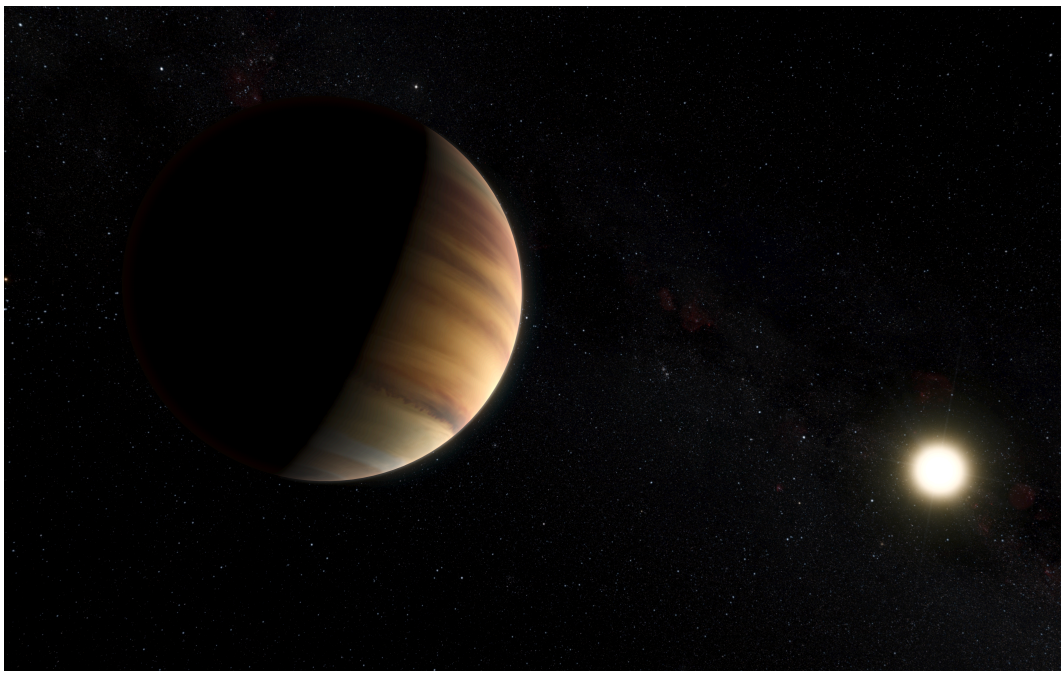

Figure 1.1: Artist's impression of 51 Peg b (left), the first hot Jupiter around a main sequence star (right). (Image credit: ESO/M. Kornmesser/Nick Risinger (`skysurvey.org`))

find periodic fractional changes in the flux of a star, and to determine the size of a planet. Both space (e.g. *Kepler*; Borucki et al. 2010 and *K2* missions; Howell et al. 2014) and ground-based (e.g. HATNet; Bakos et al. 2002, SuperWASP; Pollacco et al. 2006, KELT; Pepper et al. 2007, HATSouth; Bakos et al. 2013, NGTS; Wheatley et al. 2013) transit surveys have provided a huge sample of exoplanets for statistical studies and detailed characterisations. On the other hand, the radial velocity technique relies on the orbital reflex motion of the star-planet pair to constrain the planetary mass. The precision of this method depends heavily on the stability and resolution of spectrographs. From ELODIE (Baranne et al., 1996), to CORALIE (Queloz et al., 2000; Pepe et al., 2002a), and HARPS (Queloz et al., 2001b; Pepe et al., 2002b), the advances in instruments throughout the years have improved precisions of measurements down to below 1 m s^{-1}.

The radial velocity and transit observations are often made to compliment each other in planet detections. Detailed analyses of these observations have revealed a diverse range of exoplanets, many of which have characteristics that are unobserved in our Solar System. New theoretical challenges have emerged, and formation and evolution mechanisms of different types of planet populations are yet to be understood.

Hot Jupiters are gas giants which orbit their host stars with periods of $\leq$ 10 days, and orbital separations of $\leq$ 0.1AU (Wang et al., 2015). These Jupiter-mass planets can

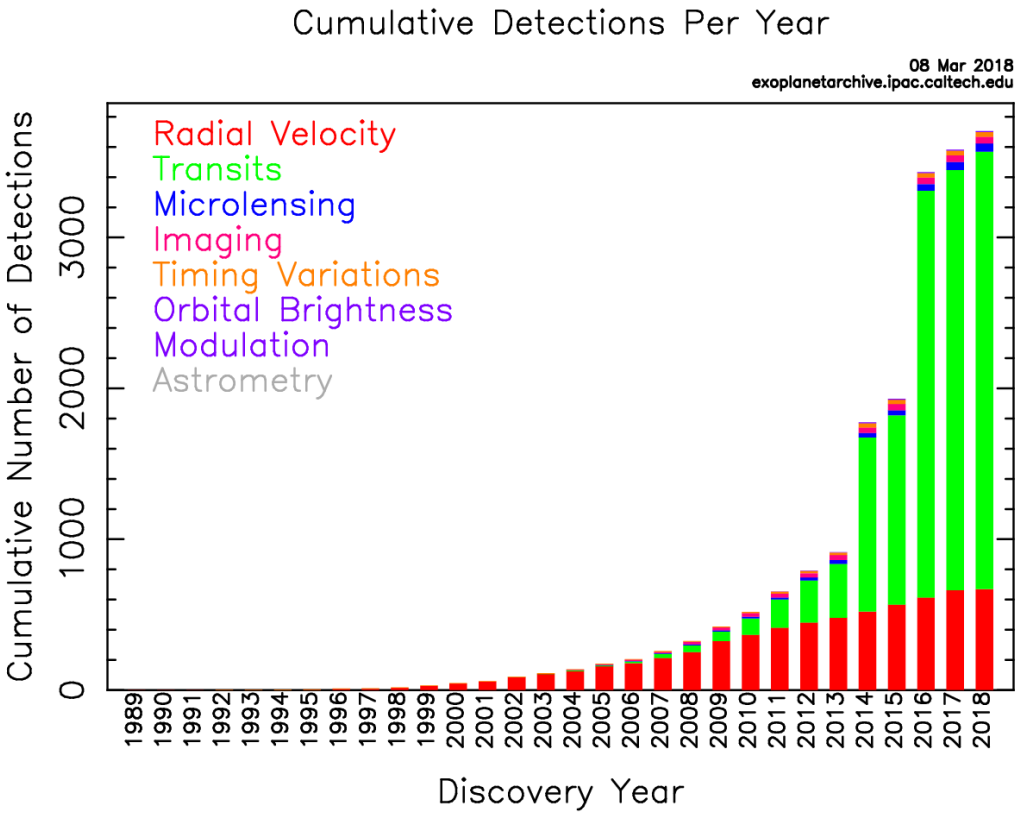

Figure 1.2: Cumulative detections of exoplanets in the past decades. (Source: NASA Exoplanet Archive)

range in radii from 0.775 R_J (WASP-59b; Hébrard et al. 2013) to 1.932 R_J (WASP-17b; Anderson et al. 2010; Southworth et al. 2012). Many of these hot Jupiters were found to have radii larger than predicted from standard coreless models (e.g. Fortney et al. 2007). Several theories were proposed to explain the observed inflated radii. These include stellar irradiation (Guillot et al., 1996), tidal heating (Bodenheimer et al., 2001, 2003), enhanced atmospheric opacity (Burrows et al., 2007), and Ohmic heating (Batygin et al., 2011).

On the opposite end of the spectrum, super-Earths are planets with sizes between the Earth and Neptune. From what we know from discoveries to date, they appear to be the most abundant type of exoplanet in our galaxy. Statistical studies have shown that 13% of main sequence GK stars host a super-Earth with orbital period < 50 days (Howard et al., 2012). Theoretical predictions showed differing evolution mechanisms can lead to a transition region among super-Earths, which separates the two distinct families with differing radii and compositions (e.g. Lopez et al. 2012; Lopez and Fortney 2013; Owen and Wu 2013). Planets with radii $R_P \leq 1.6\ R_\oplus$ (e.g. Kepler-10 b; Batalha et al. 2011, LHS1140 b; Dittmann et al. 2017) have higher bulk densities, and would possess a predominantly rocky interior. Whereas planets with lower densities (e.g. GJ 1214 b; Charbonneau et al. 2009, Kepler-11 system; Lissauer et al. 2011a) are more likely to bear solid cores and substantial gaseous envelopes.

Meanwhile, there is also a number of short-period sub-Saturn and super-Neptune mass planets such as WASP-39b ($M_p = 0.28\ M_J$; Faedi et al. 2011), HAT-P-11b ($M_p = 0.081\ M_J$; Bakos et al. 2010), and HAT-P-26b ($M_p = 0.059\ M_J$; Hartman et al. 2011). In the short-period planet population, there is a significant lack of detected planets with sizes between Jupiter and the Earth, giving rise to the so-called 'Neptune desert' (Mazeh et al., 2016). The presence of these intermediate planets are test beds for theories as to differentiates the formation and evolution histories of planet populations.

With the expanding number of exoplanets, it appears more questions emerged than are answered. However, future missions such as CHEOPS (Broeg et al., 2013), TESS (Ricker et al., 2014), PLATO (Rauer et al., 2014), along with future generations of spectrographs and near-infrared instruments, e.g. ESPRESSO (Pepe et al., 2014) and CARMENES Quirrenbach et al. 2012, we can obtain exceptional precision in radial velocity and transit measurements to aid our understanding in the present structures and dynamics of planets beyond our Solar system.

1.2 Detection Methods

This section reviews the different ways of exoplanet detection: radial velocity, transit observations, microlensing, astrometry, and direct imaging. The methodology, dedicated surveys,

notable discoveries and their detection parameter spaces are discussed.

1.2.1 Radial Velocity

The radial velocity (RV) detection technique first revealed the existence of planets around sun-like stars beyond our Solar System (Mayor and Queloz, 1995). It relies on the measurement of a star's reflex motion. In the presence of a planetary companion, the star orbits about the system's barycentre due to the planet's gravity. This results in a RV variation of the star, i.e. the change in velocity of the star towards and away from the observer (Mayor et al., 2014). Radial velocities can be measured using the Doppler shift of stellar absorption lines. Lines are redshifted (resulting in positive RV signals) if the distance between the star and the observer is increases. Meanwhile, lines are blueshifted (giving negative RV signals) when the distance between the star and the observer is reduced.

For a planet of mass M_p in an orbit with semi-major axis, a, eccentricity, e, and a period, P, the **radial velocity signal** of the star is (Wright and Howard, 2009; Perryman, 2014):

$$v_r(t) = K[\cos(\omega + \nu(t)) + e\cos\omega] + \gamma + d(t - t_0) \tag{1.1}$$

where γ is the time-independent velocity offset, and d is the linear trend parameter which accounts for the instrumental drift and/or contribution from a massive companion. The argument of pericentre ω is the angular coordinate of the orbiting body's pericentre relative to the orbital plane and direction of motion. The true anomaly $\nu(t)$ measures the angle between the pericentre and the current position of the body. K is the **radial velocity semi-amplitude**, which is expressed as:

$$K = (\frac{2\pi G}{P})^{\frac{1}{3}} \frac{M_p \sin i}{(M_s + M_p)^{2/3}(1 - e^2)^{1/2}} \tag{1.2}$$

The orbital inclination is denoted by i, G is the Gravitational constant, M_s and M_p are the masses of the star and planet, respectively. The semi-amplitude K is dominated by the term $M_p \sin i$, meaning the radial velocity method is more sensitive to massive planets.

The star's motion about the barycentre can be measured using the **Doppler shift** of stellar absorption lines. The shift in wavelength is:

$$\Delta\lambda = \frac{\lambda_{obs} - \lambda_{rest}}{\lambda_{rest}} \tag{1.3}$$

In the Solar System, the RV semi-amplitude of the Sun due to Jupiter's gravity is 12 m s^{-1} (Mayor et al., 2014). A precise measurement of the RV amplitude of the star can give constraint on the minimum mass, $M_p \sin i$, of the planet. A more massive planet will

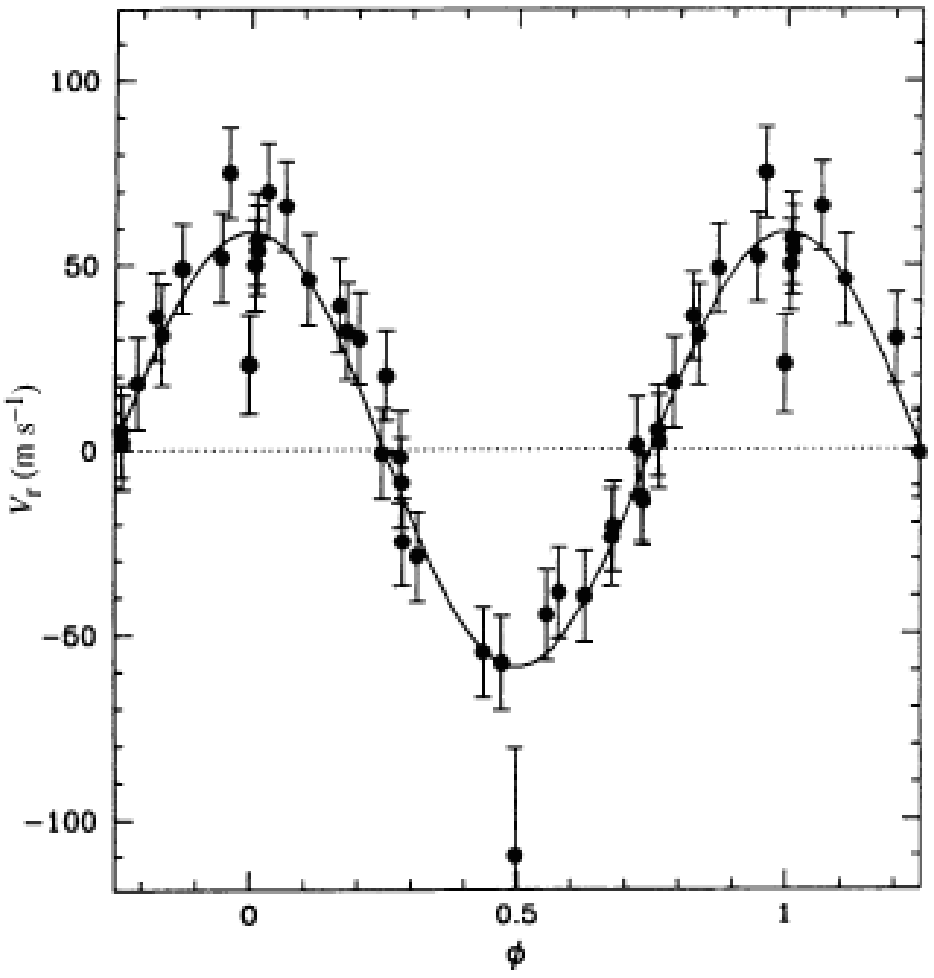

Figure 1.3: Radial velocity measurements of 51 Peg (phased at P = 4.5 d) show a semi-amplitude of 0.059 ± 0.003 ms^{-1} (from Mayor and Queloz (1995) reprinted with permission of *Nature Publishing Group*).

result in a larger RV variation. In a system where a 10 Jupiter-mass (M_J) planet orbits a solar-mass star, the corresponding RV semi-amplitude is 1.0 km s^{-1} (Bouchy et al., 2009b). A brown dwarf can have a mass as low as 30 M_J. Hence, a RV amplitude of larger than a few km s^{-1} indicates the likelihood of a stellar companion instead of a planet.

Giant planets shift the velocities of the host star by tens of m s^{-1}, therefore high precision spectrographs are necessary to reveal the accurate masses of exoplanets. The use of CORAVEL (Baranne et al., 1979) showed that Doppler motions of stars can be derived using the cross-correlation method. This knowledge was applied for the development of ELODIE (Baranne et al., 1996), a fibre-fed cross-dispersion spectrograph located on the 1.93 m telescope at the Observatoire de Haute-Provence (OHP). The instrument was able to achieve a radial velocity precision of $\sim$ 15 m s^{-1}, and 51 Peg b was soon discovered (Mayor and Queloz, 1995).

The SOPHIE spectrograph (Bouchy et al., 2009a) has replaced ELODIE since 2006. The spectrograph operates with a spectral resolution of 75, 000 and a coverage between 387 - 694 nm. It can derive RV measurements with a precision between 1 and 2 m s^{-1}.

The CORALIE spectrograph (Queloz et al., 2000; Pepe et al., 2002a) was installed at the 1.2 m Euler-Swiss Telescope at the ESO La Silla Observatory, Chile, following the success of ELODIE. With a resolving power of 50, 000, the instrument can obtain RV measurements with a precision of ~few m s^{-1}. SOPHIE and CORALIE spectrographs were instrumental in the follow-up effort for exoplanet detection in the past decade. Coupled with ground-based transiting surveys such as SuperWASP (to be discussed in detail in Section 1.2.2), and NGTS, accurate mass estimates of Jupiter and sub-Saturn mass planets can be achieved for detailed system characterisation.

The development of these spectrographs has demonstrated the need for a stable spectrograph to obtain 1 m s^{-1} precision RV measurements to constrain masses of Neptune and Earth mass planets. The HARPS (High Accuracy Radial velocity Planet Searcher) spectrograph mounted on the 3.6 m Telescope at ESO La Silla Observatory (Mayor et al., 2003) was designed for this specific purpose. The first HARPS discovery was the hot Jupiter HD 330075 b with minimum mass of 0.62 M_J (Pepe et al., 2004), where measurements were reported to have a root-mean-squared (rms) velocity of only 2 m s^{-1}. Further success came when HARPS reported the discovery of the super-Earth μ Ara b (Santos et al., 2004). The star was reported to have a semi-amplitude of just 4.1 m s^{-1}, and HARPS was capable of measuring radial velocities with precision better than 1 m s^{-1}. Early HARPS RV survey have also shown that low-mass planets are common in multiplanet systems. HARPS-N (Cosentino et al., 2012) on the 3.5 m Telescopio Nazionale Galileo (TNG) also provided accurate mass measurements for many Kepler/K2 planetary candidates. The development of next generation spectrographs such as ESPRESSO (Echelle SPectrograph for Rocky

Exoplanets and Stable Spectroscopic Observations: Pepe et al. 2014), and near infra-red spectrographs/spectropolarimeters (e.g. CARMENES: Quirrenbach et al. 2012, SPIRou: Delfosse et al. 2013), will be able to search for low-mass rocky planets in the habitable zones of quiet G - M dwarfs.

1.2.2 Transit Detection

The transit detection method remains the only direct route to determine planetary radius. The STARE telescope produced the first full transit observation of exoplanet (Charbonneau et al., 2000). From the two transits obtained, Charbonneau et al. were able to infer the planetary radius ($R_p = 1.27 \pm 0.02\ R_J$), as well as the orbital period (P = 3.52 d) and orbital separation (a = 0.0467 AU) of the system. Since then, the field of transit photometry has expanded significantly. The cost and accessibility of the transit detection method is relatively lower than for RV surveys. Many wide-field transit surveys have been established, yielding many interesting exoplanets with sizes ranging from Jupiter radii down to super-Earth radii.

Ground-based Surveys

Ground-based surveys provided a large number of candidates around stars that are sufficiently bright to enable follow up RV measurements, where strong observational constraints are obtained for theoretical studies.

Most transit detection surveys adopt the following sequence to identify candidate planets: Detection surveys monitor tens of thousands of bright stars with V $<$ 13 mag over a long period of time. The photometric data obtained are then reduced with aperture photometry using custom built pipelines. To correct for trends and systematic errors, the lightcurves are fitted with trend-removing algorithms to decorrelate systematic errors (e.g. SysRem: Tamuz et al. 2005, TFA: Kovács et al. 2005, EPD: Bakos et al. 2010). A box-firring least squares algorithm (BLS: Kovács et al. 2002) is applied to estimate the transit epoch, period, depth, and duration, such that periodic box-like signals can be identified. After a series of rigorous elimination of false positives (e.g. eclipsing binaries and giants), the best planetary candidates are subjected to follow up photometry and radial velocity observations for further detailed analyses.

SuperWASP (Wide Angle Search for Planets; Pollacco et al. 2006) is one of the most successful ground-based transit surveys. The WASP-North facility is located at the Observatorio del Roque de los Muchachos in La Palma, Canary Islands, and the WASP-South facility is located at the Sutherland Station of the South African Astronomical Observatory. Each telescope consists of an array of 8 Canon 200mm, f/1.8 telephoto lenses

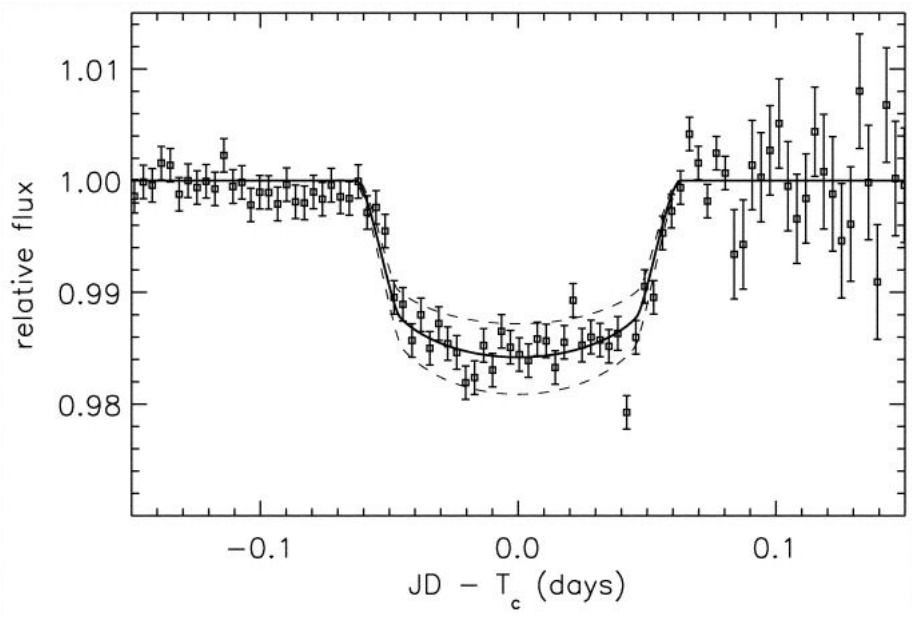

Figure 1.4: Phased-folded transit lightcurve of HD209458 b from Charbonneau et al. (2000), reproduced with permission from *The American Astronomical Society*.

coupled with e2v CCDs of 2048×2048 pixels each. The cameras in each facility provide a total field of view (FoV) of 8×64 square degrees and a pixel scale of 13.7". The telescopes can survey millions of objects and achieve a photometric precision better than 4 mmag for stars brighter than V $\sim$ 9.4 mag, and an accuracy of 1% for starts brighter than V $\sim$ 11.5 mag.

To date, over 150 exoplanet discoveries have been made with WASP, and a diverse population of planetary systems has been revealed. The Saturn-mass planet WASP-17 b (Anderson et al., 2010; Southworth et al., 2012) was found to be an inflated planet due to tidal heating from the tidal circularisation of its eccentric orbit. The Rossiter-McLaughlin effect was observed in the WASP-17 system, suggesting the planet is misaligned with a spin orbit angle of $\psi > 91.7^{\circ}$, hence a retrograde orbit (Triaud et al., 2010). Another low-density Saturn WASP-39 b was reported by Faedi et al. (2011) and a clear atmosphere was detected on this inflated planet (Sing et al., 2016; Barstow et al., 2017). WASP-12b is one of the hottest Jupiter known with an equilibrium temperature of 2516 K (Hebb et al., 2009). An enhanced transit was detected in the Near-UV (Fossati et al., 2010b). Further spectral analyses have shown complete absorption in the Mg II h & k and Ca II H & K line cores (Haswell et al., 2012; Fossati et al., 2013), suggestive of an extended exosphere around the planet WASP-12 b. The analysis of the time variability of the atmosphere of WASP-12 b will be discussed in more detail in Chapter 5.

HAT/HATNet (Hungarian Automated Telescope project; Bakos et al. 2004) comprises of the HATNorth and the HATSouth network. There are six automated telescopes at the HATNorth network, four of which are based in the Fred Lawrence Whipple Observatory (FLWO), a further two at the Submillimeter Array of SAO in the Mauna Kea Observatory. The HATSouth network is formed of six telescopes in the southern hemisphere. They are located at the Las Campanas Observatory (LCO), Chile, the High Energy Spectroscopic Survey (HESS) in Namibia, and the Siding Spring Observatory (SSO) in Australia.

Many interesting planets have been detected by HATNet. HAT-P-11b (Bakos et al., 2010) was the first transiting Neptune discovered from ground-based surveys. Transmission spectrum of HAT-P-11b revealed a cloud-free atmosphere on the planet and the presence of water vapour in its atmosphere. The irradiated massive hot Jupiter HAT-P-7b (Hartman et al., 2011) is a highly tilted planet with a retrograde orbit (Winn et al., 2009). The optical phase curve measurement of the system also found the planet's day-side temperature as 2650 ± 100 K (Borucki et al., 2009).

Ground-based surveys continue to make groundbreaking discoveries. SuperWASP and HATNet, along with **KELT** (Pepper et al., 2007), **QES** (Alsubai et al., 2013), **NGTS** (Wheatley et al., 2018), and all-sky surveys such as **MASCARA** (Snellen et al., 2012),

Evryscope (Law et al., 2015) and **Fly's Eye Camera** (Pál et al., 2016) will be able to push detection boundaries and search for smaller planets around brighter stars. These targets are crucial for characterisation with the James Webb Space Telescope in the near future.

Space-based Surveys

While ground-based projects have provided bright targets for follow up characterisations, the accuracies of transit lightcurves are limited by factors such as atmospheric extinction and scintillation. The planet detection parameter space is restricted to those with sizes of Jupiter or Neptune at best. Fortunately, the launch of space-based missions in the past decade meant that high precision photometry can be obtained, enabling the detection of sub-Neptune and Earth-sized planets.

The CoRoT satellite (Barge et al., 2008; Auvergne et al., 2009) commissioned between 2007 and 2012 was the first dedicated mission to search for transiting exoplanets in space. The telescope observed over 60, 000 stars with a photometric precision of 7×10^{-4} at V = 15.5 mag for a one hour integration. With this unprecedented precision, the first transiting super-Earth was discovered by Léger et al. (2009). The transit lightcurve of CoRoT-7 b revealed a planet with a size 1.68 times larger than the Earth and an orbital period of 0.85 d. The mass of the planet, however, has been disputed over the years. Queloz et al. (2009) determined the planet mass as 4.8 ± 0.8 $M_\oplus$ using follow up RV data from HARPS. Fourier analysis of the HARPS data by Hatzes et al. (2010) argued that the RV signal of CoRoT-7 b suggested the planet has a mass of 6.9 ± 1.4 $M_\oplus$. Further reassessment of the RV data by Pont et al. (2011), Boisse et al. (2011b), Hatzes et al. (2011), and Ferraz-Mello et al. (2011) showed a varied mass range of 1 - 8 $M_\oplus$. One valuable lesson learnt from this system was the importance of understanding the role of stellar activity and radial velocity jitter in the planetary system analysis. Accurate mass derivation is particularly important in the determination of the interior structure of an Earth-like planet.

Following the launch of the CoRoT satellite, the *Kepler* mission was launched in 2009 (Borucki et al., 2010; Koch et al., 2010) with a primary goal to determine occurrence rates, sizes and orbital separations of habitable Earth-sized planets. The telescope comprises of a 0.95 m aperture Schmidt telescope with an array of 42 1k $\times$ 2k CCDs, giving a total FoV of 113 square degrees. The instrument can acquire transit lightcurves with a precision of 10 ppm per 6hours for V= 10 stars. The Kepler mission has thus far detected over 4000 transiting planet candidates, enabling statistical study on planet populations. Not only did the Kepler studies revealed that most stars have planets, it also found that small planets with radius $R_P < 4.0$ $R_\oplus$ are by far the most common type of planets in the galaxy (e.g. Borucki et al. 2011; Howard et al. 2012; Batalha et al. 2013; Dressing and Charbonneau 2013; Petigura et al. 2013; Fressin et al. 2013).

The mission came to an end in 2013 when the second reaction wheel on the satellite failed, and the extended survey *K2* mission (Howell et al., 2014) was adopted to continue with transiting exoplanet searches. *K2* has the ability to obtain a photometric precision of 80 ppm at V = 12 mag in a 6-hour integration. So far, the mission has completed sixteen observational campaigns, producing over 20,000 lightcurves per campaign. At the time of writing, *K2* has identified hundreds of candidates (e.g. Vanderburg et al. 2016; Barros et al. 2016; Pope et al. 2016) and over 200 validated planets (e.g. Montet et al. 2015; Barros et al. 2015; Crossfield et al. 2016).

The discoveries made with *Kepler*/*K2* showed a variety of bulk densities in Earth-mass planets. For example, both Kepler-10 b ($R_P = 1.42 \pm 0.03$ $R_\oplus$, $\rho_P = 8.8 \pm 2.5$ g cm^{-3}; Batalha et al. 2011) and K2-38 b ($R_P = 1.55 \pm 0.02$ $R_\oplus$, $\rho_P = 17.5 \pm 7.35$ g cm^{-3}; Sinukoff et al. 2016) are planets with densities higher than the Earth and internal compositions which resemble a rocky world. At the same time, there are planets which were found to possess solid cores and massive gaseous envelopes (e.g. Kepler-11 system: R_P = 1.97-4.52$R_\oplus$, ρ_P = 0.5-3.1 g cm^{-3}; Lissauer et al. 2011a, K2-18 b: $R_P = 2.28 \pm 0.03$ $R_\oplus$, $\rho_P = 3.3 \pm 1.2$ g cm^{-3}; Benneke et al. 2017; Cloutier et al. 2017).

Very soon, the next generation of space missions will be commissioned. The Transiting Exoplanet Survey Satellite (TESS: Ricker et al. (2014)) was launched in April 2018. TESS contains four wide-field optical 4k × 4k CCDs, each providing a 24 × 24 square degrees FoV. The mission will monitor 200,000 bright stars (I ∼ 4 - 15) to obtain lightcurves with a precision of ∼ 200 ppm per 1 hour for V= 10 stars. The Characterising Exoplanet Satellite (CHEOPS; Broeg et al. 2013) is set to launch in December 2018. The mission will provide precision photometry (precision of 20 ppm per 6 hours for bright stars of V = 9 mag) for transit follow up on bright targets. It will be able to provide radii estimates of small planets with an accuracy of better than 10%. The PLAnetary Transits and Oscillations of stars mission (PLATO: Rauer et al. (2014)) is a transit survey anticipated to launch in 2026. The goal of the mission is to detect and characterise habitable zone planets. To fully characterise a system, the planet's mass and radius, and the stellar age must be derived with a high accuracy. PLATO will target bright stars with V ≤ 11 mag to obtain high precision lightcurves, where planetary radii with an accuracy of ∼ 2% can be achieved. Furthermore, the lightcurves will be analysed with asteroseismology to constrain stellar ages with a precision of 10%. Bright targets also means that ground-based spectroscopic instruments can make RV measurements with accuracies of 4 - 10% to achieve the end goal of finding an Earth analogue.

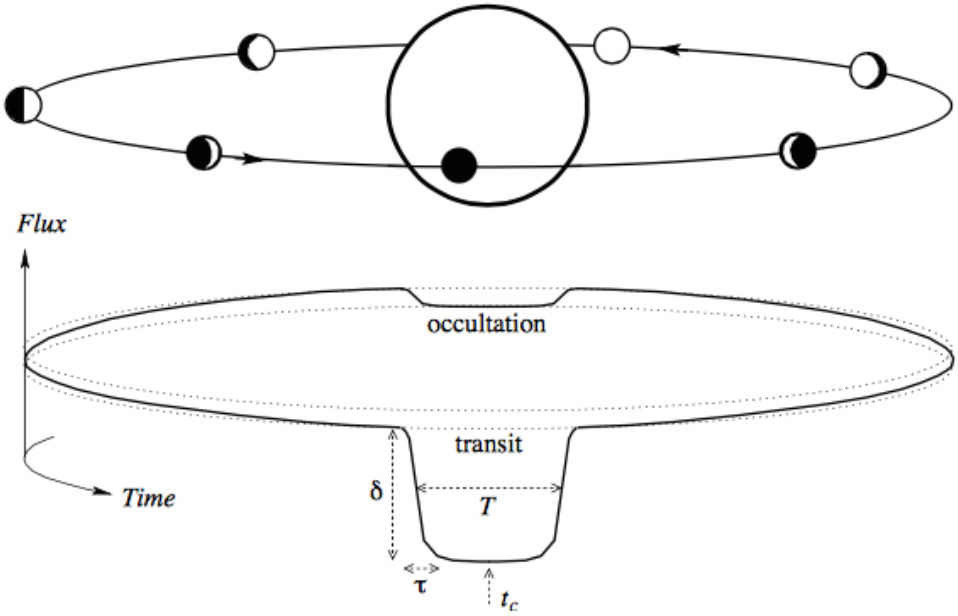

Figure 1.5: An *almost* edge-on view of a transit event (reproduced from Winn (2009) with permission from *International Astronomical Union*). When a planetary object orbits around a star, the planet will block part of the stellar flux when it passes between the observer and the star. The flux will drop again at the secondary eclipse when the planet is occulted by the star. Four parameters can be observed during a transit event: the mid-transit time t_c, the transit depth δ, the total transit duration T, and the ingress or egress duration τ.

Interpreting the Transit Lightcurve

A transit lightcurve can provide a wealth of information about an exoplanet system. Here, the physical parameters that can be inferred from a lightcurve are summarised.

The transit lightcurve in Figure 1.5 shows four of the parameters which can be measured directly from observations, namely, the mid-transit time t_c, the depth δ, the total duration T , and the ingress or egress duration τ (Winn, 2009).

If a planet with radius R_p orbits a star with radius R_s, the **star-planet size ratio** can be measured approximately by the depth of the transit:

$$\delta = \frac{\Delta F}{F} = \frac{R_P^2}{R_S^2} \tag{1.4}$$

where F is the flux of the star and ΔF is the fraction of flux blocked by the planet. The **scaled stellar radius** R_s/a is:

$$\frac{R_s}{a} = \frac{\pi\sqrt{T\tau}}{\delta^{1/4}P}\left(\frac{1+e\sin\omega}{\sqrt{1-e^2}}\right) \tag{1.5}$$

where ω is the argument of pericentre, which can be obtained from RV measurements. The mass M_s and radius R_s of a star can be estimated from spectral analysis. Using Kepler's third law, the **semi-major axis**, a, can be inferred:

$$\frac{a^3}{P^2} = \frac{G(M_s + M_p)}{4\pi^2} \tag{1.6}$$

For a planet moving in a circular orbit, the orbital velocity is $v = 2\pi a/P$. The **impact parameter** b is defined as the vertical distance between the centre of the stellar disc and the centre of the planet:

$$b \equiv \frac{a}{R_s}\cos i = 1 - \sqrt{\delta}\frac{T}{\tau} \tag{1.7}$$

where i is the orbital inclination. Furthermore, Kepler's third law can be applied to determine the **stellar mean density** ρ_s:

$$\rho_s \approx \frac{3P}{\pi^2 G}\left(\frac{\sqrt{\delta}}{T\tau}\right)^{3/2}\left[\frac{1-e^2}{(1+e\sin\omega)^2}\right]^{3/2} \tag{1.8}$$

and the **planet surface gravity** g_p is:

$$g_p \approx \frac{2\pi K}{P}\frac{\sqrt{1-e^2}}{\delta(R_s/a)^2\sin i} \tag{1.9}$$

Whether a transit can be detected depends on the geometry of the system. The probability P_{tran} of detecting a transiting planet on a circular orbit is:

$$P_{tran} = \frac{R_s + R_p}{a} \approx \frac{R_s}{a} \tag{1.10}$$

Thus the transit method is highly biased towards systems with close-in orbits, which partly explains the abundance of short period planets discovered via transit photometry.

Further details on transit lightcurve model fitting and characterisation of planetary systems will be discussed in Chapter 2, 3, and 4.

1.2.3 Microlensing

Gravitational lensing is the effect when a massive object (the lens) bends the path of light from a background source (Einstein, 1936). Under special circumstances, multiple distorted images are formed milliarcseconds apart. Although lensing events are difficult to resolve, the images would have a greater combined apparent brightness which would result in an

observable magnification event. Microlensing survey began to take form when Paczynski (1986) presented the possibility of detecting dark matter in the halo of our Galaxy. Later, Mao and Paczynski (1991) showed that the microlensing technique may also be applied to binaries and planetary companion. If a lensing star has a planetary companion which also aligns with the primary lensing event along our line-of-sight, it would perturb the image and produce a sharp spike in the microlensing lightcurve. Mao and Paczynski (1991) predicted the probability of microlensing event by planetary systems to be 0.03, assuming the star-to-planet mass ratio as 10^3.

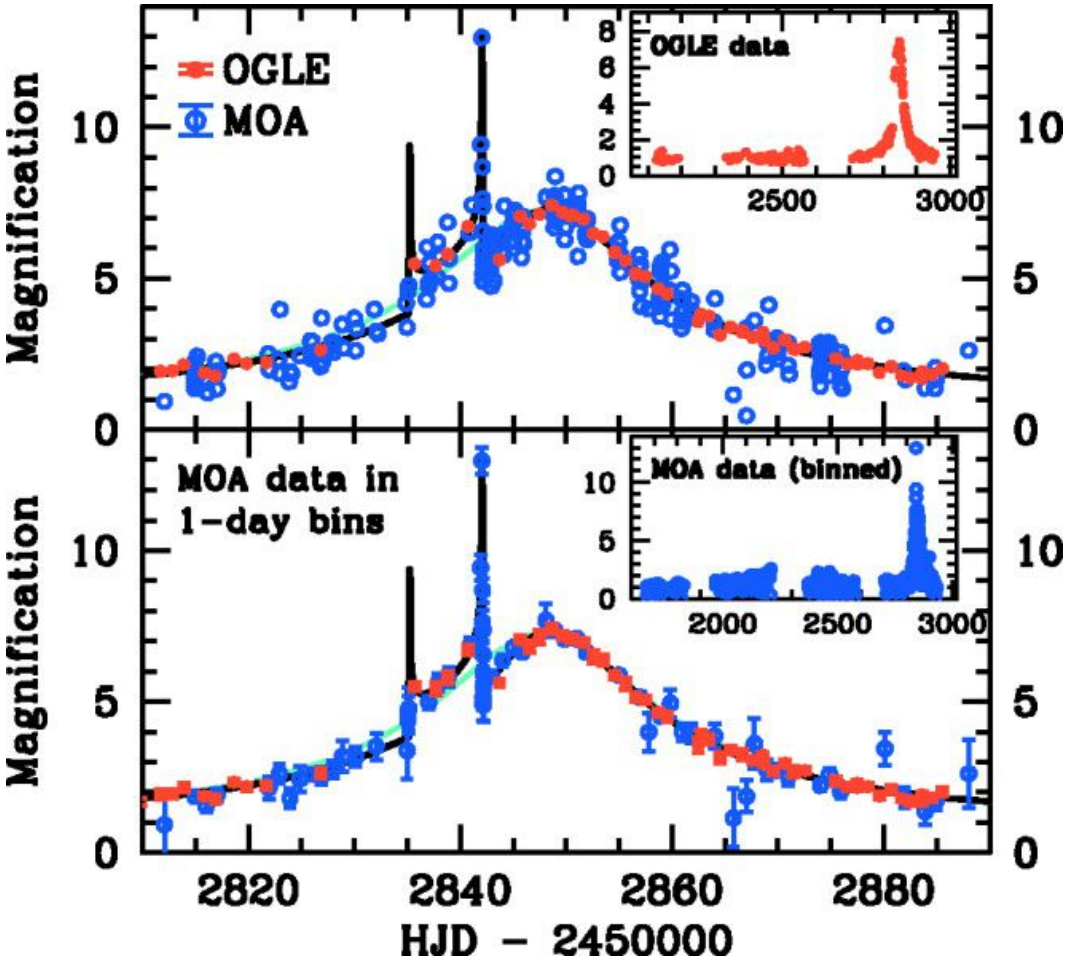

Figure 1.6: Microlensing lightcurve of OGLE 2003-BLG-235/MOA 2003-BLG-53 b. The blue open circles and red filled circles shows the OGLE and MOA measurements respectively. The best-fit binary microlensing model is plotted as the black solid line, and the single-lens model is plotted in cyan. (Figure reproduced from Bond et al. (2004) with permission by *The American Astronomical Society*.)

Microlensing planet surveys launched in 1995, e.g. Udalski et al. (1994), but the

first microlensing planet detection only came about in 2004 (Bond et al., 2004). Information such as the mass ratio of the star planet system, mass of the primary lens (i.e. the star), and the orbital separation of the pair can be derived. Figure 1.6 shows the discovery data from OGLE (Optical Gravitational Lensing Experiment; Udalski (2003)) and MOA (Microlensing Observations in Astrophysics; Bond et al. (2001)), a mass ratio of $q = 0.0039$ was found, and OGLE 2003-BLG-235/MoA 2003-BLG-53 b was determined to have a mass of 1.5 M_J and an orbital separation of $\sim$ 3 AU.

Multi-planet systems are also detectable using the microlensing method. Gaudi et al. (2008) discovered the planetary system OGLE- 2006-BLG-109L which consists of two Jupiter and Saturn-like planets. The planets were determined to have masses of $\sim$ 0.71 M_J and $\sim$ 0.27 M_J, respectively. Furthermore, these planets have orbital separations of $\sim$ 2.3 AU and $\sim$ 4.6 AU, which makes them comparable to planets within the Solar System.

Over 50 exoplanets have been detected by the microlensing method today. Although the detection probability of this technique is relatively low as it is more sensitive to planets near the Einstein ring radius of the lens, the microlensing method have weaker selection biases compared to other detection methods. Microlensing discoveries have proved that the method is sensitive to long period, low-mass planets orbiting beyond the snow line. It can therefore probe regions of the mass-radius parameter space which are otherwise challenging for transit and radial velocity methods. Many microlensing discoveries resemble planets in our solar system. They can provide important constraints on the occurrence of solar system analogues.

1.2.4 Astrometry

Bodies in a planetary system orbit around a common centre of mass (i.e. the barycentre of the system). Similar to the radial velocity method, astrometry quantifies the gravitational perturbation of the host star due to its companion by measuring the relative position of the star (Perryman, 2014). The elliptical motion of the star has a semi-major axis a_s of

$$a_s = \left(\frac{M_p}{M_s}\right) a \tag{1.11}$$

The observable *astrometric signature* in the astrometry method is therefore the angular displacement α of the stellar orbit

$$\alpha = \left(\frac{M_p}{M_*}\right)\left(\frac{a}{1AU}\right)\left(\frac{d}{1pc}\right)^{-1} \text{arcsec} \tag{1.12}$$

where d is the distance of the object from the observer. As seen in Equation 1.12, the amplitude of the astrometric signature increases with the orbital separation, hence the astrometry

technique is more sensitive to long period systems. However, this method is severely limited by the accuracy of the positional measurement of a star. At a distance of 100 pc, a Jupiter analogue would have a signature $\alpha = 50$ μas, and an Earth analogue would have $\alpha = 0.03$ μas. The astrometry method thus requires a precision of sub-mas for planet detections.

Space astrometry is able to measure trigonometric parallaxes of objects. The Hipparcos mission provided measurements of positions, proper motions, and parallaxes of $120,000$ stars with a 1 mas accuracy between 1989 and 1993 (Perryman et al., 1997). The Fine Guidance Sensor (Benedict et al., 1998) on the Hubble Space Telescope can measure parallaxes at $\sim$ 1-2 mas precision. Gaia (Perryman et al., 2001) is the successor of the Hipparcos mission. It surveys $\sim$ 1 billion stars to determine the positions of the Galactic stellar populations. With an accuracy of $\sim$ 10 μas, it is expected to yield approximately $21,000$ exoplanets out to a distance of $\sim$ 500 pc, including low-mass planets with masses of $\sim 10\ M_\oplus$ (Perryman et al., 2014), for a 5 year mission.

Radial velocity can only provide the $M_p \sin i$ estimate and give a minimum mass limit of the planetary companion since the orbital inclination i is undefined. Astrometric measurements, however, can determine the precise value of i. The combined analysis of the two methods will place constraints on the companion mass, thus reveal the true mass of the planet. Using the true planet mass and a well constraint planet radius, one can determine the planet bulk density precisely, hence infer the interior composition of the planet. In particular, the ice-mass fraction of a planetary core allows us to determine if a planet was formed beyond the snowline or assembled locally (Jin and Mordasini, 2018), the formation and evolution history of a planetary systems can then be inferred (e.g. GJ 317; Anglada-Escudé et al. (2012)).

1.2.5 Direct Imaging

Most of the exoplanets known to date were discovered by making measurements of systems indirectly. Only a handful of objects were confirmed with direct imaging. The main obstacles encountered in this method are the extreme star-to-planet contrast ratio, the angular separation of the planet, and the quasi-static speckle noise.

A planet with radius R_p and orbital separation a can reflect a fraction $(R_p/2a)^2$ of the star's luminosity at wavelength λ. The observed planet-to-star flux ratio is therefore

$$\frac{f_p(\alpha, \lambda)}{f_s(\lambda)} = p(\lambda)\left(\frac{R_p}{a}\right)^2 g(\alpha) \tag{1.13}$$

where the geometric albedo is $p(\lambda)$, and $g(\alpha)$ is a phase-dependent function (Collier Cameron et al., 1999). If a Jupiter analogue around a Sun-like star is observed at a distance of 10 pc

from the Earth, the contrast ratio f_p/f_s would be $\sim 10^{-9}$, and the system would have an angular separation of 0.5 arcsec. To image the planetary companion, the contrast ratio and the angular resolution must be significantly improved. This can be done by making observations in the infrared to limit stellar emission while increasing thermal emission from the planet. Again for a Jupiter analogue around a Sun-like star, this contrast ratio can be improved to $\sim 10^{-4}$. Another way to increase the contrast ratio is to apply a coronagraph to the telescope which masks the flux of the on-axis star, the flux and structure from the off-axis companion would remain (Lyot, 1939). Meanwhile, the angular resolution of the observations can be enhanced through adaptive optics (AO) on ground-based instruments or by making observations from space.

The contrast ratio detection limit in direct imaging is ultimately determined by speckle noise. Speckle noise can arise due to instrumental flaws and atmospheric turbulence, which can produce interference patterns and hide planetary signals in images (Racine et al., 1999). A number of post-processing techniques have been developed to suppress speckle noise. The most widely adapted technique is Angular Difference Imaging (ADI: Marois et al. 2006), where the FoV is allowed to rotate around the star while the telescope rotator is fixed. The speckle pattern correlated to the instrument is then subtracted from images to remove the noise.

Many of the present day direct imaging surveys are ground-based. To optimise the sensitivity, a Lyot coronagraph is combined with an AO system for wavefront correction (Malbet, 1996; Sivaramakrishnan et al., 2001), e.g. VLT/NACO (Rousset et al., 2000; Chauvin et al., 2015), Keck-AO/NIRC2[1], Gemini South/NICI (Chun et al., 2008; Liu et al., 2010), and Subaru-CIAO (Tamura et al., 2001; Murakawa et al., 2004). The first directly imaged exoplanet was discovered using this combined technique. The 5 M_J planet 2M1207 b was detected by VLT/NACO (Chauvin et al., 2004). It was found to orbit a brown dwarf with a separation of $\sim$ 55 AU. High contrast AO observations with Keck and Gemini have confirmed a multiplanetary system around the A5V star HR8799 (Marois et al., 2008). The planets HR8799 b, HR8799 c, and HR8799 d were determined to have masses of 7 M_J, 10 M_J, and 10 M_J, respectively, each with orbital separations of 68 AU, 38 AU, and 24 AU, from the host star. A forth planet HR8799 e orbiting interior to the other at $\sim$ 14.5 AU was reported by Marois et al. (2010) (see Figure 1.7). Another remarkable discovery of a gas giant planet was imaged in the disk of β Pictoris (Lagrange et al., 2009, 2010). β Pictoris b is at a separation of $\sim$ 8 AU from the star, and was found to be responsible for clearing the gap inside the disc.

With the development of extreme AO systems such as VLT/SPHERE (Spectro-Polarimetric High-contrast Exoplanet Research: Beuzit et al. (2008)) and the Gemini Planet

[1] `http://www2.keck.hawaii.edu/inst/nirc2/`

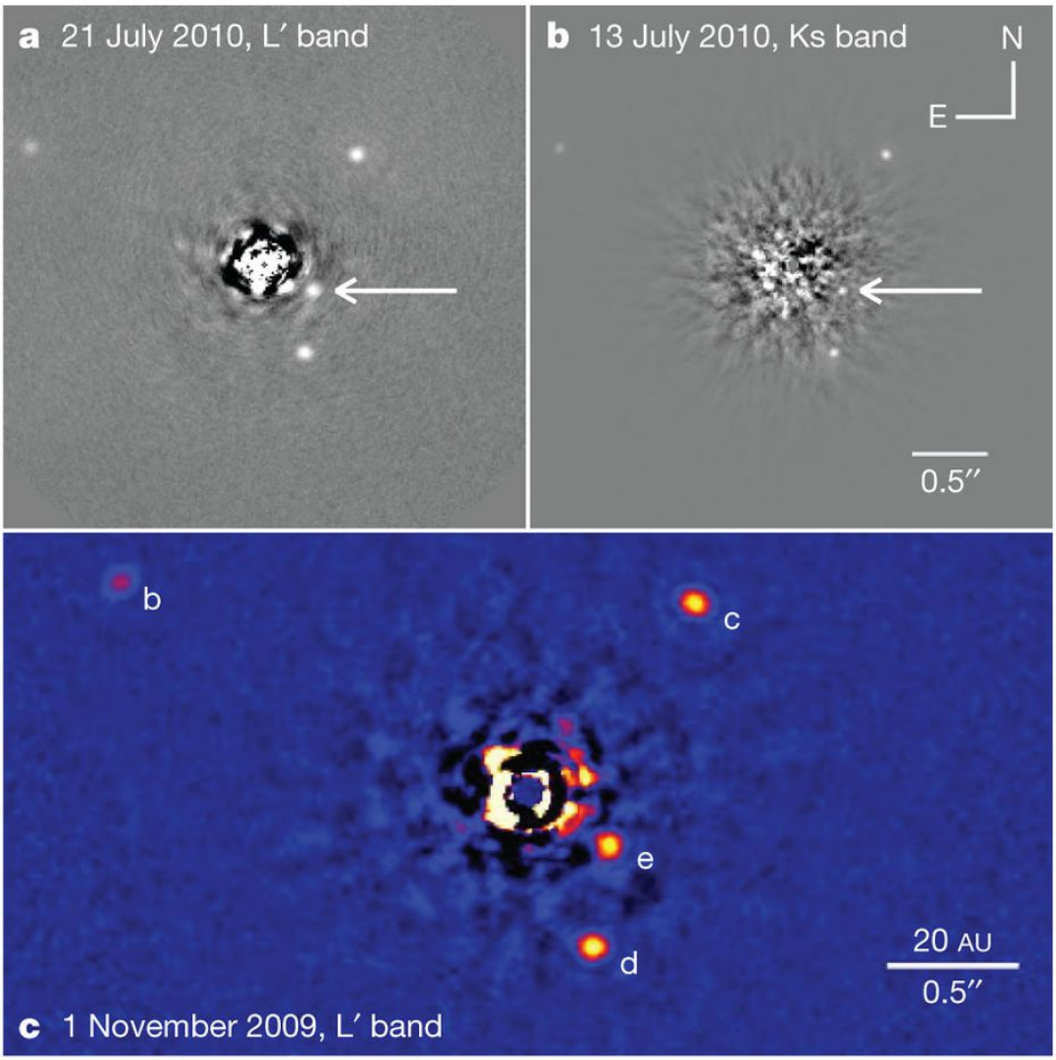

Figure 1.7: Keck-AO/NIRC2 discovery image of HR8799 e (Marois et al., 2010), reproduced with permission from *Macmillan Publishers Limited*.

Imager (GPI: Macintosh et al. (2014)), it is possible to extend planet searches down to an angular scale of ~ 0.1 arcsec. These instruments are coupled with integral field spectrograph, such that low resolution (R $\sim$ 30 spectroscopy is made available to study exoplanet atmospheres. The first low-resolution near-infrared spectra of β Pictoris b obtained from GPI have shown water absorption features in the planet atmosphere (Bonnefoy et al., 2014), a prominent characteristic for an early L dwarf.

The launch of the James Webb Space Telescope (JWST; Gardner et al. 2006) is imminent. The coronagraphs (MIRI; Boccaletti et al. 2015, TFI; Doyon et al. 2010) on board the telescope will be able to reach a contrast ratio of 10^4-10^5 at 0.5-1.0 arcsec separations. The detection of super-Earths around M dwarfs would be possible (Deming et al., 2009). WFIRST-AFTA (Wide-Field InfraRed Survey Telescope-Astrophysics Focused Telescope Assets) will contain a coronograph instrument targeted for the imaging and spectroscopy of exoplanets in the solar neighbourhood (Noecker et al., 2016).

1.3 Hot Jupiter and Super-Earth Planets

New classes of planets have been discovered since the first detection of exoplanets. The detailed analyses of exoplanets have shown systems with properties that are different from our own Solar system. In this section, properties and characteristics of hot Jupiters and super-Earths are presented. Some interesting questions and key findings are discussed.

1.3.1 Hot Jupiters

Hot Jupiters are Jupiters which orbit close to their host stars with orbital separations of $a < 0.1$ AU, periods P $\leq$ 10 days (Udry and Santos, 2007). This type of planet receives strong stellar irradiation, leading to a high equilibrium temperature. Hot Jupiters are the easiest exoplanet to find via transits and RV because they are more massive, hence they are more sensitive to the RV detection method. Indeed, the first exoplanet discovered around a solar-type star is the hot Jupiter 51 Peg b. This astonishing find challenged formation theories at the time since gas giants were thought to be forms at wider orbits of several AUs.

How Were Hot Jupiters Formed?

Multiple formation mechanisms were proposed to explain the short orbital periods of hot Jupiters. Hot Jupiters could have migrated via **gas disc migration** or through **high-eccentricity migration**. In gas disc migration, planets exchange angular momentum with the gas disc, resulting in the shrinkage of the planetary orbit (e.g. Goldreich and Tremaine 1980; Ida and

Lin 2008). Another type of migration is the high-eccentricity migration. The eccentricity of a hot Jupiter on a wide orbit is first excited by some physical processes. This could be *planet-planet scattering* (Rasio and Ford, 1996; Weidenschilling and Marzari, 1996): In a system with multiple protoplanets, one of the planets could become sufficiently large and perturb its smaller rival counterparts. These smaller planets are eventually expelled, while the largest planet would gain eccentricity in the process; or *Secular perturbation*: The Kozai-Lidov mechanism (Kozai, 1962; Lidov, 1962) can drive the angular momentum exchange between the hot Jupiter and an eccentric outer planet body or a star, resulting in the excitation of the hot Jupiter's eccentricity. When the orbit of a hot Jupiter becomes eccentric, the planet would lose orbital energy through tidal dissipation (i.e. tides raised on the planet by the star), the planet orbit is consequently circularised. Although the formation mechanisms of hot Jupiters is still unclear, a more complete study of the hot Jupiter population may shed some light on their origins.

Hot Jupiter Occurrence and Some Distinct Characteristics

The radial velocity survey by Mayor et al. (2011) reported an occurrence of 0.89% for hot Jupiters around main-sequence stars. The California Planet Survey (Wright et al., 2012) found a rate of 1.2%, while Batalha et al. (2013) estimated a rate of 0.5% for hot Jupiters in the Kepler sample. These surveys showed that hot Jupiters are intrinsically rare, despite being the easiest to find. At the same time, hot Jupiter systems are one of best characterised systems. Studying correlations between the variety of observed system properties and the planet population could allow one to distinguish the origins of exoplanets.

The hot Jupiter occurrence rate is highly dependent on the host star metallicity (Gonzalez, 1997; Santos et al., 2001; Fischer and Valenti, 2005). Metal-rich stars are more likely to host a gas giant planet. Fischer and Valenti (2005) found that 25% of stars with [Fe/H] > +0.3 dex have giant planets, whereas only < 3% of metal-poor stars have gaseous planets. Johnson et al. (2010) showed that this rate is further reduced among less massive M dwarfs. The host star metallicity might link to the amount of disc material available for giant planet formation. The more disc mass, the higher the solid surface density for the build up of planets via core accretion (Johnson et al., 2010). Meanwhile, a more massive disc could also mean that more planets can be formed at multiple locations, triggering high-eccentricity migration via secular perturbation.

Hot Jupiters are found to be less massive than their long period counterparts. Dawson and Johnson (2018) showed a paucity of massive giant planets ($M_p \geq 3\ M_J$) with separations between the Roche Limit and twice the Roche limit. This could be explained by tidal evolution where the decay in the hot Jupiter orbit leads to eventual tidal disruption. Another possibility is the in situ formation of planets through a narrow feeding zone (Baty-

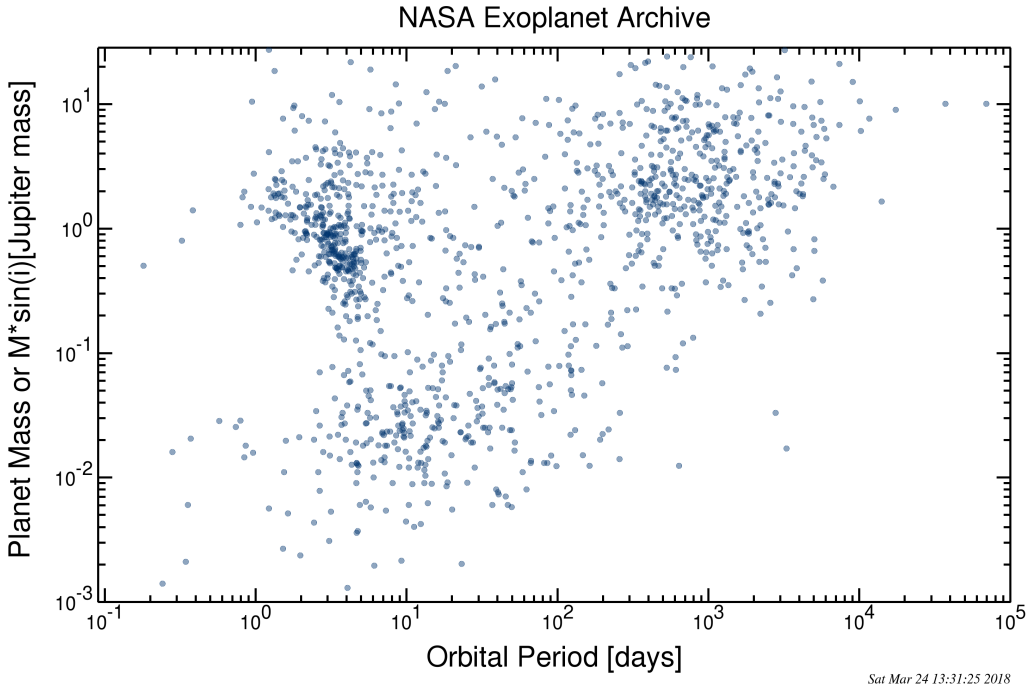

Figure 1.8: The masses and orbital periods of currently known exoplanets. Data obtained from NASA Exoplanet Archive: `http://exoplanetarchive.ipac.caltech.edu` accessed on 2018 March 24.

gin et al., 2016). Migration could also lead to lower mass hot Jupiters as they are less likely to open gaps in the gas disc, which can slow down migration through the disc (Masset and Papaloizou, 2003).

Detailed characterisations of hot Jupiter systems showed that Jupiter-mass planets can have a variety of radii. In many cases, radii of hot Jupiters are larger than standard coreless models (e.g. Fortney et al. 2007; Baraffe et al. 2008). One property that was obvious in these systems is the correlation between the planet radius and the planet equilibrium temperature (Bodenheimer et al., 2003). Planets with higher equilibrium temperatures have larger radii, so certain heating mechanism might be in place to inflate the planetary radii. For example, stellar irradiation could deposit heat in the planet atmosphere which causes inflation (Weiss et al., 2013). Tidal circularisation of a planet's orbit could also heat the interior of the planet (Bodenheimer et al., 2001). Several alternative mechanisms will be discussed in Chapter 3.

Transmission Spectroscopy

When the atmospheric scale height H of inflated hot Jupiters becomes substantial enough, their atmospheric properties can be studied in detail via transmission spectroscopy (Charbonneau et al., 2002; Vidal-Madjar et al., 2003).

A transmission spectrum is the measure of transit depth as a function of wavelength. At certain wavelengths, the planetary atmosphere can be more opaque so the transit depth becomes deeper due to absorption by atoms or molecules. In the event where haze is absent in the atmosphere, the expected transit depth is:

$$S_{tr} \approx (\frac{R_p + 10H}{R_s})^2 \tag{1.14}$$

the atmospheric scale height H is defined as:

$$H = \frac{kT_{eq}}{\mu g_p} \tag{1.15}$$

where $k = 1.38 \times 10^{-23}$ J K^{-1} is the Boltzmann constant, T_{eq} is the equilibrium temperature, μ is the mean molecular mass, and g_p is the planet surface gravity. Studying the spectrum can provide information on the absorption features of the planet's atmosphere. For example, sodium and potassium absorption lines are found in the visible spectrum. H_2O, CH_4, CO and CO_2 produce broader molecular bands, and are visible at near-infrared.

Evaporating Hot Jupiters

For both sun-like stars and M dwarfs, the stellar X-ray and ultraviolet (XUV; $\lambda \sim$ 1-1800 Å) flux remains substantial for $\sim$ 100 Myr, after which the flux and stellar activity (measured from Ca II H & K lines) begin to decrease (Findeisen and Hillenbrand, 2010; Gondoin, 2012; Shkolnik and Barman, 2014). Exoplanets with close-in orbits are susceptible to stellar irradiation. Under extreme circumstances, the incident XUV flux could deposit enough energy in the planetary atmospheres to cause atmospheric escape (Vidal-Madjar et al., 2003; Erkaev et al., 2007).

The extent of atmospheric escape is determined predominantly by properties of the thermosphere (the region which can be heated by XUV) and the exosphere (the loosely bound outer layer where gas density and pressure is low). Under the thermal regime, high temperatures drive the increase in particle velocities. When the particle velocities in the atmosphere exceed the atmospheric escape velocity, the atmosphere enters the hydrodynamic ('blow off') regime where mass loss occurs (e.g. Lammer et al. (2003); Lecavelier des Etangs et al. (2004); Erkaev et al. (2007); Murray-Clay et al. (2009)).

The escaping atmosphere of a planet would lead to an extended atmosphere. This property can be observed during a planetary transit. If column density of the gas is high enough, it would block out part of the stellar flux and enhance the transit depth.

The first exoplanet observed with an extended exosphere was HD209458 b. Vidal-Madjar et al. (2003) measured in-transit Lyman-α absorption lines using the Space Telescope Imaging Spectrograph (STIS) on the HST. Their results revealed a 15% deep transit, indicative of the evaporation of neutral hydrogen. They have further showed that gas is moving away from the star beyond the Roche lobe at a Doppler velocity of $\pm$100 km s^{-1}, which leads to Roche lobe overflow (Erkaev et al., 2007). O I and C II absorptions were also observed from transits of HD209458 b (Vidal-Madjar et al., 2004; Linsky et al., 2010), strengthening the detection of an evaporating atmosphere.

Similar effects were also observed in the Neptune-mass planet GJ 436 b (Butler et al., 2004). Kulow et al. (2014) have measured a transit depth of 8.8% in the Lyman-α, as well as an extended egress with a striking depth of 23.7%. The observation suggested that there may be a tail of neutral hydrogen trailing the planet, giving an appearance similar to a comet tail. Further observations were made by Ehrenreich et al. (2015) where they have measured a UV transit depth of 56.3% (see Figure 1.9). Ehrenreich et al. performed numerical simulations to show that low stellar radiation pressure of GJ 436 could offset the gravitational pull on the escaping hydrogen atoms from the star. Under this mechanism, not only would the escaping atoms form a comet-like tail, they also co-move with GJ 436 b to form an envelop. This result showed remarkable agreement with the HST observation where early ingress and extended egress were detected.

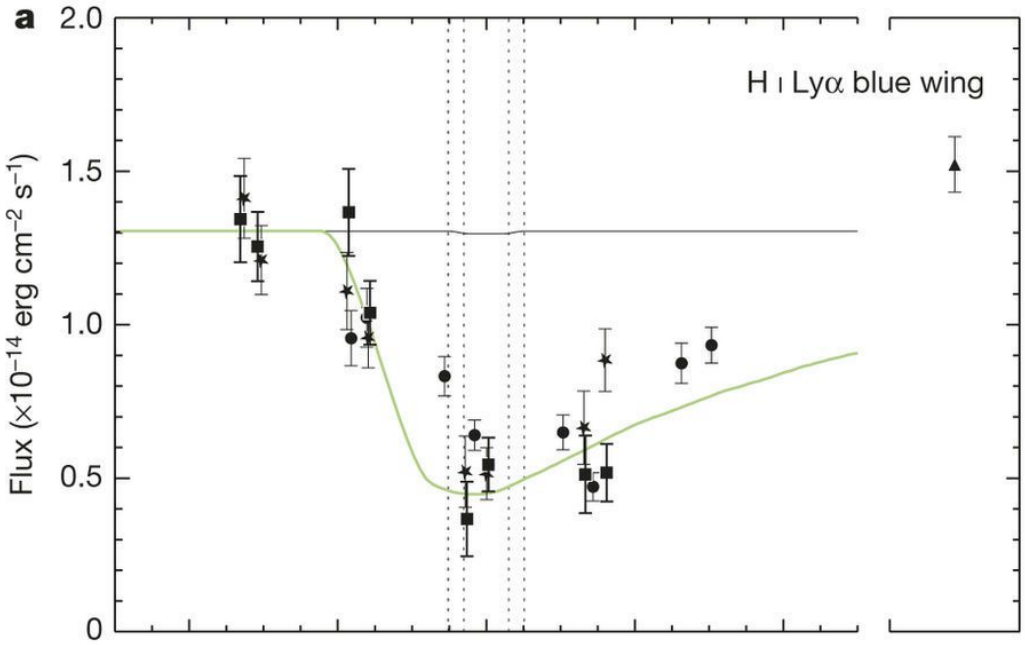

Figure 1.9: The Lyman-α transit observations of GJ 436. A transit depth of 56.3% was observed, significantly deeper than the optical transit. This is an indication of an extended atmoshpere around GJ 436 b. (Figure 2 of Ehrenreich et al. (2015), reproduced with permission from *Macmillan Publishers Limited*).

Very often, absorption lines of heavier elements are also used in addition to Lyman-α to characterise evaporating exosphere. Examples of these species are O I, C II, Mg II, and Fe II. Some of these species are reportedly detected in hot Jupiter HD189733 b (Ben-Jaffel and Ballester, 2013), and WASP-12 b (Fossati et al., 2010b; Haswell et al., 2012), as well as the rocky super-Earth 55 Cancri e (Ridden-Harper et al., 2016). Detailed analysis of the evaporating atmosphere could reveal the physics underlying the interactions between stars and close-in planets.

1.3.2 Super-Earths

The discoveries from the Kepler mission showed that planets with sizes between the Earth and Neptune are by far the most abundant in our Galaxy (Borucki et al., 2010; Batalha et al., 2013). This type of planets are known as *super-Earths*. About 50% of solar-type stars host at least one planet smaller than the size of Neptune (Howard et al., 2012; Fressin et al., 2013). This type of planet is not observed in our solar system, and it is of particular interest to study their formation and evolution paths.

Super-Earths display a more varied bulk density distribution than hot Jupiters (Lopez and Fortney, 2013; Weiss and Marcy, 2014), which implies a diversity in their interior compositions. Contrary to hot Jupiters, super-Earths are commonly found in multi-planetary systems (Lissauer et al., 2011b; Fabrycky et al., 2014). The recent California-Kepler Survey also found that 93% of these systems are tightly packed (Weiss et al., 2018).

Formation of Super-Earths

Many super-Earths are known to have short orbital periods, some of which have low bulk densities and are believed to possess substantial atmospheres. Assuming they were formed in a way similar to terrestrial planets in our solar system, a significant amount of solids are required at < 0.1 AU for super-Earths to form near their present locations (Schlichting, 2014). Instead, the more plausible scenario is the formation of a protoplanet by accretion of solids beyond several AU. This is followed by migration through the gas disc, in which gas is accreted onto the rocky core as the planet reaches its current orbit (e.g. Ginzburg et al. 2016; Lee and Chiang 2015). Ginzburg et al. noted that self-gravity of the atmosphere becomes critical when the gas mass fraction reaches $\sim 20\%$. This condition would set off runaway gas accretion and gas giants could be formed. The sweet spot for the formation of super-Earths is when planets are massive and cool enough to accrete and retain their atmospheres, but not too massive so that runaway gas accretion is triggered (shaded-region of Figure 1.10).

Super-Earths continue to evolve under several mechanisms after gas disc dispersal

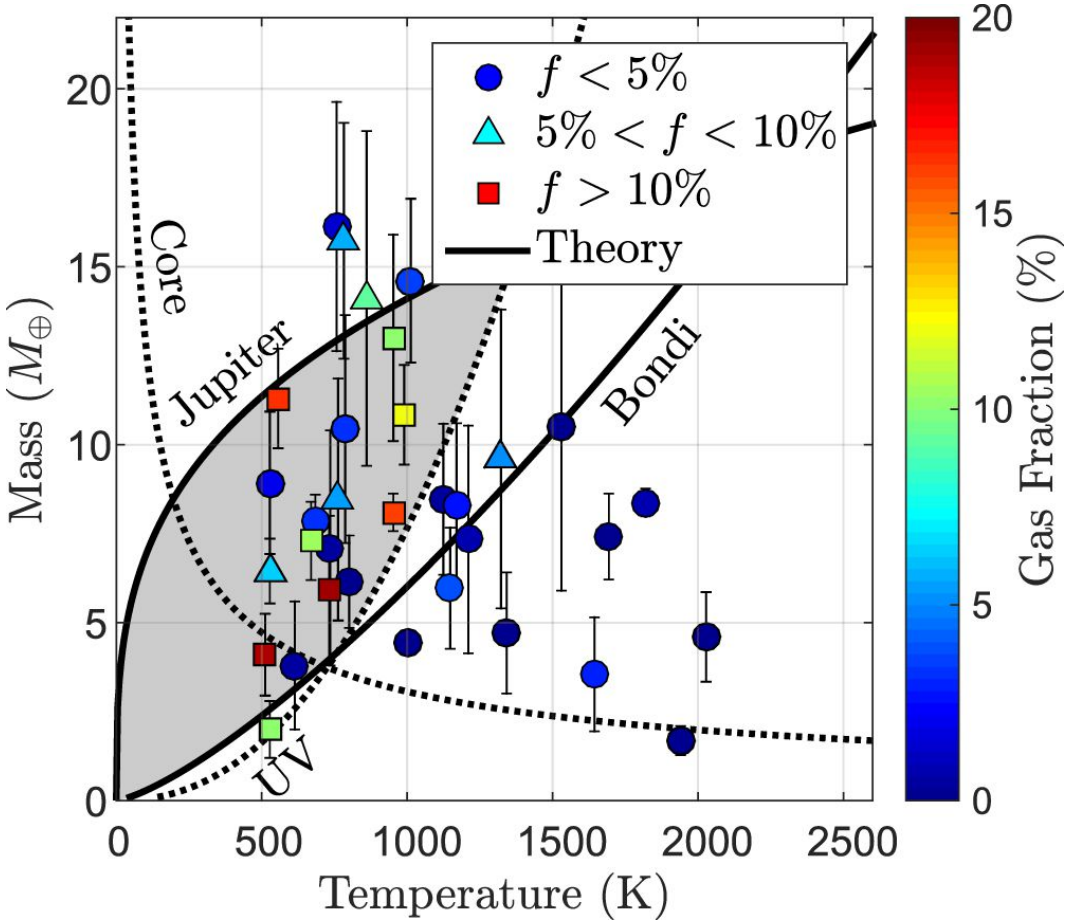

Figure 1.10: The masses of super-Earths as a function of their equilibrium temperature. Their gas mass fractions f are indicated by shape of the markers. The lines plotted are boundaries of triggering their respectively physical processes. The shaded region is the the optimal condition for which a super-Earth can form. Figure reproduced from Ginzburg et al. (2016) with permissions from *The American Astronomical Society*.

which will determine their final masses. The planet enters a cooling (or shrinking) phase as the surrounding gas disc disperses (Ginzburg et al., 2016). If gas disperses quicker than the envelope cools, the envelope will begin to lose mass until it reaches the 'thin' regime, where the radius of the planet atmosphere is comparable to the core of the planet. At this point, the core-powered mass loss may take over. Planets with heavy atmospheres will continue to cool without losing mass, while ones with lighter atmospheres will lose mass as thermal energy from the core heats the atmosphere. Finally, when the planet reaches a close orbit, its atmosphere begins to erode due to photoevaporation (Lopez et al., 2012; Owen and Jackson, 2012), a process where high energy stellar radiation (UV or X-ray) heats the planetary atmosphere, leading to evaporation.

The super-Earth migration scenario may also explain the apparent lack of Neptune-mass planets with a period of 2 - 4 days. Mazeh et al. (2016) established the so-called 'short-period Neptune desert' which may be an indication of two unique formation processes for the hot Jupiter and super-Earth populations. Hot Jupiters can survive migrating close to the star whereas intermediate mass planets would be eventually destroyed. Similarly, the formation process of short period low mass planets would cease as gas discs deplete. Thus the final mass of a planet would not reach that of Neptune's.

The Photoevaporation Gap

Recent efforts by the California-*Kepler* Survey(CKS) (Johnson et al. 2017; Fulton et al. 2017) have observed and derived the precise physical characteristics of short-period *Kepler* planets (P < 100 d), and their host stars for an in-depth study of the planet size distribution. Fulton et al. observed a significant lack of planets with sizes between 1.5 $R_\oplus$ and 2.0 $R_\oplus$ (see Figure 1.11). The gap in the radius distribution could be explained by mechanisms which drive atmospheric mass loss. The photoevaporation model is capable of generating the observed bimodal distribution. Simultations by Owen and Wu (2017) showed that the evaporation mass loss timescale is the longest when the radius of the H/He envelop is twice that of the planetary core. The mass loss timescale decreases towards either side of this radius. This is because the planet's overall radius is dominated by the core when its atmosphere becomes thinner. Meanwhile, the addition of the smallest amount of mass to the planet would significantly expand the planetary radius. However, the photoevaporation case cannot account for the bare planets at longer periods (P > 30 d). Alternatively, the core-powered mass loss mechanism could also drive the evaporation of the atmosphere. Ginzburg et al. (2018) showed that the evaporation gap can be developed naturally during the planet cooling phase. A planet with a heavier envelope would cool slowly and maintain its radius, whereas a planet with a lighter envelop would cool rapidly to leave a smaller radius. Core-powered mass loss, however, could enhance the effect and deepen the radius

gap.

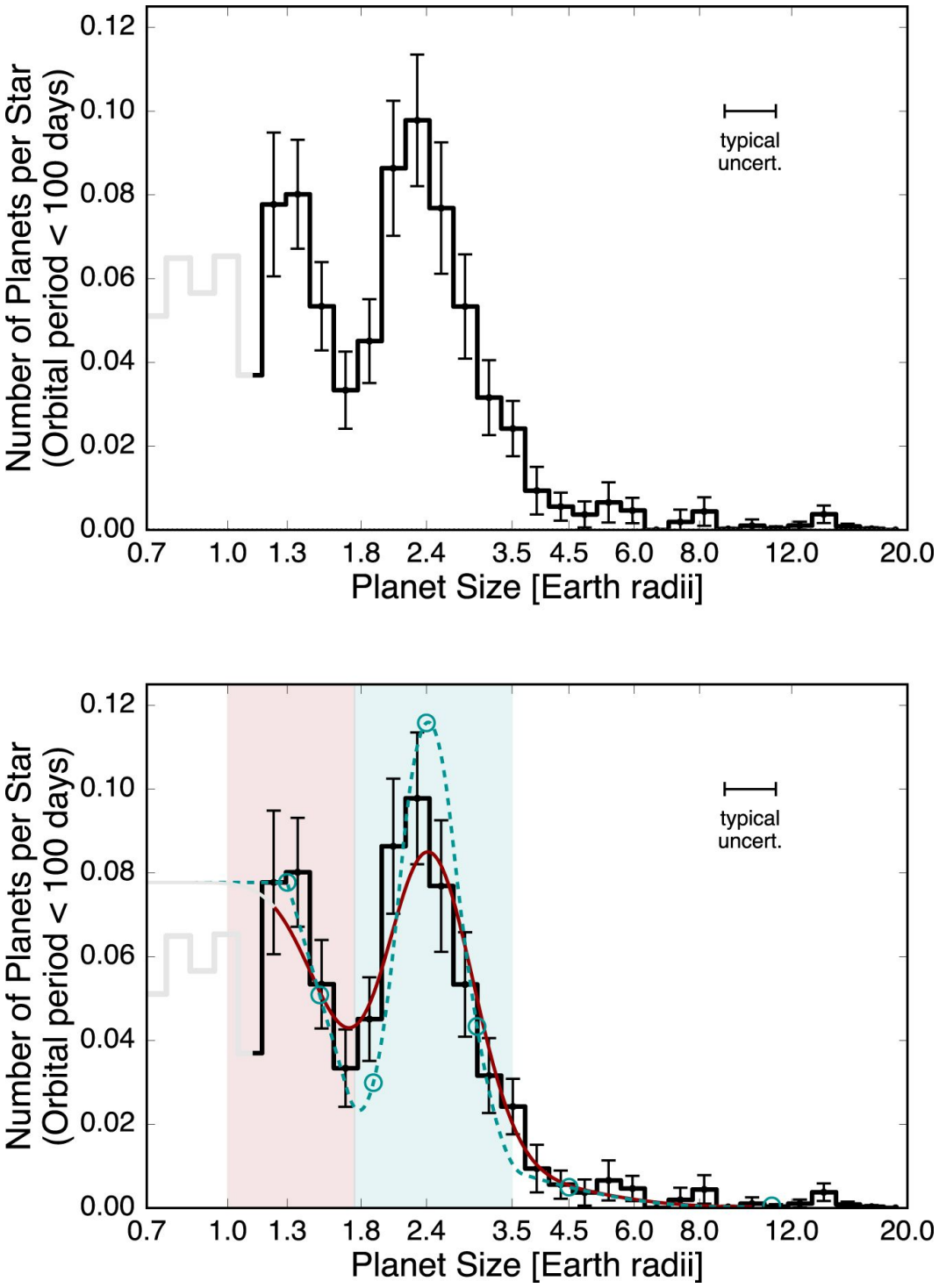

Figure 1.11: Distribution of planet radii of planets with P < 100d. A bimodal distribution is observed with peaks at $\sim 1.3 R_\oplus$ and $\sim 2.4 R_\oplus$. Figure reproduced from Fulton et al. (2017) with permissions from *The American Astronomical Society*.

1.4 Stellar Activity in Exoplanetary Science

Stellar magnetic activity is ubiquitous in stars with convective envelopes. Although the physical processes governing the magnetic activity is yet to be established, it is broadly believed that stars operate a magnetic dynamo which generates magnetic fields Moffatt (1978); Parker (1979). These magnetic fields drive the interaction between differential rotation and convection in the rotating, convecting, electrically conducting fluid in the stars outer convective layers. The resulting stellar activity is manifested by a number of physical phenomena, including starspots coverage, and chromospheric and coronal emission (Schrijver and Zwaan, 2008).

The presence of stellar activity in sunlike stars can give rise to noise in both time-series photometric and RV observations. In photometry, activity-related noise can affect accurate characterisation of transiting planets (e.g. Czesla et al. 2009, Oshagh et al. 2013, Barros et al. 2014). On the other hand, activity-induced RV jitter can hamper the detection and mass measurements of low-mass exoplanets (e.g. Santos et al. 2010, Boisse et al. 2011a). RV jitter can also mimic planetary signals which lead to false detections (e.g. Queloz et al. 2001a, Huélamo et al. 2008, Figueira et al. 2010). It is therefore crucial to consider the impact stellar activity has on photometric and RV observations in the detection and characterisation of exoplanets.

1.4.1 Stellar Activity, Rotation and Age

Stellar rotation is strongly correlated to the chromospheric activity level in cool stars (Kraft, 1967). In stellar dynamo theory, the strength of magnetic field and Ca II emission increases with stellar rotation (Moffatt, 1978). Wilson (1978) began the Mount Wilson survey to study the chromospheric variation in main-sequence stars in 1966. The survey monitored the Ca II H & K emission in sunlike stars to show that stellar activity modulate on both a short-term and long-term timescales (Vaughan and Preston, 1980; Vaughan et al., 1981). Such modulation of activity was also observed in our Sun, where sunspot number was recorded since 1800s to find a 11-year solar cycle (Clette et al., 2014).

In addition, stars of different spectral types hence different convection zone depths (or convective turnover time) also contributes to the formation of magnetic fields (Vaiana et al., 1981; Vaughan et al., 1981). Noyes et al. (1984a) used results from the Mount Wilson survey to find that chromospheric emission R_{HK} as a fraction of the bolometric luminosity can be approximated by the Rossby number R_o:

$$R_o = \frac{P_{rot}}{\tau_c} \tag{1.16}$$

where P_{rot} is the stellar rotation period and τ_c is the convective turnover time which depends on the spectral type.

As stars age, their rotation rates decrease. This is because magnetic fields that rotate with the star interact with stellar winds to create a magnetic torque that transfers angular momentum from the star to the winds (Weber and Davis, 1967). The chromospheric activity is subsequently reduced. The measure of stellar activity and the spin rate are therefore good estimates of the ages of stars (Barnes, 2003, 2007, 2010).

1.4.2 Stellar Activity in Photometry

When magnetic field lines pierces through the highly ionised stellar photospheric gas, they inhibit the convection of hot plasma (Thomas and Weiss, 2012). This leads to the formation of cool starspots which appear darker than the surrounding photospheric layer. The presence of a starspot or a group of starspots decreases the amount of observable photospheric flux. As starspots rotate into and out of the line of sight of an observer, the modulation of optical flux depends on the size and latitude of the starspot, the inclination of the stellar rotation axis, the stellar rotation period, and the spot lifetime. In photometric observations, starspots are fitted as part of the transit-search algorithm to effectively identify transiting planet candidates (e.g. Aigrain and Irwin 2004).

In a photometric observations, the presence of a starspot can bring great challenges in the characterisation of the planet. During a transit event, starspots that are not occulted by a transiting planet can reduce the out-of-transit flux measured by an observer, leading to erroneous radius estimate of the planet (Pont et al., 2008). If a planet occults starspots during transit (Figure 1.12), it can also cause problems in planet characterisation. In particular, the determination of the planet radius and the limb-darkening coefficients of the host star can affected (e.g. Pont et al. 2007, Czesla et al. 2009). Therefore, the spot area, temperature, and limb-darkening coefficients need to be accounted for during a transit fitting process to generate accurate planet radius estimation.

1.4.3 Stellar Activity in Spectroscopy

Radial velocity is an integral part of the exoplanet validation process. Accurate measurement of the Doppler motion of a star is necessary to confirm presence of a planet and estimate a planets mass. However, starspots and plages on the photosphere which arise due to stellar activity rotate with the star. Light along the line-of-sight is block by these dark features, resulting in the RV shift due to distortion in the spectral line absorption features. The stellar $v \sin i$, resolution of the spectrograph, and the size and temperature of a spot determine the RV semi-amplitude (Saar and Donahue, 1997; Hatzes, 1999; Desort et al.,

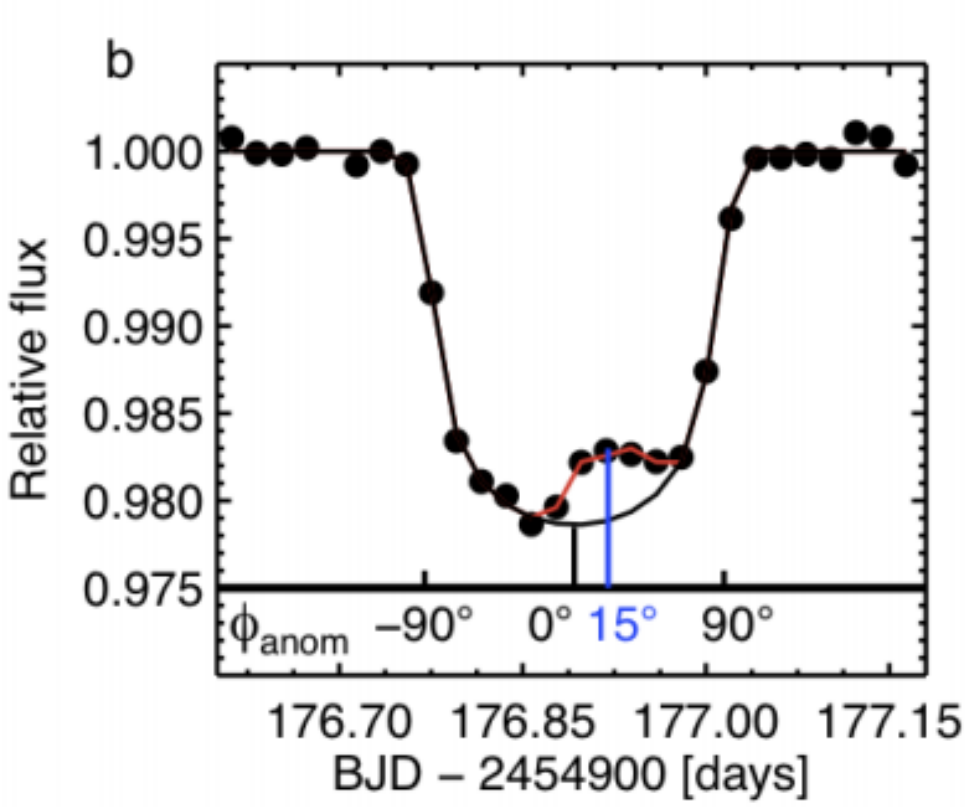

Figure 1.12: Transit lightcurve of Kepler-30 c reproduced from Sanchis-Ojeda et al. (2012) with permission from *Springer Nature*. The Kepler data are denoted by black dots. The flux anomaly observe at transit phase $\phi = 15°$ was attributed to the occultation of a starspot. The black line is a model without starspots and the red line is a model with one spot.

2007). Stellar activity can introduce RV jitters which can affect the Doppler measurements of stars.

Queloz et al. (2001a) detected the 3.7987 days RV variations in the sunlike star HD 166435 which they initially thought to be caused by a planet companion. Follow-up RV measurements and bisector analysis (method to be explained in details in Chapter 2) showed a strong correlation which was interpreted as variation originated in the stellar atmosphere. They concluded that the growth and decay of starspots with lifetime longer than the rotation period of the star can affect the RV semi-amplitude, the stellar chromospheric activity level and its photometric brightness.

In slowly rotating stars like our Sun, the dominant contribution to the RV signal is not starspot-induced variation, but the inhibition of granular convection by magnetic fields (Meunier et al., 2010). Granules are the convective elements in stellar photospheres. The upward motions of hot materials spread out over a large surface area, which then cools and sinks into dark intergranular lanes (Dravins et al., 1981; Dravins, 1987). The net upward motions lead to blueshifts with amplitudes of 8-10 m s^{-1} and asymmetry in line profiles and the long term variation in the Ca index and RV (Meunier et al., 2010), which can lead to false planet detections and inaccurate mass determination.

Stellar magnetic activity can produce starspot modulation and convection blueshift. The resulting distortion in spectral line profiles will cause RV variations which can mimic the reflex motion due to a planetary companion. Various approaches are used in modern planet modelling pipelines to account for stellar activity. For example, the anti-correlation between RV and bisector velocity span arise due to stellar activity is used to correct RV jitters and derive accurate system parameters (e.g. Boisse et al. 2009). Using high precision photometry and properties of dark starspots, Aigrain et al. (2012) devised the FF' method which predicts activity-induced RV variations from the product the flux variation F and its first derivative F'. Haywood et al. (2014) found that the residual activity signal of CoRoT-7 can be approximated by a Gaussian process regression using a quasi-periodic covariance model, and Faria et al. (2016) recovered the planetary orbits of the CoRoT-7 system with the RV data alone. Overall, if a planet candidate with orbital period similar to the stellar rotation period, it is thus important to identify the origin of RV variations to help disentangle stellar activity from planetary signals.

1.5 Thesis Outline

This thesis is outlined in the following manner: Chapter 2 describes and summarises methods used in this thesis. Chapter 3 presents the discovery of three gas giants from the WASP survey, and discusses their possible origin and prospects of follow up scientific studies. The

discovery of a super-Earth and the detailed analysis of the system is laid out in Chapter 4. Chapter 5 presents the investigation of the time variability of the evaporating planet WASP-12. Chapter 6 investigates a detection technique by targeting stars in open clusters and measuring the stellar activity indicator $\log R'_{HK}$. Finally, the outlook and future work is concluded in Chapter 7.

Chapter 2

Methods

The characterisation of a transiting exoplanet system requires both high precision spectra and transit lightcurves. This chapter outlines the general spectroscopic and photometric reduction processes which are implemented to extract spectra and lightcurves for data analyses. From here, the methods used to derive certain parameters for star-planet system characterisation are described.

2.1 Spectroscopy

Spectroscopy is the measure of radiation intensity as a function of wavelength. High resolution spectra can be used to study spectral line profiles, where the RV of a system can be extracted. This section summarises the spectroscopy reduction process and the determination of certain stellar parameters.

2.1.1 Echelle Spectrograph

Most modern high-dispersion spectrographs use echelle gratings (e.g. HARPS; Queloz et al. 2001b; Pepe et al. 2002b, HIRES Vogt et al. 1994, CORALIE Queloz et al. 2000; Pepe et al. 2002a). The echelle grating gives high spectral resolution while the prism acts as a cross dispenser so that multi orders can be recorded in a single exposure. The advantage of an echelle spectrograph is the wide wavelength coverage it can produce. As an example, HARPS, a fibre-fed, cross-dispersed echelle spectrograph has a resolution of R = $115,000$. It can produce echelle spectra of 72 orders which covers a wavelength range from 380 nm to 690 nm. The precision of the echelle spectrum, however, is compromised as the blaze function give rise to variations in the stellar continuum. The wide wavelength coverage also means that images are contaminated with scattered light. Higher orders align closer together, this may also lead to contamination from the extended light in adjacent orders.

One must take these problems into account in the spectral reduction process.

2.1.2 Data Reduction and Spectra Extration

Spectral data were obtained from multiple instruments in this thesis. In Chapter 3, CORALIE and SOPHIE spectra are used to perform host star analysis and make RV measurements. In Chapter 4, HARPS data is used to characterise the host star and measure RVs to derive the mass of the super-Earth. In chapter 5, HIRES data is used to find time-series variation in the activity-sensitive Ca II H & K lines. In Chapter 6, the FLAMES-GIRAFFE spectrograph was used to obtain spectra centred at Ca II H & K to survey the chromospheric activity of stars in open clusters. The spectra extraction pipelines of data obtained from these instruments generally follow similar reduction procedures as described in (Appenzeller, 2013), and are outlined here. HIRES data are used as examples where necessary.

Standard calibration frame reduction is first carried out on the raw images using standard `IRAF`[1] routines: (1) Bias subtraction - an overscan section is identified and subtracted from the object and arc exposures; (2) Dark current removal; (3) Flat-field correction - a normalised flat is created by taking the quotient of a flat image and a median-filtered flat. The target spectra are then divided by the normalised flat to produce flat-corrected spectra. In this step, the blaze function can also be removed; (4) Cosmic ray removal; (5) Sky subtraction - scattered light is removed by fitting the flux level outside aperture.

One-dimensional spectra are extracted from the object and arc images by adding pixels in the corresponding wavelength bin. Arc images obtained from exposures of a calibration lamp (in HIRES, a Thorium-Argon lamp is used) are used to evaluate the wavelength scale. In this step, the wavelength of each line is identified by comparing the line coordinates against the ThAr line lists. The wavelength scale solution is subsequently applied, and the extracted spectra are dispersion corrected by fitting the wavelength scale with a low-order polynomial. Finally, the orders of the dispersion corrected spectra are merged and normalised. Figure 2.1 shows the flow of the reduction procedure.

2.1.3 Cross-correlation

A star's RV about the system's barycentre is measured by the Doppler shift in wavelength of the stellar spectrum. The shift in wavelength is

$$\Delta\lambda = \lambda_{obs} - \lambda_{em} \tag{2.1}$$

[1]IRAF is distributed by the National Optical Astronomy Observatory, which is operated by the Association of Universities for Research in Astronomy, Inc., under cooperative agreement with the National Science Foundation.

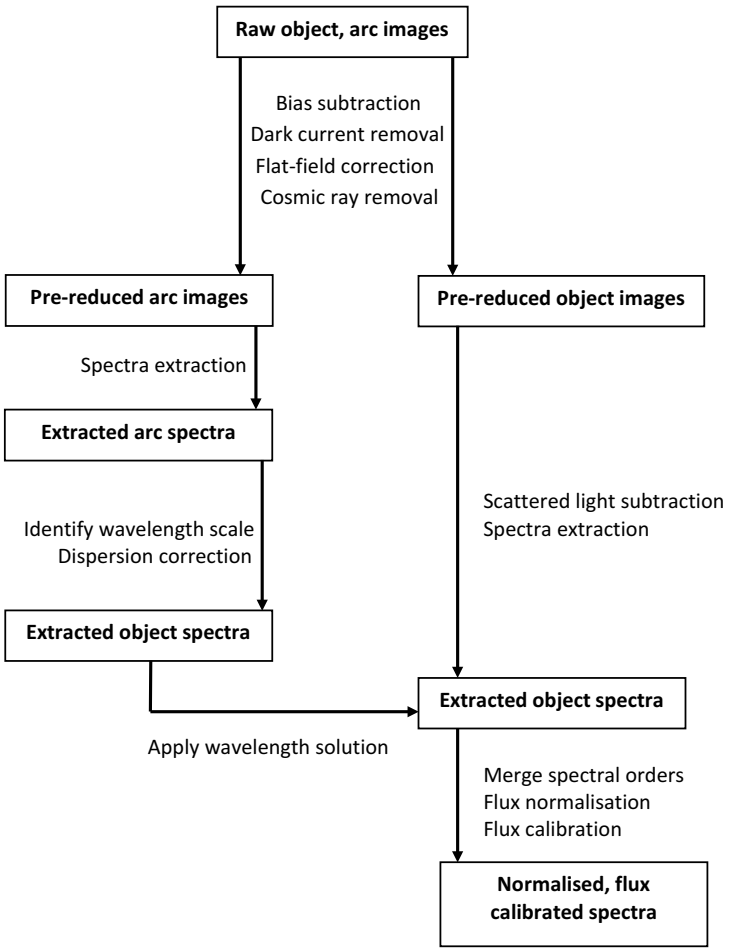

Figure 2.1: General reduction procedures implemented to extract echelle spectra.

where the λ_{obs} is the observed wavelength and λ_{em} is the emitted wavelength. $\Delta\lambda$ is related to the velocity by

$$v_R = \left(\frac{\Delta\lambda}{\lambda_{em}}\right)c. \tag{2.2}$$

A stellar spectrum contains many absorption lines, and to compute the RV from the spectrum, the cross-correlation method is employed. The use of a physical mask in the cross-correlation method was first applied to echelle spectroscopy using CORAVEL by Baranne et al. (1979). The numerical cross-correlation technique is detailed in Queloz (1995) and Baranne et al. (1996), and is summarised below.

In a numerical mask, the template spectrum is comprised of box-shaped lines, i.e. 1 and 0 zones, where 1 corresponds to the position of stellar absorption lines. The numerical mask $M(\lambda_{v_R})$ is correlated to the observed spectrum $S(\lambda)$ as the mask shifts. The cross-correlations function (CCF) is computed as a function of the Doppler velocity (v_R):

$$CCF(v_R) = \int S(\lambda)M(\lambda_{v_R})d\lambda \tag{2.3}$$

where

$$\lambda_{v_R} = \lambda\sqrt{\frac{1-\frac{v_R}{c}}{1+\frac{v_R}{c}}} \tag{2.4}$$

The numerical mask $M(\lambda_{v_R})$ is the sum of masks M_i, each corresponds to an absorption line i. Equ. 2.3 can be rewritten as

$$CCF(v_R) = \int S(\lambda)\sum_i M_i(\lambda_{v_R})d\lambda \tag{2.5}$$

$$= \sum_i \int S(\lambda)M_i(\lambda_{v_R})d\lambda \tag{2.6}$$

$$= \sum_i CCF_i(v_R) \tag{2.7}$$

The resulting CCF describes a mean profile of the absorption lines in the template. This is approximated with a Gaussian function, and the RV value is determined. The Doppler shift of the spectrum is corrected with respect to the Solar System's barycentric frame of reference to account for the Earth's orbital and rotational motion. To improve the signal-to-noise, each spectral line is weighted when building the CCF. Pepe et al. (2002a) showed that a weighted CCF can reduce the noise resulting from telluric lines. The cross-correlation method is used in Chapter 3 and 4 to derive RVs of the host stars.

2.1.4 Stellar Noise and Radial Velocity 'Jitter'

The shape of stellar absorption lines can be affected by stellar activity, stellar oscillations and surface granulation. They can introduce 'jitter' in RV measurements which affects the accuracy, and could lead to false positives in planet detection.

The stellar dynamo is responsible for generating magnetic fields on the stellar surface. Stellar magnetic fields can in turn give rise to spots, plages and faculaes, causing inhomogeneities in the stellar atmosphere. This effect will introduce asymmetry in the spectral line profile, and can perturb the RV amplitude by $\sim$5 m s^{-1} for a solar-age G-type star (Saar and Donahue, 1997). The magnetic fields, however, interact strongly with the stellar wind, which can slow down stellar rotation as the star loses angular momentum. Therefore, young stars are more severely affected by activity-induced jitter than older stars. To reduce activity-induced jitter, it is important to distinguish between the RV variations due to the stellar centre-of-mass motion and variations due to changes in the stellar atmosphere.

Bisector Analysis

The origins of RV variations can be studied using spectral line profiles, which are approximated by the CCF. If RV variations of a star are caused by changes in the star's centre-of-mass, the line profiles are preserved. On the other hand, line profiles change if RV variations are caused by changes in the stellar atmosphere.

The change in the shape of the CCF can be quantified using the spectral line bisector analysis. A line bisector traces the centre of a CCF as a function of the depth below the continuum. An example is shown in Figure 2.2. The velocity of the upper and lower regions of the line profile are calculated as $\overline{V_t}$ and $\overline{V_b}$ respectively. The bisector velocity span (BIS) (Queloz et al., 2001a; Boisse et al., 2011a) is defined as

$$BIS = \overline{V_t} - \overline{V_b} \tag{2.8}$$

If a correlation is found between the RV and BIS, it is could be an indication of jitter, or even blending from an unresolved second source. Bisector analysis was performed in Chapter 3 and 4 on all host star to determine the effect of stellar activity on the validation and characterisation of the planetary systems.

Stellar activity

RV variations can be caused by rotationally modulated of spots or the stellar magnetic activity cycle. These effects are identified by measuring the variations in stellar activity.

Stellar magnetic activity in the atmosphere can heat the gas and generate a temper-

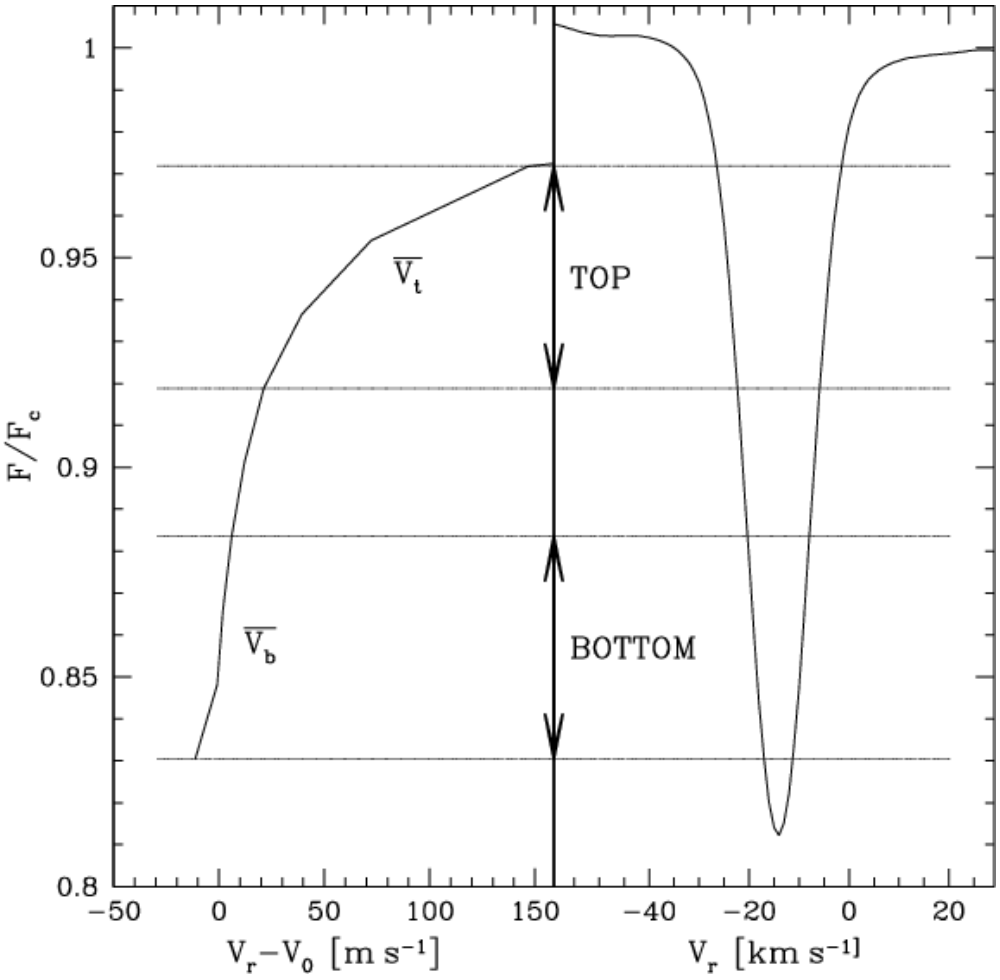

Figure 2.2: An example of a CCF profile (right panel) and the corresponding line bisector (left panel) of the profile (reproduced from (Queloz et al., 2001a) with permission from *ESO*). $\overline{V_t}$ and $\overline{V_b}$ are the bisector velocities in the upper and lower regions respectively. BIS is defined as $\overline{V_t} - \overline{V_b}$.

ature inversion in the stellar chromosphere. This cools via radiation in strong resonance lines, such as the Ca II H & K lines (Deeg and Belmonte, 2017). The spectroscopic measurements of the Ca II H & K lines is therefore is a good indicator for the stellar surface activity. The chromospheric emission parameter R'_{HK} is commonly used as a measure of stellar activity. This is derived from the ratio between the emission in the Ca II H & K line cores and the total bolometric emission of the star (Noyes et al., 1984a; Staab et al., 2017). The parameter R'_{HK} has also been shown to depend on both rotational modulations and long-term activity cycles in the past (e.g. Vaughan et al. 1981; Baliunas et al. 1995). The detailed derivations of R'_{HK} are described in Chapter 5 and 6.

Main-sequence cool stars with convective envelopes generate magnetic fields from a magnetic dynamo (Moffatt, 1978). Magnetic fields interact with highly ionised gas in the stellar atmosphere to form starspots or inhibit granular convection to cause convective blueshift (refer to Section 1.4 for more detail). In both cases, the shapes of the spectral absorption lines are distorted due to the inhomogeneity on the stellar surface (Queloz et al., 2001a; Meunier et al., 2010). Activity-induced RV variations resembles signal from a planetary companion.

Queloz et al. (2001a) performed a number of rigorous checks to find that the RV variations observed in HD 166435 were due to presence of starspots on the stellar surface. In addition to bisector analysis, where they found a negative correlation between the RVs and BIS, Queloz et al. (2001a) analysed the photometry of HD 166435 to find a sinusoidal lightcurve with a period that is consistent with the RV period. The S index measures of the flux centred on the H & K emission line cores evaluates the chromosphere emission of the star. Queloz et al. (2001a) utilised the Ca II H & K measurements from the Mount Wilson HK survey (Wilson, 1978) and found strong periodic variation consistent with the RV and photometric observations.

Simultaneous observations of the RV, photometry and S index of HD 166435 showed that these variations are phase-shifted with respect to one another (Figure 2.3, Queloz et al. 2001a). This can be explained by the visibility of starspots along the line of sight. As seen on the top two panels of Figure 2.3, the photometric variation has a $1/4$ phase shift with respect to the RVs. When a starspot rotate into our line of sight and lie on the centre of the stellar disc, the starspot covers both the approaching and receding part of the star. This result in maximum brightness depression and the RV variation is zero. When the starspot rotate out of view, the stellar brightness increases and the spot covers more of the receding part of the star, leading to maximum blueshift and RV minimum. Queloz et al. (2001a) also found a $1/8$ phase-shift between the brightness variation and the S index of the star (second and third panels of Figure 2.3). This arise due to the displacement of the photocentres of darkspots and bright plages.

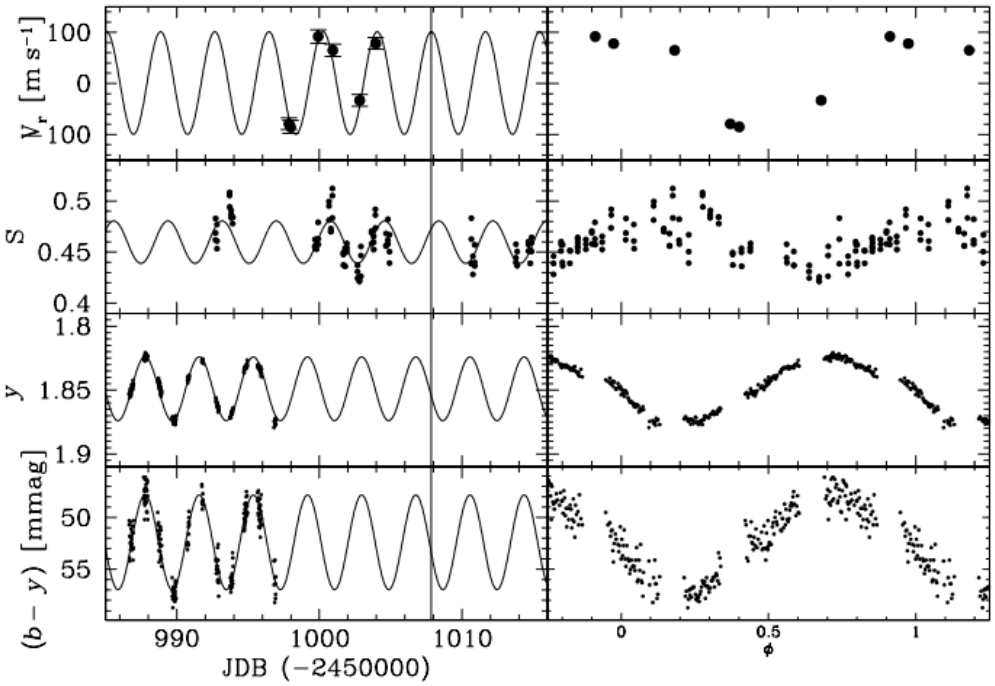

Figure 2.3: Simultaneous RV observations (top panel), S index (second panel), y magnitude (third panel), and delta $(b - y)$ colour of HD 166435 (reproduced from Queloz et al. 2001a with permission from Astronomy & Astrophysics, ©ESO). Left: Each data set are fitted with a 3.798-day sinusoid. The vertical line is plotted to show the phase shift of the observations. Right: Phase-folded observation of the same data set as the right.

Queloz et al. 2001a showed that follow-up long term monitoring are required to disentangle stellar activity from planetary signals. In Chapter 4, the time-series photometric, RV and chromospheric observations of the host star are analysed to show that the measured Rv variation is due to gravitational interaction of a planet.

2.2 Photometry

Photometry is the technique used to measure the flux of a star. A lightcurve is constructed by making many photometric measurements over time, so the variations of an object's brightness can be analysed. Several independent photometry pipelines were used in Chapter 3 and 4 because the data were obtained with different instruments. In this section, the general photometry technique (Warner, 2006) used to extract a lightcurve is outlined. The model used to analyse transit lightcurves is also describe.

Aperture Photometry

Before carrying out a photometry observation, a suitable field must be selected such that multiple comparison stars, along with the target star is placed inside the Field of View (FoV). The pre-reduction procedures are first carried out in the raw images: (1) Bias subtraction; (2) Dark current subtraction; (3) Flat-field correction. The accuracy of flat-fielding represents the limit in photometry, except when stars are kept on the same pixel. In which case, the flat-fielding errors are minimised. The brightness of the stars are then determined by performing aperture photometry. In aperture photometry, an aperture and an outer annulus are defined to measure the star and the sky background respectively. The total signal contributed from the star is calculated by taking the difference between the total pixel value within the aperture and total pixel value in the annulus. Once the brightness of each star is obtained as a function of time, differential photometry is carried out.

Differential Photometry

Stars usually have constant luminosity, hence constant apparent brightness. However, this can be affected by atmospheric extinction when measurements are made from ground-based instruments. If the target and comparison stars are observed in the same field all the time, they are affected by atmospheric extinctions to the same extent. Differential photometry compares the relative difference between the target and comparison stars. A differential lightcurve is produced by dividing the lightcurve of the target star by the lightcurves of the comparison stars. This procedure should eliminate first order atmospheric extinctions. Very often, the target and comparison stars are not of similar spectral type, so airmass-colour terms would remain. This trend can be removed by fitting a first or second order polynomial to the normalised region (i.e. the out-of-transit region) of the differential lightcurve.

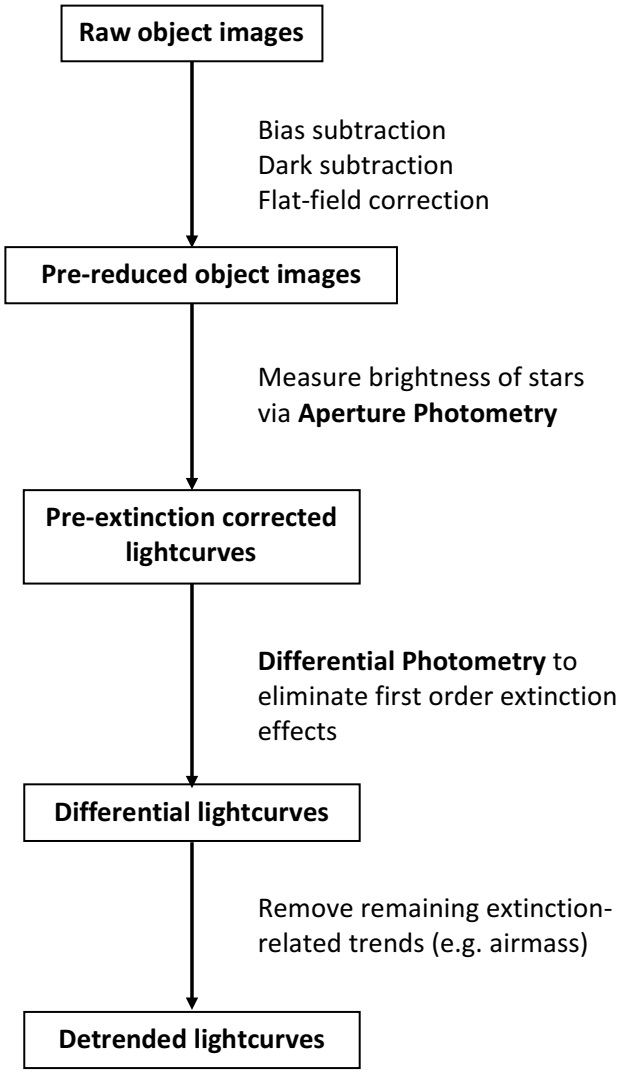

Figure 2.4: Standard lightcurve extraction procedure using aperture photometry and differential photometry.

2.2.1 Transit Lightcurve Model

The characteristics of a star-planet system can be inferred from the shape of a transit lightcurve. Some of the basic parameters which can be derived from the lightcurve are described in Chapter 1. The geometry of the transit and the limb darkening effect of the star must be taken into account in deriving the physical parameters. The analytical equations and limb darkening coefficients required to derive physical parameters of the planetary systems in Chapter 3 and 4 are described here.

Limb Darkening Effect

The intensity of stellar radiation depends on the optical depth in the stellar atmosphere. Photons in the stellar atmosphere emit radially outwards. If a photon emerges from the centre of the disc, it will travel directly towards the observer along the line-of-sight. Moving closer to the limb, a photon emitted at a depth h would travel at an angle θ along a path length $s = h/\cos\theta$ (Figure 2.6(a)). The optical depth increases towards the stellar limb, hence a reduced number of photons is emitted from the limb and fewer photons would reach the observer. As a result, the stellar limb appears dimmer than the centre of the centre of the stellar disc. This optical effect is called the *limb darkening effect*. Limb darkening is a function of the optical depth, which is wavelength-dependent. Consequently, the spectral type of the star can also affect the limb darking effect.

Limb darkening is a non-linear effect, Claret (2000, 2004) proposed the non-linear limb darkening function which can describe the intensity variation $I(r)$ of the stellar disc:

$$I(r) = 1 - \sum_{n=1}^{4} c_n(1 - \mu^{n/2}) \tag{2.9}$$

where $\mu = \cos\theta = (1 - r^2)^{1/2}$, $0 \leq r \leq 1$, and c_n are the coefficients which depends on the temperature, spectral type and metallicity of the star. Figure 2.5 shows the transit shape for various limb darkening law.

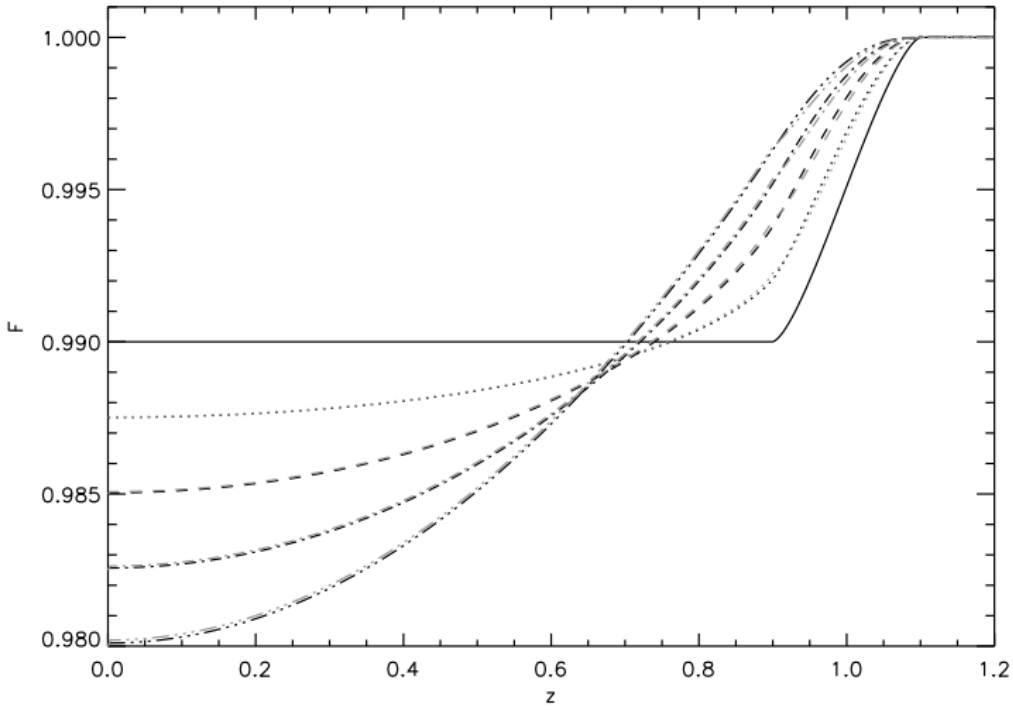

Figure 2.5: Transit lightcurves described by the non-linear limb darkening laws in Equation 2.9 for $p = 0.1$. (reproduced from Mandel and Agol (2002) with permissions from *The American Astronomical Society*). The shape of the transit lightcurve depends on the values of limb darkening coefficients. *Solid line*: $c_1 = c_2 = c_3 = c_4 = 0$. *Dotted line*: all coefficients equals to zero but c˙1 = 1. *Dashed line*: all coefficients equals to zero but c˙2 = 1. *Dash-dotted line*: all coefficients equals to zero but c˙3 = 1. *Dash-triple-dotted line*: all coefficients equals to zero but c˙4 = 1.

Transit Geometry

A transit lightcurve model determines the area of star that is occulted by the planet during a transit event. Mandel and Agol (2002) has prescribed a set of analytical functions which details the geometry of a transit event. Assuming a circular orbit, the orbital speed of a planet is

$$\omega = \frac{2\pi}{P} \tag{2.10}$$

where the orbital phase angle ωt is related to the orbital phase by

$$\phi = \frac{\omega t}{2\pi}. \tag{2.11}$$

At phase $\phi = 0$, the planet is at the inferior conjunction (i.e. mid-transit) where the projected separation d between the centres of the planet and the star is $b = a\cos i$. At other instances, the projected separation d along the line of sight is a vector addition of the displacement component $a\sin\omega t$ in the plane of the sky, and an orthogonal component $a\cos\omega t$. At an orbital inclination i, the full displacement in the plane of the sky is observed, while the observed orthogonal component is foreshortened as $a\cos i\cos\omega t$. Hence the time-dependent projected separation can be derived using Pythagorass theorem

$$d = a(\sin^2\omega t + \cos^2 i\cos^2\omega t)^{1/2}. \tag{2.12}$$

There are three cases which are considered in deriving the general expression for the occulted stellar area. First, we consider the case where the disc of the planet covers part of the stellar limb (as shown in Figure 2.6(b)). The angle between the stellar radius extending from the centre of the star to the intersection of the planet and the star, and the projected separation d is α_2. The angle between the planet radius extending from the centre of the planet to the intersection of the planet and the star is α_1. The projected separation d is parameterised in terms of the stellar radius as $d = zr_s$. The ratio between the radii of the planet disc and the stellar disc is $p = r_p/r_s$. When the stellar disc is partially occulted by the planet, the occulted area A_e is

$$\begin{aligned} A_e =& 2\times(\text{area of the sector of the planets disc} + \text{area of the sector of the stellar disc} \\ &- \text{area of triangle formed by an extension of the stellar sector}), \end{aligned} \tag{2.13}$$

where

$$\text{area of the sector of the planets disc} = \pi r_P^2 \times \frac{\alpha_1}{2\pi} = \frac{p^2 r_s^2 \alpha_1}{2} \tag{2.14}$$

$$\text{area of the sector of the stellar disc} = \pi r_s^2 \times \frac{\alpha_2}{2\pi} = \frac{r_s^2 \alpha_2}{2} \tag{2.15}$$

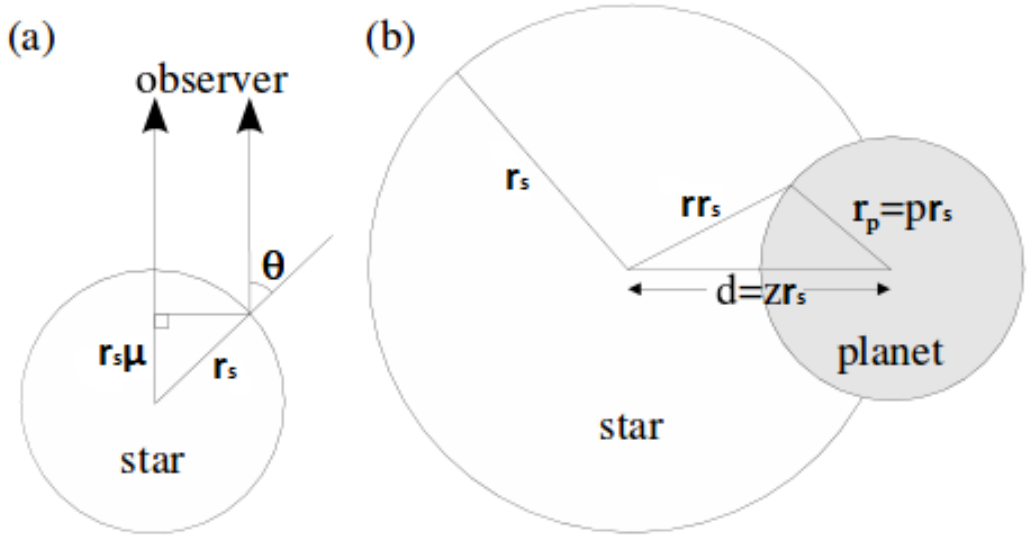

Figure 2.6: (a) Edge-on view of the star with radius r_s showing geometry of the limb darking effect. The angle between the observer and the normal to the stellar surface is defined by θ, and $\mu = \cos\theta$. (b) Geometry of a transit event along the line of sight. The projected separation between the centres of the stellar disc and the planet's disc is denoted by d, and d is parameterised in terms of stellar radius as $d = zr_s$. The ratio between the radii of the stellar and planet discs is defined by p. r is the normalised axial coordinate, which is defined as 0 at the centre of the star and 1 at the stellar limb. Figure reproduced and adapted from Mandel and Agol (2002) with permissions from *The American Astronomical Society*.

$$\begin{aligned}\text{area of triangle formed by an extension of the stellar sector} &= \frac{r_s \times z r_s \sin\alpha_2}{2} \\ &= \frac{z r_s^2}{2}\sin\alpha_2\end{aligned} \tag{2.16}$$

Using the cosine rule, the angles α_1 and α_2 can be expressed as

$$\cos\alpha_1 = \frac{p^2 + z^2 - 1}{2zp} \tag{2.17}$$

$$\cos\alpha_2 = \frac{1 + z^2 - p^2}{2z}. \tag{2.18}$$

From the identity $\sin^2\alpha_2 + \cos^2\alpha_2 = 1$, we get

$$\sin\alpha_2 = \frac{\sqrt{4z^2 - (1 + z^2 - p^2)}}{2z}. \tag{2.19}$$

Combining the equations above, the occulted area A_e is

$$\begin{aligned}A_e &= 2 \times \left(\frac{p^2 r_s^2 \alpha_1}{2} + \frac{r_s^2 \alpha_2}{2} - \frac{z r_s^2 \sqrt{4z^2 - (1 + z^2 - p^2)^2}}{4z} \right) \\ &= r_s^2 \left(p^2\alpha_1 + \alpha_2 - \frac{\sqrt{4z^2 - (1 + z^2 - p^2)^2}}{2} \right)\end{aligned} \tag{2.20}$$

The second case we consider in a transit event is when the planet falls entirely outside of the stellar disc. This occurs when the distance between the centres of the star and the planet is greater than the sum of their radii (i.e. $1 + p < z$). At this instance, $A_e = 0$. The third case is when the planet falls entirely within the disc of the star. This happens if the distance between the centres of the star and the planet is smaller than the difference of their radii (i.e. $1 - p \geq z$). The occulted area becomes $A_e = \pi p^2 r_s^2$. The occulted area of the star is thus a function of r_s, p and z, i.e. $A_e = A_e(r_s, p, z)$.

The total observed flux from the stellar disc can be determined from the stellar intensity I integrated over the surface of the stellar disc. In an axially symmetric stellar disc, the stellar intensity is $I = I(r')$, where r' is the radial distance measured from the centre of the stellar disc. The total flux from the stellar disc then becomes

$$F = \int_{\text{disc}} I(r')\mathrm{d}A = \int_{r'=0}^{r'=r_s} I(r') 2\pi r' \mathrm{d}r'. \tag{2.21}$$

The flux occulted by the planet's disc is therefore the intensity integrated over the occulted

area of the stellar disc

$$\delta F = \int_{\text{occulted area}} I(r')\mathrm{d}A. \tag{2.22}$$

The normalised axial coordinate r is defined such that $r = 0$ is at the centre of the star, and $r = 1$ is at the stellar limb. Explicitly, $r = r'/r_s$. The increment area $\mathrm{d}A(r)$ is equal to the difference between A_e for a star of radius $r_s = r'$ and for a star of radius $r_s = r' + \mathrm{d}r'$:

$$\mathrm{d}A(r) = \frac{\mathrm{d}A_e}{\mathrm{d}r'}\mathrm{d}r'. \tag{2.23}$$

The occulted area becomes

$$\begin{aligned}\int_0^{r'=rr_s} \frac{\mathrm{d}A_e}{\mathrm{d}r}\mathrm{d}r &= A_e\left(rr_s, \frac{p}{r}, \frac{z}{r}\right) \\ &= r^2 A_e\left(r_s, \frac{p}{r}, \frac{z}{r}\right).\end{aligned} \tag{2.24}$$

Finally, the flux occulted by the planet's disc is expressed as

$$\begin{aligned}\delta F = \int_{r'=0}^{r'=rr_s} I(r')\mathrm{d}A &= \int_{r=0}^{r=1} I(r)\mathrm{d}A(r) \\ &= \int_{r=0}^{r=1} I(r)\frac{\mathrm{d}}{\mathrm{d}r}\left[r^2 A_e\left(r_s, \frac{p}{r}, \frac{z}{r}\right)\right]\mathrm{d}r.\end{aligned} \tag{2.25}$$

In the limb darkened case, the stellar intensity is defined by the limb darkening law which is described in Equation 2.9.

Under the small planet approximation, $p \leq 0.1$, the case where the planet falls entirely within the disc of the star ($z < 1 - p$) is approximated by assuming a constant stellar surface brightness under the disk of the planet. The occulted flux becomes $F(p, z) = p^2 I^*(z)/4\Omega$, where Ω is defined as $\sum_{n=0}^{4} c_n(n + 4)^{-1}$, and the intensity becomes $I^*(z) = (4zp)^{-1}\int_{z-p}^{z+p} I(r)2r\mathrm{d}r$. In the case where the disc of the planet occults part of the stellar limb, $1 - p < z < 1 + p$, the occulted stellar flux is re-evaluated as

$$F(p, z) = 1 - \frac{I^*(z)}{4\Omega}\left[p^2\cos^{-1}\left(\frac{z-1}{p}\right) - (z-1)\sqrt{p^2 - (z-1)^2}\right] \tag{2.26}$$

where $I^*(z) = (1 - m)^{-1}\int_{z-p}^{1} I(r)2r\mathrm{d}r$, and m is defined as $m \equiv (z - p)^2$.

2.3 Markov Chain Monte Carlo

From the RV measurements and transit lightcurves, we want to estimate a set of system parameters (the model) which best describe the observed data. The Markov Chain Monte

Carlo (MCMC) is a powerful method which can determine a solution by sampling from a complicated parameter space. This method is applied in Section 3.3.3 of Chapter 3 and Section 4.3.3 of Chapter 4 to derive best-fit models to characterise the system parameters of planetary systems.

Given a set of observable data, d, a Bayesian approach is used to constraint the model parameters, θ. Bayes' theorem is defined such that the posterior probability for hypothesis θ given data d, $P(\theta|d)$, is proportional to the prior probability distribution, $P(\theta)$, and the likelihood function, $P(d|\theta)$, and is inversely proportional to the evidence, $P(d)$ (Bevington, 1969):

$$P(\theta|d) = \frac{P(\theta)P(d|\theta)}{P(d)}. \tag{2.27}$$

The likelihood of getting d given the model θ and a set of parameters is

$$P(d|\theta) = \prod_i P(d_i|\theta) = \prod_i \frac{1}{\sqrt{2\pi}\sigma_i} exp\left[-\frac{\chi^2}{2}\right] \tag{2.28}$$

and

$$\chi^2 = \frac{\sum_i (d_i - \theta)^2}{\sigma_i^2} \tag{2.29}$$

where the standard deviation (uncertainty) of the i^{th} observation is σ_i, d_i is the i^{th} observed data and the model parameter θ would provide a fit to the data set.

At the beginning of an MCMC run, a model θ_{old} is generated as a starting point from its corresponding parameters and the posterior probability, $P(\theta_{old}|d)$, is calculated (Tegmark et al., 2004). A random step is taken from θ_{old} to a new model θ_{new}, and its posterior probability $P(\theta_{new}|d)$ is deduced. At this stage, the Metropolis-Hastings (M-H) method (Metropolis et al., 1953; Hastings, 1970) is used as a test to accept or reject θ_{new}. θ_{new} is accepted if its posterior probability $P(\theta_{new}|d)$ is greater than $P(\theta_{old}|d)$ and it will be used as a foundation for the next random step. However, if $P(\theta_{old}|d) > P(\theta_{new}|d)$, the new state will only be accepted with a probability of $P(\theta_{new}|d)/P(\theta_{old}|d)$. This procedure repeats until a chain of models (or states) is formed. Multiple chains are computed at the same time in the 'burn-in' process to increase efficiency of the method. It also provides convergence tests to all the chains and make sure they reach the global minima. The median posterior probability of the beginning of all chains is used as the first step such that the M-H method can accept or reject the new proposals of all the chains. Any chains that do not converge to global minima will be discarded so the final result after the burn-in process is not affected by the failed chains. Using the chain with the best-fit model, the exoplanet system parameters can be inferred. The Markov character of the MCMC method is preserved in the process since

the chains are independent of each other and the random steps taken during burn-in relies on the current new model only.

The full characterisation of a planetary system requires a combination of different methods. The methods described in this chapter will be utilised in the following chapters in order to study newly discovered planets, and investigate the variability of evaporating planets.

Chapter 3

From Dense Hot Jupiter to Low-density Neptune: The Discovery of WASP-127b, WASP-136b and WASP-138b

Thousands of transiting exoplanets are known since the discovery of HD209458 b, and hundreds of these discoveries were made via ground-based transit surveys. Planets detected with ground-based surveys usually orbit around stars which are bright enough for precise follow up RV observations to fully characterise the planetary system. SuperWASP (See Chapter 1 - Section 1.2.2 for details on facilities and instruments) remains one of the most successful ground-based transit surveys. In this chapter, the discovery of three new planets from the WASP survey is presented. These planets show that gas giant planets come in a wide variety of different sizes. The diversity of densities and compositions of these planets could arise from different formation and evolution paths. Part of the work presented here were done by the wider collaboration, including the WASP photometry reduction and candidate identification process, observations and reduction of follow up photometry and spectroscopy, and host star spectral analysis. I have estimated the stellar ages from stellar evolutionary models, performed joint lightcurve and RV analysis to derive system characteristics to constrain possible evolution histories of the three systems. This work was also published in Lam et al. (2017).

3.1 Candidate Identification in the WASP Survey

The WASP photometry of WASP-127, WASP-136 and WASP-138 were obtained between 2008 February and 2013 January. A total of 24, 523, 32, 842 and 21, 004 photometric data points were obtained for WASP-127, WASP-136 and WASP-138, respectively. The photometric data were reduced with the pipeline described in Pollacco et al. (2006) (see also Methods - Section 2.2). Systematic errors in the reduced data were decorrelated using the SysRem detrending algorithm (Tamuz et al., 2005), and the Box-fitting Least-Squares algorithm (BLS; Kovács et al. 2002) was used to search for planet transit signals (Collier Cameron et al., 2006). After planet candidates were identified, multi-seasonal lightcurves were analysed using the transit search algorithm described in Collier Cameron et al. (2007) to calculate orbital parameters of planet candidates. For WASP-127, a period of $P = 4.18$ days, transit duration between the first and fourth contact is $T_{14} \approx 3.6$ hours and a depth of ~ 5.8 mmag was found. The lightcurve of WASP-136 showed a periodicity of $P = 5.22$ days, a transit duration of $T_{14} \approx 5.2$ hours, and a transit depth of ~ 2.9 mmag. In the WASP-138 data, a depth of ~ 8.2 mmag was detected, with a period of $P = 3.6$ days, and a transit duration of $T_{14} \approx 4.1$ hours. Once false positives, such as variable stars and eclipsing binaries, were rejected, WASP-127, WASP-136 and WASP-138 were flagged as high priority candidates in 2014.

We searched for rotational modulation of the WASP photometry using the method of Maxted et al. (2011). In summary, a periodogram was computed for each target, and the distribution of peak power values are fitted to find the false alarm probability for the highest peak. No rotational modulation was found above 2 mmag, suggesting that the host stars are inactive.

3.2 Follow Up Observations

3.2.1 Photometry Follow Up

Additional follow up photometric observations were made to verify the planet candidates. They can also put constraints on the system parameters in the lightcurve modelling process. Lightcurves were obtained with EulerCam at the 1.2 m Euler-Swiss telescopes (Lendl et al., 2012) and TRAPPIST (Jehin et al., 2011; Gillon et al., 2011), which are both situated at ESO's La Silla Observatory in Chile, the RISE camera on the Liverpool Telescope at the Observatorio del Roque de los Muchachos on La Palma (Steele et al., 2008) and the Zeiss 1.23m telescope at the German-Spanish Astronomical Center at Calar Alto in Spain. A summary of the follow up photometry can be found in Table 3.2. The phase-folded best-fit lightcurves using results obtained from the MCMC analysis (Section 3.3.3) are shown in

Table 3.1: Photometric properties of the three host stars WASP-127, WASP-136 and WASP-138.

Parameter	WASP-127	WASP-136	WASP-138
Identifier	1SWASP J104214.08−035006.3	1SWASP J000118.17−085534.6	1SWASP J024633.37−002750.0
RA(J2000)	10:42:14.08	00:01:18.17	02:46:33.37
Dec(J2000)	−03:50:06.3	−08:55:34.6	−00:27:50.0
B	10.79	10.39	12.28
V	10.15	9.98	11.81
R	9.74	9.71	11.40
H	8.74	8.79	10.54
K	8.64	8.81	10.49

Figures 3.1, 3.2 and 3.3.

TRAPPIST: The 0.6m TRAPPIST (TRAnsiting Planets and PlanetesImals Small Telescope; Gillon et al. 2011 and Jehin et al. 2011) robotic telescope was used to obtain lightcurves for both WASP-127 and WASP-136. The telescope is equipped with a thermoelectrically-cooled 2k $\times$ 2k CCD camera. It has a pixel scale of 0.65", giving a field-of-view of 22' $\times$ 22'.

A partial transit of WASP-127 b was observed on 2014 March 18. A Sloan-z filter (effective wavelength = 896.3 $\pm$ 0.8 nm) and an exposure time of 9 seconds was used. On 2014 November 24, the partial transit of WASP-136 b was observed using the same filter with an exposure time of 7 seconds. For both transits, the telescope was kept in focus thoughout the observations. The stars were kept within a few pixels on the detector using a software guiding system which calculates the astrometric solution for the images regularly. This is used to correct the pointing on the mount.

The data were reduced using the pipeline of Gillon et al. (2013), which follows procedures similar to those described in Chapter 2. Different sets of reduction parameters were tested to find the most precise photometry for the stars. Differential photometry was performed to obtain the final lightcurves.

EulerCam: EulerCam was used to obtain lightcurves of all three targets. The camera is an e2v 4k $\times$ 4k back-illuminated deep-depletion silicon CCD detector. It has a field-of-view of 15.68×15.73 and a pixel scale of $0.23''$/pixel.

A full transit of WASP-127 was observed on 2014 April 28 with a Gunn r filter. The telescope was defocused throughout the observation with Full Width at Half Maximum (FWHM) between 1.6 and 2.5 arcsec. The lightcurve was extracted with aperture photometry, where a circular aperture of radius 4.7 arcsec and one reference star was used.

A partial and a full transit of WASP-136 were observed on 2014 August 21 and 2015 August 21 respectively. The events were observed using a Gunn z filter and an exposure time of 50 seconds. The telescope was kept defocused throughout both nights. On the first night, the FWHM was between 1.5 and 2.3 arcsec. The lightcurve was extracted using four reference stars and a circular aperture with a radius of 2.7 arcsec. For the second night, the FWHM was between 1.9 and 3.0 arcsec. A circular aperture of radius 4.5 arcsec, and five reference stars were used for the photometry reduction.

One full transit of WASP-138 was observed on 2015 December 17 with an NGTS filter (with a custom wavelength of 550 - 900 nm), using exposure times between 50 and 85 seconds. The telescope was substantially defocused and the FWHM was between 1.3 and 2.5 arcsec. To extract the lightcurve, one reference star was used, along with a photometric aperture of 5.6 arcsec radius.

RISE: A full transit of WASP-127 was observed using the RISE camera (Steele

Table 3.2: Follow up photometric observations of WASP-127, WASP-136 and WASP-138.

Planet	Date	Instrument	Filter	Comment
WASP-127b	17/03/2014	TRAPPIST	z	partial transit
	28/04/2014	EulerCam	Gunn r	partial transit
	13/02/2016	LT RISE	V + R	full transit
	18/04/2016	Zeiss 1.23m	Cousins-I	full transit
WASP-136b	21/08/2014	EulerCam	z	partial transit
	23/11/2014	TRAPPIST	z	partial transit
	21/08/2015	EulerCam	z	full transit
WASP-138b	09/12/2015	EulerCam	NGTS	partial transit

et al., 2008). The camera has a back illuminated, frame transfer CCD of 1k $\times$ 1k pixels. A "V+R" filter and 2 $\times$ 2 binning of the detector were used for the observation, which gives a pixel scale of 1.08 arcsec/pixel. The telescope was defocused by 0.5 mm throughout the observations, and an exposure time of 1.5 seconds was used. The RISE pipeline was used to reduce the raw images and aperture photometry was carried out using four comparison stars and an aperture of 4.86 arcsec radius. The increased scatter around mid-transit (see Figure 3.1) is attributed to thin clouds.

Zeiss: The Zeiss 1.23m telescope has a focal length of 9857.1mm and is equipped with the DLR-MKIII camera, which has 4k $\times$ 4k pixels of size 15 micron. It has a pixel scale of 0.32 arcsec/pixel and a field-of-view of 21.5 $\times$ 21.5 arcmin.

This instrument was used to observe a full transit of WASP-127. Throughout the observation, the telescope was kept defocused and an exposure time between 65 and 105 seconds was used. The CCD was windowed to decrease the readout time and speed up the cadence of the observations. Aperture photometry was performed to obtained the final lightcurve using a revised version of the DEFOT code (Southworth et al., 2014). The night was not photometric and several clouds disturbed the observations, resulting in increased scatter in the lightcurve.

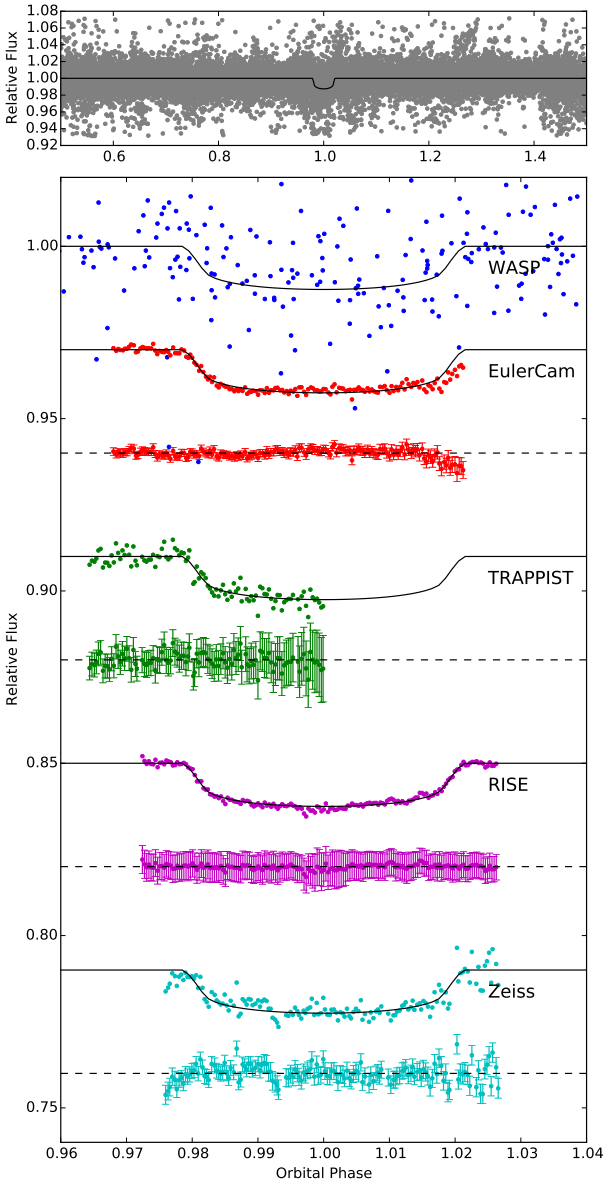

Figure 3.1: The binned WASP lightcurve (blue) of WASP-127, along with follow up lightcurves obtained from EulerCam (red), TRAPPIST (green), RISE (magenta) and Zeiss (cyan). The lightcurves are phase-folded using the ephemeris from the MCMC analysis. For clarity, arbitrary offsets from the zero-magnitute are assigned to the follow up lightcurves. The black solid lines are the best-fit transit model and the residuals are plotted under each lightcurve.

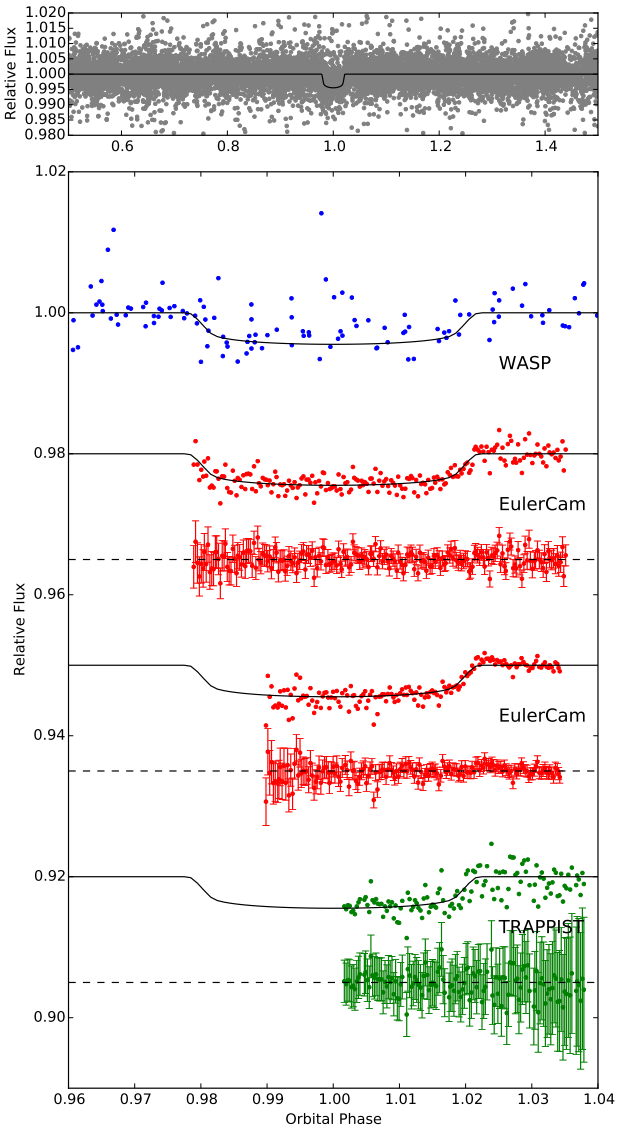

Figure 3.2: Lightcurves of WASP-136 observed from WASP (blue), EulerCam (red) and TRAPPIST (green). The data are phase-folded with the ephemeris derived from the analysis. For clarity, arbitrary offsets from the zero-magnitute are assigned to the follow up lightcurves.The black solid lines are the best-fit transit model and the residuals are plotted under each lightcurve.

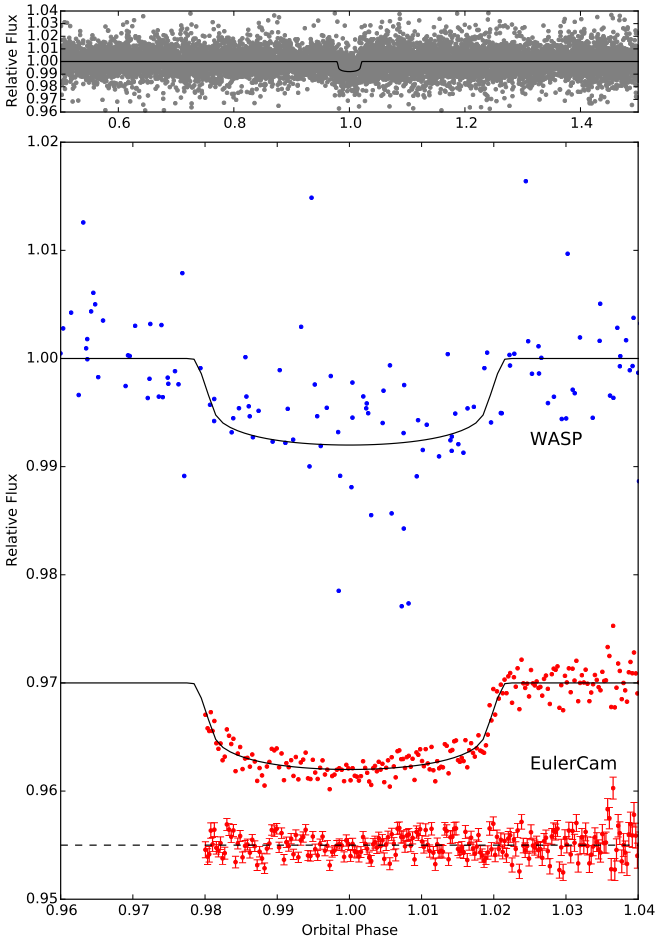

Figure 3.3: Lightcurves of WASP-138 observed from WASP (blue), and EulerCam (red). The data are phase-folded with the ephemeris from our analysis. The EulerCam lightcurve is assigned an arbitrary offset from the zero-magnitude for clarity. The black solid lines are the best-fit transit model and the residuals are plotted under each lightcurve.

3.2.2 Radial Velocity Follow Up

Spectroscopic observations of WASP-127, WASP-136 and WASP-138 were obtained with the SOPHIE and CORALIE spectrographs, using high-efficiency mode with resolutions of R= 40, 000 and R= 55, 000 respectively.

A total of 28 spectral measurements of WASP-127 were taken between 2013 April 18 and 2015 April 9 using CORALIE. 6 of these measurements were taken after the instrumental upgrade in November 2014, hence the data are affected by a zero-point offset of the instrument. In the MCMC analysis, these data were treated as if they were obtained using different instruments. In addition, 13 SOPHIE measurements of WASP-127 were obtained between 2013 April 18 and 2014 December 31. For WASP-136, 23 CORALIE spectra were taken between 2014 June 24 and 2014 October 28. 10 SOPHIE and 10 CORALIE spectra were obtained for WASP-138 between 2014 October 20 and 2015 January 25. All WASP-136 CORALIE spectra were obtained before the instrumental upgrade, whereas all WASP-138 CORALIE spectra were obtain after the upgrade. Therefore the data were not affected by the zero-point offset.

All SOPHIE and CORALIE data were reduced with their respective standard reduction pipelines, using similar procedures to those outlined in Chapter 2. The RV of each system was derived using the weighted cross-correlation method. Figures 3.4 and 3.5 show the phase-folded RV measurements of WASP-127 from two different MCMC analyses (see Section 3.3.3). Figures 3.6 and 3.7 show the phase-folded RV measurements of WASP-136 and WASP-138, respectively.

WASP-127 has a visual companion located at a separation of 41". Spectral line bisector analysis was performed to check for RV variations due to stellar activity or a blended binary system. The result of the analysis is shown in Figure 3.8, where no correlation is found between the bisector velocity span (V_{span}) and the RV measurements. Thus the RV variations are of genuine planetary origin. The bisector analyses of WASP-136 and WASP-138 also show no correlation between V_{span} and RV.

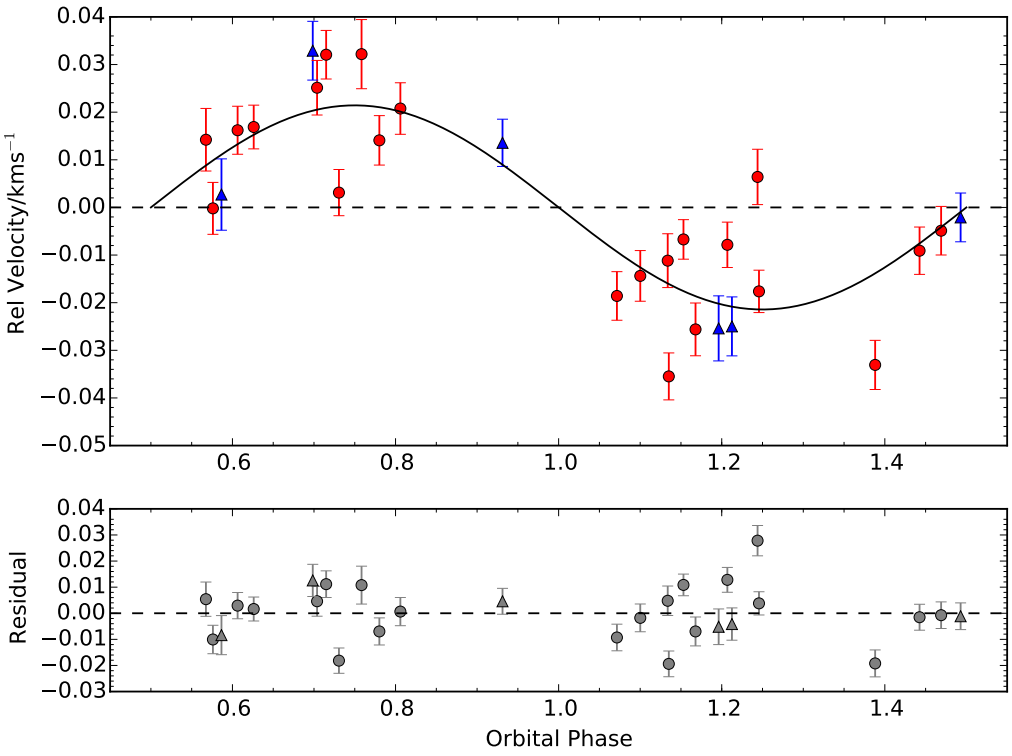

Figure 3.4: *Upper panel*: Phase-folded radial velocity measurements of WASP-127 as a function of orbital phase. The best-fit RV curve (obtained from the analysis using CORALIE RVs only) is plotted as a black solid line. CORALIE data observed before the instrumental upgrade are denoted by red circles while data taken after the upgrade is denoted by blue triangles. *Lower panel*: Residuals from the RV fit as a function of orbital phase.

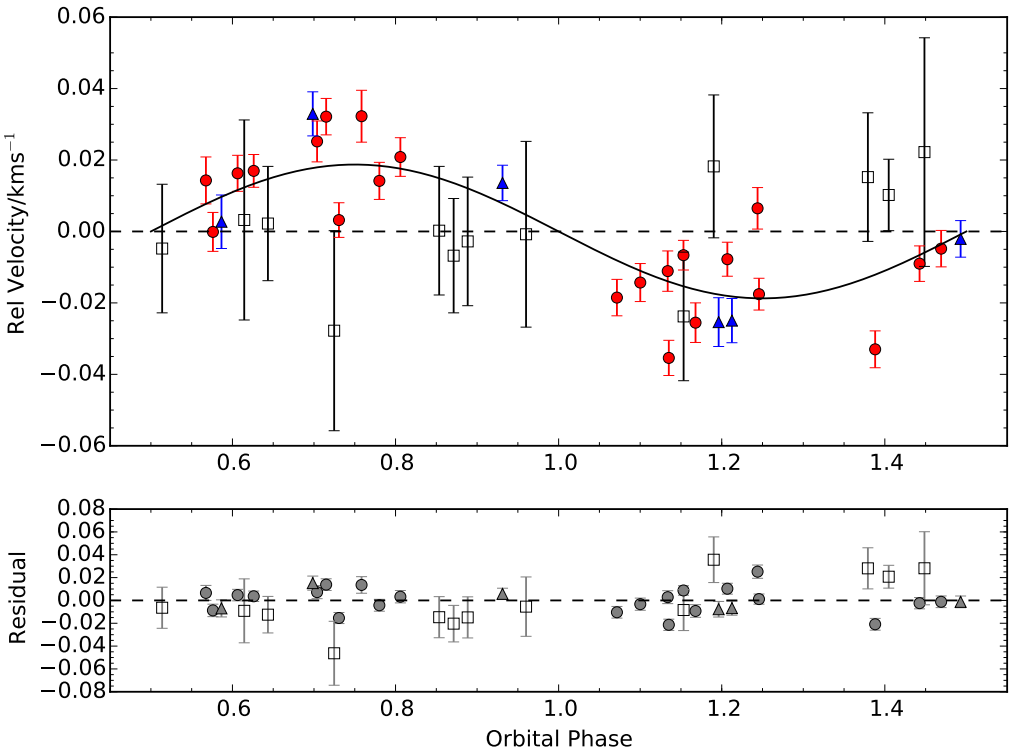

Figure 3.5: As Figure 3.4 with SOPHIE data denoted as black open squares. The SOPHIE error bars are inflated by a multiplication factor of 2. The best-fit RV curve is obtained from the analysis with both CORALIE and SOPHIE RVs.

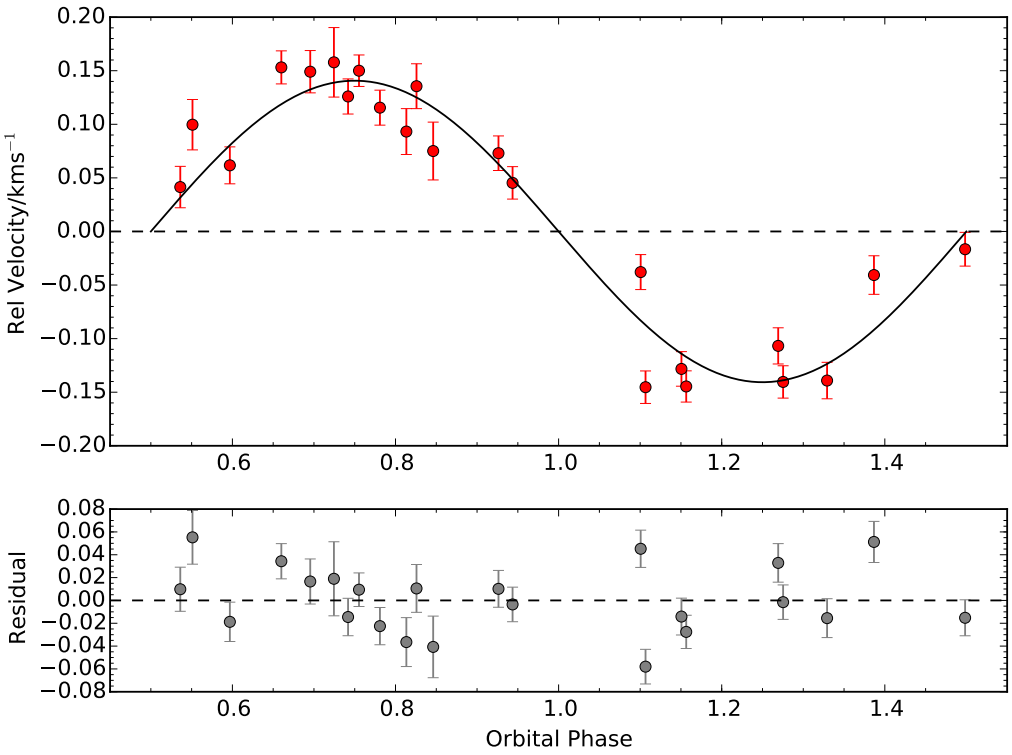

Figure 3.6: *Upper panel*: Phase-folded CORALIE radial velocity measurements (red circles) of WASP-136, as a function of the orbital phase. The best-fit RV curve is plotted as a black solid line. *Lower panel*: Residuals from the RV fit as a function of orbital phase.

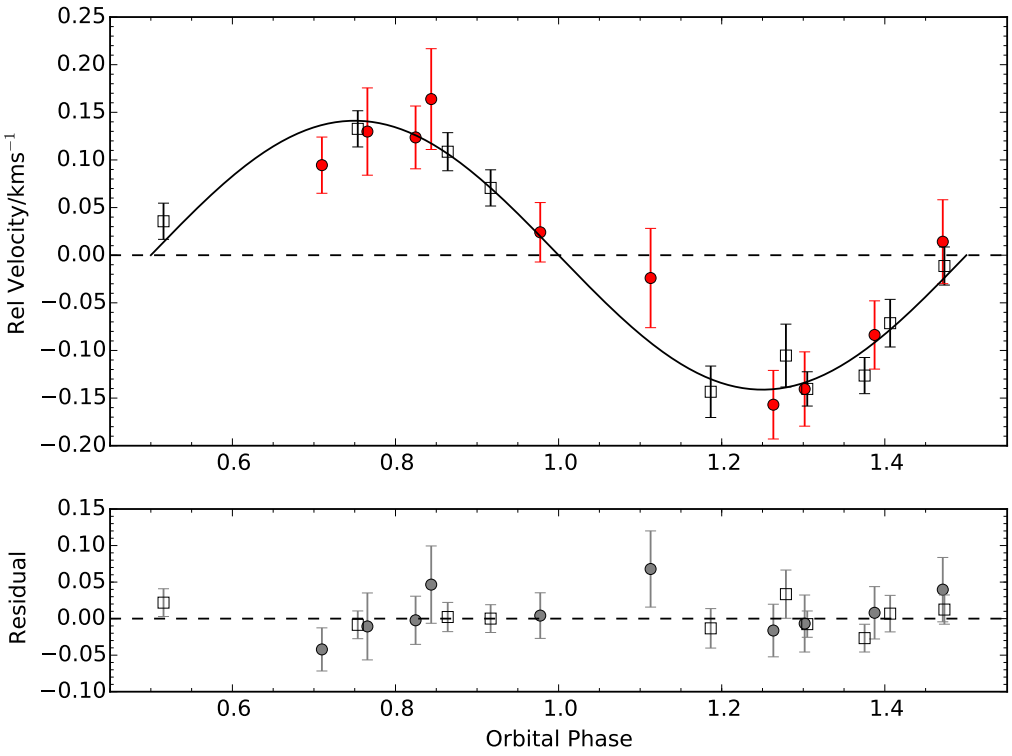

Figure 3.7: *Upper panel*: Phase-folded CORALIE (red circles) and SOPHIE (black open circles) radial velocity measurements of WASP-138 as a function of the orbital phase. The best-fit RV curve is plotted as a black solid line. *Lower panel*: Residuals from the RV fit as a function of orbital phase.

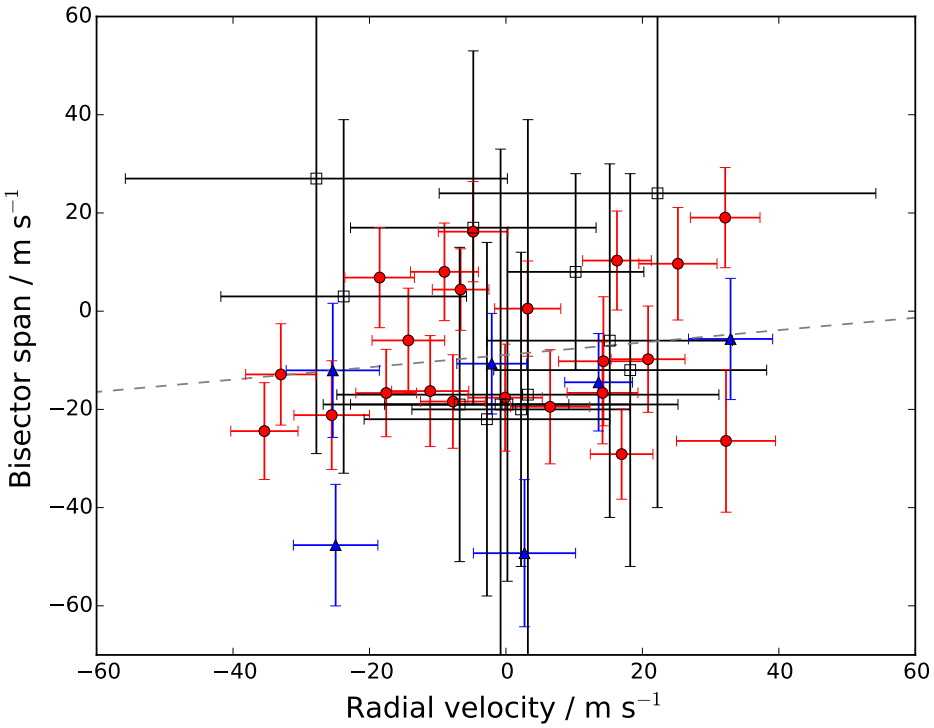

Figure 3.8: The bisector velocity span of WASP-127 as a function of the relative radial velocity. CORALIE data before and after the instrumental upgrade is represented by red circles and blue triangles, respectively. SOPHIE data is denoted by open black squares. The line of best-fit is shown in grey and no correlation is found.

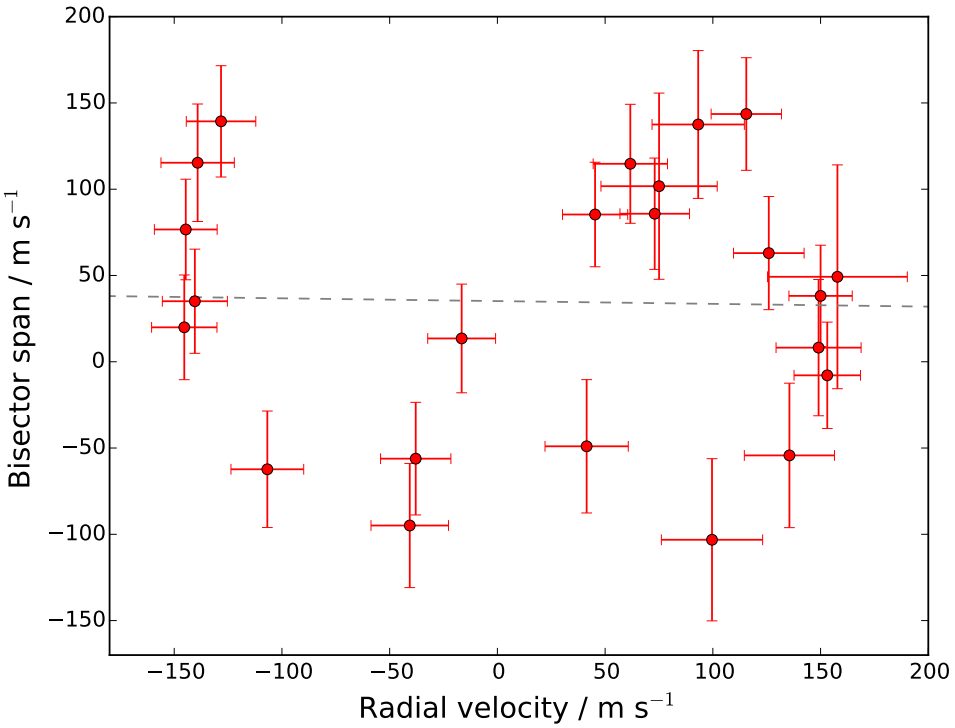

Figure 3.9: The bisector velocity span of WASP-136 as a function of the relative radial velocity. The line of best-fit is shown in grey and no correlation is found.

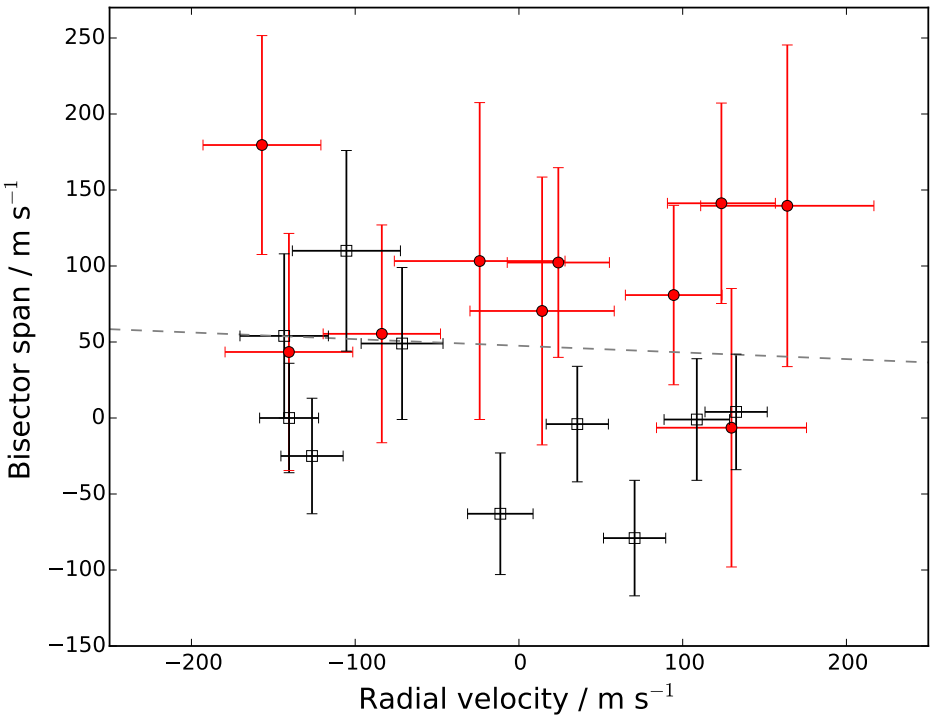

Figure 3.10: The bisector velocity span of WASP-138 as a function of the relative radial velocity. CORALIE data is denoted by red circles and SOPHIE data is represented by open black squares. The line of best-fit is shown in grey and no correlation is found.

Table 3.3: Gaia observations of WASP-127, WASP-136 and WASP-138. The G-band line-of-sight extinction is denoted by Ag, and $E(B-V)$ is the reddening.

Parameters	WASP-127	WASP-136	WASP-138
G_{mag}	10.05	9.81	11.69
Parallax (mas)	6.24 ± 0.04	3.60 ± 0.06	2.39 ± 0.04
Distance (pc)	160 ± 1	278 ± 5	419 ± 8
μ_{ra} (mas yr^{-1})	19.22 ± 0.08	2.47 ± 0.09	11.25 ± 0.07
μ_{dec} (mas yr^{-1})	17.03 ± 0.07	9.65 ± 0.06	−34.46 ± 0.07
RV (km s^{-1})	−8.25 ± 0.89	11.64 ± 0.38	-
$T_{\rm eff}$ (K)	5858^{+134}_{-85}	6400^{+368}_{-96}	6139^{+371}_{-221}
Ag	$0.33^{+0.13}_{-0.06}$	-	$0.42^{+0.26}_{-0.19}$
E(BP−RP)	$0.16^{+0.05}_{-0.03}$	-	$0.19^{+0.14}_{-0.07}$
Rs ($R_\odot$)	$1.30^{+0.04}_{-0.06}$	-	$1.46^{+0.11}_{-0.16}$

3.2.3 Gaia astrometry

The precise astrometric solutions of WASP-127, WASP-136 and WASP-138 were measured by the recent *Gaia* Data Release 2 (DR2) (Gaia Collaboration et al., 2016b, 2018b; Lindegren et al., 2018). The parallaxes of WASP-127, WASP-136 and WASP-138 are 6.24 ± 0.04 mas, 3.60 ± 0.06 mas and 2.39 ± 0.04 mas, respectively. These correspond to distances of 160 ± 1 pc, 278 ± 5 pc and 419 ± 8 pc, respectively. The effective temperatures and stellar radius of the host stars were derived from the three Gaia photometric bands (Andrae et al., 2018). The results of the derivations are summarised in Table 3.3. The parameters derived from the Gaia observations are generally consistent with the results of the joint Bayesian analysis in Section 3.3.3. In Section 3.3.1, the distances of WASP-127, WASP-136 and WASP-138 were found to be 102 ± 12 pc, 164 ± 18 pc, and 308 ± 51 pc, respectively. These estimates are inconsistent with the distance measurements derived from Gaia parallax. The Gaia distance measurements show that WASP-127, WASP-136, WASP-138 are 58 ± 12 pc, 114 ± 19 pc, and 111 ± 52 pc further away than previously estimated. This is because the distance-modulus was used to estimate the host star distances in Section 3.3.1, and the reddening $E(B-V)$ was assumed to be 0. Hence the distances measured by Gaia are more reliable.

3.3 Results

3.3.1 Host Star Spectral Analysis

The CORALIE spectra of the individual host stars were co-added to generate spectra for analysis using the methods described in Doyle et al. (2013). The Hα line was used to estimated the effective temperature ($T_{\rm eff}$), and the pressure-sensitive lines, Na I D and Mg I b

lines, were used to measure the stellar surface gravity. Multiple clean and unblended Fe I lines were used to estimate the iron abundance of the star relative to the Solar value (Asplund et al., 2009). This was done by measuring the equivalent width of the Fe I lines. The error of the abundance was derived from the uncertainty in the atomic data measurements, and uncertainties in $T_{\rm eff}$ and $\log g$. The macroturbulent velocities (v_{mac}) of the stars were calculated using calibrations of Doyle et al. (2014). The v_{mac} of each star was then used to calculate their respective projected rotation velocities ($v \sin i$) by fitting the profiles of the Fe I lines after convolving with the CORALIE instrumental resolution (R = 55,000). A summary of the results can be found in Table 3.4.

Table 3.4: Stellar parameters of WASP-127, WASP-136 and WASP-138 derived from spectral analysis in Section 3.3.1.

Parameter	WASP-127	WASP-136	WASP-138
$T_{\rm eff}$ (K)	5750 ± 100	6250 ± 100	6300 ± 100
log g	3.9 ± 0.1	3.9 ± 0.1	4.1 ± 0.1
$v \sin i$ (km s^{-1})	0.3 ± 0.2	13.1 ± 0.8	7.7 ± 1.1
[Fe/H]	−0.18 ± 0.06	−0.18 ± 0.10	−0.09 ± 0.10
log A(Li)	1.97 ± 0.09	2.50 ± 0.08	2.20 ± 0.08
Mass ($M_\odot$)	1.31 ± 0.05	1.38 ± 0.08	1.20 ± 0.03
Radius ($R_\odot$)	1.33 ± 0.03	2.07 ± 0.24	1.43 ± 0.02
Sp. Type	G5	F5	F9
Distance (pc)	102 ± 12	164 ± 18	308 ± 51

3.3.2 Host Star Age Estimates

The masses and ages of the three host stars were derived using the open source `BAGEMASS`[1] code (Maxted et al., 2015a), and the method is summarised as follow. For each star, a stellar model grid was generated from the `GARSTEC` stellar evolution code (Weiss and Schlattl, 2008) where a mixing length parameter α_{MLT} = 1.78 was assumed to calculate the grid. A Bayesian method was applied to derive the stellar mass and age, where the effective temperature $T_{\rm eff}$, stellar metallicity [Fe/H], observed stellar luminosity L_s, and stellar density ρ_s, were used as input parameters to calculate the probability distribution functions of a stars mass and age. $T_{\rm eff}$ and [Fe/H] were obtained from spectral analysis in section 3.3.1. Since this work was prepared prior to the Gaia data release, there were no accurately measured trigonometric parallax for WASP-127, WASP-136 and WASP-138. Hence the input stellar luminosity was set as $\log(L_s/L_\odot) = 0 \pm 5$ to minimise the influence of this term has on the results. The stellar density ρ_s of a planet host can be derived from the corresponding transit lightcurve using Equ. 1.8 for a known eccentricity. The results of the analysis are shown

[1] https://sourceforge.net/projects/bagemass/

in Table 3.5. Figure 3.11 shows the probability distributions of each system and the best-fit evolutionary tracks.

The isochrone age of WASP-127 is 11.4 Gyr. Its rotational velocity derived from the CORALIE spectra is too low for an age estimate from gyrochronology. However, an old star is expected to be slowly rotating. The F-type star WASP-136 has an isochronal age ($\tau_{\rm iso}$) of 3.62 ± 0.70 Gyr, and a surface gravity estimated as $\log g = 3.9 \pm 0.1$. This suggests that the star could be a subgiant that is evolving off the main-sequence. The isochronal age of WASP-138 is 3.44 ± 0.93 Gyr. In gyrochronology, the surface rotation rate of a star is used to estimate the stellar age. Barnes (2007, 2010) developed an analytical function which uses the rotation periods and colours of a star to derive its age:

$$\tau_{gyro} = \frac{\tau}{k_c} \ln\left(\frac{P}{P_0}\right) + \frac{k_I}{2\tau}(P^2 - P_0^2) \tag{3.1}$$

where τ_{gyro} is the gyrochronological age measured in Myr. τ is the convection turnover time which is taken from Barnes and Kim (2010), and the constants $k_c = 0.646$ d Myr^{-1} and $k_I = 452$ d Myr^{-1}. P is the rotation period in days, $P_0 \approx 1.1$ d is the rotation period on the zero age main sequence (ZAMS). The $\tau_{\rm gyro}$ of WASP-136 and WASP-138 were calculated as $1.3^{+1.2}_{-0.6}$ Gyr and $2.7^{+2.5}_{-1.3}$ Gyr respectively. The $v \sin i$ value of WASP-127 is too low for a sensible estimate. Note that the $v \sin i$ values derived from spectral analyses can only provide upper limits on the rotation rates of the stars. The $\tau_{\rm gyro}$ of WASP-136 and WASP-138 are therefore lower limits only. The $\tau_{\rm iso}$ of WASP-136 and WASP-138 do not agree with their respective $\tau_{\rm gyro}$. This discrepancy could be attributed to tidal interactions between the stars and the planets. Gyrochronology derives a star's age from its rotation period, but the current models do not adequately describe the relation between the stellar rotation rate and age of intermediate-age and older stars. For older stars, their rotation rates could have been spun up by the tidal forces of the planets, so they could disguise as young stars (Maxted et al., 2015b; van Saders et al., 2016). This means that gyrochronology is a less suitable way to estimate the stellar ages in the case of WASP-136 and WASP-138. Rotational modulation in a lightcurve could provide information on the stellar activity but, as mentioned in Section 3.1, no significant modulations were found, implying that the stars are inactive. This is a characteristic of an old field star. Consequently, the isochronal ages of the stars are adopted.

3.3.3 MCMC Analysis

The MCMC method describe in Chapter 2 was used to derive the physical parameters of each system. The lightcurves and RV measurements were analysed simultaneously following Collier Cameron et al. (2007) and Pollacco et al. (2008). In short, the analytical func-

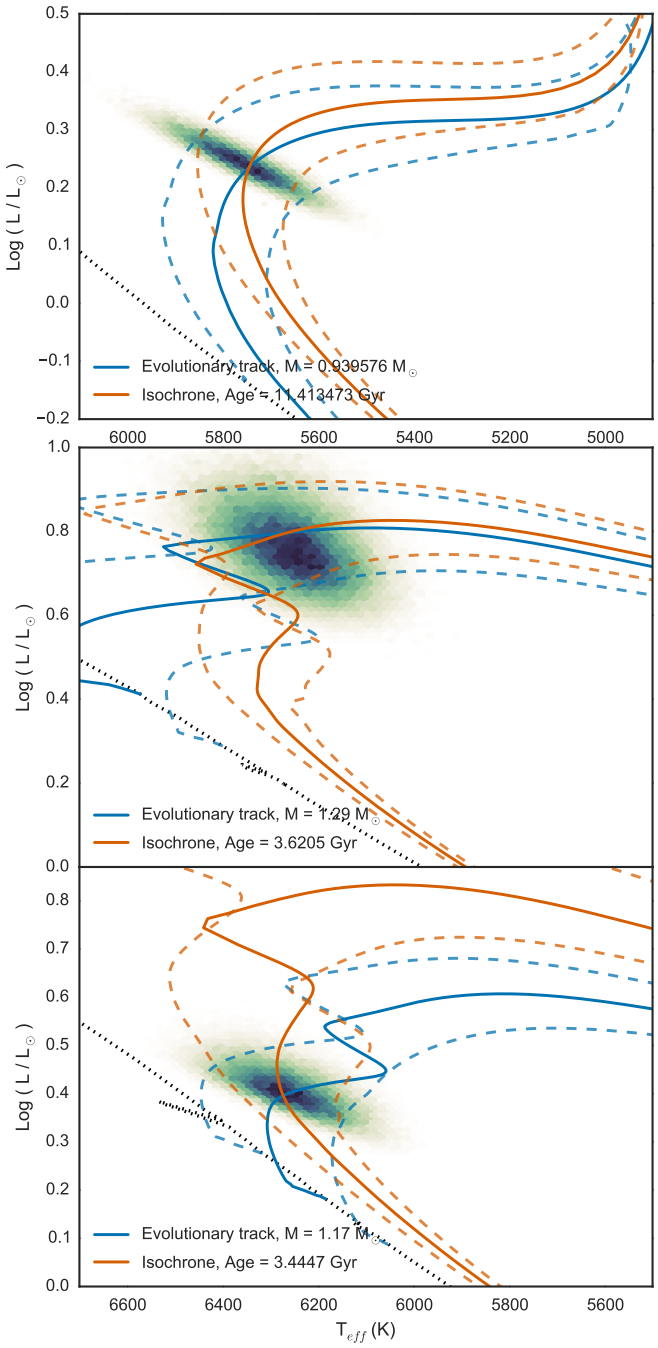

Figure 3.11: The posterior distribution of the stellar masses and ages of WASP-127 (upper panel), WASP-136 (middle panel) and WASP-138 (lower panel). The Zero Age Main Sequence (ZAMS) is plotted as a dotted black line. The solid blue lines denote the evolution tracks of the stars and the blue dashed tracks on either side are the 1-σ error on the mass. The stellar age isochrone is plotted as solid orange lines, and the orange dashed lines represents the 1-σ error.

Table 3.5: Stellar mass and age estimates of WASP-127, WASP-136 and WASP-138. The first column presents the isochronal ages, second column shows the gyrochronological ages.

Star	Mass [$M_\odot$]	$\tau_{\rm iso}$ [Gyr]	$\tau_{\rm gyro}$ [Gyr]
WASP-127	0.93 ± 0.04	11.41 ± 1.80	$v \sin i$ too low
WASP-136	1.29 ± 0.08	3.62 ± 0.70	$> 1.3^{+1.2}_{-0.6}$
WASP-138	1.17 ± 0.06	3.44 ± 0.93	$> 2.7^{+2.5}_{-1.3}$

tions of Mandel and Agol (2002) were used to model the transit lightcurves. The stellar limb darkening effect was accounted for using the non-linear limb darkening law developed by Claret (2000, 2004). The parameters used in the MCMC algorithm were: the mid-transit epoch T_0; the period P; the planet to stellar size ratio (a proxy for the transit depth) ΔF; the transit duration T_{14}; the impact parameter b; the stellar metallicity [Fe/H], the stellar effective temperature T_{eff}; the stellar reflex velocity K, and the Lagrangian elements $\sqrt{e}\cos(\omega)$ and $\sqrt{e}\sin(\omega)$ (where e is the eccentricity and ω is the longitude of periastron) which were used to define the star's RV orbit, and the system's centre-of-mass velocity γ. The median of the posterior distribution and the 1-σ uncertainties were adopted as the final solution. The MCMC solutions of each system are presented in Table 3.6 and 3.7. The phase-folded best-fit RVs and lightcurves are shown in Figures 3.4, 3.5, 3.6, 3.7 and Figures 3.1, 3.2, 3.3 respectively.

WASP-127: A main-sequence mass-radius constraint was initially placed on the MCMC analysis of WASP-127. The solution gave unrealistic posterior stellar parameters which disagreed with those derived from spectral analysis in Section 3.3.1. Hence the main-sequence constraint was relaxed in the final MCMC analysis.

(Lucy and Sweeney, 1971) argued that majority of spectroscopic binaries with derived small eccentricities ($e \leq 0.05$) are consequences of observational errors. They devised the Lucy & Sweeney F-test (LS test) to determine the statistical significance of small eccentricities in binaries. In essence, the LS test tests the hypothesis that the orbital eccentricity is zero. If the hypothesis is rejected at the 5% significance level, the non-zero eccentricity is regarded as significant. On the other hand, if the hypothesis is not rejected, a circular orbit (i.e. $e = 0$) is adopted.

The criterion deciding whether a circular orbit is rejected is based on results of the least-squares analysis and the F-distribution:

$$F = \frac{N - M}{2} \cdot \frac{\chi^2_{circ} - \chi^2_{ecc}}{\chi^2_{ecc}} \tag{3.2}$$

where N and M are the number of observations and number of elements for the elliptical orbit, respectively. χ^2_{circ} and χ^2_{ecc} are the weighted least-squares residuals. If the hypothesis

of a circular orbit is correct, then F is distributed as F_{ν_1,ν_2} where $\nu_1 = 2$ and $\nu_2 = N - M$. The probability density function of F is:

$$\phi(F) = \left(1 + \frac{F}{\beta}\right)^{-(1+\beta)} \tag{3.3}$$

where $\beta = 1/2\ (N - M)$. Assuming a circular orbit and $F = \hat{F}$, the probability of F could have exceeded $\hat{F}$ is

$$p = \int_{\hat{F}}^{\infty} \phi(F)dF = \left(1 + \frac{F}{\beta}\right)^{-\beta} \tag{3.4}$$

Following the 5% significance level as described above, the criterion used to decide the significance of a non-zero eccentricity is

$$e = \begin{cases} \hat{e}, & \text{if } p < 0.05, \\ 0, & \text{if } p \geq 0.05. \end{cases} \tag{3.5}$$

The MCMC solution for WASP-127 does not provide convincing evidence for an eccentric orbit ($\chi^2_{circ} = 37.2 \pm 8.6$ and $\chi^2_{ecc} = 37.3 \pm 8.6$). The LS test gave $p = 1.0$, thus a circular orbit is adopted.

As seen in Figure 3.5, measurements from both CORALIE and SOPHIE appear to be dispersed from the best-fit Keplerian model. The FWHM of WASP-127 spectra changed during one of the observing seasons. This could be explained by the change in the magnetic activity of the star, which could contribute to the observed scatter around the fit. However, there is no evidence in the bisector analysis (see Figure 3.8) that the V_{span} is correlated to the RV measurements. An in-phase variation is observed with the CORALIE data nonetheless. We performed joint MCMC analysis for two cases where: (1) all RV data was included, and; (2) only CORALIE RV data was included. In case (1), the preliminary analysis resulted in a best-fit solution with the planet's mass being 0.13 ± 0.02 M_J and the planet's radius 1.41 ± 0.05 R_J. The reduced chi-square statistics (χ^2_{reduced}) were used to check for the goodness-of-fit, and the χ^2_{reduced} was evaluated as 1.31 ± 0.25 for case (1). The reduced chi-square statistics of case (2) suggests that the RV variation without SOPHIE RV data is better described by a Keplerian orbit. The mass of WASP-127 b is small, thus the RV variation is in the order of a few m $s^{-}1$ which exceeds the sensitivity of both SOPHIE and CORALIE. Hence stability of the instrument could affect the RV measurements. In addition, there could be a third stellar body in the system which could offset the RV variation of the star. However, there is no evidence that such a star is bound to the system. It is unclear why SOPHIE error bars were underestimated, and that the instrument did not reach the sensitivity required to detect RV signals from WASP-127 when the RV variation is clearly manifested in the CORALIE data. We reduced the weighting of the SOPHIE RVs to improve the Keplerian

fit by inflating the error bars of SOPHIE RVs by a multiplication factor of 2. The resulting fit was improved with a $\chi^2_{\rm reduced}$ value of 0.91 ± 0.21.

In the CORALIE-only case, a best-fit RV amplitude of 21.4 ± 2.8 m s^{-1} was found, corresponding to a minimum mass of 0.18 ± 0.02M$_{\rm J}$ (Figure 3.4). In the case where CORALIE and SOPHIE (with inflated error bars) RV measurements were used in the MCMC analysis, the best-fit RV amplitude was 18.7 ± 2.7 m s^{-1}, which corresponds to a minimum mass of 0.16 ± 0.02M$_{\rm J}$ (Figure 3.5). The RV amplitude from both solutions agree within 1-σ uncertainty. The full sets of solutions from both analyses are shown in Table 3.6. WASP-127 has a RV semi-amplitude of around 20 m s^{-1}. RV measurements with precisions better than a few m s^{-1} are required to characterise lower mass objects to the same fractional precision in mass. The instruments used to measure the RV variations have achieved a precision of 5 m s^{-1} at best. Therefore, the dispersion of the RV residuals is attributed to the stability of spectrographs.

WASP-136: Isochrone fitting suggested that WASP-136 is a evolving star, therefore the main-sequence constraint was relaxed in the analysis. The χ^2 statistics was used to determine the goodness-of-fit of the model. There was no significant evidence that supports an eccentric orbit for this system (χ^2_{circ} = 46.6 ± 9.7 and χ^2_{ecc} = 43.5 ± 9.3). The LS test showed p = 0.55, hence the non-zero eccentricity is not significant and a circular orbit was adopted in the final analysis.

WASP-138: No main-sequence constraint was placed in the analysis, and the statistics of the solution found no evidence for an eccentric orbit (χ^2_{circ} = 11.2 ± 4.7 and χ^2_{ecc} = 10.4 ± 4.6). The LS test gives p = 1.0. Therefore, the non-zero eccentricity is insignificant and a circular orbit was adopted for WASP-138 b.

3.4 Discussion and Conclusion

3.4.1 WASP-127 b

WASP-127 b has a mass of 0.18 ± 0.02 M$_{\rm J}$ and a radius of 1.37 ± 0.04 R$_{\rm J}$ (M$_{\rm pl}$ = 0.16 ± 0.02 M$_{\rm J}$ and R$_{\rm pl}$ = 1.41 ± 0.06 R$_{\rm J}$ in the case where RVs from both CORALIE and SOPHIE were included for analysis). This translates to a bulk density of $0.07^{+0.01}_{-0.01}$ ρ_J, hence WASP-127 b is one of the least dense planets ever discovered. At the time these results were published, it was also the second lightest planet found by the WASP survey (the only lighter planet was WASP-139 b (Hellier et al., 2017)).

Comparing to standard coreless models from Fortney et al. (2007), WASP-127 b is found to have a radius over 30% larger then predicted. Some inflation mechanism must be in place to give WASP-127 b an anomalously large radius. WASP-127 b has a small orbital separation of 0.052 AU, and could be subjected to strong irradiation, so the inflation could

Table 3.6: MCMC solutions of WASP-127. The first column shows values derived with SOPHIE RV measurements. The values in the second column are derived using both CORALIE and SOPHIE RVs in the analysis. The final RV fits of the two solutions agree within 1-σ uncertainty.

Parameter (Unit)	Solution without SOPHIE	Solution with SOPHIE
P (d)	4.178062 ± 0.000002	4.178062 ± 0.000002
T_0 (BJD)	$2457248.74131 \pm 0.000160$	$2457248.74126 \pm 0.000184$
$\Delta F = R_{pl}^2/R_*^2$	0.01037 ± 0.00015	0.01050 ± 0.00017
T_{14} (d)	0.1795 ± 0.0007	0.1802 ± 0.0009
b	$0.15^{+0.09}_{-0.11}$	$0.25^{+0.08}_{-0.16}$
i (°)	$88.7^{+0.8}_{-0.6}$	$88.1^{+1.2}_{-0.7}$
$M_*(M_\odot)$	1.08 ± 0.03	1.08 ± 0.03
$R_*(R_\odot)$	1.39 ± 0.03	1.42 ± 0.05
$\log g_*$ (cgs)	4.18 ± 0.01	$4.17 \pm 0.0.02$
$\rho_*(\rho_\odot)$	0.404 ± 0.015	0.380 ± 0.031
$T_{\rm eff}$ (K)	5620 ± 85	5639 ± 90
$M_{pl}(M_J)$	0.18 ± 0.02	0.16 ± 0.02
$R_{pl}(R_J)$	1.37 ± 0.04	1.41 ± 0.06
$\log g_{\rm pl}$ (cgs)	2.33 ± 0.06	2.25 ± 0.7
$\rho_{pl}(\rho_J)$	$0.068^{+0.010}_{-0.010}$	$0.055^{+0.011}_{-0.009}$
a (au)	0.0520 ± 0.0005	0.0522 ± 0.0005
$T_{\rm pl,A=0}$ (K)	1400 ± 24	1417 ± 32

Table 3.7: System parameters of WASP-136 and WASP-138 from MCMC analysis.

Parameter (Unit)	WASP-136b	WASP-138b
P (d)	5.215357 ± 0.000006	3.634433 ± 0.000005
T_0 (BJD)	$2456776.90615 \pm 0.00109$	$2457326.62183 \pm 0.000319$
$\Delta F = R_{pl}^2/R_*^2$	0.00411 ± 0.00015	0.00683 ± 0.00013
T_{14} (d)	0.2272 ± 0.0033	0.1572 ± 0.0012
b	$0.59^{+0.08}_{-0.14}$	$0.19^{+0.12}_{-0.15}$
i (°)	$84.7^{+1.6}_{-1.3}$	$88.5^{+0.9}_{-1.2}$
$M_*(M_\odot)$	1.41 ± 0.07	1.22 ± 0.05
$R_*(R_\odot)$	2.21 ± 0.22	1.36 ± 0.05
$\log g_*$ (cgs)	3.90 ± 0.06	4.25 ± 0.02
$\rho_*(\rho_\odot)$	0.132 ± 0.030	0.488 ± 0.044
$T_{\rm eff}$ (K)	6260 ± 100	6272 ± 96
$M_{pl}(M_J)$	1.51 ± 0.08	1.22 ± 0.08
$R_{pl}(R_J)$	1.38 ± 0.16	1.09 ± 0.05
$\log g_{\rm pl}$ (cgs)	3.26 ± 0.09	3.36 ± 0.04
$\rho_{pl}(\rho_J)$	$0.581^{+0.230}_{-0.148}$	$0.92^{+0.097}_{-0.146}$
a (AU)	0.0661 ± 0.0012	0.0494 ± 0.0007
$T_{\rm pl,A=0}$ (K)	1742 ± 82	1590 ± 31

be caused by energy from the star being deposited in the planet's atmosphere (Weiss et al., 2013).

Another possible inflation mechanism is tidal heating (Bodenheimer et al., 2001, 2003). Short period giant planets could have formed at wider eccentric orbits via planet-planet scattering (Ford and Rasio, 2008) or the Kozai-Lidov mechanism (Kozai, 1962; Lidov, 1962; Fabrycky and Tremaine, 2007). The planet's orbital energy would dissipate as tidal heat in the interior of the planet, which drives the planet migration inwards and circularises the orbit (Wu and Lithwick, 2011). During this process, tidal heating could inflate the planet. While the anomalously large radius of WASP-127 b may have been caused by external heating mechanisms, enhanced opacity of the planet's atmosphere could also lead to a similar result (Burrows et al., 2007). If the atmosphere of WASP-127 b has enhanced metallicity, it could retain the planet's internal heat and delay the cooling effect during formation. Thus the planet would remain inflated for a longer period of time.

Batygin et al. (2011) argued that the Ohmic heating mechanism could lead to an increased planetary radius. Close-in planets tend to have higher effective temperatures, such that alkali metals in the atmosphere could be ionised, which induces electrical conductivity. When these ions interact with the planet's magnetic field, an electromotive force is developed. This can in turn heat up the interior and the atmosphere of the planet. The efficiency of the Ohmic heating mechanism relies heavily on the depth of the dissipation (Huang and Cumming, 2012). The boundary of the convective zone would move deeper towards the planet interior if Ohmic dissipation occurs between the atmosphere and the convective boundary. This can reduce the planet cooling time and Ohmic heating would become inefficient.

Planets could re-inflate if their host stars enter the red giant branch (RGB) (Lopez and Fortney, 2016). Evolving stars have increased luminosities, hence higher irradiation. This could deposit heat in the planet and expand its atmosphere again. This process is also more likely to occur for less massive planets with short periods (Lopez and Fortney, 2016). WASP-127 has an estimated main-sequence lifetime of $t_{MS} = t_{\odot}(M_s/M_{\odot})^{-2.5} \approx 8$ Gyr, where $t_{\odot}$ is the solar main-sequence lifetime, $M_{\odot}$ is the Solar mass and M_s is the stellar mass. The age of WASP-127 is 11.41 ± 1.80 Gyr, which means the star is evolving off the main sequence. Consequently, WASP-127 b may be re-inflating as its host star evolves into a subgiant.

WASP-127 b shares similar characteristics with a number of low density planets, e.g. WASP-39b (Faedi et al., 2011), HAT-P-8b (Bayliss et al., 2015), HAT-P-11b (Bakos et al., 2010), HAT-P-47b and HAT-P-48b (Bakos et al., 2016). If the atmosphere of WASP-127 b is assumed to be similar to that of Jupiter's ($\mu = 2.2$u, where the atomic mass unit is u $= 1.66 \times 10^{-27}$ kg), it would have an atmospheric scale height of $H \approx 2500 \pm 400$

km. WASP-127 is a bright G-type star with V_{mag} = 10.172. The combination of large scale height and brightness makes the system an exceptional target for atmospheric studies. In fact, follow up transmission spectroscopy by Palle et al. (2017) revealed that the planet atmosphere is likely cloud-free, and hints of Na, TiO and VO absorptions were also found.

Mazeh et al. (2005) studied properties of transiting giant planets to find that planet masses are negatively correlated to the orbital distance. With an increasing number of smaller planets being discovered, further studies showed a paucity of Neptune-mass planets at short orbital periods (e.g. Szabó and Kiss 2011). Mazeh et al. (2016) used a more up-to-date sample of transiting planets to study the location and shape of the 'Neptune desert'. They found clear upper and lower boundaries in both the period-mass and period-radius planes.

Kurokawa and Nakamoto (2014) performed numerical simulations to determine the mass loss and thermal evolution of planets. They showed that planetary atmospheres are thermally evaporated as they are exposed to X-ray and extreme ultraviolet (XUV) radiation (Jackson et al., 2012). The atmospheric escape induces Roche lobe overflow which leads to further evaporation (Kurokawa and Kaltenegger, 2013). The results of Kurokawa and Nakamoto (2014) suggests that more massive planets remain substantially intact, whereas less massive planets would be completely evaporated and leave behind a naked core. Furthermore, final planet sizes show a strong dependence on their core masses and only weakly influenced by migration processes.

Figure 3.12 plots the planet masses as a function of their orbital periods. Clearly, WASP-127 b sits inside the short-period Neptune desert (Mazeh et al., 2016) which divides the hot Jupiter and super-Earth populations. Kurokawa and Nakamoto (2014) proposed that interplanetary interactions can induce migration of sub-Jovian planets after ~0.1 - 1.0 Gyr. XUV radiation decays after this time hence these planets receive less radiation and atmospheric escape is not as effective. WASP-127 b could have retained its atmosphere because it did not receive intense stellar radiation during its youth.

3.4.2 WASP-136 b

WASP-136 b is an inflated hot Jupiter which orbits a bright (V_{mag} = 9.928) F5 star with a period of 5.21 days. The planet has a mass of 1.51 ± 0.08 M_J and a radius of 1.38 ± 0.16 R_J. This corresponds to a density of $0.58^{+0.23}_{-0.15}$ ρ_J. WASP-136 is estimated to have a main-sequence lifetime of $t_{MS} \approx 4$ Gyr. The adopted age for WASP-136 is 3.6 ± 0.7 Gyr (derived in 3.3.1), implying the star is at the end of its main-sequence lifetime. The density and surface gravity of WASP-136 is comparable to a subgiant, which is also consistent with the age analysis. Using the planet evolution model of Fortney et al. (2007), the observed radius of WASP-136 is found to be 25% larger than the theoretical prediction. As with

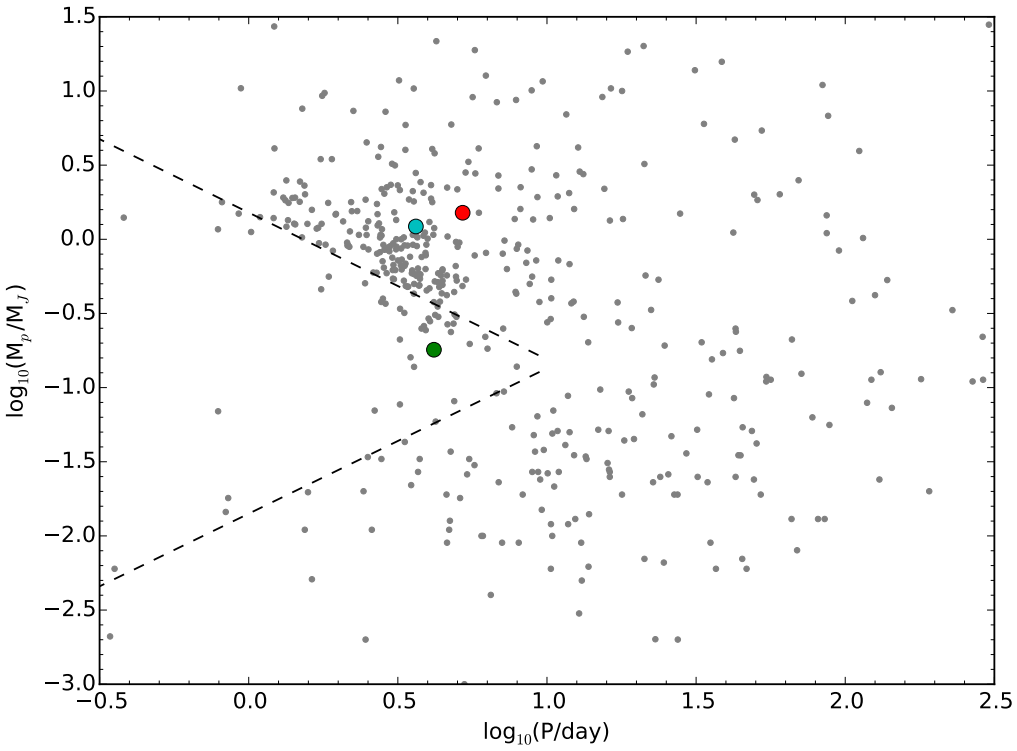

Figure 3.12: Plot of planet mass against orbital period (Data obtained from NASA Exoplanet Archive (`http://exoplanetarchive.ipac.caltech.edu/`). Grey dots are known exoplanets as of July 2016. WASP-127b, WASP-136b and WASP-138b are plotted as green, red and cyan circles respectively. The upper and lower boundaries of the Neptune desert are plotted in black dashed lines, using analytical functions of Mazeh et al. (2016). The inflated Neptune-mass planet WASP-127 b is located inside the Neptune desert which divides the Jovian and super-Earth populations.

many inflated hot Jupiters (e.g. WASP-54b: Faedi et al. 2013; WASP-78b and WASP-79b: Smalley et al. 2012), this planet is exposed to strong irradiation from its F-type host star, which could lead to inflation of the planetary radius.

The spectral analysis and age estimate of WASP-136 reveal that the star is old and is evolving off the main-sequence. As WASP-136 enters the subgiant branch, its luminosity is increasing. Consequently, WASP-136 b could be receiving an increased amount of stellar irradiation as it evolves. This excess heat is deposited in the planet's interior, which could result in the re-inflation of the planetary radius. This is the class I inflation model of Lopez and Fortney (2016).

It is uncommon to find hot Jupiters around subgiant stars; tidal disruption could be the mechanism responsible for this (Schlaufman and Winn, 2013). In a star-planet system, tide is raised on the planet by the star. The force exerted on the side of the planet facing the star is stronger than the force exerted on the side facing away from the star. The differential gravitational force which is known as tidal force. This force leads to tidal bulges which can distort the planetary body. Tidal interaction between two bodies allow the exchange of angular momentum. In a system where the planet sits inside the co-rotation radius (i.e. when the planets orbital period is shorter than its rotation period), tidal bulge raised on the planet by the star lags behind the star. This results in the deceleration of the planets orbit which leads to orbital decay (Rasio et al., 1996; Jackson et al., 2008). The planet then spirals inwards and eventually crosses the Roche limit (a critical distance where tidal force on the planet overcomes the gravitational force which holds the material of the planet) where the planet would be tidally destroyed.

The radius of the host star increases as it evolves off the main sequence. WASP-136 could move from a stable orbit to within the co-rotation radius, resulting in orbital decay. WASP-136 b is observed to orbit the star at an orbital separation of 0.0661AU, which is equivalent to $\sim$ 46 times the Roche limit. Brown et al. (2011) showed the remaining lifetime τ_{remain} of a planet can be expressed as

$$\tau_{remain} = \frac{2Q'_s}{117n}\frac{M_s}{M_p}\left(\frac{a}{R_s}\right)^5 \tag{3.6}$$

where Q'_s is the tidal quality factor of the star, $n = \sqrt{G(M_s + M_p)/a^3}$ is the orbital frequency of the planet. Assuming $Q'_s = 10^6$ for the case of WASP-136, the estimated time before WASP-136 b spirals towards the star is $\sim$ 0.420 Gyr. In addition, the radius of WASP-136 b would expand as it enters the post main-sequence phase, which can lead to the engulfment of the planet (Villaver and Livio, 2009).

3.4.3 WASP-138 b

WASP-138 b is found to have a mass of 1.22 ± 0.08 M_J and a radius of 1.09 ± 0.05 R_J, giving a density of $0.92^{+0.10}_{-0.15}\,\rho_J$. The planet orbits a slightly metal-poor F9 star which has a metallicity of [Fe/H] = −0.09 dex. Fortney et al. (2007) incorporated the effect of stellar irradiation and planet core masses in their model to computed accurate radii of planets over a wide range of masses and mixed compositions. They assumed that planets are made up of an inert core, an adiabatic convective envelope, and a model atmosphere. The presence of heavy elements in the planet's core or its convective envelope controls the cooling and contraction of the interior (Hubbard, 1977). Planets with more heavy elements have smaller radii. By comparing the observed planet radius, age and incident flux to the planet evolution model, one can determine the amount of heavy element present in the core or the convective envelope. In general, Fortney et al. (2007) found that planets with larger core have small radii, planets with smaller orbital separation have larger radii than planets at larger distances due to stellar irradiation. At an isochronal age of 3.4 ± 0.9 Gyr and orbital separation of 0.0494 ± 0.0007 AU, WASP-138 b is expected to have a core mass of $\sim$ 10 $M_\oplus$ of heavy elements (derived from Fortney et al. 2007).

Hot Jupiters were thought to be rare around metal-poor stars (Fischer and Valenti, 2005). The theoretical study by Mordasini et al. (2012) suggested that the core of hot Jupiters around metal-poor star is likely to have formed in a gas rich disc, and beyond the ice line.

3.4.4 Conclusion

This chapter has presented the discovery of three exoplanets from the SuperWASP survey. WASP-127 b is one of the least dense planets ever known, with an enormous atmospheric scale height of $\approx 2500 \pm 400$ km. The planet could serve as an exceptional target for detailed atmospheric studies using JWST in the future. Meanwhile, WASP-136 b adds to the small sample of exoplanets orbiting evolved host stars which can be used to test the evolution of planets around subgiants. The detection of WASP-138 b around a slightly metal-poor host weakens the correlation between host star metallicity and hot Jupiter occurrence. Theoretical study proposed that hot Jupiters around metal-poor stars can be formed in a gas rich disc.

Ground-based transit surveys provide a large number of unique exoplanets around bright stars. Detailed follow up observations and analysis of gas giants showed that the planet population have a wide range of radii, hence bulk densities. The variety of exoplanets found can also improve our understanding on the mass-radius relations of different planet

populations. As demonstrated in this chapter, the formation and evolution paths of the planets may be constrained from their inferred densities. The presence of the Neptune desert implies that the two distinct planet population - hot Jupiters and super-Earths, have different formation histories. In the following chapter, the characteristics of a super-Earth will be explored.

Chapter 4

EPIC 206011496 b: A Transiting Rocky Super-Earth

The space-based transit survey - *Kepler* mission (Borucki et al., 2010, 2011; Koch et al., 2010), has discovered over 2,000 confirmed planets and a further 2,000 candidates. This sample of planets revealed that by far the most common type of planets in our Galaxy are small planets with $R_p < 4.0\ R_\oplus$ (Howard et al., 2012; Batalha et al., 2013; Dressing and Charbonneau, 2013; Petigura et al., 2013). However, many planet candidates in the Kepler sample are faint, which make follow up observations difficult. Only dozens of Kepler planets have precisely determined masses so far. *K2* is the extension of the *Kepler* transit survey which targets brighter stars. TO date, the mission yielded over 300 confirmed planets (e.g. Montet et al. 2015; Barros et al. 2015; Crossfield et al. 2016).

In our Solar System, no Super-Earths are known. It is therefore interesting to determine the underlying mechanisms that are responsible for their formation and evolution, and find out how that may be different from the Solar System. However, to determine the origins of small planets, accurate masses and radii are necessary to infer their bulk densities, hence internal compositions. In this chapter, the detection and analysis of a transiting super-Earth EPIC 206011496 b is presented. Part of the analysis in this work were performed by a wider collaboration, including follow up observations (RV and direct imaging), stellar spectral analysis, and joint RV and lightcurve analysis. I have contributed to the planet detection, follow up observations (RV), stellar rotation analysis using the auto-correlation function, age estimates, planet internal composition analysis, and leading the publication of this work.

4.1 Candidate Detection - K2 Photometry

K2 is an extension to the *Kepler* space mission. It is a multi-field, ecliptic-pointed mission which targets approximately 10,000 targets per field (Howell et al., 2014). To minimise the drifting motion of the spacecraft due to the loss of its two reaction wheels, it needs to fire thrusters to offset the solar radiation pressure every 6 hours. The pointing stability of the spacecraft is compromised due to this motion, which resulted in the drifting of targets across the detector pixels and hence a 6h dominate systematic in the *K2* photometry.

EPIC 206011496 was observed during *K2* Campaign 3 in long cadence mode. The photometry was obtained between November 2014 and January 2015. The target was independently flagged as a candidate from two transit searches. The *K2* raw pixel data was reduced using the adapted CoRoT alarm pipeline (Barros et al., 2016). A second reduction pipeline was used following methods of Armstrong et al. (2015a) and Armstrong et al. (2015b), along with human input (eyeballing individual lightcurves) to eliminate false positives, and identify high priority candidates (Armstrong et al., 2015a,b). This target was also independently identified as a candidate by other search algorithms (Vanderburg et al., 2016; Crossfield et al., 2016; Mayo et al., 2018). The K2 lightcurve generated from the adapted CoRoT pipeline has less noise than that of Armstrong et al., hence the former was used for the planetary system analysis later. The adapted CoRoT reduction pipeline (Barros et al., 2016) is summarised as follows: The K2 pixel data was downloaded from the Mikulski Archive for Space Telescopes (MAST)[1]. The photometric data was extracted using the adapted CoRoT imagette pipeline. The optimal aperture size equivalent to the size of an imagette (i.e. 15×10 pixels) was chosen for the target, taking into account the signal-to-noise ratio (SNR) of the pixels before aperture photometry was performed. Furthermore, the Modified Moment Method developed by Stone (1989) was used to determine the centroid positions for systematic corrections. Flux and position variations of the star on the CCD can lead to systematics in the data. These were corrected following the self-flat-fielding methods of Vanderburg and Johnson (2014). Figure 4.1 shows the final extracted lightcurve, and Table 4.1 gives the photometric properties of EPIC 206011496.

4.2 Follow up Observations

4.2.1 Radial Velocity Follow Up - HARPS

Follow up RV measurements were obtained with the HARPS spectrograph (R$\sim 110,000$; Mayor et al. 2003. A total of 153 observations were obtained between 2016 October 29 and 2017 November 22. The data were reduced using the HARPS online pipeline which

[1] `http://archive.stsci.edu/kepler/data_search/search.php`

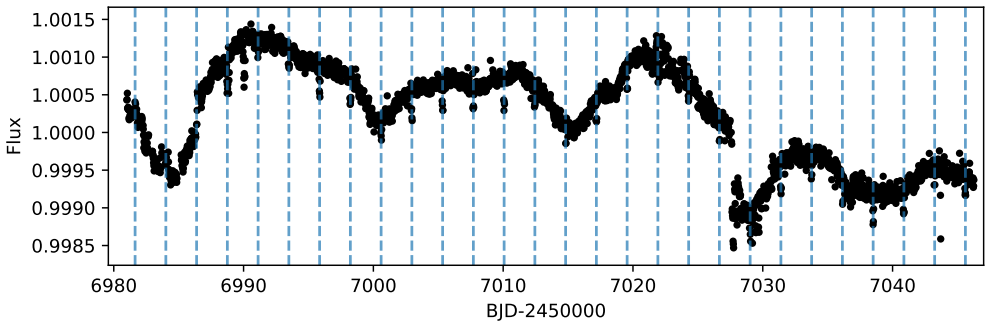

Figure 4.1: The detrended *K2* transit lightcurve of EPIC 206011496. Positions of transit signals are marked with blue dashed lines.

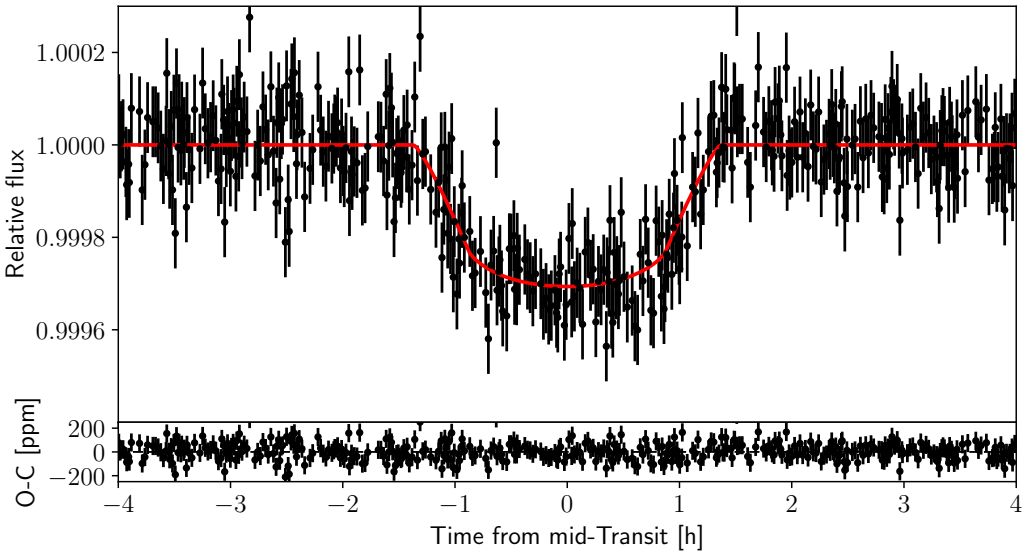

Figure 4.2: *Top panel*: Phase-folded *K2* lightcurve of EPIC 206011496 with the ephemeris from our analysis. The red solid line is the best-fit transit model. *Bottom panel*: Residuals as a function of orbital phase.

Table 4.1: Properties of EPIC 206011496. EPIC 206011496 has a nearby bound companion (see text for detailed description), hence values presented in this table are for the blended photometry. The photometric magnitudes listed were used in deriving the SED as described in Section 4.3.3.

Parameter	Value and uncertainty	Source
K2 campaign	3	a
EPIC	206011496	a
2MASS ID	2MASS J22480755−1429407	b
RA(J2000)	22:48:07.56	c
Dec(J2000)	−14:29:40.84	c
μ_{RA} (mas/yr)	30.20 ± 0.09	c
μ_{DEC} (mas/yr)	−23.34 ± 0.06	c
Parallax (mas)	7.18 ± 0.05	c
Photometric magnitudes		
Kp	10.92	a
Gaia G	10.928	c
Johnson B	11.845 ± 0.029	d
Johnson V	11.102 ± 0.037	d
Sloan g′	11.419 ± 0.042	d
Sloan r′	10.879 ± 0.047	d
Sloan i′	10.689 ± 0.084	d
2-MASS J	9.726 ± 0.026	b
2-MASS H	9.312 ± 0.022	b
2-MASS Ks	9.259 ± 0.027	b
WISE W1	9.178 ± 0.022	e
WISE W2	9.213 ± 0.020	e
WISE W3	9.162 ± 0.040	e

a. EXOFOP-K2: `https://exofop.ipac.caltech.edu/k2/`
b. Two Micron All Sky Survey (2MASS)
c. *Gaia* DR2
d. AAVSO Photometric All-Sky Survey (APASS)
e. AllWISE

follows similar procedures described in Chapter 2. Spectral analysis, which is described in a later section, revealed the target host is of spectral type G. The RV measurements were derived from the CCF using the weighted cross-correlation method with a G2V numerical template. The bisector velocity span (BIS), and the full width at half maximum (FWHM) were measured from the CCF profile. The RV measurements and their corresponding uncertainties are listed in Appendix Table A.2. The time-series RVs and the phase-folded RVs of EPIC 206011496 are shown in the top and bottom panels of Figure 4.3 respectively.

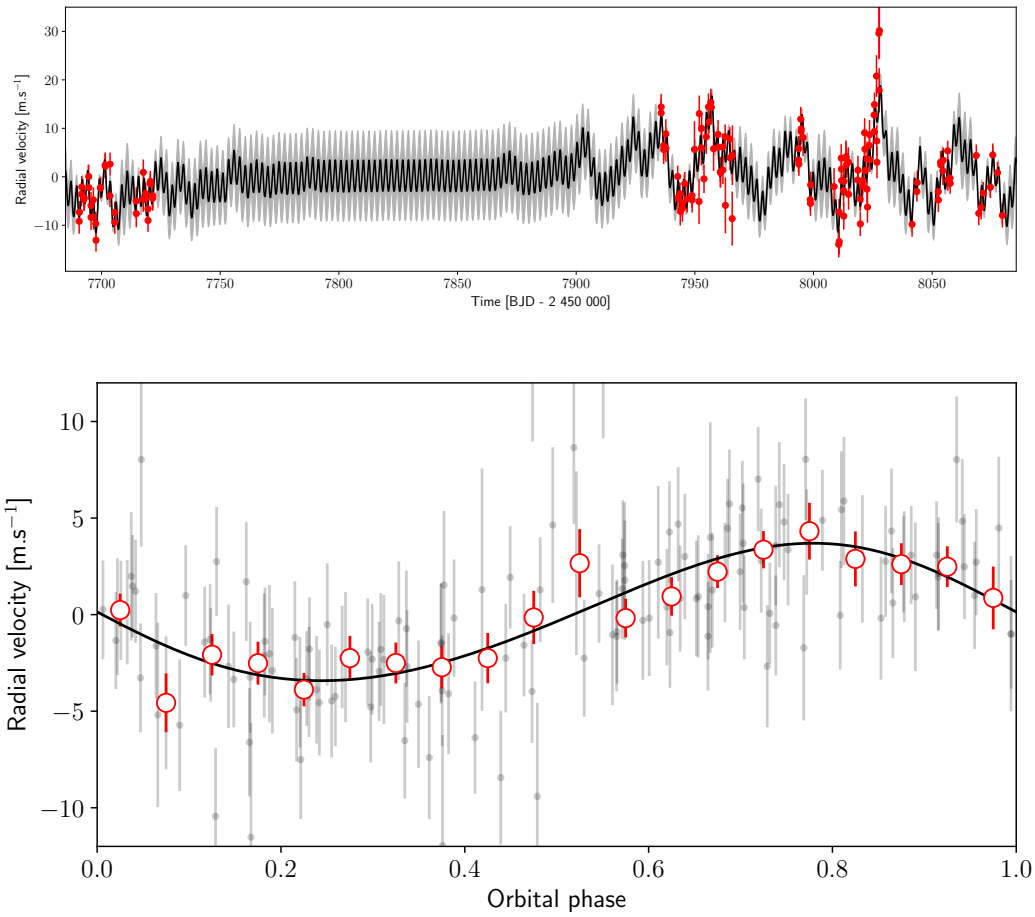

Figure 4.3: *Upper Panel*: Time-series HARPS RV measurements (red circles) of EPIC 206011496. The best-fit Keplerian orbit of EPIC 206011496 b is plotted in black. The stellar activity is fitted with a GP. The grey region show the 1σ confidence interval of the GP. *Lower Panel*: Phase-folded, stellar activity removed HARPS RV measurements (black circles) of EPIC 206011496 as a function of the orbital phase. The black solid line is the best-fit RV curve. The binned RV measurements are denoted as red open circles.

4.2.2 Direct Imaging Observations

Shallow imaging observations were obtained with the NIRC2 instrument at Keck on 2015 August 04 in the narrow-band Br_γ filter at 2.169 μm (Programme N151N2, PI: Ciardi). Multiple images were obtained with a dithering pattern on-sky. These were realigned and median-combined, and a candidate companion star (star B) was found. To determine the relative astrometry of the companion, a Gaussian fit was performed on both the star and the candidate. The estimated uncertainty of the measurement is ~0.5 pixel, i.e. ~5 mas. Following the methods of Vigan et al. (2016), a 2D Gaussian fit was used on the pre-reduced data to determine the relative Keck astrometry: $\Delta\alpha = -910 \pm 5$ mas, $\Delta\delta = -363 \pm 5$ mas, separation = 979 ± 5 mas, and position angle = 248.27 ± 0.29 deg. The K-band Keck AO image and the resulting fit is shown in Figure 4.4. The characterisation of the companion star is described in a later section in order to determine the contamination it has on the lightcurve of the target host star.

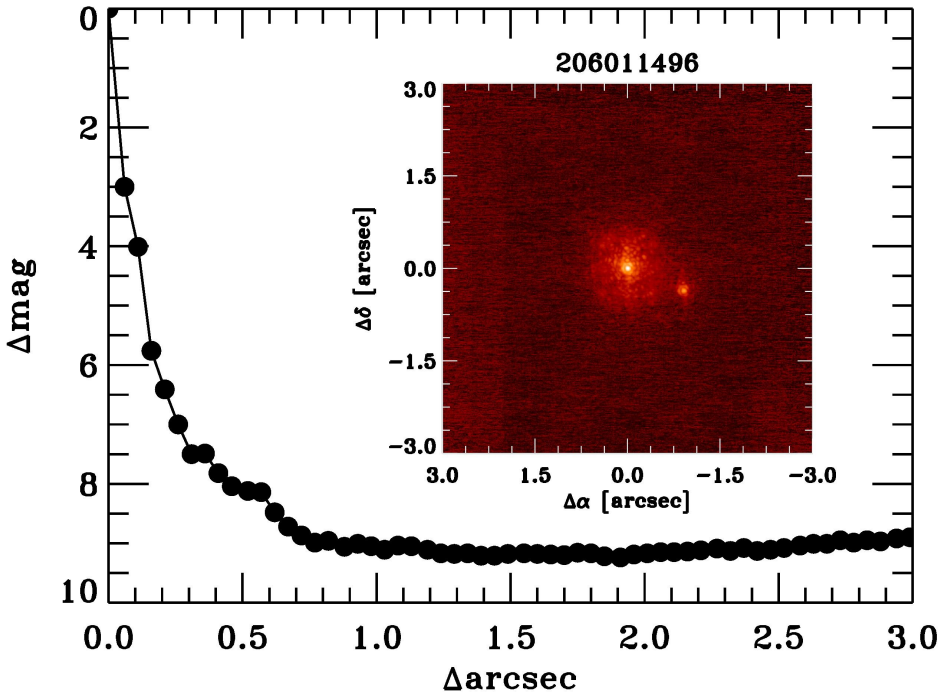

Figure 4.4: K-band Keck AO image shows a companion at a separation of = 979 ± 5 mas, and the contrast of the objects is measured to be Δmag = 8.12.

4.2.3 Gaia astrometry

The *Gaia* Data Release 2 (DR2) has surveyed over one billion stars in the Galaxy (Gaia Collaboration et al., 2016b, 2018b; Lindegren et al., 2018) and provided precise measurements of the parallaxes and proper motions for the sources. EPIC 206011496 has a measured parallax of 7.18 ± 0.05 mas, corresponding to a distance of 139 ± 1 pc. The proper motion of EPIC 206011496 is $\mu_{RA} = 30.20 \pm 0.09$ mas, $\mu_{DEC} = -23.34 \pm 0.06$ mas. As part of the *Gaia* DR2, the stellar effective temperature of EPIC 206011496 was derived from the three photometric bands (Andrae et al., 2018) as $T_{\rm eff} = 5390^{+194}_{-53}$ K. The G-band extinction $A_g = 0.101$ and the reddening $E(BP - RP) = 0.065$ estimated from the parallax and magnitudes were used to determine the stellar luminosity, which in turn provides an estimate of the stellar radius as $R_s = 0.914^{+0.02}_{-0.06}\ R_\odot$ (Andrae et al., 2018). The stellar parameters from the results of *Gaia* DR2 are consistent with the distance estimate, effective temperature, and stellar radius, which are derived in the joint Bayesian analysis in section 4.3.3. However, *Gaia* DR2 does not detect the companion star in the system and EPIC 206011496 is registered as a single object.

4.3 Results

4.3.1 Spectral Analysis

The HARPS spectra were co-added with `IRAF` to perform spectral analysis of the host star. The stellar parameters were determined following the methods of Sousa et al. (2008), where the equivalent widths (EW) of Fe I and Fe II lines were measured using the ARES code[2] (Sousa et al., 2015). The stellar parameters derived are as follow: $T_{\rm eff} = 5457 \pm 29$ K, $\log g = 4.42 \pm 0.05$ dex, [Fe/H] $= 0.08 \pm 0.02$ dex, $\xi_t = 0.81 \pm 0.05$ km s^{-1}. The chemical abundances were derived with a standard LTE analysis using the 2014 version of the code MOOG (Sneden, 1973) which utilised the *abfind* driver with the EW derived with ARES. The derived chemical abundances can be found in Appendix Table A.1.

The characterisation of star B was performed following the method of Santerne et al. (2016). The SPHERE IFS+IRDIS data (A. Vigan, *priv. comm.*) was fitted with the spectral energy distribution (SED) of both stars, which were modelled using the BT-SETTL atmosphere models (Allard, 2014). Star B was assumed to have the same age, metallicity, and distance as star A, hence they also have the same interstellar extinction and iron abundance. By fitting the difference in the SED models of star A and star B with a Markov Chain Monte Carlo algorithm, the derived parameters of star B are as follow: $T_{\rm eff} = 3428 \pm 22$ K, $\log g = 4.870 \pm 0.017$ [cgs], $M_{\rm starB} = 0.40 \pm 0.01\ M_\odot$, $R_{\rm starB} = 0.391^{+0.006}_{-0.010}\ R_\odot$, correspond-

[2]The ARES code can be downloaded at http://www.astro.up.pt/ sousasag/ares/

ing to a star of spectral type M2 (Cox, 2000). From the derived fits, the SED models in the Kepler band were integrated to compute the the flux contamination contributed from star B in the *K2* lightcurve of star A. The contamination was found to be 0.952 ± 0.024 %.

4.3.2 Stellar Rotation

Periodic variation can be seen in the *K2* lightcurve (see Figure 4.1). The variability can arise due to the presence of starspots which change visibility as the host star rotates. The rotation period of the host is examined below.

To measure the rotational modulation in the *K2* lightcurve, the auto-correlation function (ACF) technique described by McQuillan et al. (2013, 2014) and Armstrong et al. (2016) was implemented to derive the stellar rotation period. This technique measures the self-similarity of a lightcurve by building a correlation function over a range of time lags. Before the ACF was computed, the lightcurve was median normalised and transit signals were masked. The ACF is calculated as:

$$r_k = \frac{\sum_{i=1}^{N-k}(x_i - \overline{x})(x_{i+k} - \overline{x})}{\sum_{i=1}^{N}(x_i - \overline{x})^2} \tag{4.1}$$

where r_k is the auto-correlation coefficient at lag k, k is the integer multiple of the cadence, the time-series is $x_i (i = 1, ..., N)$ and the mean is $\overline{x}$. Only periods of less than half the length of the time-series data are considered. The rotation period of the host was found to be 15.14 ± 0.38 d, and the second harmonic was found at 30.48 ± 0.28 d. The resulting ACF is shown in Figure 4.5.

The periodicity in the RV data was examined using the Lomb-Scargle (LS) periodogram (Lomb, 1976; Scargle, 1982) analysis, which calculates the frequency spectrum of the time-series lightcurve data. The LS periodograms of BIS, FWHM, RV, and the S index are plotted in Figure 4.6. A clear peak is observed at 32.2 ± 0.6 d across all periodograms. This is larger than but marginally consistent with the ACF period of 30.48 d at a 2σ level. The planet signal at 2.37 d is significant in the RV periodogram at 1% false alarm probability level only.

The average FWHM of HARPS spectra was used to derive an upper limit of the sky-projected stellar rotational velocity, where $v \sin i < 1.9 \pm 0.2$ km s^{-1}. Using the stellar radius in Table 4.2, the rotation period was found to be $P_{rot} > 26.02 \pm 3.08$ d (assuming an aligned system, $i = 90°$). This value agrees with the $\sim$ 30 d period derived from the photometry and the RV data.

The rotational period was also examined using the methods of Mamajek and Hillenbrand (2008). In short, the convective turnover time τ_c of the star was determined using

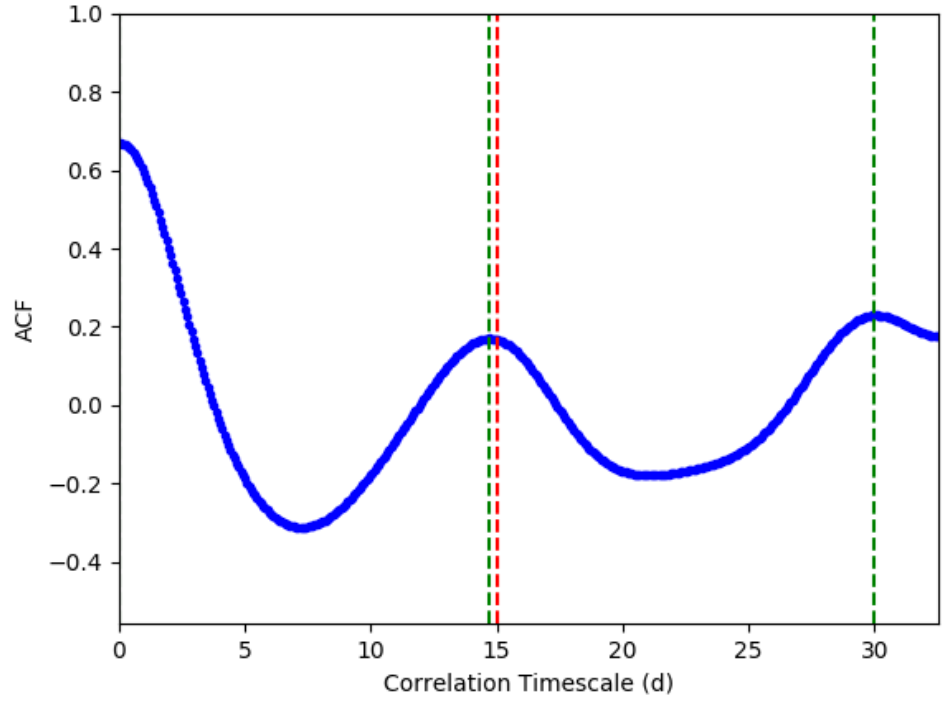

Figure 4.5: The auto-correlation function of EPIC 206011496 from the K2 lightcurve. The red dashed line marks the rotation period at 15.14 d. The green dashed lines mark the harmonics of the rotation period.

its B − V colour from APASS[3], and the calibrations from Noyes et al. (1984b). The Mount Wilson index S_{MW} was measured as 0.195 ± 0.025, hence the corresponding $\log R'_{HK}$ was −4.90 ± 0.12. This value was used to calculate the Rossby number R_o using calibrations from Mamajek and Hillenbrand (2008). The rotational period was finally derived from the relation $P_{rot} = R_o \times \tau_c = 32.8 \pm 10.0$ d.

[3]https://www.aavso.org/apass

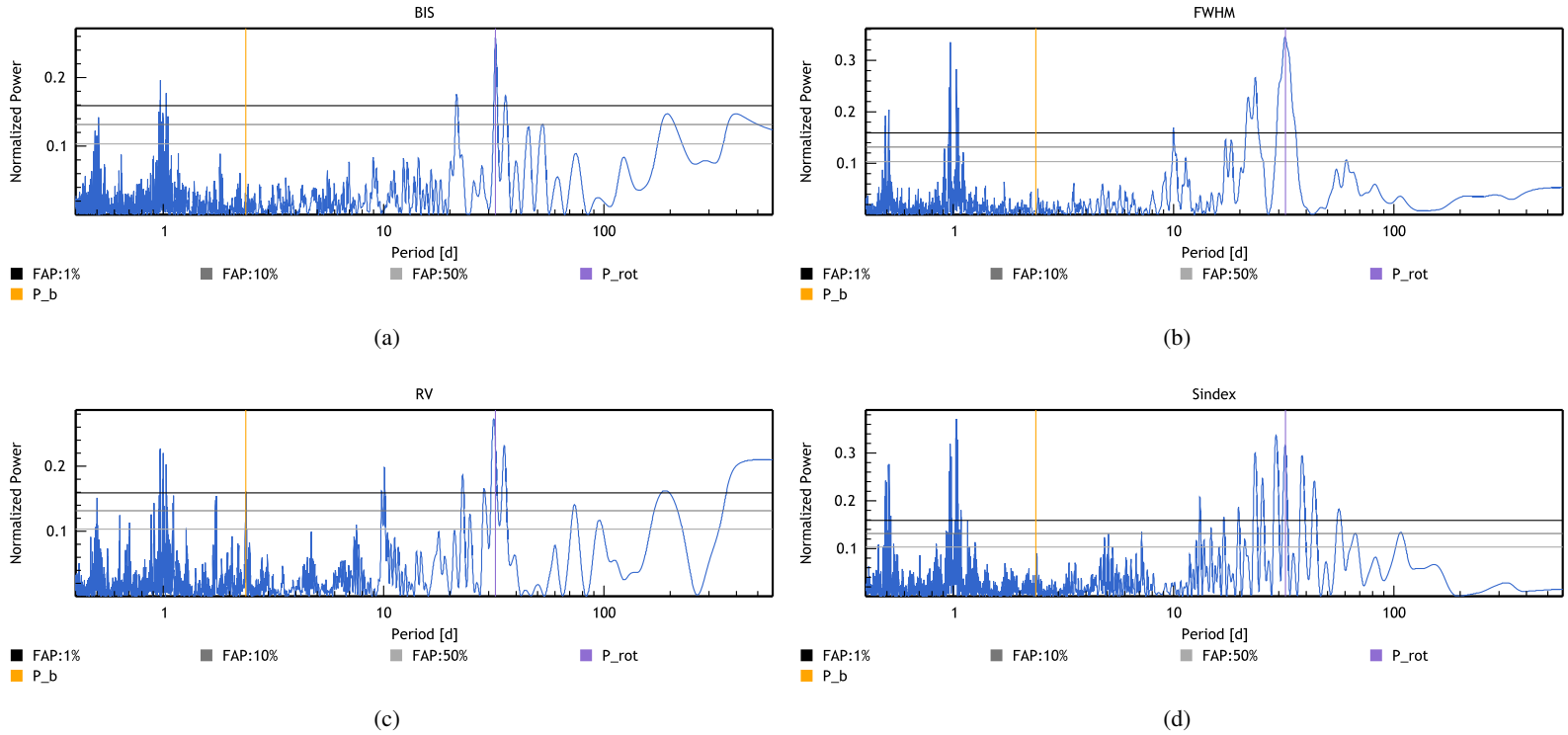

Figure 4.6: Lomb-Scargle periodogram of (a) Bisector Span; (b) Full Width Half Maximum; (c) Radial velocity; (d) S index. The peak position is marked by the purple line and corresponds to a period of 32.2 ± 0.6 d. The orbital period of EPIC 206011496 b is indicated by the yellow line, and the planet signal is only significant in the RV at the 1% FAP level.

4.3.3 Joint Bayesian Analysis with `PASTIS`

The *K2* photometry, the HARPS RV measurements and the SED observed by the APASS, 2-MASS, and WISE surveys (Munari et al., 2014; Cutri et al., 2014) were analysed simultaneously with the `PASTIS` software (Díaz et al., 2014; Santerne et al., 2015). The `jktebop` package (Southworth, 2008) was used to model the *K2* lightcurve, and an oversampling factor of 30 was used to account for the long integration time of the K2 data (Kipping, 2010). The RVs were modelled with Keplerian orbits and the effects of stellar activity was modelled using a Gaussian process (GP) with a quasi periodic kernel (Haywood et al., 2014). The BT-Settl library of stellar atmospheres (Allard et al., 2012) was used to model the SED. The system parameters and the 1-σ uncertainties are reported in Table 4.2.

The MCMC method described in Chapter 2 was used to derive the system parameters. The physical stellar parameters were computed from spectroscopic parameters using the Dartmouth evolution tracks (Dotter et al., 2008) at each step of the chain. Using these stellar parameters and tables of Claret and Bloemen (2011), the limb darkening coefficients were also derived.

For the stellar parameters, normal distribution priors centred on the values derived in Section 4.3.1 were used. The normal prior for the orbital ephemeris centred on the values found by the detection pipeline was chosen. In addition, a uniform distribution in $\sin i$ for the planet inclination was adopted as a prior. For the remaining parameters, uninformative priors were used. The full list of fitted parameters and the priors used in the model is shown in Appendix Table A.3.

Twenty MCMC chains of 3×10^5 iterations were run during the MCMC analysis, where a randomly drawn joint prior distribution was chosen as a starting point. The non-converging chains were rejected following the Kolmogorov-Smirnov test, which measures the similarity of the empirical distribution between the start and the end of the chain. The burn-in phase were then removed and the converged chains were merged to compute the posterior distribution. The median of this distribution was derived to obtain the system parameters.

4.3.4 Stellar Age

The RV measurements and *K2* lightcurve were analysed simultaneously with the Dartmouth stellar evolution tracks (Dotter et al., 2008) to derive an age of $\tau_{iso} = 9.7 \pm 3.0$ Gyr for the host star. Rotational modulation was detected in the *K2* lightcurve, and analysis in Section 4.3.2 suggested that the host star has a rotation period of $\sim$ 30 d. Following methods by Barnes (2010) and adopting the rotational period as 32.8 d, the gyrochronological age of

Table 4.2: System parameters of EPIC 206011496 derived from joint lightcurve and RV analysis using `PASTIS`.

Parameter	Value and uncertainty
Stellar Parameters	
Effective temperature $T_{\rm eff}$ [K]	5477 ± 27
Surface gravity $\log g$ [cgs]	4.419 ± 0.053
Iron abundance [Fe/H] [dex]	0.078 ± 0.020
Distance to Earth D [pc]	145 ± 8
Interstellar extinction $E(B-V)$ [mag]	$0.009^{+0.011}_{-0.007}$
Systemic radial velocity γ [km s^{-1}]	-18.186 ± 0.002
Stellar density $\rho_\star/\rho_\odot$	0.98 ± 0.19
Stellar mass $M_\star$ [$M_\odot$]	0.915 ± 0.017
Stellar radius $R_\star$ [$R_\odot$]	0.977 ± 0.053
Stellar age τ [Gyr]	9.7 ± 3.0
Planet Parameters	
Orbital Period P [d]	$2.369172 \pm 8.9 \times 10^{-5}$
Transit epoch T_0 [BJD - 2456000]	$981.6431 \pm 1.6 \times 10^{-3}$
Radial velocity semi-amplitude K [m s^{-1}]	3.34 ± 0.43
Orbital inclination i [°]	87.7 ± 1.6
Planet-to-star radius ratio k	0.01604 ± 0.00041
Orbital eccentricity e	0.084 ± 0.079
Impact parameter b	0.30 ± 0.20
Transit duration T_{14} [h]	2.266 ± 0.050
Semi-major axis a [AU]	0.03376 ± 0.00021
Planet mass M_p [$M_\oplus$]	6.54 ± 0.84
Planet radius R_p [$R_\oplus$]	1.71 ± 0.11
Planet bulk density ρ_p [g cm^{-3}]	7.1 ± 1.8

EPIC 206011496 was found to be $\tau_{gyro} = 6.11 \pm 4.16$ Gyr which agrees with τ_{iso} within error.

Tucci Maia et al. (2016) and Nissen (2015) studied a sample of solar-twins to derive the relation between the [Y/Mg] abundance ratio and the stellar age. Explicitly, the relation is expressed as:

$$[Y/Mg] = 0.186(\pm 0.008) - 0.041(\pm 0.001) \times \tau_{[Y/Mg]} \tag{4.2}$$

Following this relation, the age of EPIC 206011496 was determined as $\tau_{[Y/Mg]} = 3.97 \pm 2.59$ Gyr. $\tau_{[Y/Mg]}$ implies the host is slightly younger than the gyrochronological age and isochronal age. However, EPIC 206011496 has a main sequence lifetime of 12.5 Gyr, and its low lithium abundance A(Li II)< 0.45 obtained in Section 4.3.1 suggests that the host is

not young. Hence it is likely that the host is of at least an intermediate age.

4.4 Discussion and Conclusion

EPIC 206011496 b is a super-Earth with a mass of 6.54 ± 0.84 $M_\oplus$ and radius of 1.71 ± 0.11 $R_\oplus$, and an orbital period of P = 2.37 d. It has a bulk density of 7.1 ± 1.8 g cm^{-3}, which is comparable to the Earth's density. Several analytical models were applied to determine the composition and mass fraction of EPIC 206011496 b.

Fortney et al. (2007) computed radii of planets with different internal composition across different planet masses and orbital separations. The planet radii were fitted to determine an analytical function for rock/iron planets:

$$R = (0.0592\ rmf + 0.0975)(\log M)^2 + (0.2337\ rmf + 0.4938)\log M + (0.3102\ rmf + 0.7932) \tag{4.3}$$

where R is in $R_\oplus$, M is in $M_\oplus$, rmf is the rock mass fraction ($rmf = 1.0$ for a pure rock planet, and $rmf = 0.0$ for a pure iron planet). The rock mass fraction of EPIC 206011496 b was determined to be 0.84, so the composition of the planet is likely to be dominated by rock. Seager et al. (2007) also independently derived the mass-radius relation of solid exoplanets in an analytical form:

$$\log_{10} R = k_1 + \frac{1}{3}\log_{10} M - k_2 M^{k3} \tag{4.4}$$

where $R = R_p/r1$ and $M = M_p/m1$ are the scaled radius and mass of the planet, and the values of $r1$ and $m1$ depends on the composition of the planet, $k_1 = -0.20945$, $k2 = 0.0804$, and $k3 = 0.394$. The composition of EPIC 206011496 b was determined to be mostly rocky using this relation, where the planet was found to have > 70% of silicate mantle by mass.

A more detailed in investigation of the composition of EPIC 206011496 b was performed using interior model of Brugger et al. (2017). This model considers planets composed of three differentiated layers: core (metals), mantle (rocks), and a liquid water envelope. Figure 4.7 shows the possible compositions of EPIC 206011496 b inferred from the 1σ uncertainties on the mass and radius of the planet. In the case where the planet is assumed to have terrestrial compositions (i.e. without any water), the central mass and radius of the planet are best fitted with a rock mass fraction of 81%, which is consistent with other theoretical predictions. The rmf of the planet is poorly constrained (within the 44100% range) due to the uncertainties on the planet's fundamental parameters. Assuming that the stellar Fe/Si ratio (here 0.90 ± 0.41) can be used as a proxy for the bulk planetary value (Dorn et al., 2015; Brugger et al., 2017), the uncertainty range can be reduced to 6083%.

In the case of a water-rich EPIC 206011496 b, the interior model derives an upper limit on the water mass fraction (wmf) of the planet. Assuming an Earth-like albedo, the planet is estimated to have a high equilibrium temperature of $\sim$ 1300 K, where water would be in the gaseous and supercritical phases, which are less dense than the liquid phase. From the uncertainties on the mass, radius, and bulk Fe/Si ratio of EPIC 206011496 b, we infer that this planet cannot present a wmf larger than 31%.

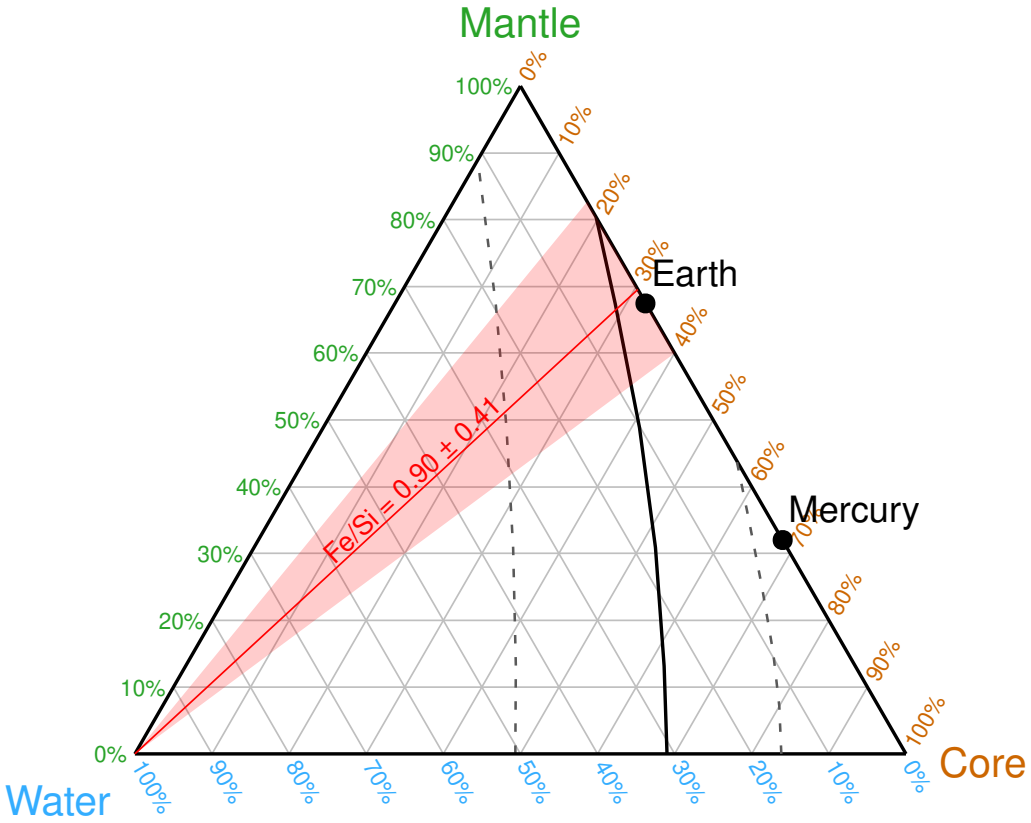

Figure 4.7: Ternary diagram showing the possible composition of EPIC 206011496 b. The thick black line indicates the allowed composition of the planet inferred from the central values of the mass and radius of the planet, and the dashed lines denote the deviations from this line allowed by the 1σ uncertainties on the fundamental parameters. The red line and area show the compositions compatible with the planetary bulk Fe/Si ratio derived for EPIC 206011496 b from the stellar value. Compositions of the Earth and Mercury are shown for reference.

Recently, the California-*Kepler* Survey (CKS) (Johnson et al., 2017; Fulton et al., 2017) revealed a bimodal radius distribution in the Kepler sample of small planets (R_p < 4 $R_\oplus$). The CKS has confirmed a deficit of planets with radii of $\sim$ 1.8 $R_\oplus$ (the 'Evaporation Gap'; Owen and Wu 2013). These planets are most susceptible to photoevaporation where their atmospheres can be eroded away. Alternatively, EPIC 206011496 b could have lost its

atmosphere via core-powered mass loss mechanism (Ginzburg et al., 2016, 2018). In this scenario, EPIC 206011496 b may have formed with a light envelope which was removed rapidly due to the planet's cooling luminosity.

EPIC 206011496 b is exposed to an enormous amount of irradiation because of its proximity to the star. The irradiance received by a planet can be estimated using $F = L/4\pi r^2$, where $L = 4\pi R_s \sigma T_{\rm eff}^4$ is the stellar luminosity, $\sigma = 5.67 \times 10^{-8}$ W m^{-2} K^{-4} is the Stefan-Boltzmann constant, and r is the distance between the star and the planet. In the case of EPIC 206011496 b, the planet is estimated to receive an irradiance of 9.32×10^5 Wm^{-2}, over 680 times greater than the Solar irradiance received at the Earth. The equilibrium temperature of the EPIC 206011496 b can be estimated using Equ. 1 of López-Morales and Seager (2007): $T_{\rm eq} = T_{\rm eff}(R_s/a)^{1/2}[f(1 - A_B)]$, where f and A_B are the reradiation factor and the Bond albedo of the planet. Assuming an Earth-like Bond albedo $A_B = 0.3$ and that the incident radiation is redistributed around the atmosphere (i.e. f = 1/4), the equilibrium temperature of EPIC 206011496 b is $T_{\rm eff} \approx 1300$ K.

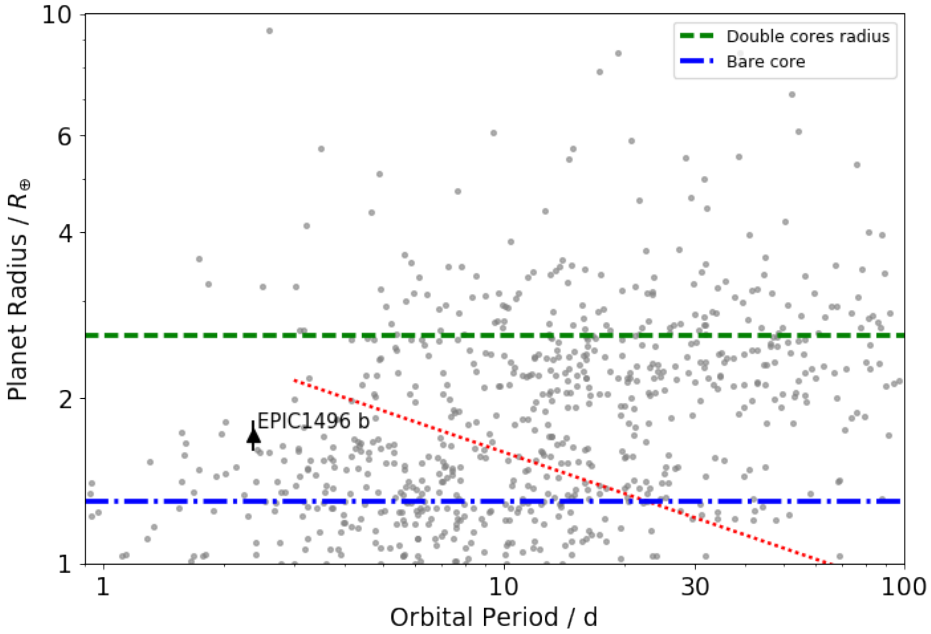

Figure 4.8: Planet radius distribution as a function of orbital period. The grey circles denote the planet sample obtained from the CKS sample (Fulton et al., 2017). The blue dot-dashed line and the green dashed line indicate the peak of the bimodal distribution of the planet radius distribution, where planets tend to favour radii of $\sim 1.3\ R_\oplus$ and $\sim 2.4\ R_\oplus$ due to the photoevaporation mechanism. The red dotted line indicates the lower limit of the photoevaporation valley derived from Owen and Wu (2017).

Indeed, this planet is found at the lower limit of the evaporation gap as shown in the 2D radius distribution plot in Figure 4.8. This implies the gas envelope of EPIC 206011496 b was probably eroded due to photoevaporation. It is likely that the photoevaporation process occurred within the first $\approx$ 100 Myr after the planet was formed when when X-ray emission is saturated (Jackson et al., 2012). After $\approx$ 100 Myr, the X-ray emission decays.

Using the X-ray-age relation of Jackson et al. (2012), the total X-ray luminosity of EPIC 206011496 over its lifetime, E_x^{tot} was estimated. Using the results of section 4.3.4, we adopted a mean age of 6.32 Gyr for the host star. The X-ray-to-bolometric luminosity ratio in the saturated regime for a $B-V = 0.743$ star is $\log(L_x/L_{bol}) = -3.71 \pm 0.05 \pm 0.47$. The corresponding turn-off age is $\log \tau_{sat} = 8.03 \pm 0.06 \pm 0.31$, where the decrease in X-ray emission follows a power law ($\alpha = 1.28 \pm 0.17$). Over the lifetime of the star, $E_x^{tot} = 6.70 \times 10^{45}$ ergs (assuming efficiency factor $\eta = 0.25$) and EPIC 206011496 b is expected to have lost 2.7% of its mass under the constant-density assumption. The predominantly rocky composition of EPIC 206011496 b indicates that the planet was likely formed inside the ice line. It could have migrated towards its current orbital separation well before $\approx$ 100 Myr and subject to intense photoevaporation, or accreted its mass locally (Owen and Wu, 2017).

A surprisingly diverse range of small planets are known to date. Super-Earths with the same masses could hold a wide range of radii, which corresponds to different planet bulk densities. Precise RV measurements are necessary to determine the accurate planetary mass. This would place strong theoretical constraints on the formation and evolutionary paths of the planet. The increasing sample of small planets will help distinguish planet origins, identify the types of mass loss mechanism, and the efficiency of atmospheric evaporation processes.

[5] https://exoplanetarchive.ipac.caltech.edu/index.html

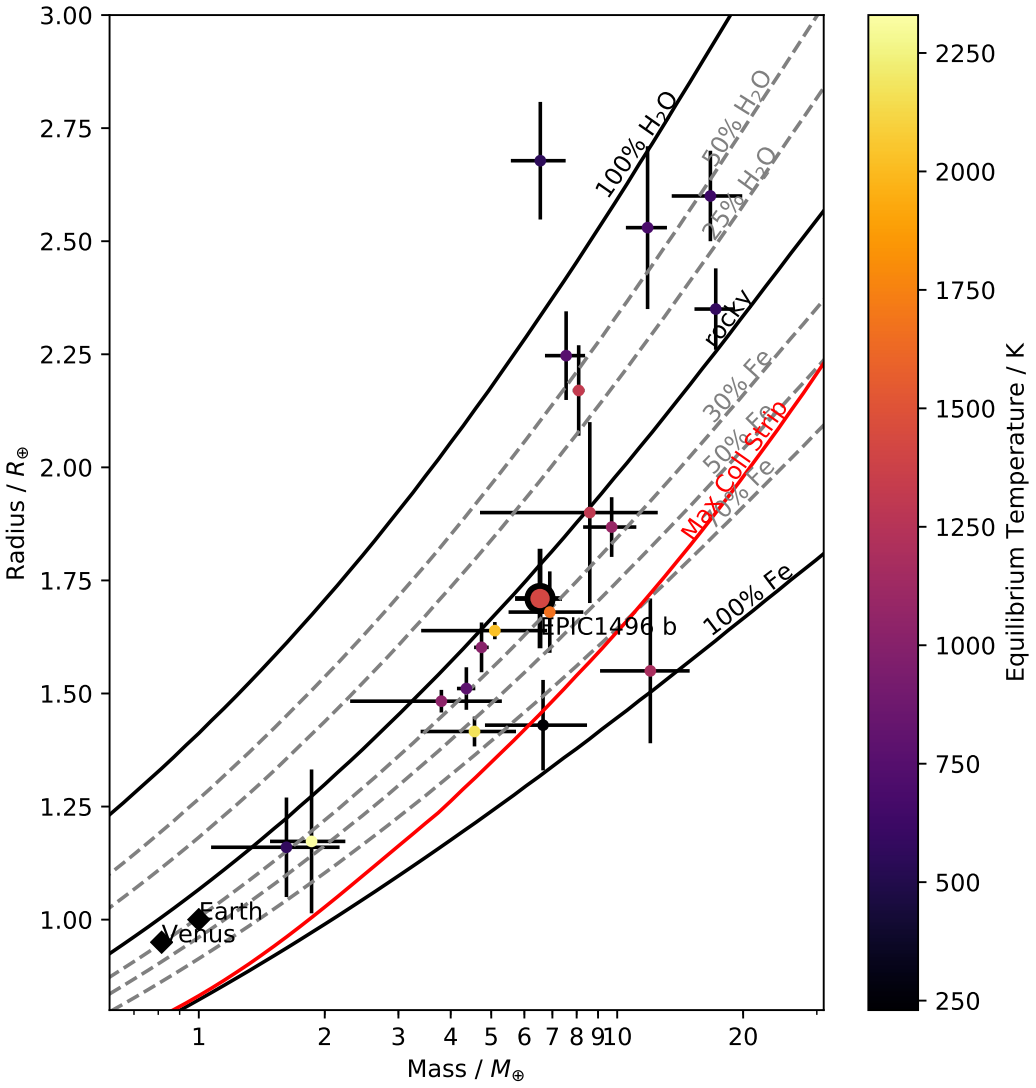

Figure 4.9: A mass-radius diagram of confirmed exoplanets with masses up to 20 $M_\oplus$. Data taken from NASA Exoplanet archive [5]. The mass-radius relations were taken from Zeng et al. (2016). From top to bottom, the black solid lines denotes a pure water, pure rock and pure iron composition. The grey dashed lines between the solid lines are mass-radius relations for water-rock and rock-iron composites. The red solid line is the lower limit of a planet radius as a result of collisional stripping (Marcus et al., 2010). EPIC 206011496 b has a composition consistent with a rocky terrestrial planet.

Chapter 5

The Evaporating Planet WASP-12 b

5.1 Motivation

Hot Jupiters orbit at close proximities to their host stars. Consequently, they are exposed to enormous amounts of stellar irradiation. The planets' atmospheres are highly irradiated, leading to inflation. Under extreme circumstances, high temperatures can drive the increase in particle velocities above the atmospheric escape velocity (Lammer et al., 2003; Lecavelier des Etangs et al., 2004). The upper atmosphere of the planet therefore evaporates. This is the case for HD 209458 b where an extended exosphere was observed via the enhanced transit in the Lyman-α absorption lines Vidal-Madjar et al. (2003). Similar feature was also observed in HD 189733 b (Lecavelier Des Etangs et al., 2010) and GJ436 b (Kulow et al., 2014). In addition to Lyman-α lines, strong resonance lines such as Na I D doublets and Ca II H & K lines are also used as proxies to detect absorption by the planetary atmosphere. Redfield et al. (2008) and Vidal-Madjar et al. (2011) detected Na I D absorption lines and constrained atmospheric properties of HD 189733b and HD 209458 b respectively. Similarly, Ca II H & K lines were also used to search for extended exospheres around the evaporating planets WASP-12 b (Fossati et al., 2013; Haswell et al., 2012) and 55 Cnc e (Ridden-Harper et al., 2016).

5.1.1 The Curious Case of WASP-12 b

WASP-12 b orbits a late-F star with an ultra-short period of $P = 1.09$ days (Hebb et al., 2009). At an orbital separation of just 0.023 AU, it is one of the hottest Jupiters known to date. The inflated exosphere of WASP-12 b implies that its Roche lobe (a region dominated by gravitational forces of an object) is overfilled, resulting in the mass loss from the planet. Table 5.1 summarises the system parameters of WASP-12.

Table 5.1: System parameter of WASP-12 obtained from Hebb et al. (2009)(H09) and Knutson et al. (2010)(K10).

Parameters	Values	Reference
V	11.96 ± 0.08	H09
$T_{\rm eff}$ (K)	6300^{+200}_{-100}	H09
[M/H]	$0.30^{+0.05}_{-0.15}$	H09
$\log g$	4.38 ± 0.10	H09
$v \sin i$ (km s^{-1})	$< 2.2 \pm 1.5$	H09
M_s ($M_\odot$)	1.35 ± 0.14	H09
R_s ($R_\odot$)	1.57 ± 0.07	H09
$\log R'_{HK}$	-5.500	K10
Age (Gyr)	2 ± 1	H09
P (days)	1.091423 ± 0.000003	H09
a (AU)	0.0229 ± 0.0008	H09
M_p (M_J)	1.41 ± 0.10	H09
R_p (R_J)	1.79 ± 0.09	H09
$T_{\rm eq}$ (K)	2516 ± 36	H09

Fossati et al. (2010b) and Haswell et al. (2012) used the Cosmic Origins Spectrograph (COS) on the Hubble Space Telescope (HST) to obtain near-UV (NUV) spectra centred on the transit of WASP-12, where enhanced transit depths were observed. This increased absorption was also observed at resonance lines. In particular, Haswell et al. (2012) found absorption in the Fe II 2586 Å, as well as the complete absorption in the Mg II h & k line cores. Their analysis showed that high Mg II column density is required for the observed line profile, and the source which could cause the absorption is gas lost from the WASP-12 b.

Ca II H & K lines are commonly used as stellar activity indicators. A survey conducted by Knutson et al. (2010) measured the activities of planet hosting stars. Among the sample, WASP-12 was measured to have an extremely low $\log R'_{HK}$ index of -5.5, far below the basal level ($\log R'_{HK} = -5.1$ for late-type main-sequence stars (Wright et al., 2004)). Fossati et al. (2013) compared the Ca II H & K line profiles against stars with similar effective temperatures and ages to reveal an enhanced absorption in the WASP-12 spectrum, which is similar to the complete absorption in Mg II lines observed with NUV spectra. This observation was interpreted as due to the extra absorption by gas lost from WASP-12 b, where evaporated planet material diffuses into the planet orbit and covers the entire system.

This chapter presents an investigation in the variability of the atmosphere of WASP-12 b. The data selection and reduction processes will be outlined. The methods used to analyse absorption features in Ca II H & K and Na I D line profiles will be discussed, and the implications will be explored.

5.2 Data Selection and Reduction

Figure 1 of Fossati et al. (2013) showed that the anomalously deep absorptions in the Ca II H & K cores extents a region that is ~ 4 Å wide. Variability in the Ca II H & K core fluxes is expected to be small and subtle. Consequently, spectra of moderate resolution and high signal-to-noise ratio (SNR) is required for an in-depth study of the system.

A total of 58 archival spectroscopic data of WASP-12 were obtained from the High Resolution Echelle Spectrometer (HIRES; Vogt (1992)). The data covers the period between 2009 December 22 and 2013 December 11, providing both in and out-of-transit coverage of the system. These observations cover the spectral range of 3360-8100 Å across three CCDs, and have a resolving power $R = 72,000$, with the exception of one spectrum obtained on 2010 January 02 where $R = 48,000$. At the Ca II H & K wavelength ranges, the spectra have signal-to-noise ratios (SNR) of $\approx$ 30-40. The list of archive observations is listed in Table 5.2.

The HIRES data were reduced with `IRAF` following procedures outlined in Chapter 2. Spectral region centred around Ca II H & K is faint hence scatter light removal is important. For each spectrum, scatter light subtraction was performed using the `iraf/echelle.apscatter` task, where regions between adjacent spectral orders were used to define the scatter light surface and fitted with a cubic spline function.

The Ca II H & K line cores are centred at 3968.5 Å and 3933.7 Å, respectively, which lies in the HIRES echelle orders 90 and 91. The Na I D_1 and D_2 lines are centred at 5889.95 Å and 5895.92 Å, respectively, corresponding to the HIRES echelle orders 60 and 61. Using the online HIRES ThAr arc-line plots[1], wavelength calibration was performed with the Th-Ar lamp comparison spectra. The wavelength solution was applied to obtain dispersion corrected spectra. For orders 90 and 91 (which contains the Ca II H & K lines), the wide absorption regions were masked before a 2^{nd} order cubic spline was fitted to the continuum for normalisation. Similar procedures were performed on orders 60 and 61 (which contains the Na I D_1 and D_2 lines), where a 1^{st} order cubic spline was fitted. The final step involves merging the adjacent orders to produce the Ca II spectrum (covers a wavelength range of 3950-3995Å) and a Na I spectrum (covers a wavelength range of 5790-5990Å).

[1] `https://www2.keck.hawaii.edu/inst/hires/ThAr_atlas.html`

Table 5.2: List of archival Keck/HIRES observations used in analysis. The aperture column provides the decker name and slit number. The filter column provides the detail on the filters used in wheel 1 and 2.

KOA ID	Observation Date (UT)	Observation Time (UT)	Exposure Time (s)	Aperture[a]	Filter[b]	SNR[c]
HI.20091222.45029	2009-12-22	12:30:29	500	C2	kv370; clear	27.00
HI.20091224.39756	2009-12-24	11:02:36	600	C2	kv370; clear	32.00
HI.20091231.29162	2009-12-31	08:06:02	500	C2	kv370; clear	39.00
HI.20100101.36355	2010-01-01	10:05:55	500	C2	kv370; clear	24.00
HI.20100102.39073	2010-01-02	10:51:13	500	C2	kv370; clear	34.00
HI.20100102.48380	2010-01-02	13:26:20	750	B3	kv370; clear	43.00
HI.20100223.31093	2010-02-23	08:38:13	600	C2	kv370; clear	42.00
HI.20100228.26010	2010-02-28	07:13:30	600	C2	kv370; clear	49.00
HI.20100301.33603	2010-03-01	09:20:03	600	C2	kv370; clear	45.00
HI.20100305.26680	2010-03-05	07:24:40	600	C2	kv370; clear	45.00
HI.20100329.24426	2010-03-29	06:47:06	600	C2	kv370; clear	32.00
HI.20100330.26780	2010-03-30	07:26:20	600	C2	kv370; clear	22.00
HI.20100403.24623	2010-04-03	06:50:23	600	C2	kv370; clear	45.00
HI.20100426.20953	2010-04-26	05:49:13	600	C2	kv370; clear	37.00
HI.20100829.54161	2010-08-29	15:02:41	600	C2	kv370; clear	40.00
HI.20101121.38938	2010-11-21	10:48:58	600	C2	kv370; clear	40.00
HI.20101212.50135	2010-12-12	13:55:35	600	C2	kv370; clear	42.00

Continued on next page

Table 5.2 – continued from previous page

KOA ID	Observation Date (UT)	Observation Time (UT)	Exposure Time (s)	Aperture[a]	Filter[b]	SNR[c]
HI.20101215.40967	2010-12-15	11:22:47	600	C2	kv370; clear	35.00
HI.20101229.34137	2010-12-29	09:28:57	900	C2	kv370; clear	45.00
HI.20101229.35081	2010-12-29	09:44:41	900	C2	kv370; clear	40.00
HI.20101229.36025	2010-12-29	10:00:25	900	C2	kv370; clear	30.00
HI.20111017.43906	2011-10-17	12:11:46	345	C2	clear; clear	33.00
HI.20111113.42340	2011-11-13	11:45:40	600	C2	clear; clear	29.00
HI.20111206.39159	2011-12-06	10:52:39	272	C2	clear; clear	35.00
HI.20120102.23765	2012-01-02	06:36:05	391	C2	clear; clear	39.00
HI.20120102.24200	2012-01-02	06:43:20	398	C2	clear; clear	39.00
HI.20120102.24642	2012-01-02	06:50:42	393	C2	clear; clear	40.00
HI.20120102.27103	2012-01-02	07:31:43	467	C2	clear; clear	44.00
HI.20120102.27614	2012-01-02	07:40:14	484	C2	clear; clear	44.00
HI.20120102.28143	2012-01-02	07:49:03	481	C2	clear; clear	44.00
HI.20120102.28669	2012-01-02	07:57:49	494	C2	clear; clear	44.00
HI.20120102.29207	2012-01-02	08:06:47	494	C2	clear; clear	44.00
HI.20120102.29745	2012-01-02	08:15:45	456	C2	clear; clear	44.00
HI.20120102.30245	2012-01-02	08:24:05	467	C2	clear; clear	44.00
HI.20120102.30756	2012-01-02	08:32:36	452	C2	clear; clear	44.00
HI.20120102.31253	2012-01-02	08:40:53	455	C2	clear; clear	44.00
HI.20120102.32256	2012-01-02	08:57:36	456	C2	clear; clear	45.00
HI.20120102.32757	2012-01-02	09:05:57	450	C2	clear; clear	45.00

Continued on next page

Table 5.2 – continued from previous page

KOA ID	Observation Date (UT)	Observation Time (UT)	Exposure Time (s)	Aperture[a]	Filter[b]	SNR[c]
HI.20120102.35360	2012-01-02	09:49:20	489	C2	clear; clear	43.00
HI.20120102.35893	2012-01-02	09:58:13	461	C2	clear; clear	45.00
HI.20120102.36398	2012-01-02	10:06:38	468	C2	clear; clear	44.00
HI.20120102.36911	2012-01-02	10:15:11	438	C2	clear; clear	44.00
HI.20120102.37394	2012-01-02	10:23:14	438	C2	clear; clear	41.00
HI.20120102.37877	2012-01-02	10:31:17	451	C2	clear; clear	46.00
HI.20120102.38373	2012-01-02	10:39:33	444	C2	clear; clear	45.00
HI.20120102.38862	2012-01-02	10:47:42	442	C2	clear; clear	45.00
HI.20120102.39348	2012-01-02	10:55:48	437	C2	clear; clear	45.00
HI.20120102.39830	2012-01-02	11:03:50	434	C2	clear; clear	45.00
HI.20120102.40309	2012-01-02	11:11:49	453	C2	clear; clear	44.00
HI.20120102.40806	2012-01-02	11:20:06	432	C2	clear; clear	45.00
HI.20120102.41282	2012-01-02	11:28:02	454	C2	clear; clear	44.00
HI.20120102.41780	2012-01-02	11:36:20	452	C2	clear; clear	44.00
HI.20120102.42276	2012-01-02	11:44:36	488	C2	clear; clear	44.00
HI.20120102.42809	2012-01-02	11:53:29	515	C2	clear; clear	44.00
HI.20120102.43369	2012-01-02	12:02:49	504	C2	clear; clear	43.00
HI.20120102.43918	2012-01-02	12:11:58	563	C2	clear; clear	42.00
HI.20120102.44525	2012-01-02	12:22:05	536	C2	clear; clear	43.00
HI.20131211.37740	2013-12-11	10:29:00	392	C2	clear; clear	31.00

Continued on next page

Table 5.2 – continued from previous page

KOA ID	Observation Date (UT)	Observation Time (UT)	Exposure Time (s)	Aperture[a]	Filter[b]	SNR[c]

[a] C2 = slit size 14.0” (length), 0.861” (width), R= 48,000; B3 = slit size 14.0” (length), 0.574” (width), R= 72,000.

[b] Filter wheels 1 & 2: clear is empty; kv370 covers a wavelength range of 0.35 - 1.1 microns.

[c] Estimated signal-to-noise of the spectrum near the image center.

5.3 Analysis and Results

The spectra were required to be aligned to the same velocity reference frame, and their fluxes standardised to the same level in order to investigate the possible variability in the line profiles effectively.

5.3.1 Standardise HIRES Spectra

The `iSpec`[2] software tool (Blanco-Cuaresma et al., 2014) was used to generate a synthetic WASP-12 spectrum (hereafter referred to as the template spectrum) using the SYNTHE radiative transfer code and the ATLAS9 atmosphere model (Kurucz, 2005). Stellar parameters derived in the discovery paper (Hebb et al., 2009) were used to define the model grid. The HIRES spectra (hereafter referred to as the observed spectra) were RV corrected to the same velocity frame as the template spectrum using the cross-correlation method. The next step was to standardise the observed spectra. First, the ratio between the observed and template spectrum was calculated. A mask was applied to the deep absorption features, and a median filter was applied to create a smoothed continuum. In the case of the Ca II spectrum, the H & K broad absorption regions (λ_H = 3962.00 - 3975.50 Å and λ_K = 3926.50 - 3940.00 Å, respectively) were masked and a 20 Å window was used to smooth the continuum. For the Na I spectrum, the deep absorption lines centred at λ = 5857.34 Å, 5889.95 Å, 5895.92 Å, 5914.15 Å were masked and a 5 Å window was used instead. Once the smooth continuum was obtained, the flux level of the observed spectra were standardised by taking the product of the observed spectrum and the smooth continuum. An extra step was taken to adjust the fluxes of the far line wings of the Ca II H & K profiles. Within the line wings, regions without absorption features (red shaded regions in Figure 5.1) were selected to compute the observed-to-template spectrum ratio. A 0.5 Å median filter was applied, and a second order polynomial was fitted to match the fluxes in the line wings. An example of the standardised spectrum is shown in Figure 5.2.

5.3.2 Residual Analysis

The goal of the investigation was to establish if there are orbit-dependent variabilities in the line profiles. The orbital phases of the spectra were calculated from their corresponding epoch, with phase 0 fixed at mid-transit. To search for variability in the lines, we compared the relative fluxes of the observed and the template spectra. A residual spectrum is defined as:

$$S(\lambda) = f_{obs} - f_{temp} \tag{5.1}$$

[2]The code is available via http://www.blancocuaresma.com/s/

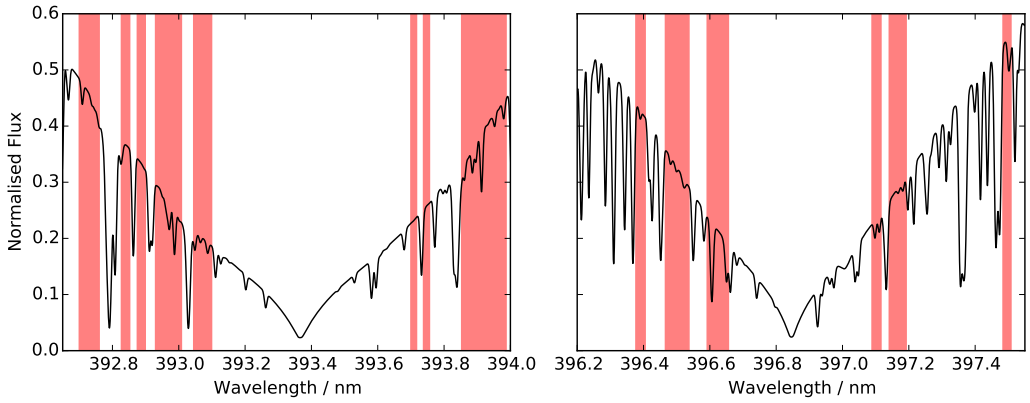

Figure 5.1: WASP-12 template spectrum centred on the Ca II K (left) and Ca II H (right). Red vertical bands show the wavelength regions used to match fluxes at the line wings.

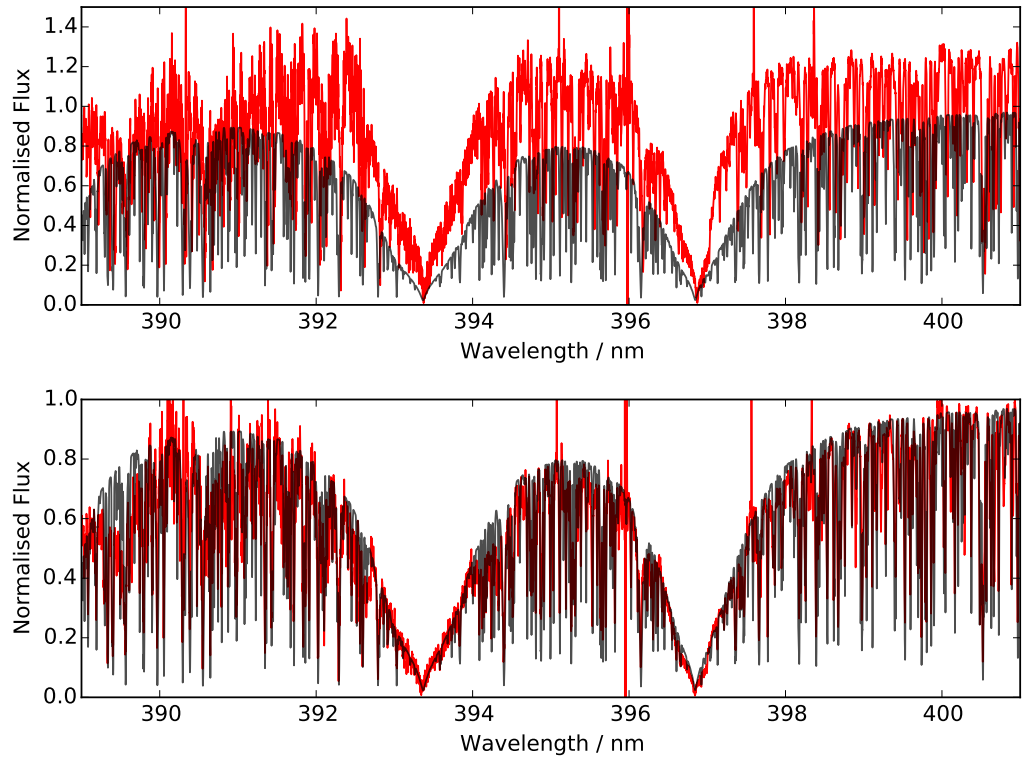

Figure 5.2: *top panel*: The extracted HIRES spectrum (red) before the standardise treatment (see text for detail) with the WASP-12 template spectrum (black). *bottom panel*: A standardised HIRES spectrum (red) generated for the time-series analysis.

where f_{obs} is the observed spectrum and f_{temp} is the template spectrum. To measure the absorption/emission across the core of the line profiles, the integrated residual fluxes were computed using the trapezoidal rule:

$$\int_{\lambda_1}^{\lambda_2} S(\lambda) d\lambda \tag{5.2}$$

where λ_1 and λ_2 are the wavelengths of lower and upper bound of the core region of interest.

Ca II H & K Profiles

The trace plots of the residual spectra centred at Ca II K (3928.0 Å - 3938.0 Å) and Ca II H (3963.5 Å - 3973.5 Å) are shown in Figures 5.3 and 5.4, respectively. Each pixel colour corresponds to the residual flux intensity according to the scale shown in the colour bar. On inspection, enhanced absorption relative to the template spectrum is seen in both Ca II H & K line cores across most orbital phases, with the exception of three residual spectra at phases 0.243, 0.250, and 0.261 where emission relative to the template spectrum is seen. The three spectra showing emissions were obtained separately on 2010 January 01, 2009 December 31, and 2011 November 13, so the effect was measured repeatedly on a night-to-night and yearly basis. The integrated residual flux across the central 1 Å regions at the Ca II H & K cores were computed according to Equation 5.2. The measured absorption is plotted as a function of orbital phase in Figure 5.5. The uncertainties of the computed integrated flux residuals were propagated from the flux error of the spectra, which was approximated from the SNR of the spectra (δ(flux) $\sim$ 1/(SNR)). Enhanced absorption throughout the planetary orbit is attributed to the circumstellar material from the evaporating planet. This is in agreement with the interpretation of Haswell et al. (2012) from the Mg II h and k lines in the NUV wavelength range. The fluctuation measured in the residual flux of Ca II H & K cores could be an indication of non-uniform absorbing material around the orbit.

Na I D Doublets

Similar analyses were performed in the Na I D doublets. The residual spectra centred at the Na I D Doublets were computed, followed by measurements of the narrow absorption features centred at the 1.5 Å line cores. The trace of the residual fluxes centred at the Na I doublet (5883.2 Å - 5902.9 Å) is shown in Figure 5.6. The integrated residual flux in the Na I D_1 and D_2 line cores as a function of the planet orbital phase is shown in Figure 5.7. The error bars of the integrated flux residuals of the Na I D_1 and D_2 estimated from the SNR of the spectra centred around Na I doublet underestimated the uncertainty of the residual fluxes. We empirically determine the uncertainties of the measured spectral fluxes to obtain realistic error bars for each data. The amount of evaporated material present along the line-of-sight during transit (phase∼0.9441-1.0559) of WASP-12 b was assumed to be constant. Therefore the spectral fluxes at in-transit phases are constant. The standard deviation (σ) associated to the in-transit fluxes was calculated using

$$\sigma = \frac{\sum (f_{\mathrm{int},i} - \bar{f_{\mathrm{int}}})}{N - 1} \tag{5.3}$$

where N is the number of in-transit spectra (16 in the archival data), $f_{\mathrm{int},i}$ is the i^{th} integrated flux residual and $\bar{f_{\mathrm{int}}}$ is the mean in-transit integrated flux residual. The error bars propagated from the SNR of the spectrum is then re-scaled using the calculated standard deviation. For both D_1 and D_2 lines, strong absorption relative to the template spectrum is observed throughout the orbit, with fluctuations of ~ 0.01 in the D_1 core and ~ 0.015 in the D_2 core.

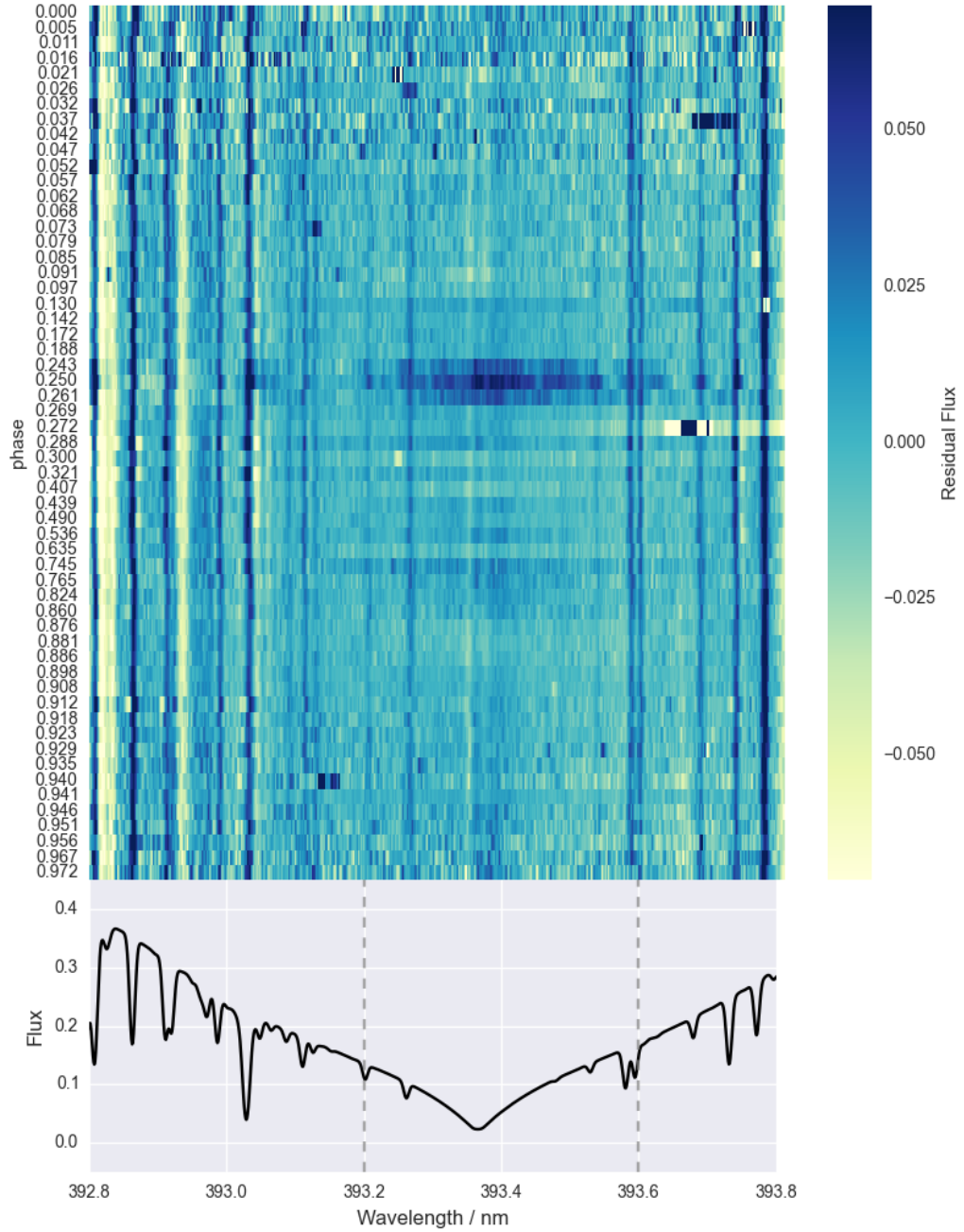

Figure 5.3: Residual WASP-12 spectra centred at Ca II K (3928.0 Å - 3938.0 Å) is plotted as a trace map. The colour of the trace show the residual flux intensity according to the scale shown in the colour bar on the right. Bluer pixels indicate higher residual flux intensity in the observed spectrum compared to the template, whereas whiter pixels indicate a lower residual flux intensity. Note that the phase axis is not in-scale. The WASP-12 template spectrum is plotted under the trace as a reference. The vertical grey dashed lines indicate the approximate 4Å bandwidth where enhanced absorption is expected to be seen.

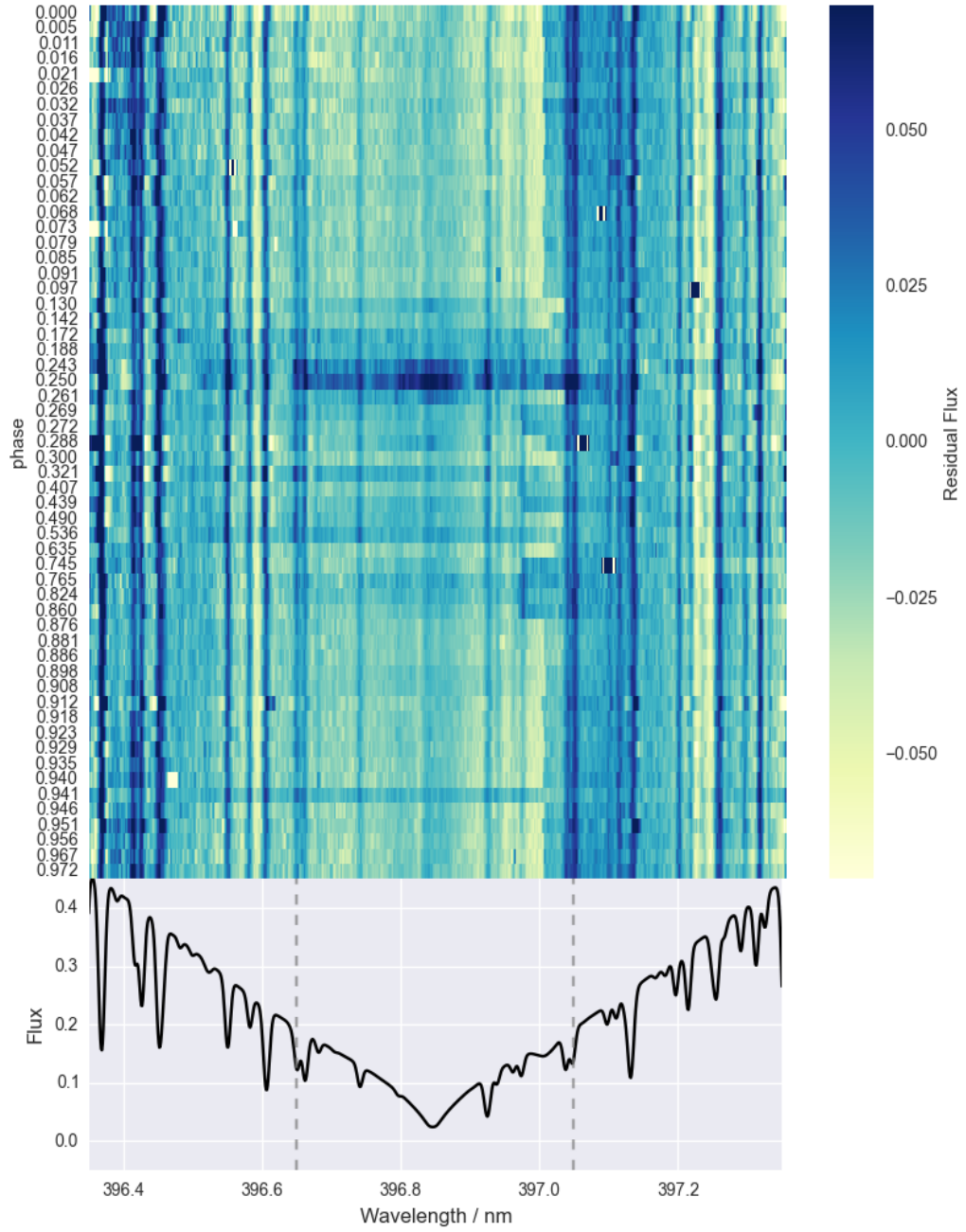

Figure 5.4: Trace plot as described in Figure. 5.3 but centred at Ca II H (3963.5 Å - 3973.5 Å).

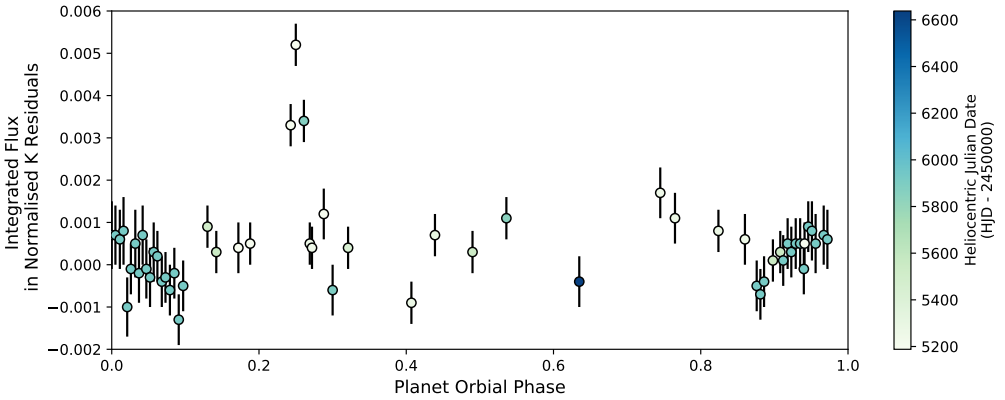

(a)

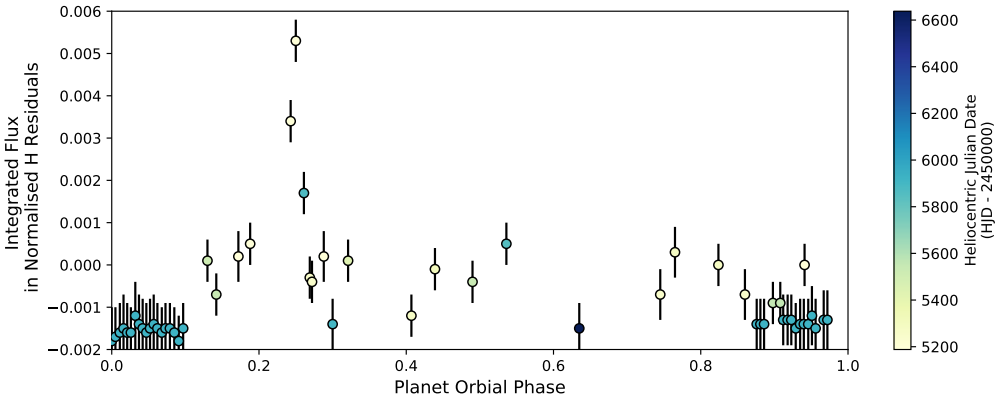

(b)

Figure 5.5: Measured absorption in the Ca II H & K line cores as a function of planet orbital phase. (a) Integrated flux in the normalised Ca II K residuals; (b) Integrated flux in the normalised Ca II H residuals.

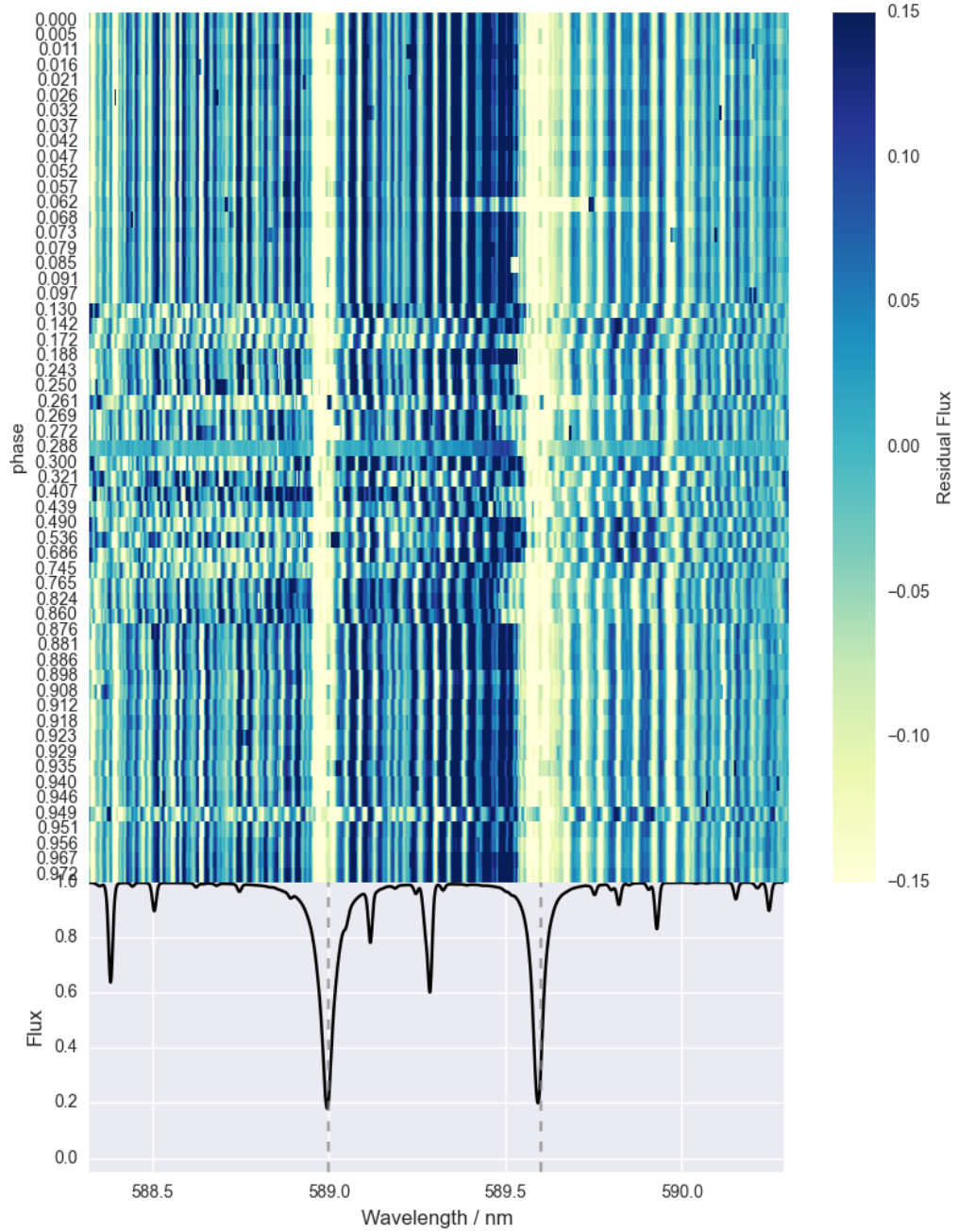

Figure 5.6: Trace of residual spectra centred at the Na I D doublet, notations as describe in Figure. 5.3.

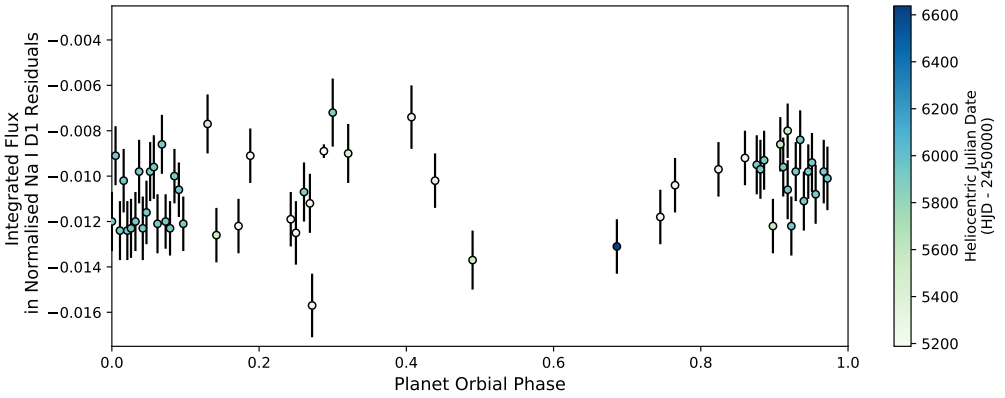

(a)

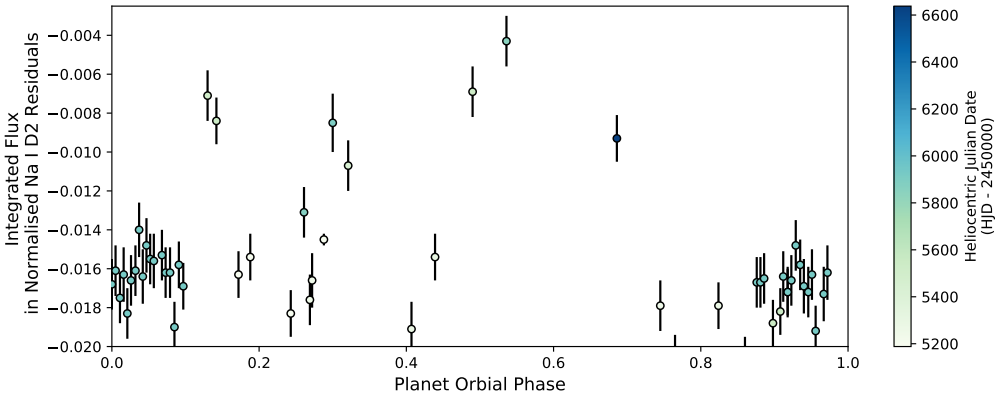

(b)

Figure 5.7: Measured absorption in the Na I D doublets according to Equation 5.2. Note the integrated flux scale is different to Figure 5.5. (a) Integrated flux in the normalised Na I D_1 residuals; (b) Integrated flux in the normalised Na I D_2 residuals.

5.4 Discussion and Conclusion

Using archival HIRES data, the variability of the evaporating atmosphere of WASP-12 b was investigated. The residual analysis showed enhanced absorptions in both the Ca II H & K and Na I D doublet line profiles, as well as hints of varying flux intensities in the line cores.

The cores of the Ca II H & K and Na I D doublet line profiles all showed strong absorptions compared to the template spectrum over all orbital phases. During transit, the absorption feature is expected for an evaporating planet. As previously noted by Fossati et al. (2010b), Haswell et al. (2012), and Fossati et al. (2013), the extended atmosphere of WASP-12 b overfills its Roche lobe and enters the blow-off phase. Gas lost from the planet diffuses into the circumstellar disc, forming a comet-like tail. The complete absorption observed in the Ca II and Na I lines is only possible if the absorbing material disperses to a considerable extent as to cover the chromospherically emitting stellar disc in its entirety (Haswell et al., 2012).

Enhanced absorption compared to the stellar template was further observed throughout the out-of-transit phases, implying the presence of an optically thick cloud of material around the system at all times. Thus suggesting the entire system is indeed shrouded by the diffused gas.

The intensities of the integrated flux residuals vary in both the Ca II H & K cores and the Na I D_1 and D_2 line cores. The measured fluctuation could suggest a varying opacity in the centres of these strong resonance lines. In fact, HST/COS NUV observations of Haswell et al. (2012) and Nichols et al. (2015) could not reproduced early ingress observed by Fossati et al. (2010b). This may imply an uneven distribution of absorbing gas around the system. This effect may be associated to the stellar radiation pressure, stellar wind, magnetic fields of the star and the planet, or a combination of all mechanisms.

5.4.1 Column Density of the Line Profiles

The density of the circumstellar gas disc required to produce the enhanced absorption can be inferred from the column density of the material. The column density N quantifies the number of particles in a unit area. This can be determined from the equivalent width W of the absorption line, and the theoretical curvature of growth (COG).

W is a measure of the strength of the spectral line, and is defined as the width of a rectangular box reaching up to the continuum of the spectrum which has the same area as the spectral line (Carroll and Ostlie, 2006):

$$W = \int \frac{F_c - F_\lambda}{F_c} \, d\lambda, \tag{5.4}$$

where F_c is the flux from the continuum spectrum outside the spectral line and F_λ is the flux of the absorption line. W is measured in angstrom Å. The COG is a logarithmic graph of W as a function of N. It describes the optical depth and the line broadening processes of a spectral line.

Column Density of Na

In the case of the Na I D lines, the absorption excess in the spectral lines were measured from the residual spectra. W of the residual Na I D lines were measured using the `splot` function of IRAF, which derives the width by fitting a Gaussian profile centred at the line core. Using the COG plot from Carroll and Ostlie (2006), the number density of Na I is derived, adopting the oscillating strength of $f = 0.645$ (Carroll and Ostlie, 2006) for Na I. The W and N of the Na I D lines are summarised in Table 5.3. The mean column density required to reproduce the observed absorption depth is around 5×10^{14} cm^{-2}. Bottom panel of Figure 5.8 shows the column density of Na I measured at respective orbital phases.

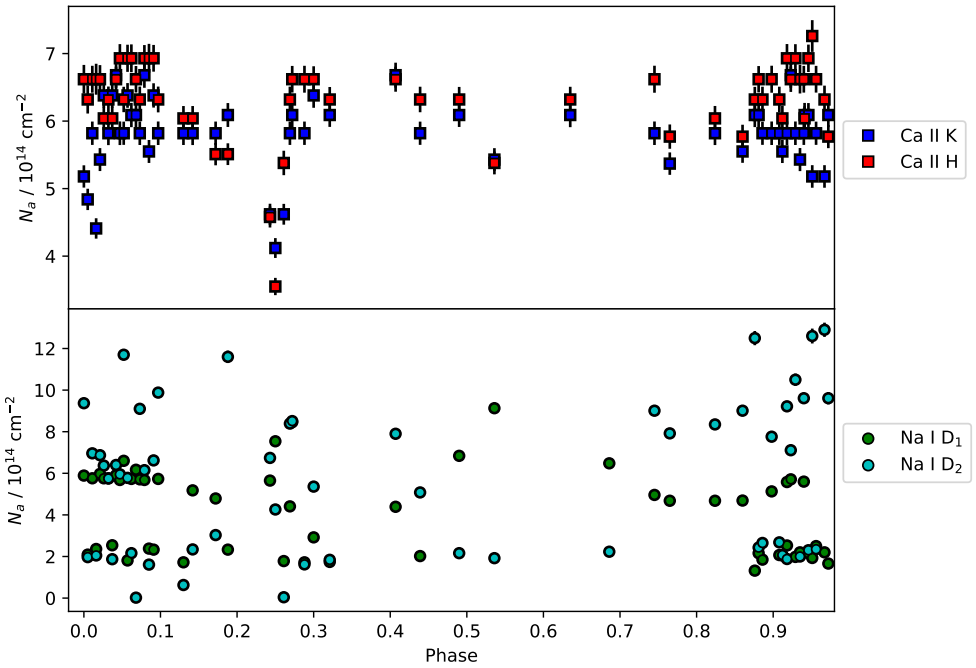

Figure 5.8: The measured column densities N_a of Ca II (top) and Na I (bottom) around the planetary orbit.

Column Density of Ca

To estimate the column density of Ca II is less straightforward. While it is believed that the activity of WASP-12 is hidden by a dense circumstellar material, the intrinsic chromospheric emission of the star is unknown. The stellar atmospheric model produced in Section 5.3.1 can only model the photospheric contribution of the star. Fossati et al. (2015), and subsequently Fossati et al. (2017), have reconstructed the Ca II H & K emission using the correlations between the intrinsic Lyα flux and the flux in Ca II H & K lines determined by Linsky et al. (2013). Unfortunately the Lyα emission of WASP-12 was not measured, thus the intrinsic chromospheric activity of WASP-12 used in this work was estimated from its age. Using the activity-age calibration of Mamajek and Hillenbrand (2008) and adopting the age of WASP-12 as 2 ± 1 Gyr from Table 5.1, the activity index $\log R'_{HK}$ of WASP-12 was determined to be -4.71.

The $\log R'_{HK}$ index is commonly derived from the S-index (S_{HIRES}) (Vaughan et al., 1978; Noyes et al., 1984a), and is a measure of the flux ratio between the H and K bandpasses centred at the Ca II H & K cores (3968.470Å and 3933.664Å with bandwidths of 1.09Å and 1.09Å, respectively), and the V and R continuum regions (centred at 3901.07Å and 4001.07Å with bandwidths of 10.0Å and 10.0Å, respectively) on either side of the line profiles:

$$S_{HIRES} = \frac{H + K}{V + R}. \tag{5.5}$$

The values of H, K, V, and R in this work were calculated from the mean fluxes of the corresponding bandpass which are shown in Figure 5.9. The wavelength windows used to measure the mean H and K fluxes are denoted by the black dashed lines. The wavelength windows used to measure the mean V and R fluxes are indicated by the shaded grey regions.

Using the calculated S_{HIRES} index, the total emission in the H and K passbands can be obtained:

$$R_{HK} = 1.340 \times 10^{-4} C_{cf} S_{HIRES}, \tag{5.6}$$

where C_{cf} is the conversion factor (Middelkoop, 1982; Rutten, 1984) which is parameterised as:

$$\log C_{cf} = 0.25(B - V)^3 - 1.33(B - V)^2 + 0.43(B - V) + 0.24. \tag{5.7}$$

$B - V$ is the colour of the star, which is 0.50 for WASP-12.

The photospheric contribution to the H and K emission must be subtracted from R_{HK} in order to obtain the true chromospheric emission of the star. Noyes et al. (1984a)

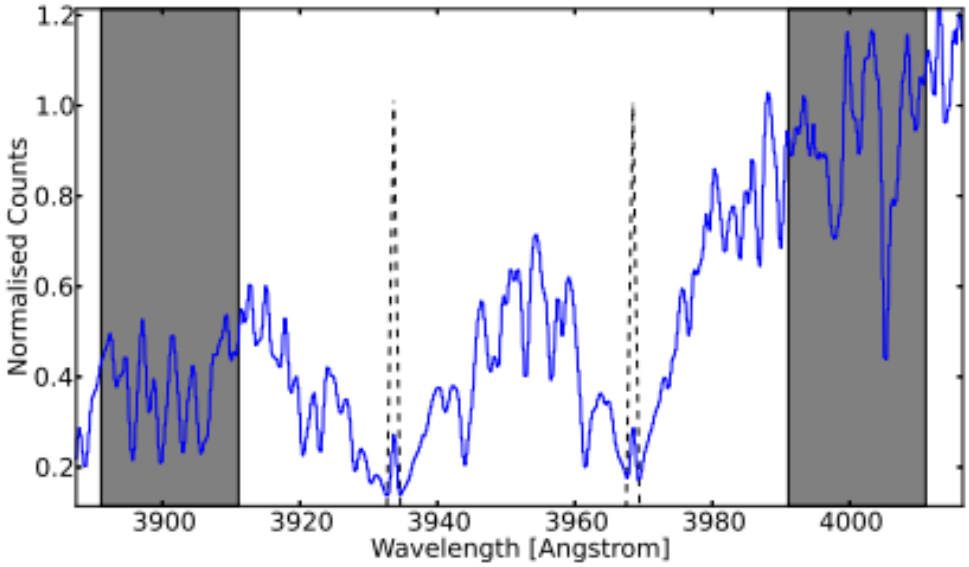

Figure 5.9: Spectrum centred at the Ca II H & K emission cores showing the wavelength windows used to calculate the S-index (Reproduced from Figure 2 of Staab et al. (2017) with permission from *Oxford University Press*). The black dashed lines indicate the 1.09Åwide bandpasses used to calculate the mean fluxes of H (3968.47Å) and K (3933.66Å). The shaded grey regions are the 20Åwide continuum windows used to measure the mean fluxes of V and R centred on 3901.07Åand 4001.07Å, repectively. The S-index is the ratio between the core fluxes H and K, and the continuum fluxes V and R.

derived a relation which estimates the photospheric emission using the $B - V$ colour:

$$\log R_{phot} = -4.02 - 1.40(B - V). \tag{5.8}$$

The true chromospheric emission R'_{HK} is obtained by $R'_{HK} = R_{phot} - R_{HK}$, and the activity index $\log R'_{HK}$ can be determined.

Using the derived activity index $\log R'_{HK}$ of WASP-12, the corresponding S_{MW} was determined as 0.2019. The chromospheric emission in the WASP-12 spectrum can be reconstructed using the definition of S_{MW} in Equation 5.5. The Ca II H & K emission profiles were modelled using a Gaussian profile with a width of $\approx$ 1Å. The flux ratio of the H and K passbands was fixed such that at the line centres $f(K)/f(H) = 1.048$ (Linsky and Avrett, 1970). The Gaussian profile was then added to the photospheric model described in Section 5.3.1. In order to obtain an emission profile with a strength equivalent to that of WASP-12's, a range of rescaling factors were used to adjust the size of the Gaussian profile. The S_{MW} index was iteratively calculated until the value matches the S_{MW} index of WASP-12.

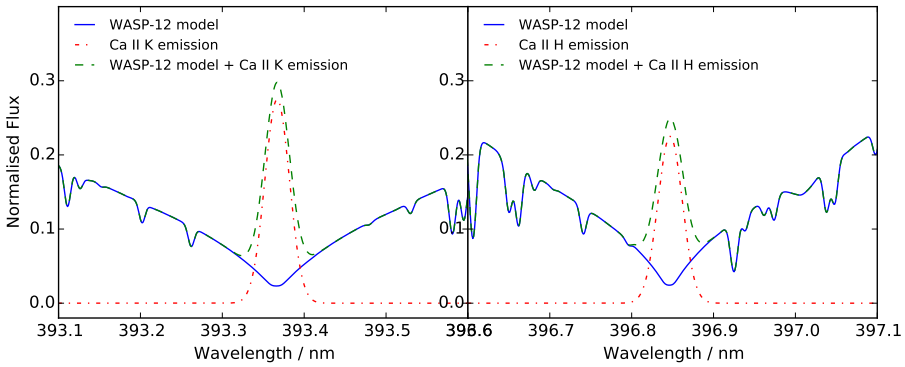

Figure 5.10: Reconstructed WASP-12 model spectrum. The model photosphere (blue solid line) of WASP-12 was generated using the SYNTHE radiative transfer code and the ATLAS9 atmospheric model. The chromospheric emission (red dashed-dot line) of WASP-12 was estimated using a Gaussian profile, and by assuming a flux equivalent to an activity index of $\log R'_{HK} = -4.71$ which was derived using the activity-age relations of Mamajek and Hillenbrand (2008). The reconstructed WASP-12 spectrum (green dashed line) is the sum of the photospheric model and the chromospheric emission.

The reconstructed WASP-12 spectrum is shown in Figure 5.10.

The residual spectra at all orbital phases were re-evaluated using the reconstructed model (see Figure 5.11 as an example). The column density of Ca II was derived following the method described in Section 5.4.1, and the oscillator strength $f = 0.66$ (Gallagher, 1967) was adopted. The mean column density of Ca II is around 6×10^{14} cm^{-2}, and the measured column densities are reported in Table 5.3. The top panel of Figure 5.8 shows the column density of Ca II measured at respective orbital phases.

Mura et al. (2011) modelled the exospheric tails and distribution of neutral sodium, ionised calcium and magnesium of close-in exoplanets. Na I atoms were found to be strongly influenced by stellar radiation pressure, forming a sodium neutral atom tail which extends in the anti-sun direction. On the other hand, photo-ionised Ca II and Mg II atoms could be influenced by the planet's magnetic fields and carried away by stellar wind to form an ion tail. More recent work by Carroll-Nellenback et al. (2017) investigated the interaction between gas lost from giant planets and stellar wind. Their simulations have demonstrated that absorbing material could disperse into up-orbit and down-orbit streams as a consequence of tidal and Coriolis forces. The streams of material would extend around the entire orbit over the star, and that the density of absorbing material appears to be non-uniformly distributed.

In Figure 5.5, a hint of emission is recorded in the Ca II H & K profiles at phase $\phi \sim 0.250$ and, to a lesser extent, just before phase $\phi \sim 0.800$. The change in residual

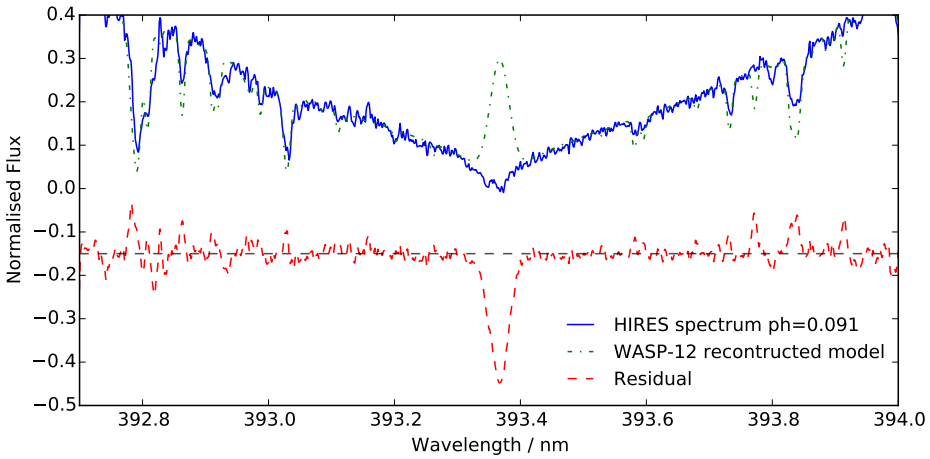

Figure 5.11: Residual analysis of WASP-12 centered at Ca II K, using the reconstructed WASP-12 model. The residual spectrum is offset by 0.15 for clarity.

flux intensity could be attributed to a change in the column density of the absorbing gas. However, such a reduction in density was not observed at the same orbital phases in the narrow Na I profiles. As discussed earlier, neutral and ionised atoms interact differently with stellar radiation, stellar winds, and magnetic fields, and the different properties of Na I and Ca II may result in different distributions hence optical thickness of absorbing material. The reduced Ca II column density may be linked to an increase in stellar wind at those phases.

Overall Gas Density of the Circumstellar Disc

The gas density of the circumstellar disc can be estimated using the mean column density of Ca II, which was measured to be $N_{Ca\ II} = 6 \times 10^{14}$ cm^{-2}. Assuming the gas disc extends to twice the planet orbital radius, the mass density of Ca II is $\rho_{Ca\ II} = (N_{Ca\ II}/2a) \times (M/N_A) = 5.83 \times 10^{-20}$ g cm^{-3}, where M/N_A is the mass of a single Ca atom ($(M/N_A)_{Ca\ II} = 6.65 \times 10^{-23}$ g). Fossati et al. (2010a) measured the Ca II abundance of WASP-12 as $\log(N/N_{\rm tot}) = -5.41 \pm 0.06$. If we further assume that Ca II constitutes around 10^{-6} of the circumstellar gas disc, the overall gas density would be $\rho_{disc} = \rho_{Ca\ II}/10^{-6} = 5.83 \times 10^{-14}$ g cm^{-3}.

Carroll-Nellenback et al. (2017) simulated the evolution of evaporating hot Jupiters leading to a circumstellar environment, and more recently, Debrecht et al. (2018) propagated the same method to simulate the evolution of the WASP-12 system. In both works, the circumstellar disc presented a 'doughnut' shape. Suppose the gas disc is a simple hollow cylinder which extends from the radius of WASP-12 to twice the orbital distance of WASP-

12 b, and has a height of R_s such that the star is entirely covered by the gas disc along the line of sight. The volume of this doughnut shaped disc is $\pi R_s \times [(2a)^2 - (R_s)^2]$. Therefore the overall gas mass of the circumstellar disc, assuming uniform density, is 9.14×10^{21} g. Following the method of Lecavelier Des Etangs (2007), the present atmospheric escape rate of WASP-12 b is 1.79×10^{11} g s^{-1}. Consequently, it would take over 1600 years to build up the measured gas density.

It is important to note that the work presented here did not account for the ISM column density in the direction of WASP-12. At a distance of 439 pc, the ISM Ca II column density was estimated as $\log N_{Ca\ II} \approx 13.50$ (Fossati et al., 2017), which is an order or magnitude lower than our measured mean $\log N_{Ca\ II} \approx 14.78$. Thus the density of the circumstellar disc is likely lower than what was derived.

5.4.2 Conclusion

A number of planet-hosting stars showed anomalously low stellar activity. Staab et al. (2017) found that 24% of their sample of planet host stars have a $\log R'_{HK}$ index below the basal level. Some of these systems, such as WASP-12, have an apparently low activity due to the presence of a circumstellar material. WASP-18, for instance, was shown to have an intrinsically low activity (Fossati et al., 2018). In order to identify the mechanism responsible for the anomalously low activity of these planet host stars, periodic spectroscopic observations centred at the Ca II H and K wavelength range are required.

The work presented here showed that enhanced absorption in the Ca II H and K and Na I D is observed across all orbital phases of the WASP-12 system, and that circumstellar material from the evaporating planet is responsible for the absence of an emission core. This effect is not unique to WASP-12 (e.g. Fossati et al. (2015)). One could take advantage of this intriguing property to investigate the feasibility to detect planets by searching for stars with anomalously low activity, as is demonstrated in the following chapter.

Table 5.3: Measured column densities of Ca II and Na I

Phase	W Ca II K Å	W Ca II H Å	N(Ca II K) cm^{-2}	N(Ca II H) cm^{-2}	W Na I D_1 Å	W Na I D_2 Å	N(Na I D_1) cm^{-2}	N(Na I D_2) cm^{-2}
0.000	0.3217	0.3669	5.18E+14	6.62E+14	0.6247	0.7970	5.89E+14	9.37E+14
0.005	0.3132	0.3635	4.84E+14	6.32E+14	0.3673	0.3572	2.09E+14	1.97E+14
0.011	0.3434	0.3722	5.82E+14	6.62E+14	0.6209	0.6834	5.76E+14	6.96E+14
0.016	0.2985	0.3686	4.41E+14	6.62E+14	0.3927	0.3642	2.36E+14	2.05E+14
0.021	0.3263	0.3698	5.43E+14	6.62E+14	0.6277	0.6775	5.97E+14	6.87E+14
0.026	0.3609	0.3570	6.38E+14	6.04E+14	0.6214	0.6522	5.76E+14	6.37E+14
0.032	0.3390	0.3632	5.82E+14	6.32E+14	0.6221	0.6294	5.76E+14	5.75E+14
0.037	0.3558	0.3504	6.38E+14	6.04E+14	0.4060	0.3478	2.54E+14	1.87E+14
0.042	0.3665	0.3731	6.68E+14	6.62E+14	0.6250	0.6559	5.91E+14	6.40E+14
0.047	0.3409	0.3781	5.82E+14	6.93E+14	0.6135	0.6281	5.68E+14	5.95E+14
0.052	0.3464	0.3636	5.82E+14	6.32E+14	0.6661	0.8915	6.60E+14	1.17E+15
0.057	0.3558	0.3795	6.38E+14	6.93E+14	0.3420	0.6205	1.81E+14	5.78E+14
0.062	0.3466	0.3748	6.09E+14	6.93E+14	0.6167	0.3737	5.73E+14	2.16E+14
0.068	0.3495	0.3727	6.09E+14	6.62E+14	0.6416	0.3697	6.17E+14	2.10E+12
0.073	0.3423	0.3580	5.82E+14	6.32E+14	0.6155	0.7849	5.71E+14	9.10E+14
0.079	0.3649	0.3822	6.68E+14	6.93E+14	0.6139	0.6412	5.68E+14	6.15E+14
0.085	0.3345	0.3781	5.55E+14	6.93E+14	0.3925	0.3216	2.38E+14	1.61E+14
0.091	0.3621	0.3761	6.38E+14	6.93E+14	0.3880	0.6676	2.33E+14	6.62E+14
0.097	0.3412	0.3612	5.82E+14	6.32E+14	0.6161	0.8212	5.73E+14	9.88E+14

Continued on next page

Table 5.3 – continued from previous page

Phase	W Ca II K Å	W Ca II H Å	N(Ca II K) cm^{-2}	N(Ca II H) cm^{-2}	W Na I D_1 Å	W Na I D_2 Å	N(Na I D_1) cm^{-2}	N(Na I D_2) cm^{-2}
0.130	0.3413	0.3574	5.82E+14	6.04E+14	0.3333	0.2133	1.72E+14	6.29E+13
0.142	0.3409	0.3504	5.82E+14	6.04E+14	0.5862	0.3892	5.18E+14	2.34E+14
0.172	0.3445	0.3396	5.82E+14	5.51E+14	0.5632	0.446	4.79E+14	3.03E+14
0.188	0.3530	0.3361	6.09E+14	5.51E+14	0.3874	0.8912	2.33E+14	1.16E+15
0.243	0.3037	0.3098	4.62E+14	4.58E+14	0.6122	0.6743	5.65E+14	6.74E+14
0.250	0.2875	0.2714	4.12E+14	3.55E+14	0.7113	0.5312	7.54E+14	4.26E+14
0.261	0.3070	0.3275	4.62E+14	5.38E+14	0.3395	0.1125	1.78E+14	4.10E+12
0.269	0.3439	0.3644	5.82E+14	6.32E+14	0.5410	0.7525	4.41E+14	8.39E+14
0.272	0.3471	0.3671	6.09E+14	6.62E+14	0.7549	0.7575	8.46E+14	8.51E+14
0.288	0.3440	0.3686	5.82E+14	6.62E+14	0.3335	0.3231	1.72E+14	1.62E+14
0.300	0.3563	0.3703	6.38E+14	6.62E+14	0.4353	0.5951	2.92E+14	5.36E+14
0.321	0.3532	0.3621	6.09E+14	6.32E+14	0.3357	0.3453	1.74E+14	1.84E+14
0.407	0.3699	0.3673	6.68E+14	6.62E+14	0.5401	0.7298	4.39E+14	7.90E+14
0.439	0.3452	0.3648	5.82E+14	6.32E+14	0.3613	0.5820	2.02E+14	5.08E+14
0.490	0.3516	0.3659	6.09E+14	6.32E+14	0.6773	0.3735	6.84E+14	2.16E+14
0.536	0.3291	0.3335	5.43E+14	5.38E+14	0.7854	0.3538	9.13E+14	1.92E+14
0.635	0.3470	0.3582	6.09E+14	6.32E+14	0.6588	0.3806	6.48E+14	2.23E+14
0.745	0.3421	0.3709	5.82E+14	6.62E+14	0.5738	0.7812	4.96E+14	9.01E+14
0.765	0.3305	0.3476	5.37E+14	5.77E+14	0.5574	0.7307	4.68E+14	7.92E+14
0.824	0.3392	0.3574	5.82E+14	6.04E+14	0.5578	0.7510	4.68E+14	8.35E+14

Continued on next page

Table 5.3 – continued from previous page

Phase	W Ca II K Å	W Ca II H Å	N(Ca II K) cm^{-2}	N(Ca II H) cm^{-2}	W Na I D_1 Å	W Na I D_2 Å	N(Na I D_1) cm^{-2}	N(Na I D_2) cm^{-2}
0.860	0.3374	0.3482	5.55E+14	5.77E+14	0.5582	0.7799	4.69E+14	9.01E+14
0.876	0.3483	0.3583	6.09E+14	6.32E+14	0.3669	0.9234	1.32E+14	1.25E+15
0.881	0.3499	0.3702	6.09E+14	6.62E+14	0.3731	0.3981	2.16E+14	2.43E+14
0.886	0.3457	0.3656	5.82E+14	6.32E+14	0.3460	0.4148	1.85E+14	2.65E+14
0.898	0.3413	0.3666	5.82E+14	6.62E+14	0.5836	0.7215	5.13E+14	7.76E+14
0.908	0.3448	0.3661	5.82E+14	6.32E+14	0.3659	0.4174	2.07E+14	2.68E+14
0.912	0.3325	0.3538	5.55E+14	6.04E+14	0.3640	0.3668	2.05E+14	2.07E+14
0.918	0.3390	0.3774	5.82E+14	6.93E+14	0.6085	0.7907	5.58E+14	9.22E+14
0.923	0.3636	0.3725	6.68E+14	6.62E+14	0.6151	0.6933	5.71E+14	7.11E+14
0.929	0.3426	0.3806	5.82E+14	6.93E+14	0.3581	0.8457	1.98E+14	1.05E+15
0.935	0.3244	0.3725	5.43E+14	6.62E+14	0.3771	0.3609	2.20E+14	2.00E+14
0.940	0.3449	0.3711	5.82E+14	6.62E+14	0.6092	0.8076	5.60E+14	9.61E+14
0.946	0.3528	0.3806	6.09E+14	6.93E+14	0.3740	0.3860	2.16E+14	2.30E+14
0.951	0.3185	0.3904	5.18E+14	7.26E+14	0.3539	0.9272	1.93E+14	1.26E+15
0.956	0.3453	0.3705	5.82E+14	6.62E+14	0.4024	0.3906	2.50E+14	2.35E+14
0.967	0.3183	0.3613	5.18E+14	6.32E+14	0.3773	0.9396	2.20E+14	1.29E+15
0.972	0.3489	0.3472	6.09E+14	5.77E+14	0.3273	0.8084	1.66E+14	9.61E+14

Chapter 6

Open Cluster Exoplanet Detection Survey

6.1 Advantages and Challenges in the Search for Exoplanets in Open Clusters

Most stars are believed to have formed in open clusters. The advantages of studying planets in open clusters have inspired a number of RV and transit surveys. In comparison to field stars, stars in open clusters are chemically and spatially homogeneous. This enables precise determination of stellar ages, distances, hence masses, radii, and temperatures using stellar evolutionary models. Precise measurements of a star's physical properties are required to infer planetary parameters. Therefore, open clusters offer ideal environments to examine planet occurrences. In addition, planets with well determined parameters could provide valuable constraints on the formation and migration paths of different systems.

Despite the thousands of exoplanets discovered to date, only a small fraction were found in open clusters. In RV surveys, stellar activity could hamper the derivation of precise RVs. This could be problematic for open clusters since young stars tend to rotate more rapidly and are more active. The first planets discovered in open clusters were ϵ Tauri b in the Hyades (M_p = 7.6 M_J; Sato et al. 2007), and TYC 5409-2156-1 b in NGC2423 (M_p = 10.6 M_J; Lovis and Mayor 2007) via the RV method. Subsequent discoveries by Quinn et al. (2012, 2014) showed that hot Jupiters do exist around Sun-like stars in open clusters, and that the hot Jupiter occurrence rate in open clusters ($0.99^{+0.96}_{-0.54}$%) is consistent with what was found in field stars (1.20 ± 0.38 %, Wright et al. 2012). The discoveries further demonstrated that the tidal circularisation timescales of hot Jupiters are comparable to the young ages of open clusters. Hence knowing the orbital properties of these hot Jupiters could help distinguish the migration mechanisms responsible for the systems.

Planets discovered via the transit method can provide physical characteristics of the systems. However, many transit surveys dedicated to the search for planets in clusters did not have the required sensitivity to acquire high precision photometry. High precision photometry became available when the *Kepler* mission came online. The quality of the data made the discoveries of small planets possible in open clusters. Meibom et al. (2013) reported the discoveries of two super-Earth sized planets, Kepler-66 b and Kepler-67 b, in the 1 Gyr old cluster NGC6811, which showed that planets can form in dense clusters and that the occurrence of small planets in open clusters is consistent with that for field stars.

While both the RV and transit surveys are beginning to produce fruitful results, these methods still require a significant amount of telescope time to monitor targets continuously for planet validation. In this chapter, a pilot study of a new detection technique is presented. The motivation, data acquisition, and reduction will be outlined, followed by the analysis, results and prospects for furture work.

6.2 Motivation

The hot Jupiter WASP-12 b presented in Chapter 5 is an example of a irradiated planet. This could trigger the blow-off phase where gas lost from the planet would diffuse into the planet orbit and form a circumstellar disc. Near-UV observations of the WASP-12 system showed enhanced absorption in the strong Mg II h & k resonance line cores. This effect was attributed to the presence of the circumstellar cloud which shrouds the entire system (Haswell et al., 2012).

The strength of the stellar chromospheric Ca II H & K emission cores is a useful measure of stellar magnetic activity. Fossati et al. (2013) examined the Ca II H & K lines of WASP-12 and found that the line cores are significantly depressed compared to HAT-P-7 and WASP-1, both of which have similar effective temperatures and ages to WASP-12. The apparently low chromospheric activity in WASP-12 was measured by Knutson et al. (2010), where its $\log R'_{HK}$ value was measured to be -5.500. The activity of WASP-12 falls well below the basal level ($\log R'_{HK} = -5.1$; Henry et al. 1996; Wright 2004) for solar metallicity dwarfs, indicative of extrinsic absorption. In fact, all six extreme low-activity outliers in the $\log R'_{HK}$-$(B-V)$ plane presented by Fossati et al. (2013) are exclusively planet hosting stars.

This observation was also echoed by Staab et al. (2017). Their extended study on the chromospheric activities of planet host stars (Knutson et al. 2010; Figueira et al. 2014) found that 24% of the sample have anomalously low $\log R'_{HK}$. They have interpreted this as an indication of gas lost from planets, where chromospheric emission in the Ca II H & K lines is hidden by the evaporated material. Staab et al. have further identified two low-mass short period planet hosts (Kepler-25 and Kepler-68), which also showed unusally

low activities. This suggested that the effect is not limited to inflated hot Jupiters. Any enhanced absorption, hence anomalously low $\log R'_{HK}$ value, could imply the presence of an evaporating planet.

In this pilot planet detection survey, the multi-object spectrograph FLAMES-GIRAFFE was used to observe stars in open clusters. Stars in open clusters are young, active and plentiful. The identification of low-activity young stars in the sample indicates the likely presence of a planet in orbit around the stars. Large number of high-resolution spectra centred on the Ca II H & K doublet can be collected at the same time on the same instrument. Thus reducing valuable telescope times to survey large number of stars.

6.3 Observations

6.3.1 Multi-Object Spectrograph FLAMES-GIRAFFE

The targets selected in this work were observed with FLAMES (Fibre Large Array Multi Element Spectrograph; Pasquini et al. (2002)), a multi-object spectrograph mounted on Unit 2 (Kueyen Telescope) of the ESO VLT (Very Large Telescope). FLAMES can access targets over a large FoV of 25 arcmin in diameter. Observations were obtained using the medium-high (R=5,500-65,100) resolution optical spectrograph, GIRAFFE, which has a 2×4 k EEV CCD (15 micron pixels). Using the MEDUSA fibre mode, the instrument can provide a pixel scale of 0.3"/pixel, and up to 132 separate objects (including sky fibres) can be observed at once. During a science exposure, the sky continuum is sampled simultaneously with the object using a sky fibre associated to the object fibre. The sky continuum is subsequently subtracted from the object spectrum during data reduction. To access the Ca II H and K lines, the HR02 (high resolution mode with filter number 2) setting with a resolving power of 22,700 was selected, which provided a wavelength coverage of 3854-4049 Å. The data were obtained in service mode, and subsequent data reduction was performed using the ESO GIRAFFE pipeline[1]. The procedures included standard calibration frame corrections, sky background subtraction, and wavelength calibration. The target selection is described below, and the observation details are listed in Table 6.1.

6.3.2 Open Clusters and Target Stars Selection

Targeting open clusters can allow a large number of stars to be observed at the same time. Planets could be detected around a large range of stellar masses. In addition, planets around stars in open clusters will also have a wide range of well determined ages. The open clusters selected in this work have a range of ages and distances in order to test this detection

[1] `http://girbldrs.sourceforge.net/`

method. The basic parameters of the clusters, including ages and distances, are listed in Table 6.1.

For each cluster, an input catalogue was generated with a list of target stars depending on a number of factors. Firstly, a list of targets was created using the Tycho-1 and Tycho-2 Catalog (Hoeg et al., 1997; Høg et al., 2000) centred around the centre of the cluster (see Table 6.1 for cluster positions). The stars in each cluster were selected based on their brightness and colours. Only bright stars with $V_{mag} < 14.0$ and $0.2 < B-V < 0.5$ were chosen, such that follow up photometry and RV are possible at ground-based facilities. The cluster membership of each star were also taken into consideration using criteria from the CSOCA catalogue (Kharchenko et al., 2005), which was based on the All-sky Compiled Catalogue of 2.5 Million Stars (ASCC-2.5; Kharchenko (2001)). The CSOCA catalogue provides cluster membership probability based on a star's proper motions (P_μ), photometry (P_{ph}) and position (P_s). To account for all aspects of the membership selection procedure, the combined probability P_c is defined as:

$$P_c = P_s \times min\{P_\mu, P_{ph}\} \tag{6.1}$$

Using equation 6.1, stars were ranked by their respective membership probability in the input catalogue. The FLAMES fibre configuration program - Fibre Positioner Observation Support Software (FPOSS), was used with the list of targets as the input catalogue. FPOSS then generated favourable fibre configurations which allocates fibres to as many targets as possible for observations.

Table 6.1: Basic properties of open clusters selected in the survey. Values were obtained from Kharchenko et al. (2005). The proper motions (μ_{RA} and μ_{DEC}) of the clusters were taken from Loktin and Beshenov (2003). E(B−V) is the reddening, and N_{stars} is the number of stars monitors in this survey.

Cluster	Observation Date	EXPTIME(s)	RA(J2000)	DEC(J2000)	μ_{RA} (mas/yr)	μ_{DEC} (mas/yr)	Distance (pc)	E(B−V)	Age (log t)	N_{stars}
NGC 5138	2015-07-26	2400	13h27m16.0s	-59d02m00s	-3.30 ± 0.30	-0.27 ± 0.25	1986	0.26	7.55	23
NCG 5460	2015-09-21	2400	14h07m27.0s	-48d20m36s	-5.96 ± 0.30	-2.35 ± 0.36	673	0.09	8.31	18
NGC 6067	2015-07-16	2400	16h13m11.0s	-54d13m06s	-0.98 ± 0.11	-4.86 ± 0.13	1417	0.4	8.01	43
NGC 6087	2015-08-06	2400	16h18m50.0s	-57d56m06s	-1.25 ± 0.14	-2.12 ± 0.14	901	0.18	7.93	35
NGC 6134	2015-08-06	2400	16h27m46.0s	-49d09m06s	0.48 ± 0.14	-3.13 ± 0.16	913	0.38	8.53	10
NGC 6281	2015-08-06	2400	17h04m41.0s	-37d59m06s	-3.25 ± 0.15	-5.03 ± 0.14	494	0.15	8.51	96
NGC 6405	2015-08-06	2400	17h40m20.0s	-32d15m12s	-2.38 ± 0.15	-7.19 ± 0.16	487	0.14	7.91	62
NGC 6494	2015-10-12	2400	17h57m04.0s	-18d59m06s	1.18 ± 0.16	-1.39 ± 0.14	628	0.36	8.52	125
NGC 6716	2015-10-12	2400	18h54m34.0s	-19d54m06s	-0.80 ± 0.24	-4.94 ± 0.25	789	0.2	7.47	11

6.4 Analysis

The Mount-Wilson method (Vaughan et al., 1978) is commonly used to measure chromospheric activity in a star. It measures the S-index, which is the flux ratio between the sum of the fluxes in the Ca II H & K line cores, and the sum of the fluxes in the nearby continuum window. This dimensionless S-index is then required to be calibrated to the Mount-Wilson scale using standard stars. However, the VLT/FLAMES-GIRAFFE spectrograph did not observe standard stars alongside open cluster targets. Hence, the method described by Linsky et al. (1979), which is described later, was applied in this survey to measure chromospheric emission in the open cluster samples.

6.4.1 Spectral Type Identification

The photometric data of individual targets were taken from the Tycho-2 catalogue (Høg et al., 2000). Some of these were measured to a relatively poor precision, with uncertainty as large as $\Delta(B-V) \sim 0.3$. The $B-V$ colour is an important ingredient in the determination of a star's chromospheric emission. Prior to measuring the $\log R'_{HK}$ values of the targets, the spectral types of the observed spectra were first classified by visual inspection. This was performed through comparing the library of stellar spectra taken from Pickles (1998), and the extinction corrected $(B-V)_0$ value of each object and the corresponding uncertainty were used as a guide.

The spectra of early-type stars are dominated by H-Balmer lines. The Ca II H and K lines are only visible from A-type stars onwards. In early A-type stars (A0 to ~A5), the Ca II H line is also heavily blended by the Hϵ λ3970 absorption line. The Ca II H and K lines grow to become the dominant absorption features in mid-A to later type spectra. For this reason, targets earlier than the A5 spectral types were removed from the sample, leaving 35 target spectra in total. A spectral type fitting procedure was carried out to accurately identify the spectral type of the remaining tagets. For each cluster, model spectra of type A5 to early G were generated using the SYNTHE radiative transfer code (Kurucz, 2005); the ATLAS9 (Kurucz, 2005) atmospheric model and the VALD line list database (Kupka et al., 2011) were used. The best-fit spectral type of each target was detemined using the reduced χ^2 goodness-of-fit test. The adopted $B-V$ colour of each target was converted from their corresponding fitted spectral type, using the table from Pecaut and Mamajek (2013). The list of surviving targets and their corresponding fitted spectral types are listed in Table 6.2. The plots of the individual spectrum of each target can be found in Appendix B.

Table 6.2: Parameters of targets with spectral type later than A5. The proper motions and parallax of the targets were obtained from (Gaia Collaboration et al., 2016a), and the $B - V$ were obtained from (Høg et al., 2000). Column 7 gives the fitted spectral type of each target and the corresponding fitted $B - V$ colours are given in column 8.

Identifier	RA (J2000)	DEC (J2000)	μ_{RA} (mas/yr)	μ_{DEC} (mas/yr)	Parallax (mas)	SpT	Fitted ($B - V$)	Cluster
TYC 8674-741-1	13h27m12.48s	-59d00m47.1s	-14.09	-9.42	2.40	F7	0.51	NGC5138
TYC 8674-1572-1	13h26m01.83s	-58d55m16.2s	6.50	-3.67	1.34	F5	0.44	NGC5138
TYC 8674-993-1	13h26m31.14s	-59d02m26.6s	-3.07	-9.51	1.35	F4	0.41	NGC5138
TYC 8674-1821-1	13h27m53.82s	-59d02m49.4s	-18.60	-2.60	...	F7	0.51	NGC5138
TYC 8268-660-1	14h06m23.94s	-48d18m18.7s	-17.58	-5.15	2.03	F8	0.53	NGC5460
TYC 8268-1748-1	14h06m46.3s	-48d12m57.4s	-5.71	-4.34	1.55	A7	0.21	NGC5460
TYC 8710-108-1	16h12m27.18s	-54d04m45.6s	-6.63	-14.61	0.77	F5	0.44	NGC6067
TYC 8710-249-1	16h13m02.79s	-54d21m36.9s	-1.88	-2.88	0.42	A9	0.26	NGC6067
TYC 8719-960-1	16h19m22.83s	-57d59m45.9s	-5.10	8.10	...	F4	0.41	NGC6087
TYC 8719-402-1	16h20m00.97s	-57d52m02.5s	-1.13	-2.34	2.45	F5	0.44	NGC6087
TYC 8719-2598-1	16h17m48.82s	-57d48m04.4s	-4.15	2.99	1.45	F9	0.55	NGC6087
TYC 8719-1382-1	16h19m34.54s	-58d06m33.2s	3.08	6.50	1.90	F9	0.55	NGC6087
TYC 8719-899-1	16h18m02.55s	-58d01m38.1s	2.60	-7.55	2.07	F9	0.55	NGC6087
TYC 8719-890-1	16h20m10.1s	-57d55m54.5s	-5.51	-12.76	1.16	F0	0.29	NGC6087
TYC 8320-1143-1	16h27m32.2s	-49d06m46s	1.78	-4.88	1.01	F5	0.44	NGC6134

Continued on next page

Table 6.2 – continued from previous page

Identifier	RA (J2000)	DEC (J2000)	μ_{RA} (mas/yr)	μ_{DEC} (mas/yr)	Parallax (mas)	SpT	Fitted $(B-V)$	Cluster
TYC 8320-1879-1	16h27m40.41s	-49d11m38.9s	4.16	-3.11	1.00	F5	0.44	NGC6134
TYC 8320-1491-1	16h27m36.27s	-49d13m04s	-1.94	-6.99	1.39	F5	0.44	NGC6134
TYC 8320-1394-1	16h27m38.32s	-49d12m06.5s	1.59	0.01	1.31	F4	0.41	NGC6134
TYC 8320-1695-1	16h28m00.18s	-49d09m06.3s	0.56	-5.10	0.77	F2	0.37	NGC6134
TYC 8320-1410-1	16h27m30.61s	-49d10m31.6s	2.04	-4.83	1.00	F3	0.39	NGC6134
TYC 7869-2283-1	17h04m31.74s	-37d55m24.7s	-2.10	-8.70	...	F0	0.29	NGC6281
TYC 7869-1925-1	17h05m07.11s	-37d51m56.8s	1.05	-2.74	1.76	F4	0.41	NGC6281
TYC 7869-2107-1	17h04m51.43s	-37d50m17.3s	-3.00	-4.66	1.81	F4	0.41	NGC6281
TYC 7869-856-1	17h04m48.45s	-37d50m05s	-1.66	-4.26	2.22	F0	0.29	NGC6281
TYC 7869-947-1	17h04m08.22s	-37d50m21.5s	2.20	-4.80	...	F1	0.33	NGC6281
TYC 7869-1257-1	17h05m32.16s	-37d56m52.4s	-0.41	-3.26	1.74	F5	0.44	NGC6281
TYC 7380-529-1	17h39m51.32s	-32d01m54.2s	-3.04	-5.23	2.09	A8	0.25	NGC6405
TYC 7380-363-1	17h40m10.97s	-32d00m19.1s	-3.40	-13.50	...	F0	0.29	NGC6405
TYC 7380-282-1	17h39m38.82s	-32d03m48.3s	6.90	-11.80	...	F0	0.29	NGC6405
TYC 7380-435-1	17h40m23.77s	-32d23m24.2s	1.50	3.50	...	A6	0.17	NGC6405
TYC 6258-518-1	17h57m41.71s	-19d04m48.4s	2.24	-3.76	1.32	F8	0.25	NGC6494
TYC 6258-685-1	17h56m21.94s	-18d52m31s	-5.64	1.61	3.06	F7	0.51	NGC6494
TYC 6289-1490-1	18h54m20.97s	-19d55m47.9s	-9.35	-35.43	3.07	F9	0.55	NGC6716
TYC 6289-1445-1	18h54m50.81s	-19d47m15.7s	5.30	0.16	1.33	F0	0.29	NGC6716
TYC 6289-1938-1	18h54m36.01s	-19d46m43.1s	-0.11	0.50	1.62	G0	0.60	NGC6716

6.4.2 The Chromospheric Emission of a star

The method developed by Linsky et al. (1979) measures the relative fluxes of the spectra and converts them to absolute surface fluxes. The observed absolute fluxes are then compared to theoretical models to derive the chromospheric emission. The details of the calibration method is described below.

Firstly, the stellar surface flux in a $\Delta\lambda = 50$ Å bandpass between 3925-3975 Å was computed using the $V - R$ colour of a star:

$$\log \mathscr{F}(\Delta\lambda) = 8.264 - 3.076(V - R) \text{ for } V - R < 1.30 \tag{6.2}$$

$$\log \mathscr{F}(\Delta\lambda) = 5.500 - 0.944(V - R) \text{ for } V - R > 1.30. \tag{6.3}$$

Very often, the $V - R$ colours are not available from literature so these values were derived from the $B - V$ colours. In this work, the $B - V$ colour were derived from the spectral type fitting process described earlier. The $B - V$ colour was then converted to $V - R$ using the table of Pecaut and Mamajek (2013).

The total surface flux above the zero flux level between the K_1 or H_1 minimum features is defined in Linsky and Ayres (1978) and Strassmeier et al. (2000) as:

$$\begin{aligned} \mathscr{F}(H_1) &= \frac{f(H_1)}{f_{50}} \times (50\mathscr{F}(\Delta\lambda)) \\ \mathscr{F}(K_1) &= \frac{f(K_1)}{f_{50}} \times (50\mathscr{F}(\Delta\lambda)). \end{aligned} \tag{6.4}$$

Here, f_{50} is the relative flux in a $\Delta\lambda = 50$ Å band (between 3925 and 3975 Å). $f(H_1)$ and $f(K_1)$ are the relative fluxes between the minimums in the H and K emission cores, which are defined as the fluxes in a $\Delta\lambda = 1$ Å band centred at 3968.47Å and 3933.66Å respectively. The relative fluxes were determined by the integration of the corresponding bandpasses between the spectrum and zero intensity. Figure 6.1 shows the spectral range used to calculate the total surface flux.

Once the total surface flux was derived, the underlying photospheric flux contribution must be subtracted to obtain the pure choromospheric emission. The net cooling rate in the chromosphere due to the H and K lines are defined as:

$$\begin{aligned} \mathscr{F}'(H_1) &= \mathscr{F}(H_1) - \mathscr{F}_{RE}(H_1) \\ \mathscr{F}'(K_1) &= \mathscr{F}(K_1) - \mathscr{F}_{RE}(K_1). \end{aligned} \tag{6.5}$$

where $\mathscr{F}_{RE}(H_1)$ and $\mathscr{F}_{RE}(K_1)$ are the H_1 and K_1 indices for radiative equilibrium (RE) model atmospheres with no chromospheres. Linsky et al. (1979) fitted the H_1 and K_1 indices

using the $\mathscr{F}_{RE}(H_1)$ and $\mathscr{F}_{RE}(K_1)$ values for 13 main-sequence stars computed by Kelch et al. (1979). From their fit, Linsky et al. (1979) further derived the $\mathscr{F}_{RE}(H_1)$ and $\mathscr{F}_{RE}(K_1)$ values for a number of dwarf stars. Figure 6.2 shows the $\mathscr{F}_{RE}(H_1)$ and $\mathscr{F}_{RE}(K_1)$ values of dwarf stars in the Linsky et al. (1979) sample. The sample was fitted with a quadratic function, and was used to determine the $\mathscr{F}_{RE}(H_1)$ and $\mathscr{F}_{RE}(K_1)$ values for the targets in this work.

The chromospheric radiative loss in the H and K lines normalised to the total surface luminosity of the star is:

$$R'_{HK} = \frac{\mathscr{F}'(H_1) + \mathscr{F}'(K_1)}{\sigma T_{eff}^4} \tag{6.6}$$

where $\sigma = 5.6704 \times 10^{-5}$ ergs cm^{-2} s^{-1} K^{-4} is the Stefan-Boltzmann constant. T_{eff} is the effective temperature, estimated from the $B - V$ colour of the star and conversion table of Pecaut and Mamajek (2013). Figure 6.3 shows the conversion between the effective temperatures $T_{\rm eff}$, the $V - R$ colours, and the $B - V$ colours. The derived chromospheric radiative loss R'_{HK} and the activity index $\log R'_{HK}$ of the each target are reported in Table 6.3.

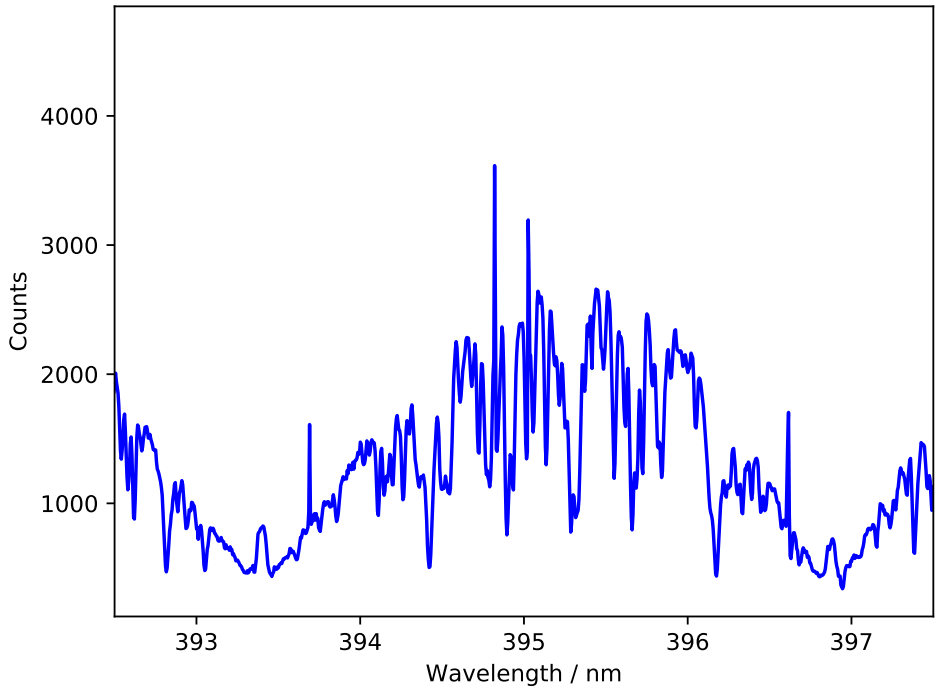

Figure 6.1: The observed spectrum of TYC6289-1938-1. Spectral range centred at the Ca II H and K (between 3925 and 3975 Å) was used to calculate the total surface flux.

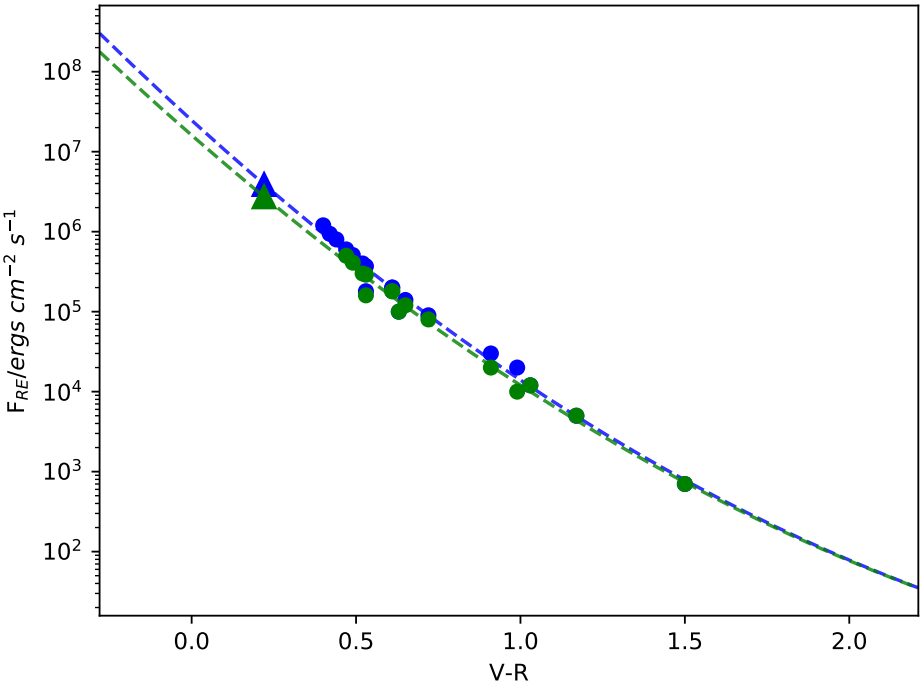

Figure 6.2: The H_1 (green circles) and K_1 (blue circles) indices for radiative equilibrium (RE) model atmospheres with no chromospheres. The values were taken from Table 1A of Linsky et al. (1979). The green and blue dashed lines are the quadratic fits for the H_1 and K_1 indices respectively. The green and blue triangles are the interpolated H_1 and K_1 indices of TYC6289-1938-1, respectively.

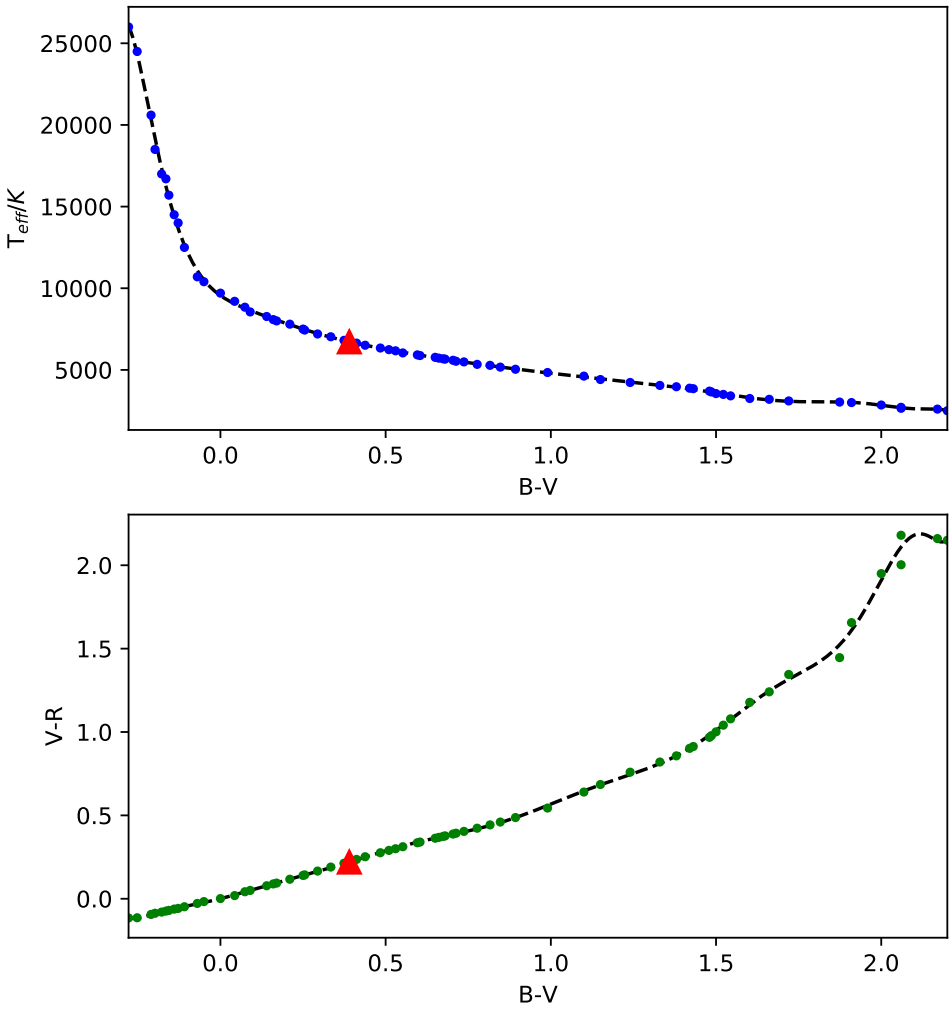

Figure 6.3: The effective temperature T_{eff} (top panel) and the $V-R$ colour (bottom panel) of a star was interpolated from the $B-V$ colour of a star, using the conversion table of Pecaut and Mamajek (2013). The red triangles are the interpolated T_{eff} and the $V-R$ colour of TYC6289-1938-1.

Table 6.3: Chromospheric activity measurements of stars in open clusters. The $B-V$ values were adopted from the target's best-fit spectral type described in Section 6.4.1. The $V-R$ values were interpolated from the conversion table of Pecaut and Mamajek (2013). Column 5 shows the flux ratio between the relative fluxes at the minimums in the H and K emission cores. The chromospheric radiative loss in the H and K lines R'_{HK} are reports in column 6. The derived activity index $\log R'_{HK}$ is in column 7. Column 8 and 9 gives the derived age t/yr from the activity-age relation described in Section 6.5.1 and the mean age τ_{cl}/yr of the Clusters respectively. The signal-to-noise ratio (SNR) of at the Ca II spectral range is given in column 10.

Identifier	Cluster	$B-V$	$V-R$	f_H/f_K	R'_{HK}	$\log R'_{HK}$	$\log(t)$	$\log(\tau_{cl})$	SNR
TYC 8674-741-1	NGC 5138	0.51	0.29	0.9173	9.08E-05	-4.04	8.42	7.55	55.76
TYC 8674-1572-1	NGC 5138	0.44	0.25	1.0313	9.74E-05	-4.01	8.38	...	59.45
TYC 8674-993-1	NGC 5138	0.41	0.23	1.0328	9.84E-05	-4.01	8.37	...	85.08
TYC 8674-1821-1	NGC 5138	0.51	0.29	0.9137	9.42E-05	-4.03	8.40	...	60.96
TYC 8268-660-1	NGC 5460	0.53	0.30	0.9084	1.02E-04	-3.99	8.35	8.31	50.33
TYC 8268-1748-1	NGC 5460	0.21	0.12	0.6529	2.56E-04	-3.59	7.84	...	83.27
TYC 8710-108-1	NGC 6067	0.44	0.25	0.7376	3.04E-04	-3.52	7.75	8.01	45.61
TYC 8710-249-1	NGC 6067	0.26	0.14	0.8186	4.24E-05	-4.37	8.84	...	211.49
TYC 8719-960-1	NGC 6087	0.41	0.23	0.9060	2.46E-04	-3.61	7.86	7.93	18.12
TYC 8719-402-1	NGC 6087	0.44	0.25	0.9052	2.09E-04	-3.68	7.96	...	36.63
TYC 8719-2598-1	NGC 6087	0.55	0.32	0.8032	2.24E-04	-3.65	7.92	...	35.55

Continued on next page

Table 6.3 – continued from previous page

Identifier	Cluster	$B-V$	$V-R$	f_H/f_K	R'_{HK}	$\log R'_{HK}$	$\log(t)$	$\log(\tau)$	SNR
TYC 8719-1382-1	NGC 6087	0.55	0.32	0.8484	1.61E-04	-3.79	8.10	7.93	22.22
TYC 8719-899-1	NGC 6087	0.55	0.32	0.8198	2.11E-04	-3.68	7.95	...	21.85
TYC 8719-890-1	NGC 6087	0.29	0.16	0.9442	2.75E-04	-3.56	7.80	...	25.59
TYC 8320-1143-1	NGC 6134	0.44	0.25	1.0751	5.32E-05	-4.27	8.71	8.53	29.95
TYC 8320-1879-1	NGC 6134	0.44	0.25	0.9287	1.54E-04	-3.81	8.13	...	31.89
TYC 8320-1491-1	NGC 6134	0.44	0.25	0.9579	5.40E-04	-3.27	7.43	...	39.02
TYC 8320-1394-1	NGC 6134	0.41	0.23	1.0213	9.89E-05	-4.00	8.37	...	69.85
TYC 8320-1695-1	NGC 6134	0.37	0.21	1.0520	9.52E-05	-4.02	8.39	...	44.36
TYC 8320-1410-1	NGC 6134	0.39	0.22	1.1843	5.88E-05	-4.23	8.66	...	64.69
TYC 7869-2283-1	NGC 6281	0.29	0.16	0.7776	2.27E-04	-3.64	7.91	8.51	77.03
TYC 7869-1925-1	NGC 6281	0.41	0.23	0.7551	3.35E-04	-3.48	7.69	...	47.91
TYC 7869-2107-1	NGC 6281	0.41	0.23	0.8714	1.48E-04	-3.83	8.14	...	95.77
TYC 7869-856-1	NGC 6281	0.29	0.16	0.8091	2.18E-04	-3.66	7.93	...	96.37
TYC 7869-947-1	NGC 6281	0.33	0.19	0.9415	1.06E-04	-3.97	8.33	...	114.26
TYC 7869-1257-1	NGC 6281	0.44	0.25	0.9801	1.66E-04	-3.78	8.08	...	79.36
TYC 7380-529-1	NGC 6405	0.25	0.14	0.9346	1.08E-04	-3.97	8.32	7.91	256.60
TYC 7380-363-1	NGC 6405	0.29	0.16	0.9593	1.96E-04	-3.71	7.99	...	154.63
TYC 7380-282-1	NGC 6405	0.29	0.16	0.8535	2.26E-04	-3.65	7.91	...	102.02
TYC 7380-435-1	NGC 6405	0.17	0.10	0.8331	1.65E-04	-3.78	8.09	...	135.61
TYC 6258-518-1	NGC 6494	0.25	0.14	0.7935	4.59E-04	-3.34	7.52	8.52	31.10
TYC 6258-685-1	NGC 6494	0.51	0.29	1.0093	8.25E-05	-4.08	8.47	...	64.19

Continued on next page

Table 6.3 – continued from previous page

Identifier	Cluster	$B-V$	$V-R$	f_H/f_K	R'_{HK}	$\log R'_{HK}$	$\log(t)$	$\log(\tau)$	SNR
TYC 6289-1490-1	NGC 6716	0.55	0.32	0.8596	1.18E-04	-3.93	8.27	7.47	26.95
TYC 6289-1445-1	NGC 6716	0.29	0.16	0.7513	1.98E-04	-3.70	7.99	...	99.56
TYC 6289-1938-1	NGC 6716	0.60	0.34	0.8790	1.82E-04	-3.74	8.03	...	53.05

6.5 Discussion

The chromospheric activity of a star can be measured in the Ca II H and K cores. In the presence of a close-in evaporating planet, the chromospheric emission could be masked by the evaporated material, leading to an anomalously low activity index. The stellar activities of the open cluster samples were derived using the method prescribed by Linsky et al. (1979), which measures the chromospheric contribution to the stellar surface fluxes from the relative fluxes of the H and K cores. Figure 6.4 shows the activity index $\log R'_{HK}$ of each target as a function of $B - V$.

Vaughan and Preston (1980) presented the chromospheric emission of F to G type northern stars in an attempt to elucidate the relation between chromospheric activity and age. The result of the survey showed a bimodal distribution in the stellar chromospheric emission, which could indicate the fluctuation of star formation rates in the past, or that the relation between activity and age is not linear across different stages of stellar ages. To verify this observation, Henry et al. (1996) conducted a survey to measure the chromospheric activity of southern solar-type stars ($0.50 < B - V < 1.00$). Not only did the two samples agreed in terms of the distribution of stellar activity, Henry et al. also found an overabundance of very inactive stars with $\log R'_{HK} < -5.10$. The presence of very inactive stars were attributed to the Maunder Minimum phase, in which the stars have entered a phase of temporary inactivity. Wright (2004) analysed activity catalogues from multiple surveys and found that nearly all of the very inactive stars in the Henry et al. sample are evolved or subgiant stars instead. The lack of main-sequence stars with $\log R'_{HK} < -5.10$ may imply a minimum activity that must be present in main-sequence stars.

Using activity measurements from multiple surveys, Fossati et al. (2013) showed that main-sequence stars with anomalously low activity indices are almost exclusively hot Jupiter hosts, and that the apparent flux suppression in the Ca II H and K cores is a result of the presence of an evaporating planet. Observations by Staab et al. (2017) further depicted the anomalously low activity of a star can be observed in multiplanet systems with low mass, short period planets. As seen in Figure 6.4, the analysis of the cluster samples found no candidates below the basal level ($\log R'_{HK} = -5.10$). However, only middle to late-type stars $0.4 < B - V < 1.0$ were used to determine this basal level in literatures. The chromospheric activity in earlier type stars are not as well understood, thus the basal activity level may be different.

6.5.1 Chromospheric Activity and Age of Open Clusters

Chromospheric activity is strongly correlated to the stellar rotation rate. A star spins down as it ages, the chromospheric emission also decreases (Wilson, 1963; Kraft, 1967; Noyes

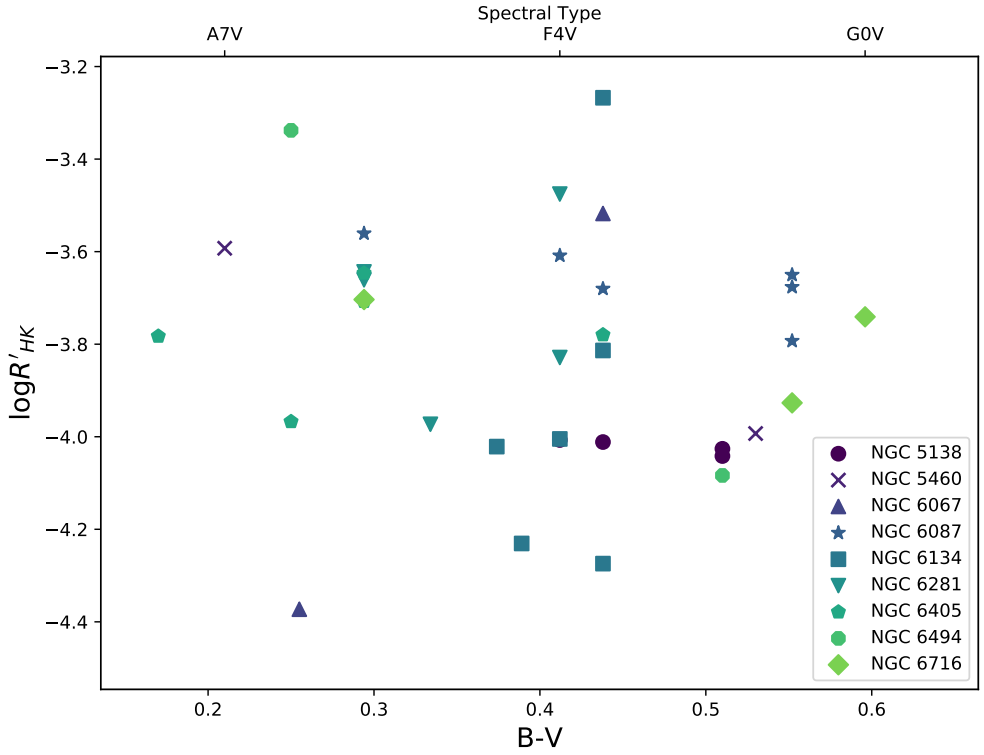

Figure 6.4: Chromospheric activity index $\log R'_{HK}$ as a function of $B-V$ of the open cluster samples listed in Table 6.3.

et al., 1984a). For this reason, the measurement of chromospheric emission via the activity index $\log R'_{HK}$ is a common practice to estimate stellar ages. Mamajek and Hillenbrand (2008) analysed the R'_{HK} measurements of young stellar clusters to constrain the activity-age relation for solar type dwarfs ($0.5 < B - V < 0.9$). By fitting the mean $\log R'_{HK}$ of each cluster as a function of their ages, Mamajek and Hillenbrand parametrised the activity-age relation as:

$$\log \tau = -38.053 - 17.912 \log R'_{HK} - 1.6675 (\log R'_{HK})^2 \tag{6.7}$$

where τ is the stellar age in years, and this relation can be approximately applied to stars with $-5.1 < \log R'_{HK} < -4.0$ and $6.7 < \log \tau < 9.9$. Mamajek and Hillenbrand noted in their study that stellar activity is correlated to the colour of a star. Moreover, stars with high cluster membership probabilities have $\log R'_{HK}$ values close to the mean $\log R'_{HK}$ value of the cluster, which is not a surprise as cluster members should have similar ages.

Following similar philosophy, an effort was made to derive an activity-age relation for earlier type stars using the cluster samples in this survey. If a target has an age significantly older than the mean age of the cluster, it implies that the star has a significantly lower chromospheric activity than expected. For each cluster, the slope $m = \Delta \log R'_{HK} / \Delta(B - V)$ was calculated. The mean $\log R'_{HK}$ value of each cluster was then evaluated for a hypothetical cluster member at $B - V = 0.4$. The mean $\log R'_{HK}$ value of the hypothetical cluster member is plotted as a function of the cluster age in Figure 6.5. Due to limited sample size in the clusters, we only fit the mean activity of clusters with more than 3 members in our sample. Similar to Soderblom et al. (1991), a linear fit to the data set gives:

$$\log \tau = 3.27 - 1.27 \log R'_{HK}. \tag{6.8}$$

The mean $\log R'_{HK}$ of NGC5138 appears to be an outlier, and the removal of this value from the entire data set improves the standard deviation from 0.42 to 0.40. Therefore, the final adopted fit does not contain the mean $\log R'_{HK}$ of NGC5138. However, the unexpectedly low mean activity of the NGC5138 may imply that the activity-age relation of late A to F stars may not be a simple linear correlation. Using Equation 6.8, the ages of individual targets were evaluated and listed in Table 6.3. To 3-σ confidence, we do not find any stars with an age significantly older than the age of the cluster.

6.5.2 Outlook

The occurrence rate of hot Jupiters in open clusters is $\sim 0.99\%$ (Quinn et al., 2014), which is comparable to what is expected in field stars. The sample size of our targets is too small to determine whether probing the stellar chromospheric activity of members in open clusters is a feasible way for planet detection.

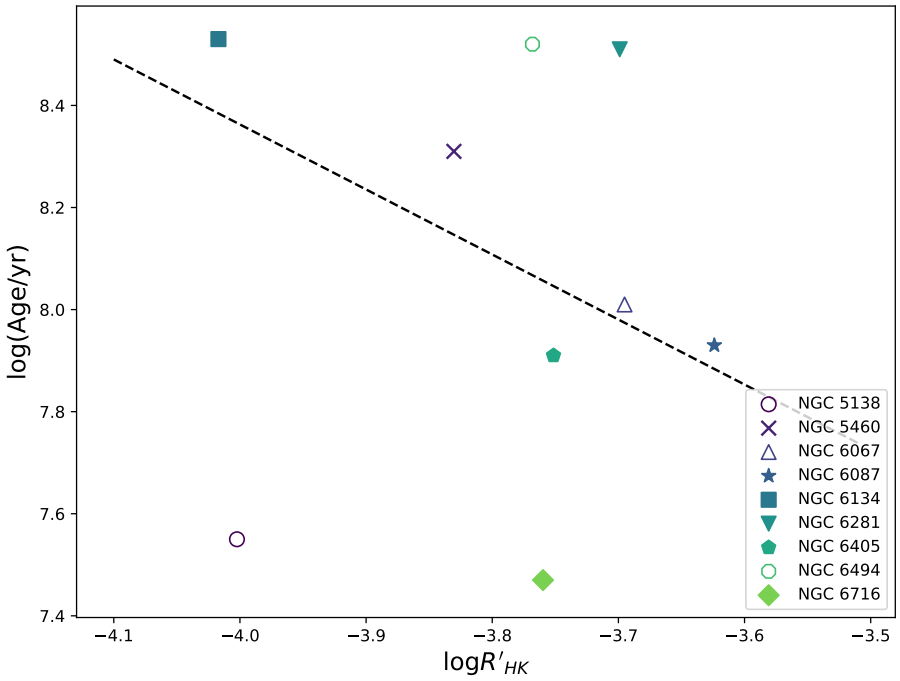

Figure 6.5: The mean $\log R'_{HK}$ values of a hypothetical cluster member with $B - V = 0.4$ as a function of the cluster ages. The filled points were used to fit the activity-age relation. The best-fit linear relation is denoted as the black dashed line.

A number of improvements are required to further investigate the feasibility of this method:

1. **Increase sample size significantly** - Our initial selection process selected targets based on membership probability and the visual magnitude of the stars only. This proved to be problematic as open clusters are, on average, several hundreds parsecs away. Hence, only early type stars would be bright enough for spectroscopic observations. The large distances of the clusters also mean that the photometric precision of individual targets can be somewhat inaccurate. This can lead to erroneous activity measurements and target selection. Although the spectral type of the star can be correctly classified by spectral type fitting (see Section 6.4.1), an initial sample of the order 1000 is required such that a final sample of at least several hundreds of stars can be drawn. In our sample, $\sim$ 30% of the stars have a $B-V$ uncertainty of > 0.25, corresponding to a difference of several sub-spectral types.

2. **Select nearby open clusters** - Because of the large distances of open clusters, the majority of bright targets are early type stars. To overcome this, targets should be selected in nearby clusters. At $\sim$ 500 pc, a G0 type star would have $V_{mag} \approx 12.0$. With similar set up as this work, a spectrum with SNR $\sim$ 30 can be acheived. The data would provide reasonable quality for activity measurements. Furthermore, the recent GAIA data release (Gaia Collaboration et al., 2018a) contains improved measurements of the astrometry, photometry and radial velocities of stars which can be used in the selection of high probablity cluster members.

Some positive outcomes can be drawn from this experiment. Firstly, the quality of the spectra observed showed that high SNR data can be achieved which enables flux measurements at the H and K cores (see Table 6.3 for SNR of individual spectra and Appendix B for plots of each spectra). Secondly, the technique employed in this work demonstrated that the chromospheric activity of multiple targets can be studied at the same time. Although inconclusive at this stage, the methods described in this work place target stars on the same $\log R'_{HK}$ - $B-V$ scale such that activities of young stars can be analysed, and hence stars with anomalously low activity can be efficiently identified.

Chapter 7

Conclusion

7.1 Summary

A majority of the currently known exoplanetary systems have physical properties and configurations that are remarkably different from our own solar system. In this thesis, the characteristics of a diverse range of newly discovered planets were explored. The variability of a planet's evaporating atmosphere was examined. This work also investigated a novel planet detection method in an attempt to reduce precious telescope time that is normally required to identify planet host stars.

Using the ground-based transit survey SuperWASP, three new exoplanets were discovered, and the analyses of the systems were presented in Chapter 3. Because of the limit in the precision of ground-based photometry, the detection of Neptunes or super-Earths has always been a challenge. The discovery of WASP-127 b demonstrated the capability of the detection of Neptunes from ground-based facilities. Combined with follow up RV observations, WASP-127 b was validated to be a highly inflated Neptune mass planet which has a radius as large as the radius of the Jupiter, making it one of the least dense planets ever known. By inferring the bulk density of the planet, we found a number of planet evolution theories that could explain the unusually inflated radius of WASP-127 b. These included increased stellar irradiation, tidal heating, Ohmic heating, and increased atmospheric opacity of the planet. WASP-127 b also lies inside the short-period Neptune desert, where a lack of intermediate-mass planets is believed to be a consequence of the distinct formation mechanisms of two different planet populations. To have found WASP-127 b inside this region may imply that the Neptune desert is smaller than previously thought.

In addition to an inflated Neptune, two other hot Jupiters were also detected. WASP-136 b is an inflated hot Jupiter which orbits a slightly evolved star. Finding planets around evolved stars is rare since the star's corotation radius increases with the increasing radius

of an evolving star. The planet would experience orbital decay and eventually reach the Roche limit and be tidally destroyed. An estimated remaining lifetime of $\sim$ 0.420 Gyr is predicted before WASP-136 b is engulfed by its host. The inferred bulk density of WASP-138 b suggests that the planet has $\sim$ 10 $M_{\oplus}$ of heavy elements in the core. The detection of WASP-138 b around a slightly metal poor star, however, weakens the planet discovery dependence on stellar metallicity. The discovery of such a system implies that WASP-138 b may have accreted its mass from a gas rich disc in the past.

It is best to utilise space missions to detect small planets. The *K2* mission succeeded *Kepler* in the search for transiting planets. The data obtained with *Kepler*/*K2* provided exceptional photometric precision which have a significant increase in the number of known Neptunes and super-Earths. Small planets have a wide range of radii and hence a range of bulk compositions. Their internal compositions can be deduced if their masses are known. A large planetary mass uncertainty can lead to a poorly constrained planet composition. The exact mass of CoRoT-7 b, for example, has been disputed in the past, and consequently its inferred internal structure could vary from a pure rocky planet to a pure water planet. In Chapter 4, the detection and validation of the super-Earth EPIC 206011496 b was presented. Thanks to the high precision radial velocity measurements with HARPS, the mass of EPIC 206011496 b was constrained with a precision of 13%. This in turns provided clues on the evolution history of the planetary system. Theoretical models predict the planet to be predominantly rocky with over 70% of silicate mantle by mass. Moreover, we noticed that the planet lies on the lower limit of the photoevaporation gap, where a paucity of planets was observed. EPIC 206011496 b has a short orbital period, thus the planet is susceptible to strong irradiation which could have seen the atmosphere of the planet completely eroded away after it was formed.

Finding planets beyond our Solar System is only the first hurdle. Additional analysis must be performed to understand the features and star-planet interaction in extreme environments. Exoplanets discovered from ground-based surveys usually provide bright enough targets which can be subjected to follow up observations. One of many interesting phenomena observed in exoplanetary systems was the evaporating atmospheres of hot Jupiters. This particular characteristic was observed in the system WASP-12, where in-transit NUV observations of the system showed enhanced transit depths, as well as the complete absorption in the Mg II doublet. This lead to speculations that the system is shrouded by evaporated planet material.

Chapter 5 presented the investigation of the variability of the evaporating atmosphere of WASP-12 b. Using archival HIRES spectra centred on the Ca II H and K and the Na I D lines, the correlation between the planet's orbital period and its evaporating atmosphere was explored. Enhanced absorptions were measured in the cores of the Ca II H and

K and the Na I D lines across most orbital phases, supporting the presence of a circumstellar material. Furthermore, a varying flux intensity was seen in the line cores, indicating the circumstellar material has a non-uniform density. The chromospheric emission of WASP-12 b was reconstructed such that the column density $N_{Ca\ II}$ of Ca II can be measured. The result showed that $N_{Ca\ II} = 6 \times 10^{14}$ cm^{-2} is required to produce the observed absorption in the Ca II H and K lines. Similar result was obtained for Na I, where $N_{Na\ I} = 5 \times 10^{14}$ cm^{-2}. Using the Ca II abundance measured by Fossati et al. (2010a), the overall gas density of this circumstellar disc was determined to be 5.38×10^{-14} g cm^{-3}.

The most widely used planet detection methods are transit photometry and the radial velocity method. While both methods are successfully producing statistically validated planets and candidates, they still require a significant amount of dedicated telescope time to identify planet host stars. Building on the established results of WASP-12 b and a number of chromospheric activity surveys of planet host stars, Chapter 6 investigated a novel method which aimed to provide an efficient, alternative way for planet detection.

Approximately 24% of planet host stars were confirmed to have anomalously low activity index in previous literatures. The result was attributed to the presence of an evaporating planet, where out-flowing atmospheric material suppresses the intrinsic activity of the host star. In the pilot detection survey, the multi-object spectrograph FLAMES-GIRAFFE was used to observe stars in open clusters, where a large number of high resolution, high SNR spectra centred at the Ca II H and K cores can be obtained at once. Stars in open clusters are young and hence have an active chromosphere. Finding a star with an anomalously low activity in the cluster survey is an indication of the presence of an evaporating planet. Due to the large distances of open clusters, only mid-A to F type stars ($0.2 < B - V < 0.6$) are bright enough to be observed, which resulted in a small sample size. Using this sample, the activity-age relation was derived based on the mean activity and the age of each cluster. Stars with unexpectedly low chromospheric activity may be identified using this relation. No anomalously low activity stars were identified in our sample. Although further improvement is necessary, the survey showed that the technique can obtain a large number of good quality spectra where stellar activity of the targets can be measured from the Ca II H and K cores. Any stars with anomalously low $\log R'_{HK}$ can be identified quickly.

7.2 Future work

The discoveries of new planets provide exceptional targets for follow up observations and characterisations in the future. WASP-127 b has a massive atmospheric scale height of 2500 km, and orbits a bright star of $V_{\rm mag} = 10.17$, which makes the planet one of the best for atmospheric characterisation. Recent follow up transmission spectroscopy have

indeed showed that the planet is cloud free, and have hints of metal elements (TiO, VO and Na) in its atmosphere. The launch of JWST is highly anticipated as it can constrain bulk atmospheric properties (e.g. Greene et al. (2016)) of highly inflated planets such as WASP-127 b.

On the other hand, the slightly evolved system WASP-136 is a great example to explore the tidal interaction between a close-in planet and an evolving star. Along with the sample of other evolved systems (e.g. HD 192699, HD 210702 and HD 175541; Johnson et al. (2007), HIP 105854; Jones et al. (2014)), it is possible to put theoretical constraints on the eventual fate of hot Jupiters. With the detection of WASP-138 b, the correlation between stellar metallicity and hot Jupiter occurrence is somewhat weakened. One can investigate a revised metallicity dependence on the formation of planets, which could improve observing strategy to be employed in future planet detection surveys.

The photoevaporation valley/gap was first predicted by Owen and Wu (2013) and Lopez and Fortney (2013). Recent observational evidence presented by the California-*Kepler* Survey has confirmed the paucity of planets in the valley, which sparked great interests in the community. There are two interesting planet size distribution dependency that are still rather uncertain. The first is the evaporating efficiency η of planets. Owen and Wu (2017) pointed out that η may not be constant for all planets, and that the value depends on the planet's atmospheric scale height and the planetary mass. With a varying η, Owen and Wu showed that the radius of the most massive planet which can be stripped by evaporation has a shallower dependence on the orbital period. To distinguish the different evaporation efficiencies and the planet core compositions requires a planetary radius uncertainty below 10%. This precision can be achieved by the recently launched TESS satellite, and the up-and-coming space missions CHEOPS and PLATO. The mission will further increase the sample size of small planets, and address the second uncertainty of the planet size distribution, where the presence of small planets at large distances could not be explained by the photoevaporation mechanism, and that these bare planets may be primordial.

The TESS mission (Ricker et al., 2014) has a primary goal of finding small planets that are suitable for precise follow-up radial velocity measurements. The satellite employs four wide-field optical CCD cameras, which provide a combined FoV of $24^\circ \times 96^\circ$. During two years of the mission, the north and south ecliptic hemisphere are divided into partially overlapping sectors, where each sector will be observed continuously for 27.4 days. The overlapping sectors are observed for at least 27 days, with regions surrounding the ecliptic poles being monitored for more than 300 days. Over the course of the mission, 85% of the sky will be observed. TESS will target over 200,000 main-sequence dwarfs with spectral types F5 to M5 with $I_C \approx$ 4-13 (Ricker et al., 2014). The targets monitored through the TESS mission will be brighter than those observed by the Kepler mission, therefore transit

planet candidates will be easier for follow-up characterisation.

A number of simulations were performed to predict the planet yield of TESS (e.g. Sullivan et al. 2015, Bouma et al. 2017, Barclay et al. 2018, Huang et al. 2018) which helps planning resources for follow-up observations and prioritise targets. Sullivan et al. (2015) estimated the properties of TESS transiting planets using simulation of nearby stellar populations. Based on the Kepler occurrence rates (Fressin et al., 2013; Dressing and Charbonneau, 2015), the sky coverage of TESS and the expected SNR of the transit events, Sullivan et al. (2015) predicted that 1700 transiting planets will be found. 556 of these transiting planets are predicted to have sizes two times smaller than the size of the Earth. More recently, Barclay et al. (2018) adopted different selection strategies to provide a revised planet yield from TESS. They reported that a total of 4373 planets would be found from the TESS Candidate Target List (CTL). Among these planets, 41 will be smaller than 1.25 $R_\oplus$, 238 will have R_p = 1.25−2.0 $R_\oplus$, 1872 will have R_p = 2.0−4.0 $R_\oplus$, and 2222 will be gas giants with radii larger than 4 $R_\oplus$. Barclay et al. (2018) further predicted that TESS will find 69 habitable zone-planets orbiting around M dwarfs.

Planets around stars fainter than $V = 12$ are challenging for RV follow-up. Barclay et al. (2018) predicted that TESS will find 1300 planets with $R_p < R_\oplus$ around $V < 12$ stars which will allow precise RV observations for mass determination. The number of small planets with measured density uncertainty smaller than 20% will increase significantly. This will help us to understand the mechanisms responsible for the formation and evolution of small planets. In addition, Barclay et al. (2018) predicted 70 planets which would be bright targets for atmospheric studies using JWST. 10 habitable-zone planets in their simulated sample have radii between 1.25 $R_\oplus$ and 2.5 $R_\oplus$ could potentially hold an inflated atmosphere. For the simulated giant planets, it was predicted that TESS would find 45 over-inflated planets. Some of these inflated planets may have evaporating atmospheres which make interesting targets to study their extended atmospheres and planet-tails using methods in Chapter 6.

Photoevaporation is not limited to small planets, it is also experienced in hot Jupiters. Detailed analysis of archival WASP-12 spectra revealed enhanced absorptions in both the Ca II H and K and the Na I D lines. This was observed both in- and out-of-transit to a varying extent, confirming the hypothesis of Haswell et al. (2012) and Fossati et al. (2013) in which the entire system is shrouded by evaporated planet material. WASP-12 was not the only system which has an anomalously low $\log R'_{HK}$ index. Staab et al. (2017) gathered data from chromospheric activity surveys and showed that 24% of the 22 planet host sample have apparently low activities. Fossati et al. (2015) demonstrated that a low $\log R'_{HK}$ index could arise from ISM absorption, as in the case of WASP-13. Moreover, Fossati et al.

(2018) studied the massive hot Jupiter WASP-18 b and showed that the host has an intrinsically low activity which could have caused by tidal interaction between the bodies. To differentiate whether the anomalously low $\log R'_{HK}$ of a star is caused by the intrinsically low stellar activity, extrinsic absorption by ISM, or by circumstellar absorption, extended observational programme is needed to monitor individual system.

The apparently low stellar activity in planet host stars also inspired the open cluster survey presented in this thesis. Clearly, improvements are required in order to assess the feasibility of the planet detection method. An increased sample size with a carefully selected set of targets is recommended to proceed with this work, such that a large number of stars with well determined ages, distances and metallicities can be analysed.

Appendix A

Supplementary Tables of Chapter 4

A.1 Spectral Analysis of EPIC 206011496

Table A.1: Chemical abundances of the host star, relative to the Sun.

Element [X/H]	Abundance [dex]	Lines number
C I	0.01 ± 0.05	2
O I	0.14 ± 0.10	2
Na I	0.059 ± 0.023	2
Mg I	0.068 ± 0.068	3
Al I	0.012 ± 0.023	2
Si I	0.053 ± 0.037	11
Ca I	0.102 ± 0.051	9
Sc I	0.081 ± 0.053	3
Sc II	0.099 ± 0.026	6
Ti I	0.117 ± 0.045	18
Ti II	0.064 ± 0.034	5
Cr I	0.088 ± 0.036	17
Co I	0.130 ± 0.04	7
Ni I	0.069 ± 0.023	40
Cu I	0.10 ± 0.04	4
Zn I	0.00 ± 0.02	3
Sr I	0.17 ± 0.08	1
Y II	0.09 ± 0.04	6
Zr II	0.13 ± 0.04	4
Ba II	0.07 ± 0.04	3
Ce II	0.13 ± 0.07	4
Nd II	0.11 ± 0.03	2
A(Li II)*	< 0.45	1

*A(Li) = log[N(Li)/N(H)] + 12

A.2 Radial Velocity Measurements of EPIC 206011496 b

Table A.2: **Radial velocity data.** Signal-to-noise ratio (S/N) is given per CCD pixel at 550nm.

Time [BJD]	RV [km s^{-1}]	σRV [m s^{-1}]	FWHM [km s^{-1}]	σFWHM [m s^{-1}]	BIS [m s^{-1}]	σBIS [m s^{-1}]	S_{MW}	σS_{MW}	S/N
57690.54527	-18.19493	2.01	6.9428	4.0	-27.1	4.0	0.1820	0.0064	46.8
57690.65420	-18.19306	1.70	6.9393	3.4	-24.5	3.4	0.1826	0.0056	57.3
57691.52542	-18.18932	1.84	6.9423	3.7	-27.3	3.7	0.1755	0.0056	51.0
57691.64089	-18.18784	1.57	6.9380	3.1	-19.0	3.1	0.1789	0.0052	62.8
57692.54337	-18.19043	1.82	6.9336	3.6	-17.0	3.6	0.1799	0.0057	52.2
57692.66890	-18.19007	2.03	6.9400	4.1	-18.4	4.1	0.1868	0.0082	48.1
57694.55555	-18.18570	1.90	6.9404	3.8	-30.9	3.8	0.1873	0.0061	50.0
57694.65367	-18.18799	1.89	6.9472	3.8	-17.4	3.8	0.1825	0.0071	51.6
57695.53842	-18.19169	2.29	6.9375	4.6	-34.0	4.6	0.1877	0.0077	40.8
57695.55993	-18.19412	2.09	6.9479	4.2	-24.2	4.2	0.1730	0.0065	44.5
57696.54203	-18.19052	2.05	6.9560	4.1	-26.0	4.1	0.1857	0.0068	45.8
57696.67629	-18.19411	1.94	6.9507	3.9	-22.7	3.9	0.1817	0.0075	50.1
57697.56269	-18.19541	1.90	6.9536	3.8	-29.4	3.8	0.1788	0.0061	49.7
57697.64405	-18.19883	1.74	6.9470	3.5	-26.9	3.5	0.1855	0.0058	55.5
57699.51415	-18.18805	1.53	6.9476	3.1	-24.6	3.1	0.2188	0.0041	62.7
57699.56041	-18.18795	1.56	6.9584	3.1	-18.3	3.1	0.2205	0.0048	62.6

Continued on next page

Table A.2 – continued from previous page

Time	RV	σRV	FWHM	σFWHM	BIS	σBIS	S˙MW	σS˙MW	S/N
57701.53183	-18.18327	2.03	6.9532	4.1	-26.0	4.1	0.2197	0.0061	45.9
57701.57985	-18.18358	2.01	6.9494	4.0	-26.0	4.0	0.2343	0.0061	46.5
57703.53660	-18.18968	1.74	6.9375	3.5	-15.2	3.5	0.2164	0.0054	55.2
57703.57238	-18.18313	1.78	6.9565	3.6	-15.9	3.6	0.2190	0.0055	53.8
57705.53138	-18.19312	1.53	6.9390	3.1	-12.6	3.1	0.2031	0.0045	64.9
57705.57766	-18.19513	1.76	6.9337	3.5	-16.9	3.5	0.2142	0.0060	55.6
57714.60057	-18.19074	2.33	6.9600	4.7	-13.1	4.7	0.2277	0.0086	41.2
57714.62010	-18.19333	2.37	6.9489	4.7	-12.6	4.7	0.2225	0.0099	41.4
57717.55993	-18.19042	2.01	6.9418	4.0	-17.8	4.0	0.1746	0.0073	48.1
57717.58112	-18.18483	2.13	6.9487	4.3	-17.2	4.3	0.1940	0.0079	45.2
57718.53008	-18.19030	1.78	6.9488	3.6	-17.7	3.6	0.1990	0.0061	54.1
57718.55149	-18.18923	1.73	6.9507	3.5	-12.9	3.5	0.2019	0.0060	56.2
57719.55290	-18.19238	1.71	6.9511	3.4	-22.8	3.4	0.1884	0.0056	56.5
57719.57368	-18.19477	1.71	6.9425	3.4	-18.4	3.4	0.1994	0.0057	56.7
57720.53108	-18.18721	1.45	6.9469	2.9	-14.2	2.9	0.1922	0.0046	70.4
57720.55102	-18.18671	1.52	6.9397	3.0	-17.1	3.0	0.1968	0.0051	65.7
57721.53077	-18.19020	2.01	6.9556	4.0	-24.1	4.0	0.1938	0.0070	47.5
57721.55300	-18.18965	2.09	6.9408	4.2	-14.9	4.2	0.1838	0.0076	45.7
57935.79544	-18.17258	2.34	6.9898	4.7	-7.0	4.7	0.2700	0.0091	42.0
57935.81684	-18.17136	2.21	6.9761	4.4	-5.1	4.4	0.2564	0.0084	44.2
57936.84590	-18.17932	2.48	6.9803	5.0	-15.5	5.0	0.2820	0.0100	39.7

Continued on next page

Table A.2 – continued from previous page

Time	RV	σRV	FWHM	σFWHM	BIS	σBIS	S˙MW	σS˙MW	S/N
57936.86711	-18.18014	2.53	6.9722	5.1	1.8	5.1	0.2668	0.0104	39.1
57937.77515	-18.17689	2.58	6.9604	5.2	-6.9	5.2	0.2415	0.0105	38.3
57937.82206	-18.17986	2.30	6.9765	4.6	-15.1	4.6	0.2444	0.0088	42.4
57942.77873	-18.18570	1.58	6.9310	3.2	-19.1	3.2	0.2124	0.0046	61.4
57942.88776	-18.19012	1.65	6.9373	3.3	-15.1	3.3	0.2270	0.0066	61.1
57943.75116	-18.18923	1.62	6.9337	3.2	-13.2	3.2	0.1961	0.0048	60.4
57943.86160	-18.19289	2.46	6.9371	4.9	-21.2	4.9	0.1863	0.0097	39.7
57944.77832	-18.19228	2.24	6.9244	4.5	-15.5	4.5	0.1864	0.0082	42.9
57944.86188	-18.19112	1.99	6.9344	4.0	-25.0	4.0	0.1829	0.0075	48.7
57945.75844	-18.18714	1.79	6.9247	3.6	-23.8	3.6	0.1759	0.0057	53.7
57946.77897	-18.19034	2.30	6.9292	4.6	-25.4	4.6	0.1791	0.0080	42.0
57948.80722	-18.18963	2.00	6.9241	4.0	-25.8	4.0	0.1690	0.0069	48.4
57948.86573	-18.19051	2.09	6.9274	4.2	-21.6	4.2	0.1760	0.0080	46.5
57949.84184	-18.18010	5.61	6.9040	11.2	-11.5	11.2	0.1322	0.0280	20.3
57951.76491	-18.19084	4.40	6.9380	8.8	-23.9	8.8	0.2072	0.0226	24.4
57951.85922	-18.17271	3.38	6.9374	6.8	-17.4	6.8	0.1802	0.0169	30.3
57952.73957	-18.17978	3.26	6.9507	6.5	-13.5	6.5	0.1720	0.0148	31.2
57952.86046	-18.17574	2.49	6.9466	5.0	-27.4	5.0	0.1881	0.0111	39.7
57953.85555	-18.18618	2.46	6.9581	4.9	-19.0	4.9	0.1945	0.0105	40.1
57954.82099	-18.17750	3.16	6.9479	6.3	-23.7	6.3	0.1541	0.0150	32.5
57955.75309	-18.17132	2.30	6.9634	4.6	-16.6	4.6	0.1838	0.0080	41.8

Continued on next page

Table A.2 – continued from previous page

Time	RV	σRV	FWHM	σFWHM	BIS	σBIS	S˙MW	σS˙MW	S/N
57955.91602	-18.17448	1.72	6.9752	3.4	-26.9	3.4	0.1939	0.0077	59.6
57956.72888	-18.17041	2.32	6.9676	4.6	-25.0	4.6	0.2022	0.0082	41.8
57956.91804	-18.17142	2.42	6.9667	4.8	-33.5	4.8	0.2255	0.0106	41.0
57957.89416	-18.17995	4.32	6.9690	8.6	-10.7	8.6	0.1634	0.0218	25.0
57959.78548	-18.17701	2.51	6.9612	5.0	-15.7	5.0	0.2194	0.0103	39.4
57959.90585	-18.17966	1.91	6.9555	3.8	-16.3	3.8	0.2075	0.0084	52.1
57960.74725	-18.18476	2.68	6.9651	5.4	-20.1	5.4	0.2090	0.0104	36.9
57960.84628	-18.18490	2.65	6.9605	5.3	-12.9	5.3	0.1981	0.0108	37.4
57961.76442	-18.17957	2.22	6.9582	4.4	-7.1	4.4	0.2149	0.0087	44.4
57961.83425	-18.18436	2.41	6.9526	4.8	-16.7	4.8	0.2094	0.0171	43.3
57962.78393	-18.17748	1.96	6.9541	3.9	-2.2	3.9	0.2119	0.0081	51.1
57962.87271	-18.19164	5.55	6.9251	11.1	-18.0	11.1	0.2266	0.0438	21.7
57964.74231	-18.17793	1.84	6.9650	3.7	-11.6	3.7	0.2149	0.0061	52.7
57964.83225	-18.18182	1.94	6.9492	3.9	-20.0	3.9	0.2078	0.0089	51.7
57965.73570	-18.19438	5.34	6.9277	10.7	-25.5	10.7	0.1945	0.0308	21.4
57965.83742	-18.18131	5.94	6.9409	11.9	-8.8	11.9	0.2740	0.0440	20.4
57993.66968	-18.18228	2.03	6.9482	4.1	-22.7	4.1	0.2104	0.0075	47.0
57993.78491	-18.17993	2.08	6.9523	4.2	-18.3	4.2	0.1954	0.0086	46.3
57993.84799	-18.18314	1.83	6.9520	3.7	-27.1	3.7	0.1934	0.0088	53.9
57994.63060	-18.17385	1.98	6.9446	4.0	-22.7	4.0	0.1980	0.0070	47.8
57994.74383	-18.17639	2.22	6.9466	4.4	-16.1	4.4	0.1864	0.0091	43.3

Continued on next page

Table A.2 – continued from previous page

Time	RV	σRV	FWHM	σFWHM	BIS	σBIS	S˙MW	σS˙MW	S/N
57994.82005	-18.17586	2.19	6.9553	4.4	-23.9	4.4	0.2004	0.0102	44.6
57995.63098	-18.17764	3.46	6.9558	6.9	-23.8	6.9	0.1701	0.0174	29.9
57998.62754	-18.19046	1.56	6.9459	3.1	-15.7	3.1	0.1987	0.0046	61.3
57998.71879	-18.19124	2.02	6.9506	4.0	-14.9	4.0	0.1797	0.0087	48.3
57998.81073	-18.18741	2.21	6.9488	4.4	-17.8	4.4	0.1645	0.0116	45.0
58008.66469	-18.18777	3.48	6.9314	7.0	-7.3	7.0	0.1958	0.0153	29.0
58010.65231	-18.19970	2.19	6.9277	4.4	-28.0	4.4	0.1689	0.0085	43.3
58010.77942	-18.19305	2.25	6.9234	4.5	-26.8	4.5	0.1921	0.0107	43.3
58010.83344	-18.19911	2.07	6.9391	4.1	-28.7	4.1	0.1985	0.0115	47.9
58011.68577	-18.18190	2.40	6.9283	4.8	-9.4	4.8	0.1728	0.0105	40.2
58011.77789	-18.18417	2.23	6.9321	4.5	-15.3	4.5	0.1739	0.0104	43.6
58011.83205	-18.18652	2.60	6.9261	5.2	-37.8	5.2	0.1888	0.0150	38.6
58012.67262	-18.18860	2.91	6.9347	5.8	-29.1	5.8	0.1680	0.0137	34.0
58012.75336	-18.19386	2.31	6.9312	4.6	-35.4	4.6	0.1780	0.0106	42.0
58012.82174	-18.18669	2.43	6.9230	4.9	-17.5	4.9	0.1579	0.0132	40.9
58013.67492	-18.18197	3.38	6.9334	6.8	-28.1	6.8	0.1733	0.0158	30.1
58013.74342	-18.18162	2.52	6.9295	5.0	-21.7	5.0	0.1862	0.0109	38.5
58013.81433	-18.18331	2.17	6.9467	4.3	-31.5	4.3	0.1964	0.0106	45.2
58014.68555	-18.18273	2.62	6.9207	5.2	-26.3	5.2	0.2481	0.0102	37.1
58014.77534	-18.18936	2.77	6.9302	5.5	-28.6	5.5	0.1661	0.0130	36.0
58018.63224	-18.18640	2.33	6.9479	4.7	-28.0	4.7	0.1890	0.0095	40.9

Continued on next page

Table A.2 – continued from previous page

Time	RV	σRV	FWHM	σFWHM	BIS	σBIS	S˙MW	σS˙MW	S/N
58018.72534	-18.18438	2.52	6.9262	5.0	-23.1	5.0	0.1978	0.0108	38.2
58019.62715	-18.19033	1.99	6.9432	4.0	-20.6	4.0	0.1888	0.0077	47.8
58019.72843	-18.19547	1.92	6.9260	3.8	-25.9	3.8	0.1963	0.0080	49.9
58020.66431	-18.18766	3.01	6.9468	6.0	-5.8	6.0	0.1870	0.0121	32.5
58020.75915	-18.18656	2.21	6.9431	4.4	-19.1	4.4	0.1977	0.0099	43.6
58021.55154	-18.17666	2.55	6.9344	5.1	-19.9	5.1	0.2109	0.0103	37.6
58021.66021	-18.18003	3.07	6.9414	6.1	-35.5	6.1	0.2225	0.0132	32.3
58021.75738	-18.18448	2.24	6.9325	4.5	-15.9	4.5	0.1845	0.0100	43.1
58022.53363	-18.18830	2.59	6.9472	5.2	-24.9	5.2	0.1947	0.0103	37.1
58022.59935	-18.18210	3.26	6.9427	6.5	-17.1	6.5	0.1937	0.0128	30.2
58022.74556	-18.19200	2.80	6.9414	5.6	-22.3	5.6	0.2040	0.0124	35.0
58023.53440	-18.17930	1.81	6.9489	3.6	-32.0	3.6	0.2030	0.0058	51.1
58023.63020	-18.17708	2.62	6.9523	5.2	-19.1	5.2	0.1963	0.0106	36.7
58023.75632	-18.18220	2.00	6.9325	4.0	-24.1	4.0	0.1824	0.0092	48.3
58025.54957	-18.17300	1.67	6.9443	3.3	-17.9	3.3	0.2031	0.0055	56.1
58025.64932	-18.17642	1.82	6.9560	3.6	-19.6	3.6	0.1990	0.0074	52.8
58025.70429	-18.17085	1.93	6.9569	3.9	-4.2	3.9	0.2057	0.0089	50.3
58026.55716	-18.16496	4.02	6.9580	8.0	-8.4	8.0	0.2396	0.0170	25.7
58026.65617	-18.17836	2.73	6.9569	5.5	-22.0	5.5	0.2263	0.0112	35.7
58026.74871	-18.18277	2.88	6.9711	5.8	-22.1	5.8	0.1771	0.0154	35.2
58027.56593	-18.15614	5.14	6.9831	10.3	-11.8	10.3	0.2023	0.0274	21.8

Continued on next page

Table A.2 – continued from previous page

Time	RV	σRV	FWHM	σFWHM	BIS	σBIS	S˙MW	σS˙MW	S/N
58027.67900	-18.16790	4.30	7.0036	8.6	-8.0	8.6	0.1720	0.0246	25.4
58027.74799	-18.15559	5.45	6.9669	10.9	28.2	10.9	0.1827	0.0322	21.1
58041.54788	-18.19556	2.00	6.9314	4.0	-31.2	4.0	0.1730	0.0067	47.1
58043.56762	-18.18878	1.35	6.9287	2.7	-24.3	2.7	0.2094	0.0039	73.6
58043.72519	-18.18693	1.89	6.9299	3.8	-25.9	3.8	0.2145	0.0086	52.1
58052.55248	-18.18881	1.46	6.9380	2.9	-22.7	2.9	0.2180	0.0046	66.9
58052.61595	-18.19051	1.95	6.9391	3.9	-27.6	3.9	0.2350	0.0085	50.3
58053.56897	-18.18273	1.70	6.9377	3.4	-27.6	3.4	0.2239	0.0060	56.8
58053.64640	-18.18326	1.80	6.9436	3.6	-23.4	3.6	0.2202	0.0074	54.6
58054.52491	-18.18453	2.44	6.9497	4.9	-36.6	4.9	0.2112	0.0083	39.1
58054.67331	-18.18235	2.09	6.9612	4.2	-21.0	4.2	0.2261	0.0086	46.9
58056.53663	-18.18039	1.35	6.9497	2.7	-23.1	2.7	0.2132	0.0039	74.8
58056.62290	-18.18640	1.60	6.9600	3.2	-33.6	3.2	0.2198	0.0064	62.6
58057.53537	-18.18602	1.32	6.9511	2.6	-28.4	2.6	0.2202	0.0038	76.5
58057.59482	-18.18711	1.41	6.9528	2.8	-29.3	2.8	0.2291	0.0049	71.7
58068.58875	-18.18136	1.63	6.9330	3.3	-14.5	3.3	0.1845	0.0055	59.0
58069.65402	-18.19329	1.90	6.9399	3.8	-17.5	3.8	0.1783	0.0062	49.6
58070.66278	-18.19205	1.93	6.9408	3.9	-20.7	3.9	0.1868	0.0086	50.8
58071.54887	-18.18911	1.69	6.9187	3.4	-23.1	3.4	0.1924	0.0061	56.8
58074.55346	-18.18790	1.55	6.9236	3.1	-18.4	3.1	0.1788	0.0060	62.4
58075.53852	-18.18124	1.76	6.9243	3.5	-18.9	3.5	0.1630	0.0069	54.5

Continued on next page

Table A.2 – continued from previous page

Time	RV	σRV	FWHM	σFWHM	BIS	σBIS	S˙MW	σS˙MW	S/N
58077.54947	-18.18492	1.60	6.9297	3.2	-23.9	3.2	0.1872	0.0063	61.9
58079.61835	-18.19371	1.94	6.9281	3.9	-21.6	3.9	0.1803	0.0084	49.5

A.3 Joint Bayesian Analysis of EPIC 206011496 b

Table A.3: List of parameters used in the analysis. The respective priors are provided together with the posteriors for both the Dartmouth and PARSEC stellar evolution tracks. The posterior values represent the median and 68.3% credible interval. Fixed and derived values that might be useful for follow-up work are also reported.

Parameter	Prior	Posterior	
		Dartmouth (adopted)	PARSEC
Stellar Parameters			
Effective temperature T_eff [K]	$\mathcal{N}(5457, 29)$	5477 ± 27	5480 ± 24
Surface gravity $\log g$ [cgs]	$\mathcal{N}(4.42, 0.10)$	4.419 ± 0.053	4.429 ± 0.045
Iron abundance [Fe/H] [dex]	$\mathcal{N}(0.08, 0.02)$	0.078 ± 0.020	0.079 ± 0.020
Distance to Earth D [pc]	$\mathcal{N}(143.5, 10.9)$	145 ± 8	141 ± 6
Interstellar extinction $E(B-V)$ [mag]	$\mathcal{U}(0, 1)$	$0.009^{+0.011}_{-0.007}$	$0.009^{+0.011}_{-0.007}$
Systemic radial velocity γ [km s^{-1}]	$\mathcal{U}(-20, -15)$	-18.186 ± 0.002	-18.186 ± 0.002
Linear limb-darkening coefficient u_a	(derived)	0.4631 ± 0.0061	0.4625 ± 0.0057
Quadratic limb-darkening coefficient u_b	(derived)	0.2270 ± 0.0041	0.2273 ± 0.0037
Stellar density $\rho_\star/\rho_\odot$	(derived)	0.98 ± 0.19	1.03 ± 0.16
Stellar mass $M_\star$ [$M_\odot$]	(derived)	0.915 ± 0.017	0.884 ± 0.018

Continued on next page

Table A.3 – continued from previous page

Parameter	Prior	Posterior	
		Dartmouth	PARSEC
Stellar radius $R_\star$ [$R_\odot$]	(derived)	0.977 ± 0.053	0.950 ± 0.040
Stellar age τ [Gyr]	(derived)	9.7 ± 3.0	10.8 ± 2.8
Planet b Parameters			
Orbital Period P [d]	$\mathcal{N}(2.369193, 0.01)$	$2.369172 \pm 8.9 \times 10^{-5}$	$2.369173 \pm 9.0 \times 10^{-5}$
Transit epoch T_0 [BJD - 2456000]	$\mathcal{N}(981.6425, 0.1)$	$981.6431 \pm 1.6 \times 10^{-3}$	$981.6431 \pm 1.6 \times 10^{-3}$
Radial velocity semi-amplitude K [m s^{-1}]	$\mathcal{U}(0, 10^2)$	3.34 ± 0.43	3.33 ± 0.43
Orbital inclination i [°]	$\mathcal{S}(70, 90)$	87.7 ± 1.6	88.1 ± 1.4
Planet-to-star radius ratio k	$\mathcal{U}(0, 1)$	0.01604 ± 0.00041	0.01599 ± 0.00035
Orbital eccentricity e	$\mathcal{U}(0, 1)$	0.084 ± 0.079	0.080 ± 0.068
Argument of periastron ω [°]	$\mathcal{U}(0, 360)$	99^{+220}_{-77}	94^{+220}_{-71}
System scale $a/R_\star$	(derived)	7.43 ± 0.45	7.56 ± 3.8
Impact parameter b	(derived)	0.30 ± 0.20	0.25 ± 0.19
Transit duration T_{14} [h]	(derived)	2.266 ± 0.050	2.264 ± 0.049
Semi-major axis a [AU]	(derived)	0.03376 ± 0.00021	0.03337 ± 0.00023
Planet mass M_p [$M_\oplus$]	(derived)	6.54 ± 0.84	6.38 ± 0.83
Planet radius R_p [$R_\oplus$]	(derived)	1.71 ± 0.11	1.654 ± 0.84
Planet bulk density ρ_p [g cm^{-3}]	(derived)	7.1 ± 1.8	7.7 ± 1.7
Gaussian Process Hyperparameters			

Continued on next page

Table A.3 – continued from previous page

Parameter	Prior	Posterior	
		Dartmouth	PARSEC
A [m s^{-1}]	$\mathcal{U}(0, 100)$	$6.0^{+1.3}_{-0.8}$	5.96 ± 1.2
λ_1 [d]	$\mathcal{U}(0, 100)$	34 ± 12	34 ± 12
λ_2	$\mathcal{U}(0, 10)$	0.46 ± 0.12	0.46 ± 0.12
P_{rot} [d]	$\mathcal{N}(32.2, 0.6)$	32.2 ± 0.5	32.2 ± 0.5
Instrument-related Parameters			
HARPS jitter [m s^{-1}]	$\mathcal{U}(0, 10^2)$	1.9 ± 0.4	1.9 ± 0.4
K2 contamination [%]	$\mathcal{N}_{\mathcal{U}}(0.952, 0.024, 0, 100)$	0.952 ± 0.024	0.952 ± 0.024
K2 jitter [ppm]	$\mathcal{U}(0, 10^5)$	59 ± 1	59 ± 1
K2 out-of-transit flux	$\mathcal{U}(0.99, 1.01)$	$1.000006 \pm 2 \times 10^{-6}$	$1.000006 \pm 2 \times 10^{-6}$
SED jitter [mag]	$\mathcal{U}(0, 0.1)$	0.054 ± 0.021	0.054 ± 0.022

Notes:

- $\mathcal{N}(\mu, \sigma^2)$: normal distribution with mean μ and width σ^2
- $\mathcal{U}(a, b)$: uniform distribution between a and b
- $\mathcal{N}_{\mathcal{U}}(\mu, \sigma^2, a, b)$: normal distribution with mean μ and width σ^2 multiplied with a uniform distribution between a and b
- $\mathcal{S}(a, b)$: sine distribution between a and b
- $\beta(a, b)$: Beta distribution with parameters a and b

Appendix B

Supplementary Figures of Chapter 6

B.1 Spectra of Surviving Targets in the Cluster Survey

NGC5138

ADP.2015-07-26T14:06:32.503.fits: $(B-V)_0$=0.51 log R'_{HK}=-4.04

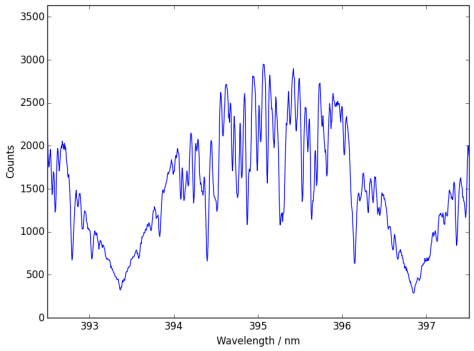

ADP.2015-07-26T14:06:32.657.fits: $(B-V)_0$=0.44 logR'_{HK}=-4.01

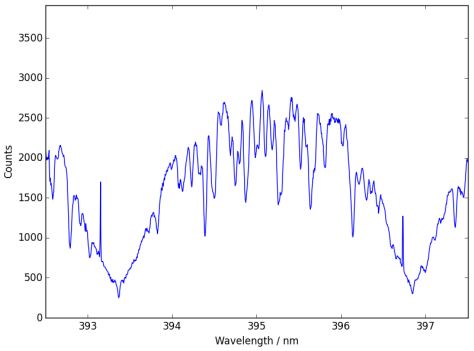

ADP.2015-07-26T14:06:32.860.fits: $(B-V)_0$=0.41 log R'_{HK}=-4.01

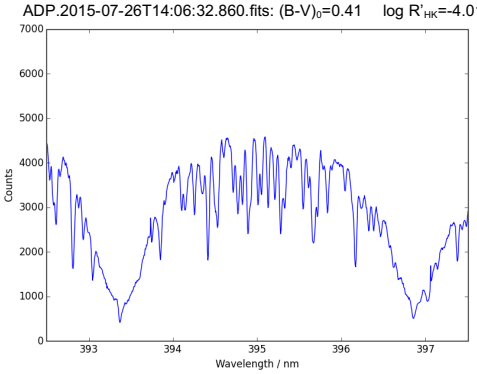

ADP.2015-07-26T14:06:32.110.fits: $(B-V)_0$=0.26 log R'_{HK}=-4.03

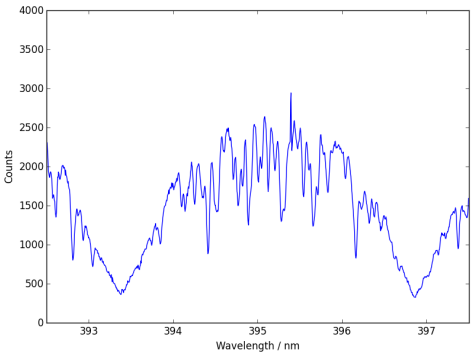

NGC5460

ADP.2015-09-21T13:47:55.737.fits: $(B-V)_0$=0.53 log R'_{HK}=-3.99

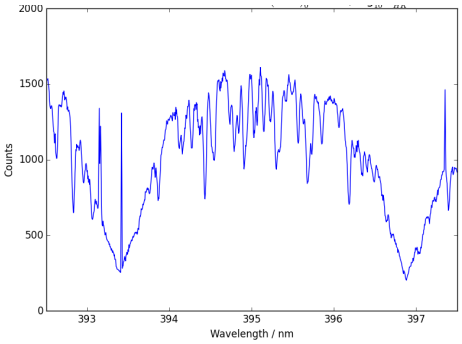

ADP.2015-09-21T13:47:55.737.fits: $(B-V)_0$=0.21 log R'_{HK}=-3.59

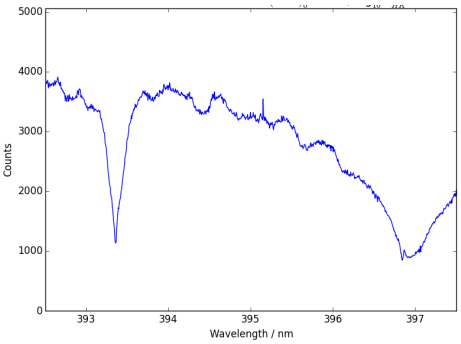

NGC6067

ADP.2015-07-26T13:19:54.303.fits: $(B-V)_0$=0.44 log R'_{HK}=-3.52

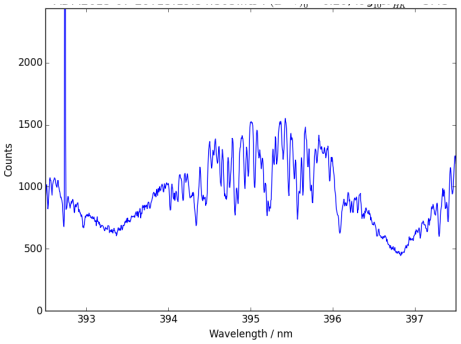

ADP.2015-07-26T13:19:54.417.fits: $(B-V)_0$=0.26 log R'_{HK}=-4.37

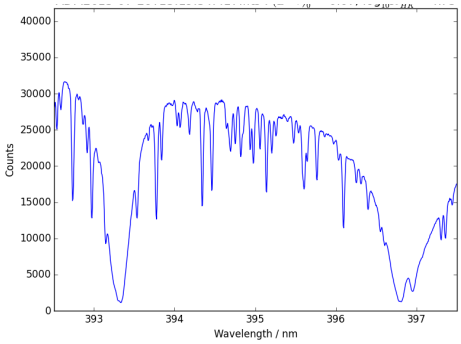

NGC6087

ADP.2015-08-06T02:46:38.860.fits: $(B-V)_0$=0.41 log R'_{HK}=-3.61

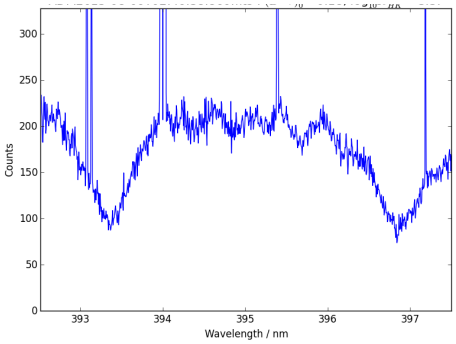

ADP.2015-08-06T02:46:40.213.fits: $(B-V)_0$=0.44 log R'_{HK}=-3.68

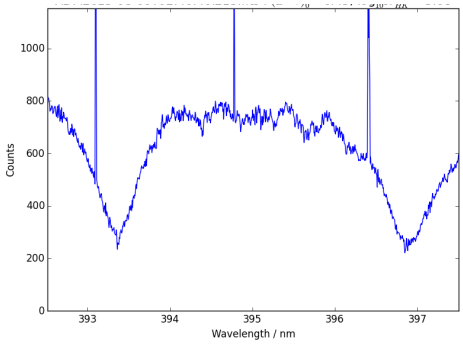

ADP.2015-08-06T02:46:40.347.fits: $(B-V)_0$=0.55 log R'_{HK}=-3.65

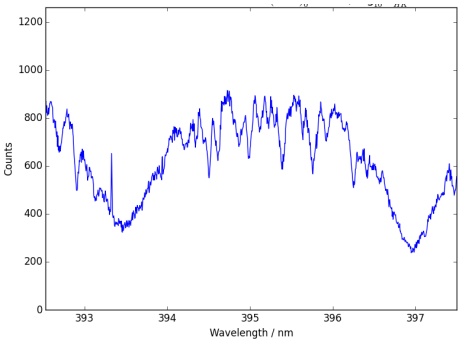

ADP.2015-08-06T02:46:40.553.fits: $(B-V)_0$=0.55 log R'_{HK}=-3.79

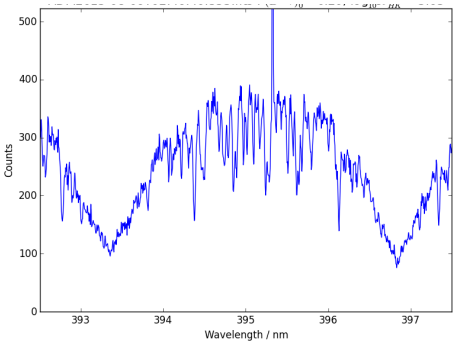

NGC6087

ADP.2015-08-06T02:46:46.493.fits: $(B-V)_0$=0.55 log R'_{HK}=-3.68

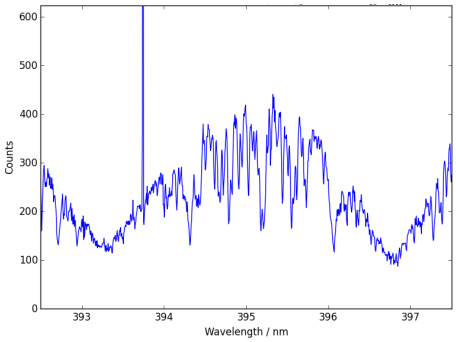

ADP.2015-08-06T02:46:48.980.fits: $(B-V)_0$=0.29 log R'_{HK}=-3.56

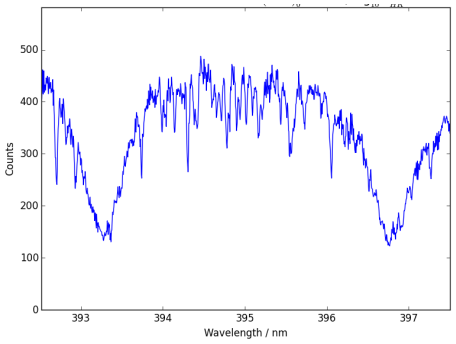

NGC6134

ADP.2015-08-06T10:28:02.360.fits: $(B-V)_0$=0.44 log R'_{HK}=-4.27

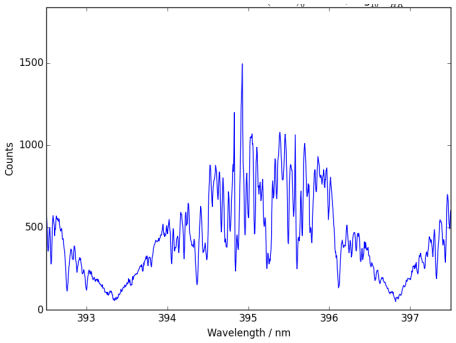

ADP.2015-08-06T10:28:03.160.fits: $(B-V)_0$=0.44 log R'_{HK}=-3.81

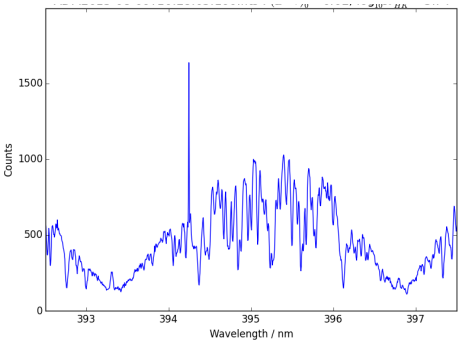

ADP.2015-08-06T10:28:04.900.fits: $(B-V)_0$=0.44 log R'_{HK}=-3.26

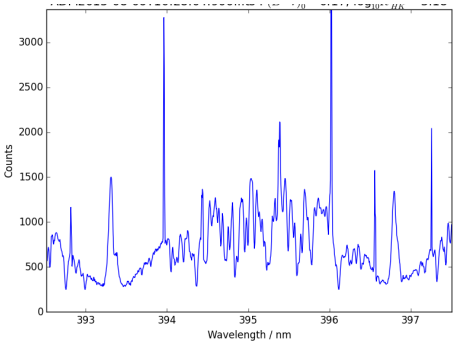

ADP.2015-08-06T10:28:05.950.fits: $(B-V)_0$=0.41 log R'_{HK}=-4.00

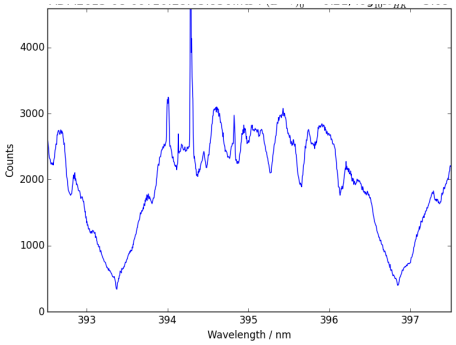

NGC6134

ADP.2015-08-06T10:28:07.440.fits: $(B-V)_0$=0.37 log R'_{HK}=-4.02

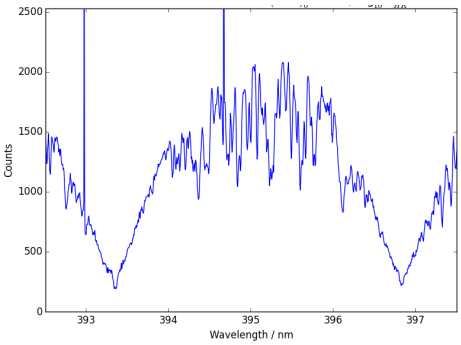

ADP.2015-08-06T10:28:09.483.fits: $(B-V)_0$=0.39 log R'_{HK}=-4.23

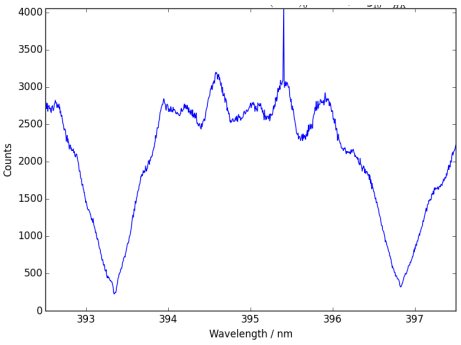

NGC6281

ADP.2015-08-06T01:30:04.343.fits: $(B-V)_0$=0.29 log R'_{HK}=-3.64

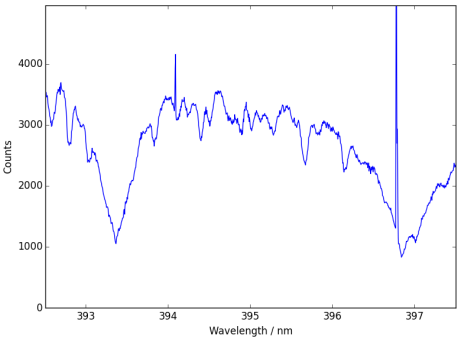

ADP.2015-08-06T01:30:04.930.fits: $(B-V)_0$=0.41 log R'_{HK}=-3.48

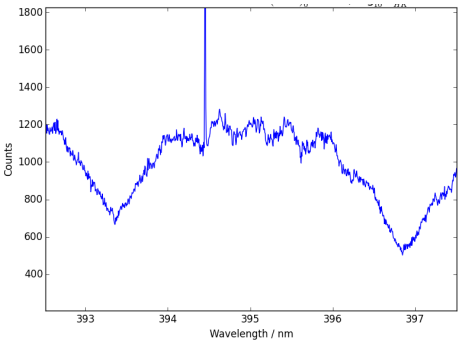

ADP.2015-08-06T01:30:04.977.fits: $(B-V)_0$=0.41 log R'_{HK}=-3.83

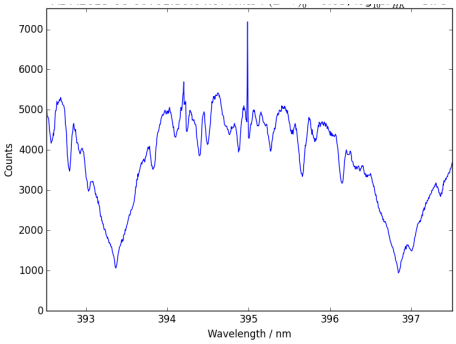

ADP.2015-08-06T01:30:06.373.fits: $(B-V)_0$=0.294 log R'_{HK}=-3.66

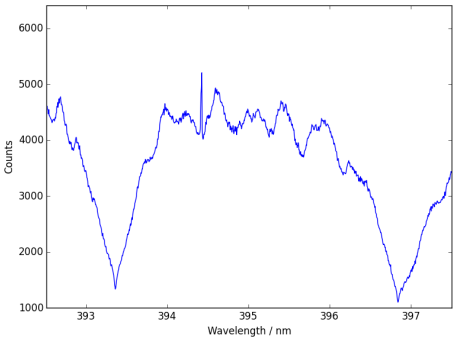

NGC6281

ADP.2015-08-06T01:30:11.627.fits: $(B-V)_0$=0.334 log R'_{HK}=-3.97

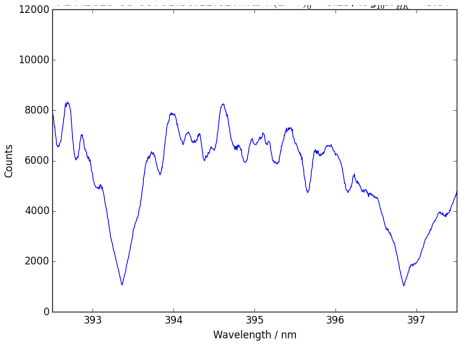

ADP.2015-08-06T01:30:15.360.fits: $(B-V)_0$=0.438 log R'_{HK}=-3.78

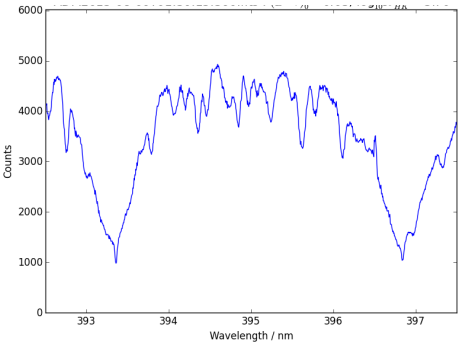

NGC6405

ADP.2015-07-26T13:19:53.083.fits: $(B-V)_0$=0.25 log R'_{HK}=-3.97

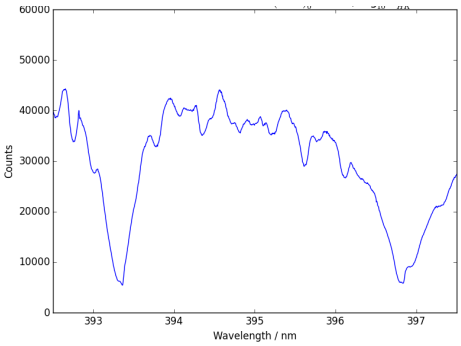

ADP.2015-07-26T13:19:53.703.fits: $(B-V)_0$=0.29 log R'_{HK}=-3.71

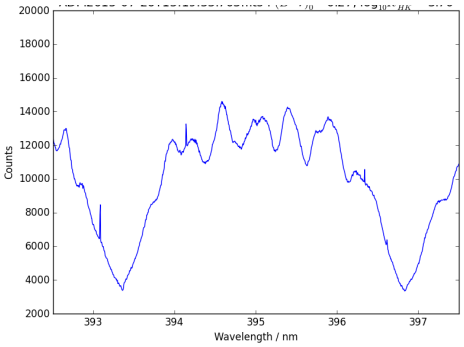

ADP.2015-07-26T13:19:53.757.fits: $(B-V)_0$=0.29 log R'_{HK}=-3.65

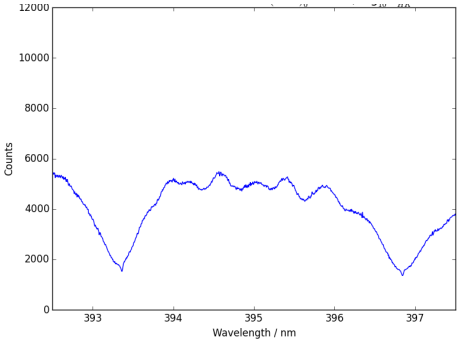

ADP.2015-08-06T10:28:11.060.fits: $(B-V)_0$=0.17 log R'_{HK}=-3.78

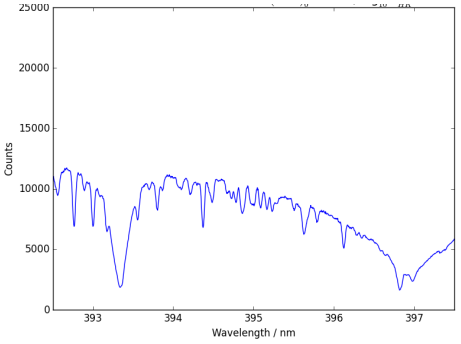

NGC6494

ADP.2015-07-26T06:58:10.173.fits: $(B-V)_0$=0.25 log R'_{HK}=-3.34

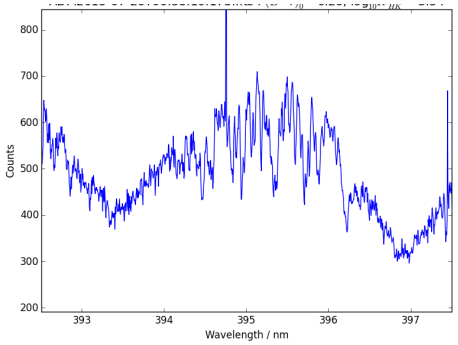

ADP.2015-10-12T17:08:24.320.fits: $(B-V)_0$=0.51 log R'_{HK}=-4.08

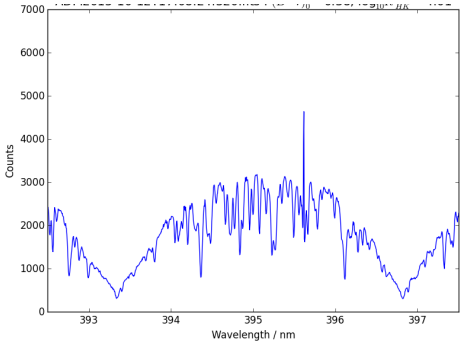

NGC6716

ADP.2015-10-12T17:08:19.100.fits: $(B-V)_0$=0.55 log R'_{HK}=-3.92

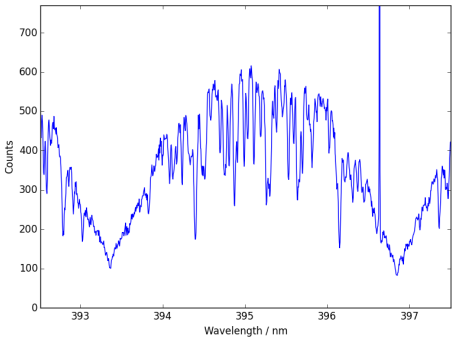

ADP.2015-10-12T17:08:26.960.fits: $(B-V)_0$=0.294 log R'_{HK}=-3.70

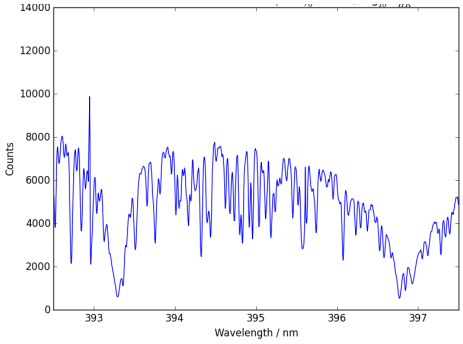

ADP.2015-10-12T17:08:29.860.fits: $(B-V)_0$=0.60 log R'_{HK}=-3.74

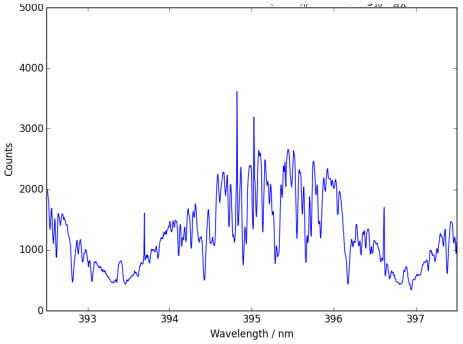

Bibliography

Aigrain, S. and Irwin, M. Practical planet prospecting. *MNRAS*, 350:331–345, May 2004.

Aigrain, S., Pont, F., and Zucker, S. A simple method to estimate radial velocity variations due to stellar activity using photometry. *MNRAS*, 419:3147–3158, Feb. 2012.

Allard, F. The BT-Settl Model Atmospheres for Stars, Brown Dwarfs and Planets. In Booth, M., Matthews, B. C., and Graham, J. R., editors, *Exploring the Formation and Evolution of Planetary Systems*, volume 299 of *IAU Symposium*, pages 271–272, Jan. 2014.

Allard, F., Homeier, D., and Freytag, B. Models of very-low-mass stars, brown dwarfs and exoplanets. *Philosophical Transactions of the Royal Society of London Series A*, 370: 2765–2777, June 2012.

Alsubai, K. A., Parley, N. R., Bramich, D. M. *et al.* The Qatar Exoplanet Survey. *Acta Astron.*, 63:465–480, Dec. 2013.

Anderson, D. R., Hellier, C., Gillon, M. *et al.* WASP-17b: An Ultra-Low Density Planet in a Probable Retrograde Orbit. *ApJ*, 709:159–167, Jan. 2010.

Andrae, R., Fouesneau, M., Creevey, O. *et al.* Gaia Data Release 2. First stellar parameters from Apsis. *A&A*, 616:A8, Aug. 2018.

Anglada-Escudé, G., Boss, A. P., Weinberger, A. J. *et al.* Astrometry and Radial Velocities of the Planet Host M Dwarf GJ 317: New Trigonometric Distance, Metallicity, and Upper Limit to the Mass of GJ 317b. *ApJ*, 746:37, Feb. 2012.

Appenzeller, I. *Introduction to Astronomical Spectroscopy*. Feb. 2013.

Armstrong, D. J., Kirk, J., Lam, K. W. F. *et al.* K2 Variable Catalogue: Variable stars and eclipsing binaries in K2 campaigns 1 and 0. *A&A*, 579:A19, July 2015a.

Armstrong, D. J., Santerne, A., Veras, D. *et al.* One of the closest exoplanet pairs to the 3:2 mean motion resonance: K2-19b and c. *A&A*, 582:A33, Oct. 2015b.

Armstrong, D. J., Pugh, C. E., Broomhall, A.-M. *et al.* The host stars of Kepler's habitable exoplanets: superflares, rotation and activity. *MNRAS*, 455:3110–3125, Jan. 2016.

Asplund, M., Grevesse, N., Sauval, A. J. *et al.* The Chemical Composition of the Sun. *ARA&A*, 47:481–522, Sept. 2009.

Auvergne, M., Bodin, P., Boisnard, L. *et al.* The CoRoT satellite in flight: description and performance. *A&A*, 506:411–424, Oct. 2009.

Bakos, G., Noyes, R. W., Kovács, G. *et al.* Wide-Field Millimagnitude Photometry with the HAT: A Tool for Extrasolar Planet Detection. *PASP*, 116:266–277, Mar. 2004.

Bakos, G. Á., Lázár, J., Papp, I. *et al.* System Description and First Light Curves of the Hungarian Automated Telescope, an Autonomous Observatory for Variability Search. *PASP*, 114:974–987, Sept. 2002.

Bakos, G. Á., Torres, G., Pál, A. *et al.* HAT-P-11b: A Super-Neptune Planet Transiting a Bright K Star in the Kepler Field. *ApJ*, 710:1724–1745, Feb. 2010.

Bakos, G. Á., Csubry, Z., Penev, K. *et al.* HATSouth: A Global Network of Fully Automated Identical Wide-Field Telescopes. *PASP*, 125:154, Feb. 2013.

Bakos, G. Á., Hartman, J. D., Torres, G. *et al.* HAT-P-47b AND HAT-P-48b: Two Low Density Sub-Saturn-Mass Transiting Planets on the Edge of the Period–Mass Desert. *ArXiv e-prints*, June 2016.

Baliunas, S. L., Donahue, R. A., Soon, W. H. *et al.* Chromospheric variations in main-sequence stars. *ApJ*, 438:269–287, Jan. 1995.

Baraffe, I., Chabrier, G., and Barman, T. Structure and evolution of super-Earth to super-Jupiter exoplanets. I. Heavy element enrichment in the interior. *A&A*, 482:315–332, Apr. 2008.

Baranne, A., Mayor, M., and Poncet, J. L. CORAVEL - A new tool for radial velocity measurements. *Vistas in Astronomy*, 23:279–316, 1979.

Baranne, A., Queloz, D., Mayor, M. *et al.* ELODIE: A spectrograph for accurate radial velocity measurements. *A&AS*, 119:373–390, Oct. 1996.

Barclay, T., Pepper, J., and Quintana, E. V. A Revised Exoplanet Yield from the Transiting Exoplanet Survey Satellite (TESS). *ArXiv e-prints*, Apr. 2018.

Barge, P., Baglin, A., Auvergne, M. *et al.* CoRoT: pioneer space mission for exoplanet transit search. In Sun, Y.-S., Ferraz-Mello, S., and Zhou, J.-L., editors, *Exoplanets: Detection, Formation and Dynamics*, volume 249 of *IAU Symposium*, pages 3–16, May 2008.

Barnes, S. A. On the Rotational Evolution of Solar- and Late-Type Stars, Its Magnetic Origins, and the Possibility of Stellar Gyrochronology. *ApJ*, 586:464–479, Mar. 2003.

Barnes, S. A. Ages for Illustrative Field Stars Using Gyrochronology: Viability, Limitations, and Errors. *ApJ*, 669:1167–1189, Nov. 2007.

Barnes, S. A. A Simple Nonlinear Model for the Rotation of Main-sequence Cool Stars. I. Introduction, Implications for Gyrochronology, and Color-Period Diagrams. *ApJ*, 722: 222–234, Oct. 2010.

Barnes, S. A. and Kim, Y.-C. Angular Momentum Loss from Cool Stars: An Empirical Expression and Connection to Stellar Activity. *ApJ*, 721:675-685, Sept. 2010.

Barros, S. C. C., Almenara, J. M., Deleuil, M. *et al.* Revisiting the transits of CoRoT-7b at a lower activity level. *A&A*, 569:A74, Sept. 2014.

Barros, S. C. C., Almenara, J. M., Demangeon, O. *et al.* Photodynamical mass determination of the multiplanetary system K2-19. *MNRAS*, 454:4267–4276, Dec. 2015.

Barros, S. C. C., Demangeon, O., and Deleuil, M. New planetary and eclipsing binary candidates from campaigns 1-6 of the K2 mission. *A&A*, 594:A100, Oct. 2016.

Barstow, J. K., Aigrain, S., Irwin, P. G. J. *et al.* A Consistent Retrieval Analysis of 10 Hot Jupiters Observed in Transmission. *ApJ*, 834:50, Jan. 2017.

Batalha, N. M., Borucki, W. J., Bryson, S. T. *et al.* Kepler's First Rocky Planet: Kepler-10b. *ApJ*, 729:27, Mar. 2011.

Batalha, N. M., Rowe, J. F., Bryson, S. T. *et al.* Planetary Candidates Observed by Kepler. III. Analysis of the First 16 Months of Data. *ApJS*, 204:24, Feb. 2013.

Batygin, K., Stevenson, D. J., and Bodenheimer, P. H. Evolution of Ohmically Heated Hot Jupiters. *ApJ*, 738:1, Sept. 2011.

Batygin, K., Bodenheimer, P. H., and Laughlin, G. P. In Situ Formation and Dynamical Evolution of Hot Jupiter Systems. *ApJ*, 829:114, Oct. 2016.

Bayliss, D., Hartman, J. D., Bakos, G. Á. *et al.* HATS-8b: A Low-density Transiting Super-Neptune. *AJ*, 150:49, Aug. 2015.

Ben-Jaffel, L. and Ballester, G. E. Hubble Space Telescope detection of oxygen in the atmosphere of exoplanet HD 189733b. *A&A*, 553:A52, May 2013.

Benedict, G. F., McArthur, B., Nelan, E. P. *et al.* Working with a space-based optical interferometer: HST Fine Guidance Sensor 3 small-field astrometry. In Reasenberg, R. D., editor, *Astronomical Interferometry*, volume 3350 of *Proc. SPIE*, pages 229–236, July 1998.

Benneke, B., Werner, M., Petigura, E. *et al.* Spitzer Observations Confirm and Rescue the Habitable-zone Super-Earth K2-18b for Future Characterization. *ApJ*, 834:187, Jan. 2017.

Beuzit, J.-L., Feldt, M., Dohlen, K. *et al.* SPHERE: a 'Planet Finder' instrument for the VLT. In *Ground-based and Airborne Instrumentation for Astronomy II*, volume 7014 of *Proc. SPIE*, page 701418, July 2008.

Bevington, P. R. *Data reduction and error analysis for the physical sciences*. 1969.

Blanco-Cuaresma, S., Soubiran, C., Heiter, U. *et al.* Determining stellar atmospheric parameters and chemical abundances of FGK stars with iSpec. *A&A*, 569:A111, Sept. 2014.

Boccaletti, A., Lagage, P.-O., Baudoz, P. *et al.* The Mid-Infrared Instrument for the James Webb Space Telescope, V: Predicted Performance of the MIRI Coronagraphs. *PASP*, 127:633, July 2015.

Bodenheimer, P., Lin, D. N. C., and Mardling, R. A. On the Tidal Inflation of Short-Period Extrasolar Planets. *ApJ*, 548:466–472, Feb. 2001.

Bodenheimer, P., Laughlin, G., and Lin, D. N. C. On the Radii of Extrasolar Giant Planets. *ApJ*, 592:555–563, July 2003.

Boisse, I., Moutou, C., Vidal-Madjar, A. *et al.* Stellar activity of planetary host star HD 189 733. *A&A*, 495:959–966, Mar. 2009.

Boisse, I., Bouchy, F., Hébrard, G. *et al.* Disentangling between stellar activity and planetary signals. *A&A*, 528:A4, Apr. 2011a.

Boisse, I., Bouchy, F., Hébrard, G. *et al.* Disentangling between stellar activity and planetary signals. In Prasad Choudhary, D. and Strassmeier, K. G., editors, *Physics of Sun and Star Spots*, volume 273 of *IAU Symposium*, pages 281–285, Aug. 2011b.

Bond, I. A., Abe, F., Dodd, R. J. *et al.* Real-time difference imaging analysis of MOA Galactic bulge observations during 2000. *MNRAS*, 327:868–880, Nov. 2001.

Bond, I. A., Udalski, A., Jaroszyński, M. *et al.* OGLE 2003-BLG-235/MOA 2003-BLG-53: A Planetary Microlensing Event. *ApJ*, 606:L155–L158, May 2004.

Bonnefoy, M., Marleau, G.-D., Galicher, R. *et al.* Physical and orbital properties of β Pictoris b. *A&A*, 567:L9, July 2014.

Borucki, W. J. and Summers, A. L. The photometric method of detecting other planetary systems. *Icarus*, 58:121–134, Apr. 1984.

Borucki, W. J., Scargle, J. D., and Hudson, H. S. Detectability of extrasolar planetary transits. *ApJ*, 291:852–854, Apr. 1985.

Borucki, W. J., Koch, D., Jenkins, J. *et al.* Kepler's Optical Phase Curve of the Exoplanet HAT-P-7b. *Science*, 325:709, Aug. 2009.

Borucki, W. J., Koch, D., Basri, G. *et al.* Kepler Planet-Detection Mission: Introduction and First Results. *Science*, 327:977, Feb. 2010.

Borucki, W. J., Koch, D. G., Basri, G. *et al.* Characteristics of Planetary Candidates Observed by Kepler. II. Analysis of the First Four Months of Data. *ApJ*, 736:19, July 2011.

Bouchy, F., Hébrard, G., Udry, S. *et al.* The SOPHIE search for northern extrasolar planets . I. A companion around HD 16760 with mass close to the planet/brown-dwarf transition. *A&A*, 505:853–858, Oct. 2009a.

Bouchy, F., Moutou, C., Queloz, D. *et al.* Radial velocity follow-up for confirmation and characterization of transiting exoplanets. *ArXiv e-prints*, Feb. 2009b.

Bouma, L. G., Winn, J. N., Kosiarek, J. *et al.* Planet Detection Simulations for Several Possible TESS Extended Missions. *ArXiv e-prints*, May 2017.

Broeg, C., Fortier, A., Ehrenreich, D. *et al.* CHEOPS: A transit photometry mission for ESA's small mission programme. In *European Physical Journal Web of Conferences*, volume 47 of *European Physical Journal Web of Conferences*, page 03005, Apr. 2013.

Brown, D. J. A., Collier Cameron, A., Hall, C. *et al.* Are falling planets spinning up their host stars? *MNRAS*, 415:605–618, July 2011.

Brugger, B., Mousis, O., Deleuil, M. *et al.* Constraints on Super-Earth Interiors from Stellar Abundances. *ApJ*, 850:93, Nov. 2017.

Burrows, A., Hubeny, I., Budaj, J. *et al.* Possible Solutions to the Radius Anomalies of Transiting Giant Planets. *ApJ*, 661:502–514, May 2007.

Butler, R. P., Vogt, S. S., Marcy, G. W. *et al.* A Neptune-Mass Planet Orbiting the Nearby M Dwarf GJ 436. *ApJ*, 617:580–588, Dec. 2004.

Carroll, B. W. and Ostlie, D. A. *An introduction to modern astrophysics and cosmology*. July 2006.

Carroll-Nellenback, J., Frank, A., Liu, B. *et al.* Hot planetary winds near a star: dynamics, wind-wind interactions, and observational signatures. *MNRAS*, 466:2458–2473, Apr. 2017.

Charbonneau, D., Brown, T. M., Latham, D. W. *et al.* Detection of Planetary Transits Across a Sun-like Star. *ApJ*, 529:L45–L48, Jan. 2000.

Charbonneau, D., Brown, T. M., Noyes, R. W. *et al.* Detection of an Extrasolar Planet Atmosphere. *ApJ*, 568:377–384, Mar. 2002.

Charbonneau, D., Berta, Z. K., Irwin, J. *et al.* A super-Earth transiting a nearby low-mass star. *Nature*, 462:891–894, Dec. 2009.

Chauvin, G., Lagrange, A.-M., Dumas, C. *et al.* A giant planet candidate near a young brown dwarf. Direct VLT/NACO observations using IR wavefront sensing. *A&A*, 425: L29–L32, Oct. 2004.

Chauvin, G., Vigan, A., Bonnefoy, M. *et al.* The VLT/NaCo large program to probe the occurrence of exoplanets and brown dwarfs at wide orbits. II. Survey description, results, and performances. *A&A*, 573:A127, Jan. 2015.

Chun, M., Toomey, D., Wahhaj, Z. *et al.* Performance of the near-infrared coronagraphic imager on Gemini-South. In *Adaptive Optics Systems*, volume 7015 of *Proc. SPIE*, page 70151V, July 2008.

Claret, A. A new non-linear limb-darkening law for LTE stellar atmosphere models. Calculations for -5.0 ¡= log[M/H] ¡= +1, 2000 K ¡= Teff ¡= 50000 K at several surface gravities. *A&A*, 363:1081–1190, Nov. 2000.

Claret, A. A new non-linear limb-darkening law for LTE stellar atmosphere models III. Sloan filters: Calculations for -5.0 ¡= log [M/H] ¡= +1, 2000 K ¡= T_{eff} ¡= 50 000 K at several surface gravities. *A&A*, 428:1001–1005, Dec. 2004.

Claret, A. and Bloemen, S. Gravity and limb-darkening coefficients for the Kepler, CoRoT, Spitzer, uvby, UBVRIJHK, and Sloan photometric systems. *A&A*, 529:A75, May 2011.

Clette, F., Svalgaard, L., Vaquero, J. M. *et al.* Revisiting the Sunspot Number. A 400-Year Perspective on the Solar Cycle. *Space Sci. Rev.*, 186:35–103, Dec. 2014.

Cloutier, R., Astudillo-Defru, N., Doyon, R. *et al.* Characterization of the K2-18 multi-planetary system with HARPS. A habitable zone super-Earth and discovery of a second, warm super-Earth on a non-coplanar orbit. *A&A*, 608:A35, Dec. 2017.

Collier Cameron, A., Horne, K., Penny, A. *et al.* Probable detection of starlight reflected from the giant planet orbiting τ Boötis. *Nature*, 402:751–755, Dec. 1999.

Collier Cameron, A., Pollacco, D., Street, R. A. *et al.* A fast hybrid algorithm for exoplanetary transit searches. *MNRAS*, 373:799–810, Dec. 2006.

Collier Cameron, A., Wilson, D. M., West, R. G. *et al.* Efficient identification of exoplanetary transit candidates from SuperWASP light curves. *MNRAS*, 380:1230–1244, Sept. 2007.

Cosentino, R., Lovis, C., Pepe, F. *et al.* Harps-N: the new planet hunter at TNG. In *Ground-based and Airborne Instrumentation for Astronomy IV*, volume 8446 of *Proc. SPIE*, page 84461V, Sept. 2012.

Cox, A. N. *Allen's astrophysical quantities*. 2000.

Crossfield, I. J. M., Ciardi, D. R., Petigura, E. A. *et al.* 197 Candidates and 104 Validated Planets in K2's First Five Fields. *ApJS*, 226:7, Sept. 2016.

Cutri et al., R. M. VizieR Online Data Catalog: AllWISE Data Release (Cutri+ 2013). *VizieR Online Data Catalog*, 2328, Jan. 2014.

Czesla, S., Huber, K. F., Wolter, U. *et al.* How stellar activity affects the size estimates of extrasolar planets. *A&A*, 505:1277–1282, Oct. 2009.

Dawson, R. I. and Johnson, J. A. Origins of Hot Jupiters. *ArXiv e-prints*, Jan. 2018.

Debrecht, A., Carroll-Nellenback, J., Frank, A. *et al.* Generation of a Circumstellar Gas Disk by Hot Jupiter WASP-12b. *MNRAS*, May 2018.

Deeg, H. J. and Belmonte, J. A. *Handbook of Exoplanets*. 2017.

Delfosse, X., Donati, J.-F., Kouach, D. *et al.* World-leading science with SPIRou - The nIR spectropolarimeter / high-precision velocimeter for CFHT. In Cambresy, L., Martins, F., Nuss, E. *et al.*, editors, *SF2A-2013: Proceedings of the Annual meeting of the French Society of Astronomy and Astrophysics*, pages 497–508, Nov. 2013.

Deming, D., Seager, S., Winn, J. *et al.* Discovery and Characterization of Transiting Super Earths Using an All-Sky Transit Survey and Follow-up by the James Webb Space Telescope. *PASP*, 121:952, Sept. 2009.

Desort, M., Lagrange, A.-M., Galland, F. *et al.* Search for exoplanets with the radial-velocity technique: quantitative diagnostics of stellar activity. *A&A*, 473:983–993, Oct. 2007.

Díaz, R. F., Almenara, J. M., Santerne, A. *et al.* PASTIS: Bayesian extrasolar planet validation - I. General framework, models, and performance. *MNRAS*, 441:983–1004, June 2014.

Dittmann, J. A., Irwin, J. M., Charbonneau, D. *et al.* A temperate rocky super-Earth transiting a nearby cool star. *Nature*, 544:333–336, Apr. 2017.

Dorn, C., Khan, A., Heng, K. *et al.* Can we constrain the interior structure of rocky exoplanets from mass and radius measurements? *A&A*, 577:A83, May 2015.

Dotter, A., Chaboyer, B., Jevremović, D. *et al.* The Dartmouth Stellar Evolution Database. *ApJS*, 178:89-101, Sept. 2008.

Doyle, A. P., Smalley, B., Maxted, P. F. L. *et al.* Accurate spectroscopic parameters of WASP planet host stars. *MNRAS*, 428:3164–3172, Feb. 2013.

Doyle, A. P., Davies, G. R., Smalley, B. *et al.* Determining stellar macroturbulence using asteroseismic rotational velocities from Kepler. *MNRAS*, 444:3592–3602, Nov. 2014.

Doyon, R., Hutchings, J., Rowlands, N. *et al.* The JWST tunable filter imager (TFI). In *Space Telescopes and Instrumentation 2010: Optical, Infrared, and Millimeter Wave*, volume 7731 of *Proc. SPIE*, page 77310F, July 2010.

Dravins, D. Stellar granulation. I - The observability of stellar photospheric convection. *A&A*, 172:200–224, Jan. 1987.

Dravins, D., Lindegren, L., and Nordlund, A. Solar granulation - Influence of convection on spectral line asymmetries and wavelength shifts. *A&A*, 96:345–364, Mar. 1981.

Dressing, C. D. and Charbonneau, D. The Occurrence Rate of Small Planets around Small Stars. *ApJ*, 767:95, Apr. 2013.

Dressing, C. D. and Charbonneau, D. The Occurrence of Potentially Habitable Planets Orbiting M Dwarfs Estimated from the Full Kepler Dataset and an Empirical Measurement of the Detection Sensitivity. *ApJ*, 807:45, July 2015.

Ehrenreich, D., Bourrier, V., Wheatley, P. J. *et al.* A giant comet-like cloud of hydrogen escaping the warm Neptune-mass exoplanet GJ 436b. *Nature*, 522:459–461, June 2015.

Einstein, A. Lens-Like Action of a Star by the Deviation of Light in the Gravitational Field. *Science*, 84:506–507, Dec. 1936.

Erkaev, N. V., Kulikov, Y. N., Lammer, H. *et al.* Roche lobe effects on the atmospheric loss from "Hot Jupiters". *A&A*, 472:329–334, Sept. 2007.

Fabrycky, D. and Tremaine, S. Shrinking Binary and Planetary Orbits by Kozai Cycles with Tidal Friction. *ApJ*, 669:1298–1315, Nov. 2007.

Fabrycky, D. C., Lissauer, J. J., Ragozzine, D. *et al.* Architecture of Kepler's Multi-transiting Systems. II. New Investigations with Twice as Many Candidates. *ApJ*, 790: 146, Aug. 2014.

Faedi, F., Barros, S. C. C., Anderson, D. R. *et al.* WASP-39b: a highly inflated Saturn-mass planet orbiting a late G-type star. *A&A*, 531:A40, July 2011.

Faedi, F., Pollacco, D., Barros, S. C. C. *et al.* WASP-54b, WASP-56b, and WASP-57b: Three new sub-Jupiter mass planets from SuperWASP. *A&A*, 551:A73, Mar. 2013.

Faria, J. P., Haywood, R. D., Brewer, B. J. *et al.* Uncovering the planets and stellar activity of CoRoT-7 using only radial velocities. *A&A*, 588:A31, Apr. 2016.

Ferraz-Mello, S., Tadeu Dos Santos, M., Beaugé, C. *et al.* On the mass determination of super-Earths orbiting active stars: the CoRoT-7 system. *A&A*, 531:A161, July 2011.

Figueira, P., Marmier, M., Bonfils, X. *et al.* Evidence against the young hot-Jupiter around BD +20 1790. *A&A*, 513:L8, Apr. 2010.

Figueira, P., Oshagh, M., Adibekyan, V. Z. *et al.* Revisiting the correlation between stellar activity and planetary surface gravity. *A&A*, 572:A51, Dec. 2014.

Findeisen, K. and Hillenbrand, L. Ultraviolet-selected Field and Pre-main-sequence Stars Toward Taurus and Upper Scorpius. *AJ*, 139:1338–1359, Apr. 2010.

Fischer, D. A. and Valenti, J. The Planet-Metallicity Correlation. *ApJ*, 622:1102–1117, Apr. 2005.

Ford, E. B. and Rasio, F. A. Origins of Eccentric Extrasolar Planets: Testing the Planet-Planet Scattering Model. *ApJ*, 686:621-636, Oct. 2008.

Fortney, J. J., Marley, M. S., and Barnes, J. W. Planetary Radii across Five Orders of Magnitude in Mass and Stellar Insolation: Application to Transits. *ApJ*, 659:1661–1672, Apr. 2007.

Fossati, L., Bagnulo, S., Elmasli, A. *et al.* A Detailed Spectropolarimetric Analysis of the Planet-hosting Star WASP-12. *ApJ*, 720:872–886, Sept. 2010a.

Fossati, L., Haswell, C. A., Froning, C. S. *et al.* Metals in the Exosphere of the Highly Irradiated Planet WASP-12b. *ApJ*, 714:L222–L227, May 2010b.

Fossati, L., Ayres, T. R., Haswell, C. A. *et al.* Absorbing Gas around the WASP-12 Planetary System. *ApJ*, 766:L20, Apr. 2013.

Fossati, L., France, K., Koskinen, T. *et al.* Far-UV Spectroscopy of the Planet-hosting Star WASP-13: High-energy Irradiance, Distance, Age, Planetary Mass-loss Rate, and Circumstellar Environment. *ApJ*, 815:118, Dec. 2015.

Fossati, L., Marcelja, S. E., Staab, D. *et al.* The effect of ISM absorption on stellar activity measurements and its relevance for exoplanet studies. *A&A*, 601:A104, May 2017.

Fossati, L., Koskinen, T., France, K. *et al.* Suppressed Far-UV Stellar Activity and Low Planetary Mass Loss in the WASP-18 System. *AJ*, 155:113, Mar. 2018.

Fressin, F., Torres, G., Charbonneau, D. *et al.* The False Positive Rate of Kepler and the Occurrence of Planets. *ApJ*, 766:81, Apr. 2013.

Fulton, B. J., Petigura, E. A., Howard, A. W. *et al.* The California-Kepler Survey. III. A Gap in the Radius Distribution of Small Planets. *AJ*, 154:109, Sept. 2017.

Gaia Collaboration, Brown, A. G. A., Vallenari, A. *et al.* Gaia Data Release 1. Summary of the astrometric, photometric, and survey properties. *A&A*, 595:A2, Nov. 2016a.

Gaia Collaboration, Prusti, T., de Bruijne, J. H. J. *et al.* The Gaia mission. *A&A*, 595:A1, Nov. 2016b.

Gaia Collaboration, Brown, A. G. A., Vallenari, A. *et al.* Gaia Data Release 2. Summary of the contents and survey properties. *ArXiv e-prints*, Apr. 2018a.

Gaia Collaboration, Brown, A. G. A., Vallenari, A. *et al.* Gaia Data Release 2. Summary of the contents and survey properties. *A&A*, 616:A1, Aug. 2018b.

Gallagher, A. Oscillator Strengths of Ca II, Sr II, and Ba II. *Physical Review*, 157:24–30, May 1967.

Gardner, J. P., Mather, J. C., Clampin, M. *et al.* The James Webb Space Telescope. *Space Sci. Rev.*, 123:485–606, Apr. 2006.

Gaudi, B. S., Bennett, D. P., Udalski, A. *et al.* Discovery of a Jupiter/Saturn Analog with Gravitational Microlensing. *Science*, 319:927, 2008.

Gillon, M., Jehin, E., Magain, P. *et al.* TRAPPIST: a robotic telescope dedicated to the study of planetary systems. In *European Physical Journal Web of Conferences*, volume 11 of *European Physical Journal Web of Conferences*, page 06002, Feb. 2011.

Gillon, M., Anderson, D. R., Collier-Cameron, A. *et al.* WASP-64 b and WASP-72 b: two new transiting highly irradiated giant planets. *A&A*, 552:A82, Apr. 2013.

Ginzburg, S., Schlichting, H. E., and Sari, R. Super-Earth Atmospheres: Self-consistent Gas Accretion and Retention. *ApJ*, 825:29, July 2016.

Ginzburg, S., Schlichting, H. E., and Sari, R. Core-powered mass-loss and the radius distribution of small exoplanets. *MNRAS*, 476:759–765, May 2018.

Goldreich, P. and Tremaine, S. Disk-satellite interactions. *ApJ*, 241:425–441, Oct. 1980.

Gondoin, P. Dynamo regime transition among Sun-like stars in M 34. A time evolution model of X-ray activity on the main sequence. *A&A*, 546:A117, Oct. 2012.

Gonzalez, G. The stellar metallicity-giant planet connection. *MNRAS*, 285:403–412, Feb. 1997.

Greene, T. P., Line, M. R., Montero, C. *et al.* Characterizing Transiting Exoplanet Atmospheres with JWST. *ApJ*, 817:17, Jan. 2016.

Guillot, T., Burrows, A., Hubbard, W. B. *et al.* Giant Planets at Small Orbital Distances. *ApJ*, 459:L35, Mar. 1996.

Hartman, J. D., Bakos, G. Á., Kipping, D. M. *et al.* HAT-P-26b: A Low-density Neptune-mass Planet Transiting a K Star. *ApJ*, 728:138, Feb. 2011.

Hastings, W. K. Monte Carlo Sampling Methods using Markov Chains and their Applications. *Biometrika, Vol. 57, No. 1, p. 97-109, 1970*, 57:97–109, Apr. 1970.

Haswell, C. A., Fossati, L., Ayres, T. *et al.* Near-ultraviolet Absorption, Chromospheric Activity, and Star-Planet Interactions in the WASP-12 system. *ApJ*, 760:79, Nov. 2012.

Hatzes, A. P. Radial-Velocity Variations from Starspots. In Hearnshaw, J. B. and Scarfe, C. D., editors, *IAU Colloq. 170: Precise Stellar Radial Velocities*, volume 185 of *Astronomical Society of the Pacific Conference Series*, page 259, 1999.

Hatzes, A. P., Dvorak, R., Wuchterl, G. *et al.* An investigation into the radial velocity variations of CoRoT-7. *A&A*, 520:A93, Sept. 2010.

Hatzes, A. P., Fridlund, M., Nachmani, G. *et al.* The Mass of CoRoT-7b. *ApJ*, 743:75, Dec. 2011.

Haywood, R. D., Collier Cameron, A., Queloz, D. *et al.* Planets and stellar activity: hide and seek in the CoRoT-7 system. *MNRAS*, 443:2517–2531, Sept. 2014.

Hebb, L., Collier-Cameron, A., Loeillet, B. *et al.* WASP-12b: The Hottest Transiting Extrasolar Planet Yet Discovered. *ApJ*, 693:1920–1928, Mar. 2009.

Hébrard, G., Collier Cameron, A., Brown, D. J. A. *et al.* WASP-52b, WASP-58b, WASP-59b, and WASP-60b: Four new transiting close-in giant planets. *A&A*, 549:A134, Jan. 2013.

Hellier, C., Anderson, D. R., Cameron, A. C. *et al.* WASP-South transiting exoplanets: WASP-130b, WASP-131b, WASP-132b, WASP-139b, WASP-140b, WASP-141b and WASP-142b. *MNRAS*, 465:3693–3707, Mar. 2017.

Henry, G. W., Marcy, G. W., Butler, R. P. *et al.* A Transiting "51 Peg-like" Planet. *ApJ*, 529:L41–L44, Jan. 2000.

Henry, T. J., Soderblom, D. R., Donahue, R. A. *et al.* A Survey of Ca II H and K Chromospheric Emission in Southern Solar-Type Stars. *AJ*, 111, Jan. 1996.

Hoeg, E., Bässgen, G., Bastian, U. *et al.* The TYCHO Catalogue. *A&A*, 323:L57–L60, July 1997.

Høg, E., Fabricius, C., Makarov, V. V. *et al.* The Tycho-2 catalogue of the 2.5 million brightest stars. *A&A*, 355:L27–L30, Mar. 2000.

Howard, A. W., Marcy, G. W., Bryson, S. T. *et al.* Planet Occurrence within 0.25 AU of Solar-type Stars from Kepler. *ApJS*, 201:15, Aug. 2012.

Howell, S. B., Sobeck, C., Haas, M. *et al.* The K2 Mission: Characterization and Early Results. *PASP*, 126:398, Apr. 2014.

Huang, C. X., Shporer, A., Dragomir, D. *et al.* Expected Yields of Planet discoveries from the TESS primary and extended missions. *ArXiv e-prints*, July 2018.

Huang, X. and Cumming, A. Ohmic Dissipation in the Interiors of Hot Jupiters. *ApJ*, 757: 47, Sept. 2012.

Hubbard, W. B. The Jovian surface condition and cooling rate. *Icarus*, 30:305–310, Feb. 1977.

Huélamo, N., Figueira, P., Bonfils, X. *et al.* TW Hydrae: evidence of stellar spots instead of a Hot Jupiter. *A&A*, 489:L9–L13, Oct. 2008.

Ida, S. and Lin, D. N. C. Toward a Deterministic Model of Planetary Formation. IV. Effects of Type I Migration. *ApJ*, 673:487-501, Jan. 2008.

Jackson, A. P., Davis, T. A., and Wheatley, P. J. The coronal X-ray-age relation and its implications for the evaporation of exoplanets. *MNRAS*, 422:2024–2043, May 2012.

Jackson, B., Greenberg, R., and Barnes, R. Tidal evolution of close-in extrasolar planets. *The Astrophysical Journal*, 678(2):1396, 2008. URL `http://stacks.iop.org/0004-637X/678/i=2/a=1396`.

Jehin, E., Gillon, M., Queloz, D. *et al.* TRAPPIST: TRAnsiting Planets and PlanetesImals Small Telescope. *The Messenger*, 145:2–6, Sept. 2011.

Jin, S. and Mordasini, C. Compositional Imprints in Density-Distance-Time: A Rocky Composition for Close-in Low-mass Exoplanets from the Location of the Valley of Evaporation. *ApJ*, 853:163, Feb. 2018.

Johnson, J. A., Fischer, D. A., Marcy, G. W. *et al.* Retired A Stars and Their Companions: Exoplanets Orbiting Three Intermediate-Mass Subgiants. *ApJ*, 665:785–793, Aug. 2007.

Johnson, J. A., Aller, K. M., Howard, A. W. *et al.* Giant Planet Occurrence in the Stellar Mass-Metallicity Plane. *PASP*, 122:905, Aug. 2010.

Johnson, J. A., Petigura, E. A., Fulton, B. J. *et al.* The California-Kepler Survey. II. Precise Physical Properties of 2025 Kepler Planets and Their Host Stars. *AJ*, 154:108, Sept. 2017.

Jones, M. I., Jenkins, J. S., Bluhm, P. *et al.* The properties of planets around giant stars. *A&A*, 566:A113, June 2014.

Kelch, W. L., Linsky, J. L., and Worden, S. P. Stellar model chromospheres. IX - Chromospheric activity in dwarf stars. *ApJ*, 229:700–712, Apr. 1979.

Kharchenko, N. V. All-sky compiled catalogue of 2.5 million stars. *Kinematika i Fizika Nebesnykh Tel*, 17:409–423, Oct. 2001.

Kharchenko, N. V., Piskunov, A. E., Röser, S. *et al.* Astrophysical parameters of Galactic open clusters. *A&A*, 438:1163–1173, Aug. 2005.

Kipping, D. M. Binning is sinning: morphological light-curve distortions due to finite integration time. *MNRAS*, 408:1758–1769, Nov. 2010.

Knutson, H. A., Howard, A. W., and Isaacson, H. A Correlation Between Stellar Activity and Hot Jupiter Emission Spectra. *ApJ*, 720:1569–1576, Sept. 2010.

Koch, D. G., Borucki, W. J., Basri, G. *et al.* Kepler Mission Design, Realized Photometric Performance, and Early Science. *ApJ*, 713:L79-L86, Apr. 2010.

Kovács, G., Zucker, S., and Mazeh, T. A box-fitting algorithm in the search for periodic transits. *A&A*, 391:369–377, Aug. 2002.

Kovács, G., Bakos, G., and Noyes, R. W. A trend filtering algorithm for wide-field variability surveys. *MNRAS*, 356:557–567, Jan. 2005.

Kozai, Y. Secular perturbations of asteroids with high inclination and eccentricity. *AJ*, 67: 591, Nov. 1962.

Kraft, R. P. Studies of Stellar Rotation. V. The Dependence of Rotation on Age among Solar-Type Stars. *ApJ*, 150:551, Nov. 1967.

Kulow, J. R., France, K., Linsky, J. *et al.* Lyα Transit Spectroscopy and the Neutral Hydrogen Tail of the Hot Neptune GJ 436b. *ApJ*, 786:132, May 2014.

Kupka, F., Dubernet, M.-L., and VAMDC Collaboration. Vamdc as a Resource for Atomic and Molecular Data and the New Release of Vald. *Baltic Astronomy*, 20:503–510, 2011.

Kurokawa, H. and Kaltenegger, L. Atmospheric mass-loss and evolution of short-period exoplanets: the examples of CoRoT-7b and Kepler-10b. *MNRAS*, 433:3239–3245, Aug. 2013.

Kurokawa, H. and Nakamoto, T. Mass-loss Evolution of Close-in Exoplanets: Evaporation of Hot Jupiters and the Effect on Population. *ApJ*, 783:54, Mar. 2014.

Kurucz, R. L. ATLAS12, SYNTHE, ATLAS9, WIDTH9, et cetera. *Memorie della Societa Astronomica Italiana Supplementi*, 8:14, 2005.

Lagrange, A.-M., Gratadour, D., Chauvin, G. *et al.* A probable giant planet imaged in the β Pictoris disk. VLT/NaCo deep L'-band imaging. *A&A*, 493:L21–L25, Jan. 2009.

Lagrange, A.-M., Bonnefoy, M., Chauvin, G. *et al.* A Giant Planet Imaged in the Disk of the Young Star β Pictoris. *Science*, 329:57, July 2010.

Lam, K. W. F., Faedi, F., Brown, D. J. A. *et al.* From dense hot Jupiter to low-density Neptune: The discovery of WASP-127b, WASP-136b, and WASP-138b. *A&A*, 599:A3, Mar. 2017.

Lammer, H., Selsis, F., Ribas, I. *et al.* Atmospheric Loss of Exoplanets Resulting from Stellar X-Ray and Extreme-Ultraviolet Heating. *ApJ*, 598:L121–L124, Dec. 2003.

Law, N. M., Fors, O., Ratzloff, J. *et al.* Evryscope Science: Exploring the Potential of All-Sky Gigapixel-Scale Telescopes. *PASP*, 127:234, Mar. 2015.

Lecavelier Des Etangs, A. A diagram to determine the evaporation status of extrasolar planets. *A&A*, 461:1185–1193, Jan. 2007.

Lecavelier des Etangs, A., Vidal-Madjar, A., McConnell, J. C. *et al.* Atmospheric escape from hot Jupiters. *A&A*, 418:L1–L4, Apr. 2004.

Lecavelier Des Etangs, A., Ehrenreich, D., Vidal-Madjar, A. *et al.* Evaporation of the planet HD 189733b observed in H I Lyman-α. *A&A*, 514:A72, May 2010.

Lee, E. J. and Chiang, E. To Cool is to Accrete: Analytic Scalings for Nebular Accretion of Planetary Atmospheres. *ApJ*, 811:41, Sept. 2015.

Léger, A., Rouan, D., Schneider, J. *et al.* Transiting exoplanets from the CoRoT space mission. VIII. CoRoT-7b: the first super-Earth with measured radius. *A&A*, 506:287–302, Oct. 2009.

Lendl, M., Anderson, D. R., Collier-Cameron, A. *et al.* WASP-42 b and WASP-49 b: two new transiting sub-Jupiters. *A&A*, 544:A72, Aug. 2012.

Lidov, M. L. The evolution of orbits of artificial satellites of planets under the action of gravitational perturbations of external bodies. *Planet. Space Sci.*, 9:719–759, Oct. 1962.

Lindegren, L., Hernández, J., Bombrun, A. *et al.* Gaia Data Release 2. The astrometric solution. *A&A*, 616:A2, Aug. 2018.

Linsky, J. L. and Avrett, E. H. The Solar H and K Lines. *PASP*, 82:169, Apr. 1970.

Linsky, J. L. and Ayres, T. R. Stellar model chromospheres. VI - Empirical estimates of the chromospheric radiative losses of late-type stars. *ApJ*, 220:619–628, Mar. 1978.

Linsky, J. L., Worden, S. P., McClintock, W. *et al.* Stellar model chromospheres. X - High-resolution, absolute flux profiles of the CA II H and K lines in stars of spectral types F0-M2. *ApJS*, 41:47–74, Sept. 1979.

Linsky, J. L., Yang, H., France, K. *et al.* Observations of Mass Loss from the Transiting Exoplanet HD 209458b. *ApJ*, 717:1291–1299, July 2010.

Linsky, J. L., France, K., and Ayres, T. Computing Intrinsic LYα Fluxes of F5 V to M5 V Stars. *ApJ*, 766:69, Apr. 2013.

Lissauer, J. J., Fabrycky, D. C., Ford, E. B. *et al.* A closely packed system of low-mass, low-density planets transiting Kepler-11. *Nature*, 470:53–58, Feb. 2011a.

Lissauer, J. J., Ragozzine, D., Fabrycky, D. C. *et al.* Architecture and Dynamics of Kepler's Candidate Multiple Transiting Planet Systems. *ApJS*, 197:8, Nov. 2011b.

Liu, M. C., Wahhaj, Z., Biller, B. A. *et al.* The Gemini NICI Planet-Finding Campaign. In *Adaptive Optics Systems II*, volume 7736 of *Proc. SPIE*, page 77361K, July 2010.

Loktin, A. V. and Beshenov, G. V. Proper Motions of Open Star Clusters and the Rotation Rate of the Galaxy. *Astronomy Reports*, 47:6–10, Jan. 2003.

Lomb, N. R. Least-squares frequency analysis of unequally spaced data. *Ap&SS*, 39:447–462, Feb. 1976.

Lopez, E. D. and Fortney, J. J. The Role of Core Mass in Controlling Evaporation: The Kepler Radius Distribution and the Kepler-36 Density Dichotomy. *ApJ*, 776:2, Oct. 2013.

Lopez, E. D. and Fortney, J. J. Re-inflated Warm Jupiters around Red Giants. *ApJ*, 818:4, Feb. 2016.

Lopez, E. D., Fortney, J. J., and Miller, N. How Thermal Evolution and Mass-loss Sculpt Populations of Super-Earths and Sub-Neptunes: Application to the Kepler-11 System and Beyond. *ApJ*, 761:59, Dec. 2012.

López-Morales, M. and Seager, S. Thermal Emission from Transiting Very Hot Jupiters: Prospects for Ground-based Detection at Optical Wavelengths. *ApJ*, 667:L191–L194, Oct. 2007.

Lovis, C. and Mayor, M. Planets around evolved intermediate-mass stars. I. Two substellar companions in the open clusters NGC 2423 and NGC 4349. *A&A*, 472:657–664, Sept. 2007.

Lucy, L. B. and Sweeney, M. A. Spectroscopic binaries with circular orbits. *AJ*, 76:544–556, Aug. 1971.

Lyot, B. The study of the solar corona and prominences without eclipses (George Darwin Lecture, 1939). *MNRAS*, 99:580, June 1939.

Macintosh, B., Graham, J. R., Ingraham, P. *et al.* First light of the Gemini Planet Imager. *Proceedings of the National Academy of Science*, 111:12661–12666, Sept. 2014.

Malbet, F. High angular resolution coronography for adaptive optics. *A&AS*, 115:161, Jan. 1996.

Mamajek, E. E. and Hillenbrand, L. A. Improved Age Estimation for Solar-Type Dwarfs Using Activity-Rotation Diagnostics. *ApJ*, 687:1264-1293, Nov. 2008.

Mandel, K. and Agol, E. Analytic Light Curves for Planetary Transit Searches. *ApJ*, 580: L171–L175, Dec. 2002.

Mao, S. and Paczynski, B. Gravitational microlensing by double stars and planetary systems. *ApJ*, 374:L37–L40, June 1991.

Marcus, R. A., Sasselov, D., Hernquist, L. *et al.* Minimum Radii of Super-Earths: Constraints from Giant Impacts. *ApJ*, 712:L73–L76, Mar. 2010.

Marois, C., Lafrenière, D., Doyon, R. *et al.* Angular Differential Imaging: A Powerful High-Contrast Imaging Technique. *ApJ*, 641:556–564, Apr. 2006.

Marois, C., Macintosh, B., Barman, T. *et al.* Direct Imaging of Multiple Planets Orbiting the Star HR 8799. *Science*, 322:1348, Nov. 2008.

Marois, C., Zuckerman, B., Konopacky, Q. M. *et al.* Images of a fourth planet orbiting HR 8799. *Nature*, 468:1080–1083, Dec. 2010.

Masset, F. S. and Papaloizou, J. C. B. Runaway Migration and the Formation of Hot Jupiters. *ApJ*, 588:494–508, May 2003.

Maxted, P. F. L., Anderson, D. R., Collier Cameron, A. *et al.* WASP-41b: A Transiting Hot Jupiter Planet Orbiting a Magnetically Active G8V Star. *PASP*, 123:547, May 2011.

Maxted, P. F. L., Serenelli, A. M., and Southworth, J. Bayesian mass and age estimates for transiting exoplanet host stars. *A&A*, 575:A36, Mar. 2015a.

Maxted, P. F. L., Serenelli, A. M., and Southworth, J. Comparison of gyrochronological and isochronal age estimates for transiting exoplanet host stars. *A&A*, 577:A90, May 2015b.

Mayo, A. W., Vanderburg, A., Latham, D. W. *et al.* 275 Candidates and 149 Validated Planets Orbiting Bright Stars in K2 Campaigns 0-10. *AJ*, 155:136, Mar. 2018.

Mayor, M. and Queloz, D. A Jupiter-mass companion to a solar-type star. *Nature*, 378: 355–359, Nov. 1995.

Mayor, M., Pepe, F., Queloz, D. *et al.* Setting New Standards with HARPS. *The Messenger*, 114:20–24, Dec. 2003.

Mayor, M., Marmier, M., Lovis, C. *et al.* The HARPS search for southern extra-solar planets XXXIV. Occurrence, mass distribution and orbital properties of super-Earths and Neptune-mass planets. *ArXiv e-prints*, Sept. 2011.

Mayor, M., Lovis, C., and Santos, N. C. Doppler spectroscopy as a path to the detection of Earth-like planets. *Nature*, 513:328–335, Sept. 2014.

Mazeh, T., Zucker, S., and Pont, F. An intriguing correlation between the masses and periods of the transiting planets. *MNRAS*, 356:955–957, Jan. 2005.

Mazeh, T., Holczer, T., and Faigler, S. Dearth of short-period Neptunian exoplanets: A desert in period-mass and period-radius planes. *A&A*, 589:A75, May 2016.

McQuillan, A., Mazeh, T., and Aigrain, S. Stellar Rotation Periods of the Kepler Objects of Interest: A Dearth of Close-in Planets around Fast Rotators. *ApJ*, 775:L11, Sept. 2013.

McQuillan, A., Mazeh, T., and Aigrain, S. Rotation Periods of 34,030 Kepler Main-sequence Stars: The Full Autocorrelation Sample. *ApJS*, 211:24, Apr. 2014.

Meibom, S., Torres, G., Fressin, F. *et al.* The same frequency of planets inside and outside open clusters of stars. *Nature*, 499:55–58, July 2013.

Metropolis, N., Rosenbluth, A. W., Rosenbluth, M. N. *et al.* Equation of State Calculations by Fast Computing Machines. *J. Chem. Phys.*, 21:1087–1092, June 1953.

Meunier, N., Desort, M., and Lagrange, A.-M. Using the Sun to estimate Earth-like planets detection capabilities . II. Impact of plages. *A&A*, 512:A39, Mar. 2010.

Middelkoop, F. Magnetic structure in cool stars. IV - Rotation and CA II H and K emission of main-sequence stars. *A&A*, 107:31–35, Mar. 1982.

Moffatt, H. K. *Magnetic field generation in electrically conducting fluids*. 1978.

Montet, B. T., Morton, T. D., Foreman-Mackey, D. *et al.* Stellar and Planetary Properties of K2 Campaign 1 Candidates and Validation of 17 Planets, Including a Planet Receiving Earth-like Insolation. *ApJ*, 809:25, Aug. 2015.

Mordasini, C., Alibert, Y., Benz, W. *et al.* Extrasolar planet population synthesis . IV. Correlations with disk metallicity, mass, and lifetime. *A&A*, 541:A97, May 2012.

Munari, U., Henden, A., Frigo, A. *et al.* APASS Landolt-Sloan BVgri Photometry of RAVE Stars. I. Data, Effective Temperatures, and Reddenings. *AJ*, 148:81, Nov. 2014.

Mura, A., Wurz, P., Schneider, J. *et al.* Comet-like tail-formation of exospheres of hot rocky exoplanets: Possible implications for CoRoT-7b. *Icarus*, 211:1–9, Jan. 2011.

Murakawa, K., Suto, H., Tamura, M. *et al.* CIAO: Coronagraphic Imager with Adaptive Optics on the Subaru Telescope. *PASJ*, 56:509–519, June 2004.

Murray-Clay, R. A., Chiang, E. I., and Murray, N. Atmospheric Escape From Hot Jupiters. *ApJ*, 693:23–42, Mar. 2009.

Nichols, J. D., Wynn, G. A., Goad, M. *et al.* Hubble Space Telescope Observations of the NUV Transit of WASP-12b. *ApJ*, 803:9, Apr. 2015.

Nissen, P. E. High-precision abundances of elements in solar twin stars. Trends with stellar age and elemental condensation temperature. *A&A*, 579:A52, July 2015.

Noecker, M. C., Zhao, F., Demers, R. *et al.* Coronagraph instrument for WFIRST-AFTA. *Journal of Astronomical Telescopes, Instruments, and Systems*, 2(1):011001, Jan. 2016.

Noyes, R. W., Hartmann, L. W., Baliunas, S. L. *et al.* Rotation, convection, and magnetic activity in lower main-sequence stars. *ApJ*, 279:763–777, Apr. 1984a.

Noyes, R. W., Weiss, N. O., and Vaughan, A. H. The relation between stellar rotation rate and activity cycle periods. *ApJ*, 287:769–773, Dec. 1984b.

Oshagh, M., Santos, N. C., Boisse, I. *et al.* Effect of stellar spots on high-precision transit light-curve. *A&A*, 556:A19, Aug. 2013.

Owen, J. E. and Jackson, A. P. Planetary evaporation by UV & X-ray radiation: basic hydrodynamics. *MNRAS*, 425:2931–2947, Oct. 2012.

Owen, J. E. and Wu, Y. Kepler Planets: A Tale of Evaporation. *ApJ*, 775:105, Oct. 2013.

Owen, J. E. and Wu, Y. The Evaporation Valley in the Kepler Planets. *ApJ*, 847:29, Sept. 2017.

Paczynski, B. Gravitational microlensing by the galactic halo. *ApJ*, 304:1–5, May 1986.

Pál, A., Mészáros, L., Jaskó, A. *et al.* A Hexapod Design for All-sky Sidereal Tracking. *PASP*, 128(4):045002, Apr. 2016.

Palle, E., Chen, G., Prieto-Arranz, J. *et al.* Feature-rich transmission spectrum for WASP-127b. Cloud-free skies for the puffiest known super-Neptune? *A&A*, 602:L15, June 2017.

Parker, E. N. *Cosmical magnetic fields: Their origin and their activity*. 1979.

Pasquini, L., Avila, G., Blecha, A. *et al.* Installation and commissioning of FLAMES, the VLT Multifibre Facility. *The Messenger*, 110:1–9, Dec. 2002.

Pecaut, M. J. and Mamajek, E. E. Intrinsic Colors, Temperatures, and Bolometric Corrections of Pre-main-sequence Stars. *ApJS*, 208:9, Sept. 2013.

Pepe, F., Mayor, M., Galland, F. *et al.* The CORALIE survey for southern extra-solar planets VII. Two short-period Saturnian companions to ¡ASTROBJ¿HD 108147¡/ASTROBJ¿ and ¡ASTROBJ¿HD 168746¡/ASTROBJ¿. *A&A*, 388:632–638, June 2002a.

Pepe, F., Mayor, M., Rupprecht, G. *et al.* HARPS: ESO's coming planet searcher. Chasing exoplanets with the La Silla 3.6-m telescope. *The Messenger*, 110:9–14, Dec. 2002b.

Pepe, F., Mayor, M., Queloz, D. *et al.* The HARPS search for southern extra-solar planets. I. HD 330075 b: A new "hot Jupiter". *A&A*, 423:385–389, Aug. 2004.

Pepe, F., Molaro, P., Cristiani, S. *et al.* ESPRESSO: The next European exoplanet hunter. *ArXiv e-prints*, Jan. 2014.

Pepper, J., Pogge, R. W., DePoy, D. L. *et al.* The Kilodegree Extremely Little Telescope (KELT): A Small Robotic Telescope for Large-Area Synoptic Surveys. *PASP*, 119:923–935, Aug. 2007.

Perryman, M. *The Exoplanet Handbook*. Jan. 2014.

Perryman, M., Hartman, J., Bakos, G. Á. *et al.* Astrometric Exoplanet Detection with Gaia. *ApJ*, 797:14, Dec. 2014.

Perryman, M. A. C., Lindegren, L., Kovalevsky, J. *et al.* The HIPPARCOS Catalogue. *A&A*, 323:L49–L52, July 1997.

Perryman, M. A. C., de Boer, K. S., Gilmore, G. *et al.* GAIA: Composition, formation and evolution of the Galaxy. *A&A*, 369:339–363, Apr. 2001.

Petigura, E. A., Howard, A. W., and Marcy, G. W. Prevalence of Earth-size planets orbiting Sun-like stars. *Proceedings of the National Academy of Science*, 110:19273–19278, Nov. 2013.

Pickles, A. J. A Stellar Spectral Flux Library: 1150-25000 Å. *PASP*, 110:863–878, July 1998.

Pollacco, D., Skillen, I., Collier Cameron, A. *et al.* WASP-3b: a strongly irradiated transiting gas-giant planet. *MNRAS*, 385:1576–1584, Apr. 2008.

Pollacco, D. L., Skillen, I., Collier Cameron, A. *et al.* The WASP Project and the SuperWASP Cameras. *PASP*, 118:1407–1418, Oct. 2006.

Pont, F., Gilliland, R. L., Moutou, C. *et al.* Hubble Space Telescope time-series photometry of the planetary transit of HD 189733: no moon, no rings, starspots. *A&A*, 476:1347–1355, Dec. 2007.

Pont, F., Knutson, H., Gilliland, R. L. *et al.* Detection of atmospheric haze on an extrasolar planet: the 0.55-1.05 μm transmission spectrum of HD 189733b with the HubbleSpaceTelescope. *MNRAS*, 385:109–118, Mar. 2008.

Pont, F., Aigrain, S., and Zucker, S. Reassessing the radial-velocity evidence for planets around CoRoT-7. *MNRAS*, 411:1953–1962, Mar. 2011.

Pope, B. J. S., Parviainen, H., and Aigrain, S. Transiting exoplanet candidates from K2 Campaigns 5 and 6. *MNRAS*, 461:3399–3409, Oct. 2016.

Queloz, D. Echelle Spectroscopy with a CCD at Low Signal-To-Noise Ratio. In Philip, A. G. D., Janes, K., and Upgren, A. R., editors, *New Developments in Array Technology and Applications*, volume 167 of *IAU Symposium*, page 221, 1995.

Queloz, D., Eggenberger, A., Mayor, M. *et al.* Detection of a spectroscopic transit by the planet orbiting the star HD209458. *A&A*, 359:L13–L17, July 2000.

Queloz, D., Henry, G. W., Sivan, J. P. *et al.* No planet for HD 166435. *A&A*, 379:279–287, Nov. 2001a.

Queloz, D., Mayor, M., Udry, S. *et al.* From CORALIE to HARPS. The way towards 1 m s^{-1} precision Doppler measurements. *The Messenger*, 105:1–7, Sept. 2001b.

Queloz, D., Bouchy, F., Moutou, C. *et al.* The CoRoT-7 planetary system: two orbiting super-Earths. *A&A*, 506:303–319, Oct. 2009.

Quinn, S. N., White, R. J., Latham, D. W. *et al.* Two "b"s in the Beehive: The Discovery of the First Hot Jupiters in an Open Cluster. *ApJ*, 756:L33, Sept. 2012.

Quinn, S. N., White, R. J., Latham, D. W. *et al.* HD 285507b: An Eccentric Hot Jupiter in the Hyades Open Cluster. *ApJ*, 787:27, May 2014.

Quirrenbach, A., Amado, P. J., Seifert, W. *et al.* CARMENES. I: instrument and survey overview. In *Ground-based and Airborne Instrumentation for Astronomy IV*, volume 8446 of *Proc. SPIE*, page 84460R, Sept. 2012.

Racine, R., Walker, G. A. H., Nadeau, D. *et al.* Speckle Noise and the Detection of Faint Companions. *PASP*, 111:587–594, May 1999.

Rasio, F. A. and Ford, E. B. Dynamical instabilities and the formation of extrasolar planetary systems. *Science*, 274:954–956, Nov. 1996.

Rasio, F. A., Tout, C. A., Lubow, S. H. *et al.* Tidal Decay of Close Planetary Orbits. *ApJ*, 470:1187, Oct. 1996.

Rauer, H., Catala, C., Aerts, C. *et al.* The PLATO 2.0 mission. *Experimental Astronomy*, 38:249–330, Nov. 2014.

Redfield, S., Endl, M., Cochran, W. D. *et al.* Sodium Absorption from the Exoplanetary Atmosphere of HD 189733b Detected in the Optical Transmission Spectrum. *ApJ*, 673: L87, Jan. 2008.

Ricker, G. R., Winn, J. N., Vanderspek, R. *et al.* Transiting Exoplanet Survey Satellite (TESS). In *Space Telescopes and Instrumentation 2014: Optical, Infrared, and Millimeter Wave*, volume 9143 of *Proc. SPIE*, page 914320, Aug. 2014.

Ridden-Harper, A. R., Snellen, I. A. G., Keller, C. U. *et al.* Search for an exosphere in sodium and calcium in the transmission spectrum of exoplanet 55 Cancri e. *A&A*, 593: A129, Oct. 2016.

Rousset, G., Lacombe, F., Puget, P. *et al.* Status of the VLT Nasmyth adaptive optics system (NAOS). In Wizinowich, P. L., editor, *Adaptive Optical Systems Technology*, volume 4007 of *Proc. SPIE*, pages 72–81, July 2000.

Rutten, R. G. M. Magnetic structure in cool stars. VII - Absolute surface flux in CA II H and K line cores. *A&A*, 130:353–360, Jan. 1984.

Saar, S. H. and Donahue, R. A. Activity-Related Radial Velocity Variation in Cool Stars. *ApJ*, 485:319–327, Aug. 1997.

Sanchis-Ojeda, R., Fabrycky, D. C., Winn, J. N. *et al.* Alignment of the stellar spin with the orbits of a three-planet system. *Nature*, 487:449–453, July 2012.

Santerne, A., Díaz, R. F., Almenara, J.-M. *et al.* PASTIS: Bayesian extrasolar planet validation - II. Constraining exoplanet blend scenarios using spectroscopic diagnoses. *MNRAS*, 451:2337–2351, Aug. 2015.

Santerne, A., Hébrard, G., Lillo-Box, J. *et al.* K2-29 b/WASP-152 b: An Aligned and Inflated Hot Jupiter in a Young Visual Binary. *ApJ*, 824:55, June 2016.

Santos, N. C., Israelian, G., and Mayor, M. The metal-rich nature of stars with planets. *A&A*, 373:1019–1031, July 2001.

Santos, N. C., Bouchy, F., Mayor, M. *et al.* The HARPS survey for southern extra-solar planets. II. A 14 Earth-masses exoplanet around μ Arae. *A&A*, 426:L19–L23, Oct. 2004.

Santos, N. C., Gomes da Silva, J., Lovis, C. *et al.* Do stellar magnetic cycles influence the measurement of precise radial velocities? *A&A*, 511:A54, Feb. 2010.

Sato, B., Izumiura, H., Toyota, E. *et al.* A Planetary Companion to the Hyades Giant ϵ Tauri. *ApJ*, 661:527–531, May 2007.

Scargle, J. D. Studies in astronomical time series analysis. II - Statistical aspects of spectral analysis of unevenly spaced data. *ApJ*, 263:835–853, Dec. 1982.

Schlaufman, K. C. and Winn, J. N. Evidence for the Tidal Destruction of Hot Jupiters by Subgiant Stars. *ApJ*, 772:143, Aug. 2013.

Schlichting, H. E. Formation of Close in Super-Earths and Mini-Neptunes: Required Disk Masses and their Implications. *ApJ*, 795:L15, Nov. 2014.

Schrijver, C. J. and Zwaan, C. *Solar and Stellar Magnetic Activity*. Oct. 2008.

Seager, S., Kuchner, M., Hier-Majumder, C. A. *et al.* Mass-Radius Relationships for Solid Exoplanets. *ApJ*, 669:1279–1297, Nov. 2007.

Shkolnik, E. L. and Barman, T. S. HAZMAT. I. The Evolution of Far-UV and Near-UV Emission from Early M Stars. *AJ*, 148:64, Oct. 2014.

Sing, D. K., Fortney, J. J., Nikolov, N. *et al.* A continuum from clear to cloudy hot-Jupiter exoplanets without primordial water depletion. *Nature*, 529:59–62, Jan. 2016.

Sinukoff, E., Howard, A. W., Petigura, E. A. *et al.* Eleven Multiplanet Systems from K2 Campaigns 1 and 2 and the Masses of Two Hot Super-Earths. *ApJ*, 827:78, Aug. 2016.

Sivaramakrishnan, A., Koresko, C. D., Makidon, R. B. *et al.* Ground-based Coronagraphy with High-order Adaptive Optics. *ApJ*, 552:397–408, May 2001.

Smalley, B., Anderson, D. R., Collier-Cameron, A. *et al.* WASP-78b and WASP-79b: two highly-bloated hot Jupiter-mass exoplanets orbiting F-type stars in Eridanus. *A&A*, 547: A61, Nov. 2012.

Sneden, C. A. *Carbon and Nitrogen Abundances in Metal-Poor Stars.* PhD thesis, The University of Texas at Austin., 1973.

Snellen, I. A. G., Stuik, R., Navarro, R. *et al.* Ground-based search for the brightest transiting planets with the Multi-site All-Sky CAmeRA: MASCARA. In *Ground-based and Airborne Telescopes IV*, volume 8444 of *Proc. SPIE*, page 84440I, Sept. 2012.

Soderblom, D. R., Duncan, D. K., and Johnson, D. R. H. The chromospheric emission-age relation for stars of the lower main sequence and its implications for the star formation rate. *ApJ*, 375:722–739, July 1991.

Sousa, S. G., Santos, N. C., Mayor, M. *et al.* Spectroscopic parameters for 451 stars in the HARPS GTO planet search program. Stellar [Fe/H] and the frequency of exo-Neptunes. *A&A*, 487:373–381, Aug. 2008.

Sousa, S. G., Santos, N. C., Adibekyan, V. *et al.* ARES v2: new features and improved performance. *A&A*, 577:A67, May 2015.

Southworth, J. Homogeneous studies of transiting extrasolar planets - I. Light-curve analyses. *MNRAS*, 386:1644–1666, May 2008.

Southworth, J., Hinse, T. C., Dominik, M. *et al.* High-precision photometry by telescope defocusing - IV. Confirmation of the huge radius of WASP-17 b. *MNRAS*, 426:1338–1348, Oct. 2012.

Southworth, J., Hinse, T. C., Burgdorf, M. *et al.* High-precision photometry by telescope defocussing - VI. WASP-24, WASP-25 and WASP-26. *MNRAS*, 444:776–789, Oct. 2014.

Staab, D., Haswell, C. A., Smith, G. D. *et al.* SALT observations of the chromospheric activity of transiting planet hosts: mass-loss and star-planet interactions. *MNRAS*, 466: 738–748, Apr. 2017.

Steele, I. A., Bates, S. D., Gibson, N. *et al.* RISE: a fast-readout imager for exoplanet transit timing. In *Ground-based and Airborne Instrumentation for Astronomy II*, volume 7014 of *Proc. SPIE*, page 70146J, July 2008.

Stone, R. C. A comparison of digital centering algorithms. *AJ*, 97:1227–1237, Apr. 1989.

Strassmeier, K., Washuettl, A., Granzer, T. *et al.* The Vienna-KPNO search for Doppler-imaging candidate stars. I. A catalog of stellar-activity indicators for 1058 late-type Hipparcos stars. *A&AS*, 142:275–311, Mar. 2000.

Sullivan, P. W., Winn, J. N., Berta-Thompson, Z. K. *et al.* The Transiting Exoplanet Survey Satellite: Simulations of Planet Detections and Astrophysical False Positives. *ApJ*, 809: 77, Aug. 2015.

Szabó, G. M. and Kiss, L. L. A Short-period Censor of Sub-Jupiter Mass Exoplanets with Low Density. *ApJ*, 727:L44, Feb. 2011.

Tamura, M., Suto, H., Murakawa, K. *et al.* Coronagraphic Imager with Adaptive Optics (CIAO) for the Subaru 8.2m Telescope. In *American Astronomical Society Meeting Abstracts #198*, volume 33 of *Bulletin of the American Astronomical Society*, page 902, May 2001.

Tamuz, O., Mazeh, T., and Zucker, S. Correcting systematic effects in a large set of photometric light curves. *MNRAS*, 356:1466–1470, Feb. 2005.

Tegmark, M., Strauss, M. A., Blanton, M. R. *et al.* Cosmological parameters from SDSS and WMAP. *Phys. Rev. D*, 69(10):103501, May 2004.

Thomas, J. H. and Weiss, N. O. *Sunspots and Starspots*. Oct. 2012.

Triaud, A. H. M. J., Collier Cameron, A., Queloz, D. *et al.* Spin-orbit angle measurements for six southern transiting planets. New insights into the dynamical origins of hot Jupiters. *A&A*, 524:A25, Dec. 2010.

Tucci Maia, M., Ramírez, I., Meléndez, J. *et al.* The Solar Twin Planet Search. III. The [Y/Mg] clock: estimating stellar ages of solar-type stars. *A&A*, 590:A32, May 2016.

Udalski, A. The Optical Gravitational Lensing Experiment. Real Time Data Analysis Systems in the OGLE-III Survey. *Acta Astron.*, 53:291–305, Dec. 2003.

Udalski, A., Szymanski, M., Kaluzny, J. *et al.* The Optical Gravitational Lensing Experiment. The Early Warning System: Real Time Microlensing. *Acta Astron.*, 44:227–234, July 1994.

Udry, S. and Santos, N. C. Statistical Properties of Exoplanets. *ARA&A*, 45:397–439, Sept. 2007.

Vaiana, G. S., Cassinelli, J. P., Fabbiano, G. *et al.* Results from an extensive Einstein stellar survey. *ApJ*, 245:163–182, Apr. 1981.

van Saders, J. L., Ceillier, T., Metcalfe, T. S. *et al.* Weakened magnetic braking as the origin of anomalously rapid rotation in old field stars. *Nature*, 529:181–184, Jan. 2016.

Vanderburg, A. and Johnson, J. A. A Technique for Extracting Highly Precise Photometry for the Two-Wheeled Kepler Mission. *PASP*, 126:948, Oct. 2014.

Vanderburg, A., Latham, D. W., Buchhave, L. A. *et al.* Planetary Candidates from the First Year of the K2 Mission. *ApJS*, 222:14, Jan. 2016.

Vaughan, A. H. and Preston, G. W. A survey of chromospheric CA II H and K emission in field stars of the solar neighborhood. *PASP*, 92:385–391, Aug. 1980.

Vaughan, A. H., Preston, G. W., and Wilson, O. C. Flux measurements of CA II H and K emission. *PASP*, 90:267–274, June 1978.

Vaughan, A. H., Preston, G. W., Baliunas, S. L. *et al.* Stellar rotation in lower main-sequence stars measured from time variations in H and K emission-line fluxes. I - Initial results. *ApJ*, 250:276–283, Nov. 1981.

Vidal-Madjar, A., Lecavelier des Etangs, A., Désert, J.-M. *et al.* An extended upper atmosphere around the extrasolar planet HD209458b. *Nature*, 422:143–146, Mar. 2003.

Vidal-Madjar, A., Désert, J.-M., Lecavelier des Etangs, A. *et al.* Detection of Oxygen and Carbon in the Hydrodynamically Escaping Atmosphere of the Extrasolar Planet HD 209458b. *ApJ*, 604:L69–L72, Mar. 2004.

Vidal-Madjar, A., Sing, D. K., Lecavelier Des Etangs, A. *et al.* The upper atmosphere of the exoplanet HD 209458 b revealed by the sodium D lines. Temperature-pressure profile, ionization layer, and thermosphere. *A&A*, 527:A110, Mar. 2011.

Vigan, A., Bonnefoy, M., Ginski, C. *et al.* First light of the VLT planet finder SPHERE. I. Detection and characterization of the substellar companion GJ 758 B. *A&A*, 587:A55, Mar. 2016.

Villaver, E. and Livio, M. The Orbital Evolution of Gas Giant Planets Around Giant Stars. *ApJ*, 705:L81–L85, Nov. 2009.

Vogt, S. S. HIRES - a High Resolution Echelle Spectrometer for the Keck Ten-Meter Telescope. In Ulrich, M.-H., editor, *European Southern Observatory Conference and Workshop Proceedings*, volume 40 of *European Southern Observatory Conference and Workshop Proceedings*, page 223, June 1992.

Vogt, S. S., Allen, S. L., Bigelow, B. C. *et al.* HIRES: the high-resolution echelle spectrometer on the Keck 10-m Telescope. In Crawford, D. L. and Craine, E. R., editors, *Instrumentation in Astronomy VIII*, volume 2198 of *Proc. SPIE*, page 362, June 1994.

Wang, J., Fischer, D. A., Horch, E. P. *et al.* On the Occurrence Rate of Hot Jupiters in Different Stellar Environments. *ApJ*, 799:229, Feb. 2015.

Warner, B. D. *A Practical Guide to Lightcurve Photometry and Analysis*. 2006.

Weber, E. J. and Davis, L., Jr. The Angular Momentum of the Solar Wind. *ApJ*, 148: 217–227, Apr. 1967.

Weidenschilling, S. J. and Marzari, F. Gravitational scattering as a possible origin for giant planets at small stellar distances. *Nature*, 384:619–621, Dec. 1996.

Weiss, A. and Schlattl, H. GARSTEC - the Garching Stellar Evolution Code. The direct descendant of the legendary Kippenhahn code. *Ap&SS*, 316:99–106, Aug. 2008.

Weiss, L. M. and Marcy, G. W. The Mass-Radius Relation for 65 Exoplanets Smaller than 4 Earth Radii. *ApJ*, 783:L6, Mar. 2014.

Weiss, L. M., Marcy, G. W., Rowe, J. F. *et al.* The Mass of KOI-94d and a Relation for Planet Radius, Mass, and Incident Flux. *ApJ*, 768:14, May 2013.

Weiss, L. M., Marcy, G. W., Petigura, E. A. *et al.* The California-Kepler Survey. V. Peas in a Pod: Planets in a Kepler Multi-planet System Are Similar in Size and Regularly Spaced. *AJ*, 155:48, Jan. 2018.

Wheatley, P. J., Pollacco, D. L., Queloz, D. *et al.* The Next Generation Transit Survey (NGTS). In *European Physical Journal Web of Conferences*, volume 47 of *European Physical Journal Web of Conferences*, page 13002, Apr. 2013.

Wheatley, P. J., West, R. G., Goad, M. R. *et al.* The Next Generation Transit Survey (NGTS). *MNRAS*, 475:4476–4493, Apr. 2018.

Wilson, O. C. A Probable Correlation Between Chromospheric Activity and Age in Main-Sequence Stars. *ApJ*, 138:832, Oct. 1963.

Wilson, O. C. Chromospheric variations in main-sequence stars. *ApJ*, 226:379–396, Dec. 1978.

Winn, J. N. Measuring accurate transit parameters. In Pont, F., Sasselov, D., and Holman, M. J., editors, *Transiting Planets*, volume 253 of *IAU Symposium*, pages 99–109, Feb. 2009.

Winn, J. N., Johnson, J. A., Albrecht, S. *et al.* HAT-P-7: A Retrograde or Polar Orbit, and a Third Body. *ApJ*, 703:L99–L103, Oct. 2009.

Wolszczan, A. and Frail, D. A. A planetary system around the millisecond pulsar PSR1257 + 12. *Nature*, 355:145–147, Jan. 1992.

Wright, J. T. Do We Know of Any Maunder Minimum Stars? *AJ*, 128:1273–1278, Sept. 2004.

Wright, J. T. and Howard, A. W. Efficient Fitting of Multiplanet Keplerian Models to Radial Velocity and Astrometry Data. *ApJS*, 182:205-215, May 2009.

Wright, J. T., Marcy, G. W., Butler, R. P. *et al.* Chromospheric Ca II Emission in Nearby F, G, K, and M Stars. *ApJS*, 152:261–295, June 2004.

Wright, J. T., Marcy, G. W., Howard, A. W. *et al.* The Frequency of Hot Jupiters Orbiting nearby Solar-type Stars. *ApJ*, 753:160, July 2012.

Wu, Y. and Lithwick, Y. Secular Chaos and the Production of Hot Jupiters. *ApJ*, 735:109, July 2011.

Zeng, L., Sasselov, D. D., and Jacobsen, S. B. Mass-Radius Relation for Rocky Planets Based on PREM. *ApJ*, 819:127, Mar. 2016.